

MINERALOGICAL INDICATORS OF MAGMATIC AND HYDROTHERMAL
PROCESSES IN CONTINENTAL ARC CRUST

by
CELESTINE NICOLE MERCER

A DISSERTATION

Presented to the Department of Geological Sciences
and the Graduate School of the University of Oregon
in partial fulfillment of the requirements
for the degree of
Doctor of Philosophy

June 2009

University of Oregon Graduate School

Confirmation of Approval and Acceptance of Dissertation prepared by:

Celestine Mercer

Title:

"Mineralogical Indicators of Magmatic and Hydrothermal Processes in Continental Arc Crust "

This dissertation has been accepted and approved in partial fulfillment of the requirements for the Doctor of Philosophy degree in the Department of Geological Sciences by:

A. Dana Johnston, Chairperson, Geological Sciences

Mark Reed, Member, Geological Sciences

Paul Wallace, Member, Geological Sciences

Richard P. Taylor, Outside Member, Physics

and Richard Linton, Vice President for Research and Graduate Studies/Dean of the Graduate School for the University of Oregon.

June 13, 2009

Original approval signatures are on file with the Graduate School and the University of Oregon Libraries.

© 2009 Celestine Nicole Mercer

An Abstract of the Dissertation of

Celestine Nicole Mercer for the degree of Doctor of Philosophy
in the Department of Geological Sciences to be taken June 2009

Title: MINERALOGICAL INDICATORS OF MAGMATIC AND HYDROTHERMAL
PROCESSES IN CONTINENTAL ARC CRUST

Approved: _____
A. Dana Johnston

This dissertation explores several important consequences of H₂O-rich fluids in magmatic and ore-forming systems within continental arc crust.

North Sister, a stratovolcano in the Oregon High Cascades, provides a window into magma generation processes in the deep crust. Eruption of a remarkably limited basaltic andesite composition over the lifespan of this volcano may reflect last equilibration of mantle derived magma within a deep crustal hot zone. High pressure, water-undersaturated phase equilibrium experiments show that an anhydrous, augite-rich gabbro at ~12 kbar (40 km depth) and ~1175°C is the most probable lithology with which North Sister basaltic andesite with ~3.5 wt% H₂O last equilibrated within the deep crust before erupting.

While magma often erupts at the planet's surface as at North Sister, a greater volume never reaches the surface and solidifies within the upper crust. Exsolution of

magmatic fluids is an inevitable consequence of crystallization of hydrous crustal magmas. The fate of these fluids is the focus of the remainder of this dissertation.

Modeling of CO₂ and H₂O variations during crystallization of granitic magma reveals that exsolution of a large mass of fluid occurs only after CO₂ is largely degassed, creating ideal conditions for hydrofracturing and formation of porphyry copper deposits. CO₂ and H₂O solubility relations suggest that H₂O-rich magma was required to produce the porphyry-Cu-Mo deposit at Butte, Montana, which may explain its distinctively deep generation. Electron microprobe analyses of Ti in quartz and Zr in rutile in samples from Butte yield porphyry magma temperatures (630-770°C) that overlap substantially with hydrothermal vein temperatures (<430-750°C). Veins display large temperature ranges (50-250°C) that signify variable degrees of cooling of hot magmatic fluids upon contact with cooler wall rock during vein growth. Modeling of Ti diffusion in quartz suggests that individual dikes and veins likely cooled over short timescales (10s-1000s years), indicating that porphyry systems may evolve by episodic magmatic fluid injections with discrete thermal spikes. Modeling of Ti diffusion in quartz combined with electron backscatter diffraction maps show that small hydrothermal quartz veins likely formed by epitaxial growth.

This dissertation includes co-authored material both previously published and in preparation for submission.

CURRICULUM VITAE

NAME OF AUTHOR: Celestine Nicole Mercer

PLACE OF BIRTH: Libby, Montana, USA

DATE OF BIRTH: 17 October 1979

GRADUATE AND UNDERGRADUATE SCHOOLS ATTENDED:

University of Oregon, Eugene, Oregon

Oberlin College, Oberlin, Ohio

DEGREES AWARDED:

Doctor of Philosophy in Geological Sciences, 2009, University of Oregon

Bachelor of Arts in Physics, 2003, Oberlin College

AREAS OF SPECIAL INTEREST:

Igneous Petrology

Magmatic-Hydrothermal Interactions

PROFESSIONAL EXPERIENCE:

Graduate Teaching Fellow, University of Oregon, 2003-2009

Mineralogy Instructor (sabbatical replacement), University of Oregon, 2008

Substitute Teacher, Montrose County School District Re-1J, Colorado, 2003

Student Intern, Jet Propulsion Laboratory, Earth & Space Science Division,
California, 2001

GRANTS, AWARDS AND HONORS:

EBSD Workshop Scholarship, National Science Foundation and Microbeam Analysis Society, 2008

Lipman Research Award, Geological Society of America, 2006

Staples Fellowship for Petrology, University of Oregon, 2006

Elected to Sigma Xi Scientific Research Society, 2002

PUBLICATIONS:

Mercer CN, Johnston AD (2008) Experimental studies of the P-T-H₂O near-liquidus phase relations of basaltic andesite from North Sister Volcano, High Oregon Cascades: constraints on lower-crustal mineral assemblages. *Contributions to Mineralogy and Petrology* 155:571-592

Castro JM, Mercer CN (2004) Microlite textures and volatile contents of obsidian from the Inyo volcanic chain, California. *Geophysical Research Letters* 31(L18605):doi: 10.1029/2004GL02489

ACKNOWLEDGEMENTS

With the acceptance of this dissertation I will become the first woman in my family to be awarded a Ph.D. This achievement is not representative of my aspirations alone, but of all those in my family who have taught me to love and appreciate nature, to work and play hard, and to have the courage to chase my curiosity of nature wherever it may lead. I am happy to dedicate this dissertation to the inspiring women of my heritage.

I would like to thank Dana Johnston, my advisor who took me in green and provided me with academic and financial support to help me find my way to become a true scientist. Not only is he an example of a great scientist, teacher, and advisor, but he is an example of a well balanced person. He has been a role model for how to make the most of life and I am grateful for all of his guidance in life outside the lab. Thank you to Muffin Milligan, Dana's better half, for all of her support over the past six years.

I am grateful to Mark Reed, my advisor who opened my horizons beyond igneous petrology to gain an appreciation for some of the most complex rocks on Earth, hydrothermally "improved" rocks. He has given me much academic and financial support as well as the freedom to explore magmatic hydrothermal systems from a non-traditional point of view. His ability to think outside of the box has been inspiring. I would like to thank Mark for his endless encouragement both in the lab and in life.

Thank you to John Donovan, whose guidance and cutting-edge creativity has greatly strengthened my research, and to Paul Wallace whose door was always open to

discuss my work. Thank you to the DoGS staff who make this department a great place to work, and to the rest of the University of Oregon faculty who have provided me great scientific guidance, especially Alan Rempel, Kathy Cashman, Josh Roering, and Richard Taylor. Thank you to Dave Senkovitch, the “miracle worker”, and Clarisse Heinhorst who were always ready to have fun! I appreciate all that I have learned from the Oregon State University VIPERs John Dilles, Anita Grunder, and Mariek Schmidt.

Thank you to many other scientists who provided guidance for my research, including Glenn Gaetani, Mike Baker, Charlie Mandeville, Gordon Moore, Kurt Langworthy, Nobu Shimizu, Peter Ulmer, Mark Ghiorso, Adam Soule, Lihua Zhang, Hannah Grist, Brendan Hodge, Steve Weimholt, Brian Rusk, Scott Sitzman, and Dave Prior. This research was supported by NSF grants EAR-0230373 and EAR-0440198.

Finally, I would like to recognize the support of the many friends that I have made during my time in Oregon, in particular, my scientific big sister, Julie Roberge, and my experimental petrology sister, Stephanie Weaver. Many thanks to the rest of the girl gang who helped me keep my life balanced, especially Jenny Riker, Emily Johnson, Nathalie Vigouroux, Emily Gottesfeld, Daniele Mckay, Lisa Emerson, Beth Erlund, Rachel Troyer, Christine Metzger, Katherine Watts, Isolde Belien, and Haiying Gao. Thank you to David Levering, Sara Auer, Amanda Macleod, and Matt Hansen for getting me out climbing, hiking, and cycling, and to Dan Ruscitto for good science talks and laughs. And many thanks to Mr. Maian and the late Mr. Apollo, my little rascals who remind me why life is good.

*For Elizabeth Marie Boeh, Velma Vergean Mercer, Beatrice Anna Rickert,
and Pauline Ann Mercer*

TABLE OF CONTENTS

Chapter	Page
I. INTRODUCTION.....	1
II. EXPERIMENTAL STUDIES OF THE P-T-H ₂ O NEAR-LIQUIDUS PHASE RELATIONS OF BASALTIC ANDESITE FROM NORTH SISTER VOLCANO, HIGH OREGON CASCADES: CONSTRAINTS ON LOWER- CRUSTAL MINERAL ASSEMBLAGES.....	4
Introduction.....	4
Background.....	5
Nature of the Mid- to Lower-Arc Crust.....	5
Cascadia Subduction.....	6
North Sister Volcano	6
Methods	9
Starting Materials and Bulk Compositions.....	9
Experimental Methods.....	10
Analytical Techniques	15
SEM and EPMA Analyses.....	15
Infrared Spectroscopy	17
Ion Probe Analyses	18
Iron and Water Loss.....	18
Attainment of Equilibrium.....	20
Results.....	21
P-T-H ₂ O Near-Liquidus Phase Relations	21
Phase Compositions.....	30
Glass	30
Vesicles.....	31
Minerals	31

Chapter	Page
Trace Element Distribution Coefficients	33
Discussion.....	35
Comparison with Mineral Phases in North Sister Lavas	35
Potential Lower-Crustal Mineral Assemblages	36
Proposed Equilibration Conditions and Ascent Path.....	41
Summary and Conclusions	42
Bridge.....	43
 III. MAGMATIC VOLATILE CONTROLS ON THE FORMATION DEPTH OF PORPHYRY COPPER ORE DEPOSITS	 44
Introduction.....	44
Methods	47
Volatile Solubility Model Results.....	48
High H ₂ O Content in the Butte Porphyry Magma.....	52
CO ₂ and H ₂ O Controls on Porphyry Deposit Formation Depth	55
Bridge.....	57
 IV. THE TEMPERATURE CONNECTION BETWEEN MAGMATIC AND HYDROTHERMAL REALMS OF THE PORPHYRY-Cu-Mo DEPOSIT AT BUTTE, MONTANA	 58
1. Introduction.....	58
1.1. Porphyry Ore Deposits.....	58
1.2. Geologic Background of Butte, MT	60
1.3. Petrography of Igneous and Hydrothermal Rocks.....	66
Butte Granite	66
Porphyry Dikes.....	66
Biotite Breccias and Biotite Crackles.....	67
Early Dark Micaceous Veins.....	67
Pale Green Sericitic Veins.....	68
Barren Quartz and Quartz-Molybdenite Veins	68

Chapter	Page
Pyrite-Quartz Grey Sericitic Veins	68
2. Methods	69
2.1. SEM Analyses.....	69
2.2. Microprobe Analyses.....	71
2.3. Mineral Geothermometry	72
Ti-in-Quartz Thermometry.....	72
Zr-in-Rutile Thermometry.....	73
Ti-in-Biotite Thermometry.....	73
2.4. Fluid Inclusion Microthermometry.....	74
3. Results.....	74
3.1. Plutonic, Porphyry, and Hydrothermal Quartz	74
3.2. Hydrothermal Rutile	85
3.3. Plutonic and Hydrothermal Biotite.....	89
3.4. Fluid Inclusion Thermobarometry.....	95
4. Discussion.....	99
4.1. The Magmatic-Hydrothermal Temperature Connection	99
4.2. Porphyry Deposit Thermal Profile.....	103
4.3. Reevaluation of Fluid Inclusion Thermobarometry: Butte Goes from Deep to Deeper?	105
5. Conclusions.....	108
6. Bridge.....	109
 V. TIMESCALES OF PORPHYRY-Cu DEPOSIT FORMATION: INSIGHTS FROM SEM-CATHODOLUMINESCENCE AND TITANIUM DIFFUSION IN QUARTZ	110
Introduction	110
Geologic Setting and Sample Suite.....	112
Methods.....	115
SEM-Cathodoluminescence.....	115
Microprobe Trace Element Traverses and Mapping	115

Chapter	Page
SEM-CL Brightness as a Proxy for Ti Concentration in Quartz	116
Ti Diffusion in Quartz and Time Scales	117
Heat Conduction Profiles.....	120
Results	122
Quartz Generations in SEM-CL	122
Correlation of Trace Elements with SEM-CL Brightness	123
Modeling of Ti Diffusion in Quartz.....	125
Modeling of Heat Conduction for Dikes and Veins	130
Discussion	132
Ti as the Primary SEM-CL Activator in Magmatic and Hydrothermal Quartz	132
Timescales of Porphyry Deposit Formation and Cooling	133
Conclusions	135
Bridge.....	135
 VI. SEAMLESS EPITAXIAL GROWTH OF HYDROTHERMAL QUARTZ VEINS: AN EBSD, SEM-CL, AND CHEMICAL DIFFUSION STUDY	136
Introduction.....	136
Geologic Setting	139
Methods	140
Quartz Vein Textures and Crystallography	142
Modeled SEM-CL Textures from Ti Diffusion in Quartz.....	144
Discussion and Implications	146
 VII. CONCLUSIONS	148
 APPENDIX: MELT INCLUSION ANALYSES FROM NORTH SISTER VOLCANO, OREGON	152
 REFERENCES	155

LIST OF FIGURES

Figure	Page
Chapter II	
1. Location Maps for North Sister Volcano.....	7
2. Backscattered Electron Images of Experimental Run Products.	16
3. Variation in Fe-Loss and Water Contents in Experimental Run Products	19
4. Water-Undersaturated Liquidus Surface with H ₂ O Contours.....	28
5. Variation of Near-Liquidus Augite Compositions.....	32
6. Average Mineral/Melt Distribution Coefficients.....	34
7. Water-Undersaturated Liquidus Surface Showing Possible “Deep Crustal Hot Zone” and ascent path.....	38
8. Primitive Mantle Normalized Rare Earth Elements	40
Chapter III	
1. Schematic Cross Section of Fluid-Saturated Crystallizing Magma Beneath a Porphyry Copper Deposit	45
2. Modeled CO ₂ and H ₂ O Fluid Saturation Isobars and Isopleths.....	49
3. Variation in H ₂ O and CO ₂ in Melt and Fluid During Isobaric Fractional Crystallization.....	50
4. Experimental Hornblende and Biotite Stability.....	54
5. Schematic Depth Profile for Porphyry Deposits in this Study	56
Chapter IV	
1. Schematic Cross Section of a Porphyry Deposit	59
2. Location Map and Regional Geologic Setting of the Butte District.....	62
3. Maps of Porphyry Dikes, Pre-Main Stage Mineralization, and Sample Locations.....	63
4. Examples of Cathodoluminescent Textures in Quartz	75
5. Ti-in-Quartz Temperatures	83

Figure	Page
6. Analytical Error and Temperature Precision of Quartz Geothermometer	84
7. Example Images of Hydrothermal Rutile	85
8. Zr-in-Rutile Temperatures	88
9. Average Zr-in-Rutile Temperatures for Rutile in Veins and in Adjacent Alteration Envelopes.....	88
10. Analytical Error and Temperature Precision of Rutile Geothermometer	89
11. Optical Photomicrographs of Biotite Types	90
12. Plutonic and Hydrothermal Biotite Compositions.....	92
13. Histograms Showing Fluid Inclusion Melting Temperatures of Ice and Clathrate and Homogenization Temperatures	98
14. Composite Graph of Temperatures.....	100
15. Pressure-Temperature Diagram for Hydrothermal and Magmatic Components	107
 Chapter V	
1. Location Map and Regional Geologic Setting of the Butte District.....	111
2. East-West Cross Section of Pre-Main Stage Porphyry-Cu-Mo Mineralization at Butte.....	114
3. Schematic Diagram of Cathodoluminescent Brightness Changes Caused by Diffusion of Ti in Quartz	119
4. Examples of Cathodoluminescent Textures in Quartz	121
5. Examples of Microprobe Trace Element Traverses, Corresponding SEM-CL Images, and SEM-CL Brightness Calibration	124
6. High Sensitivity Microprobe Trace Element Maps	126
7. Examples of Modeling Ti Diffusion in Quartz.....	127
8. Summary of Modeled Timescales as a Function of Assumed Model Temperature	129
9. Model Results for Conduction of Heat from Injections of Magma or Hydrothermal Fluids.....	131

Figure	Page
Chapter VI	
1. Vein Formation Possibilities.....	138
2. Crystallography of Cross-Cutting Quartz Veins.....	143
3. Model Results for Diffusion of Ti in Quartz	145

LIST OF TABLES

Table	Page
Chapter II	
1. Compositions of Natural and Experimental Starting Materials.....	11
2. Summary of Experimental Run Conditions and Phase Percentages Present.....	13
3. Major Element Compositions from Microprobe Analyses of Experimental Run Products.....	22
4. Ion Microprobe Analyses of Select Run Products.....	26
5. Mineral/Melt Distribution Coefficients	34
Chapter IV	
1. Sample Locations and Types	70
2. Microprobe Analyses of Trace Elements in Quartz and Calculated Ti-in-Quartz Temperatures.....	81
3. Microprobe Analyses of Trace Elements in Rutile and Calculated Zr-in-Rutile Temperatures.....	86
4. Microprobe Analyses of Biotite, Calculated Formulas (Based on 22 O), and Calculated Ti-in-Biotite Temperatures.....	91
5. Fluid Inclusion Homogenization Temperatures, Melting Temperatures, and Calculated Compositions and Densities.....	96
Chapter V	
1. Sample Locations, Descriptions, and Modeled SEM-CL Boundary Types	113
2. Temperatures and Ti Diffusivities Used in Modeling	118

CHAPTER I

INTRODUCTION

The products of magmatic and hydrothermal processes operating within the continental arc crust are abundantly evident at the Earth's surface in chains of active stratovolcanoes and belts of large mineral deposits, however, the processes themselves are elusive. Minerals can be used as indicators of magmatic and hydrothermal processes because they record geochemical and textural information that reflects the conditions under which they grew. For example, the pressure, temperature, or composition of the magma or aqueous fluid from which a mineral precipitated is reflected in the mineral composition, while episodes of mineral growth, resorption, or fracturing are reflected in the mineral form.

In this dissertation, I use mineralogical indicators to investigate several important magmatic and hydrothermal processes within continental arc crust. First I explore hydrous magma generation in the lower crust beneath a young subduction-related stratovolcano. Then I examine degassing of hydrous magma in a granitic pluton within the upper crust. Finally I explore the transition from magmatic to hydrothermal processes in the shallow crust as I unravel the development of a porphyry copper deposit.

Magma generation processes in the lower crust arc are complex and difficult to constrain. Hildreth and Moorbath (1988) proposed a conceptual model, the MASH model, whereby mantle-derived basalts attain a geochemical signature characteristic of the particular pressure, temperature, and H₂O conditions of the lower crust by a process involving Melting, Assimilation, Storage, and Homogenization. Annen et al. (2006) developed a numerical model of deep crustal processes occurring in "deep crustal hot zones". In such zones, mantle-derived hydrous basalts are emplaced as sills in the lower crust, where they partially crystallize, yielding H₂O-rich melts that mix and equilibrate with volumetrically lesser liquids produced by melting of pre-existing amphibolitic

crustal rocks (Annen et al. 2006). Deep crustal magma generation is an important process by which many intermediate and silicic igneous rocks are produced, therefore a better understanding of the pressure, temperature, composition, and H₂O content of the lower-arc crust would be useful to help constrain this process.

It has long been known that H₂O plays an important role in deep crustal magma generation because H₂O has a dramatic effect on the stability of crystallizing minerals (e.g., Kushiro 1972; Wyllie 1979). H₂O also plays a significant role in the evolution of magma in the shallow crust. Exsolution of magmatic fluids, such as H₂O and CO₂, is an inevitable consequence of crystallization of hydrous upper crustal magmas. These magma-derived H₂O-rich fluids drive shallow crustal hydrothermal systems and are essential to the formation of many ore deposits.

Porphyry copper deposits are large magmatic ore deposits that are the world's primary source of Cu and Mo. They form in and around silicic plutons, porphyry dikes, and co-genetic volcanic rocks from exsolved magmatic fluids that carry metals and sulfur from large magma volumes and concentrate them into a cupola. Above the cupola, pulses of hydro-fracturing, porphyry dike injection, and fluid flow through fractures lead to host rock alteration and metal sulfide deposition (Cloos 2001; Seedorff et al. 2005). Despite recognition of this close spatial and genetic relationship between magmatic and hydrothermal components in porphyry systems, much remains unknown about the transition between magmatic and hydrothermal processes.

In this dissertation I explore several important consequences of H₂O-rich fluids in magmatic and ore-forming systems within continental arc crust. I start by investigating hydrous magma generation within the deep crust beneath a subduction-related stratovolcano in the Oregon Cascades (Chapter II). High pressure, water-undersaturated phase equilibrium experiments provide constraints on the deep crustal lithology, pressure, and temperature with which hydrous basaltic andesite last equilibrated before erupting at the surface. A great volume of magma never reaches the planet's surface, but instead solidifies within the upper crust, exsolving magmatic volatiles. I examine the variations of H₂O and CO₂ during crystallization of hydrous silicic crustal magma and explore how

this inevitable process plays a key role in determining the formation depth of ore-forming magmatic-hydrothermal systems (Chapter III). Overpressure of exsolved magmatic H₂O-rich fluids creates ideal conditions for hydrofracturing and formation of porphyry copper deposits. I investigate the temperature connection between the magmatic and hydrothermal realms of a porphyry copper deposit in Butte, Montana by applying three geothermometers utilizing magmatic and hydrothermal minerals (Chapter IV). Using these analyses, I then model trace element diffusion in magmatic and hydrothermal quartz to determine the timescales of magmatic and hydrothermal processes that form this deposit (Chapter V). These studies illustrate that the transition from magmatic to hydrothermal systems within a porphyry deposit is gradational, and occurs on relatively short timescales akin to magmatism at stratovolcanoes. Finally, I examine the physical processes by which hydrothermal veins form from magmatic-derived fluids (Chapter VI). The results presented in this dissertation illustrate the importance of H₂O-rich fluids in the generation of crustal magma and the origin of ore-forming hydrothermal systems.

I am the primary author of all chapters in this dissertation, and I was responsible for the majority of micro-analytical work, data processing, and modeling in each chapter. Chapter II was published in *Contributions to Mineralogy and Petrology* in 2008, volume 155, pages 571-592. This paper was co-authored with A. Dana Johnston, who provided advising and editorial support as well as funding for the project. Chapter III is in preparation for submission to the journal *Geology* and is co-authored with Paul J. Wallace and Mark H. Reed who provided advising and manuscript reviews. Chapters IV, V, and VI are in preparation for submission to the *Journal of Volcanology and Geothermal Research*, *Economic Geology*, and *American Mineralogist*, respectively, and are all co-authored with Mark H. Reed who provided advising, editorial support, and project funding.

CHAPTER II

EXPERIMENTAL STUDIES OF THE P-T-H₂O NEAR-LIQUIDUS PHASE
RELATIONS OF BASALTIC ANDESITE FROM NORTH SISTER
VOLCANO, HIGH OREGON CASCADES: CONSTRAINTS ON
LOWER-CRUSTAL MINERAL ASSEMBLAGES

This chapter was published in *Contributions to Mineralogy and Petrology* in 2008, volume 155, pages 571-592. This paper was co-authored with A. Dana Johnston, who provided advising and editorial support as well as funding for the project.

Introduction

Arc magmatism worldwide is dominated by the eruption of basalt and basaltic andesite (Crawford et al. 1987; Sisson and Grove 1993b) and melting of the mantle wedge is an important first stage in the evolution of such magmas. For example, high-MgO, high-alumina basalt and basaltic andesite (>8 wt% MgO, >17 wt% Al₂O₃) are widely thought to be hydrous (1-6 wt% H₂O) primary melts of mantle peridotite, fluxed by slab-derived fluids (Baker et al. 1994; Bartels et al. 1991; Grove et al. 2006; Grove et al. 2003; Grove et al. 2002; Tatsumi and Eggins 1995). More evolved low MgO (<6 wt% MgO) basalt and basaltic andesite may be generated within arc crust by accumulation of plagioclase in parental melts (Crawford et al. 1987) or by fractionation of hydrous (≥ 4 wt% H₂O) parental magmas that pond at moderate (>6 km) crustal levels (e.g., Grove et al. 2003; Kay et al. 1982; Sisson and Grove 1993b).

Processes occurring within the deep crust remain elusive and especially difficult to constrain. The MASH model of Hildreth and Moorbath (1988) provided a conceptual

framework that these authors used to account for the enigmatic geochemical differences between large magmatic centers along a section of the Chilean arc that has identical subduction parameters but different crustal compositions. They asserted that zones of Melting, Assimilation, Storage, and Homogenization exist in the deep crust beneath each large magmatic center where mantle derived melts attain a local geochemical signature characteristic of the particular P-T-H₂O conditions of the MASH zone. More recently, Annen et al. (2006) developed a numerical model of deep crustal processes occurring in what they referred to as “deep crustal hot zones”. In such zones, mantle-derived hydrous basalts are emplaced as sills in the lower crust. Here they promote melt generation by mixing and equilibration of H₂O-rich melts produced by partial crystallization of the basaltic sills with volumetrically lesser liquids produced by melting of pre-existing, amphibolitic crustal rocks (Annen et al. 2006).

Despite the diversity of models of arc basalt and basaltic andesite generation, many questions remain, especially regarding deep crustal processes. A better understanding of the pressure, temperature, composition, and water content of the lower-arc crust would be useful to help constrain these processes. The aim of this study is to use inverse approach high pressure experiments to put specific P-T-H₂O and compositional constraints on possible lower-crustal mineral assemblages that may be involved in deep crustal magma generation processes.

Background

Nature of the mid- to lower-arc crust

Observations from xenoliths and uplifted arc sections around the world reveal that arcs are commonly underlain by ultramafic cumulates (e.g., dunite, harzburgite), pyroxenites, amphibolites, granulites, gabbros, and anorthosites (e.g., Arculus and Wills 1980; Berly et al. 2006; Claeson and Meurer 2004; Conrad and Kay 1984; DeBari and Sleep 1991;

Greene et al. 2006). Seismic studies in the Cascades arc suggest that the mid- to lower-crust is composed of greenschists, amphibolites, and mafic granulites underlain by a diffuse zone of mafic underplating (gabbroic rocks?) which defines the MOHO (Stanley et al. 1990). Water in the lower crust is important in controlling the mineral assemblages and compositions found there (Baker and Eggler 1983; Berly et al. 2006; Müntener et al. 2001). Although the distribution of water in “average” sub-arc mantle and lower crust is not known in detail, melt inclusion studies from basalts and basaltic andesites in the Cascades, Mexico, and Guatemala have reported 3.5-8 wt% H₂O in many pre-eruptive arc melts (Cervantes and Wallace 2003; Grove et al. 2002; Johnson et al. 2005; Sisson and Grove 1993a; Sisson and Grove 1993b; Sisson and Layne 1993), suggesting quite variable water contents in the mantle wedge and lower arc crust.

Cascadia subduction

Cascadia is an exceptionally hot subduction zone (Blackwell et al. 1990; Kelemen et al. 2003; Leeman et al. 2005; Stanley et al. 1990) with a relatively young (11 Ma), hot, and buoyant down-going oceanic slab (Wilson 1988). The Central Oregon Cascades arc is built on thin (~40 km) mafic crust consisting of the mafic Siletz accreted terrane (Parsons et al. 1999; Stanley et al. 1990; Trehu et al. 1994). The Columbia embayment, the boundary between the Siletz terrane and older Mesozoic crust (Couch and Riddihough 1989), underlies our study area, the Three Sisters Volcanic Complex (Fig. 1a). For this reason, the crust beneath the Three Sisters Volcanic Complex probably varies in thickness and composition.

North Sister Volcano

North Sister Volcano is a large, mafic stratovolcano in the Central Oregon High Cascades (Fig. 1b). It is the oldest of the Three Sisters Volcanic Complex and has been active

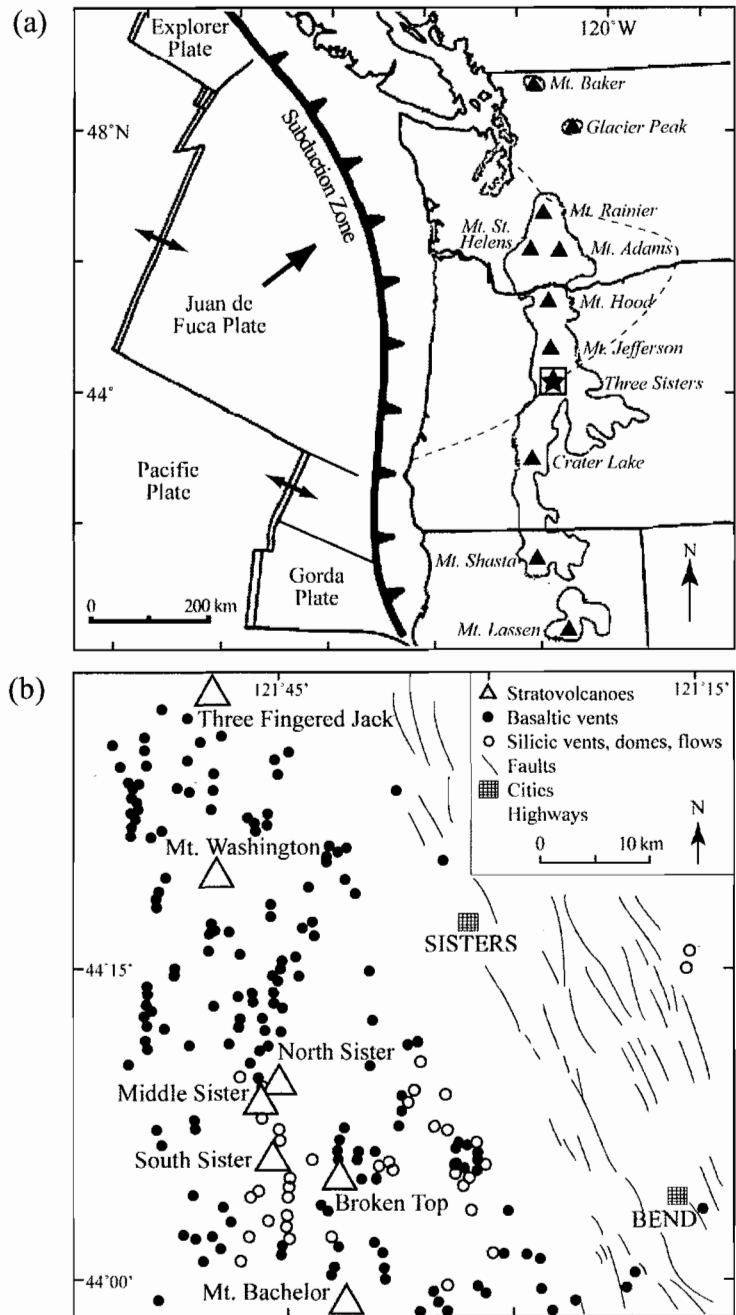


Fig. 1 Location maps for North Sister Volcano. (a) General tectonic setting of the Cascadia Subduction Zone, showing major Quaternary stratovolcanoes, distribution of Neogene volcanic rocks (*gray shaded area*), the Columbia Embayment boundary (*dashed line*; Trehu et al., 1994), and location of the Three Sisters Volcanic Complex (modified from Leeman et al., 2004). (b) Quaternary vents in the Three Sisters area (modified from Scott, 1987)

from 320-15 ka. During this time, North Sister has erupted $\sim 40 \text{ km}^3$ of a remarkably limited compositional range of basaltic andesite as a series of overlapping shields, scoria cones, and fissure eruptions (Schmidt and Grunder 2009). For example, the entire known range in composition of North Sister lavas is only 53-55 wt% SiO_2 , 4-6 wt% MgO , and 0.6-0.8 wt% K_2O (Schmidt 2005; Schmidt and Grunder 2009). This near-uniform composition is common at monogenetic eruptive centers but is unusual for longer-lived subduction-related stratovolcanoes. In fact, most Oregon High Cascade stratovolcanoes exhibit a wide spectrum of evolved compositions ranging from basalt to rhyodacite throughout their eruptive history (Bacon and Nathenson 1996; Brophy and Dreher 2000; Conrey et al. 2001; Scott 2001; Sherrod et al. 1997; Wright and Pierson 1992).

Thus the question of how these “monotonous” basaltic andesites are generated arises. They cannot be direct products of either dry or hydrous mantle melting, based on their low Mg #'s (~ 56), low Ni contents (~ 98 ppm), and comparison with mantle melting experiments (Baker and Stolper 1994; Gaetani and Grove 1998; Gaetani and Grove 2003; Hirose and Kawamoto 1995; Hirose and Kushiro 1993; Langmuir et al. 1992; Pickering-Witter and Johnston 2000; Schwab and Johnston 2001). Nor can they be the product of direct melting of crustal materials lacking, or poor in olivine, as these Mg#'s and Ni contents are too large for this. Instead, petrologic modeling by Schmidt (2005) suggests that rapid recharge rates of originally mantle-derived tholeiitic basalt and reaction with mafic cumulates in the deep crust are important processes for the sustained production of North Sister basaltic andesite with little further evolution due to upper crustal fractionation. Therefore, it is likely that the compositionally monotonous character of North Sister lavas can be explained by some deep crustal process occurring in a MASH or deep crustal hot zone, which is responsible for buffering the basaltic andesite composition over the lifespan of the volcano. Thus, North Sister provides a good opportunity to examine the character of the lower-arc crust and to further explore such deep crustal processes.

Methods

Starting materials and bulk compositions

Our starting material was a natural basaltic andesite lava sample from North Sister Volcano provided by Dr. M. Schmidt (Schmidt 2005; Schmidt and Grunder 2009). XRF, ICP-MS, and electron microprobe analyses of the bulk rock starting material are given in Table 1. This sample was chosen because it is the most “primitive”, crystal-poor (<20 % phenocrysts) lava from the limited compositional range erupted at North Sister Volcano. It has the lowest SiO₂ content and the highest MgO content (52.5 wt% and 5.9 wt%, respectively); therefore we assume that it provides the closest approximation to the original magma generated in the MASH or deep crustal hot zone, and is least affected by shallow fractionation.

The sample was crushed and ground under ethanol with an alumina mortar and pestle to a fine powder (~10 μm) and stored in a drying oven at 120°C. Anhydrous experiments were performed using the dry, natural powder. Experiments with nominal water contents of 5, 10, and 15 wt% H₂O were performed using the dry, natural powder with the appropriate mass of distilled liquid water added with a micro-syringe. By contrast, the starting material for experiments with 3.5 wt% H₂O was synthesized from analytical-grade oxide and carbonate powders (SiO₂, Al₂O₃, TiO₂, Fe₂O₃, MgO, MnO, CaCO₃, Na₂CO₃, and K₂CO₃). The oxide and carbonate powders were dried at 110-900°C, depending on the compound, for up to 96 hours to drive off any adsorbed water. They were then weighed and ground together under ethanol, after which the dried mixture was decarbonated at 850°C in air for 48 hours. Ferric iron was reduced to ferrous iron in a one-atmosphere gas-mixing furnace at $f_{O_2} \sim NNO$ at 900°C for 17 hours. Water (and MgO) was added as a solid using analytical grade brucite, Mg(OH)₂. The mixture was reground and then stored in a drying oven at 120°C. The composition of this starting mix was verified by fusing it completely at 10 kbar and 1300°C using a piston-cylinder apparatus and analyzing the glass by electron microprobe (Table 1, analysis 9).

Specifically, the composition was determined by re-normalizing the mean electron microprobe analysis of a 10 kbar super-liquidus experiment run in a graphite-lined Pt capsule (to prevent Fe-loss) to 3.57 wt% H₂O, the H₂O content determined by FTIR from another 10 kbar super-liquidus experiment run in a Au₇₅Pd₂₅ capsule (to prevent H₂O-loss). For comparison, 3.89 wt% H₂O was calculated by difference from the microprobe analysis total (Table 1, analysis 9). The FTIR analysis also detected 0.36 wt% CO₃²⁻ indicating that the mixture did not fully decarbonate despite being held at 850°C for two full days. By contrast, just 0.05 wt% CO₃²⁻ was measured in the nominally anhydrous glass (actually 0.19 wt% H₂O, by FTIR) recovered from a graphite-lined Pt capsule (Table 1, analysis 8).

Experimental methods

Experiments were performed in 1/2 inch (1.27 cm) end-loaded solid-medium piston-cylinder apparatuses with CaF₂-based furnace assemblies as described by Pickering et al. (1998). Sample position was carefully measured before and after each experiment to ensure that both the thermocouple and sample capsule were located within the furnace hot spot.

Anhydrous experiment sample capsules consisted of graphite-lined Pt “ash cans” (Sneeringer and Watson 1985) 3.5 mm in diameter and ~5 mm tall. Starting rock powder (~20 mg) was loaded into a graphite lined Pt capsule and covered with a graphite disk to ensure isolation from the Pt lid which was then welded on top of the can.

Hydrous experiments utilized Au₇₅Pd₂₅ capsules. Synthetic, hydrous rock powder (~20 mg) was loaded into the Au₇₅Pd₂₅ capsules for the 3.5 wt% H₂O experiments and then the capsule was crimped and welded shut. We had no difficulties with rupturing of single layer Au₇₅Pd₂₅ capsules so we saw no need for a double capsule technique like that used by (Hall et al. 2004). For all other hydrous experiments, natural rock powder

Table 1 Compositions of natural and experimental starting materials

Sample set	1 Natural bulk sample	2 Natural plagioclase	3 Natural olivine	4 Natural clinopyroxene	5 Natural orthopyroxene	6 Natural Ti-magnetite	7 Natural chromite	8 Experiment anhydrous	9 Experiment ~3.5 wt% H ₂ O
<i>Major elements (wt%)</i>									
SiO ₂	52.52(18)	52.5(2.5)	39.25(64)	50.99(24)	53.6	0.17(6)	1.5	52.92(20)	51.48(45)
Al ₂ O ₃	18.38(11)	29.7(1.7)	0.04(2)	2.73(41)	1.8	0.72(9)	17.4	18.57(9)	19.12(15)
TiO ₂	1.208(4)	MDL	MDL	1.02(15)	0.36	18.58(18)	2.44	1.18(3)	1.10(6)
FeO ^a	8.14(1)	0.71(17)	19.3(3.3)	11.38(68)	16.6	70.05(35)	33.5	7.84(13)	7.35(11)
MgO	5.93(10)	0.14(1)	41.1(2.8)	15.99(50)	26.1	1.59(16)	13.2	5.49(9)	5.20(6)
CaO	9.07(1)	13.0(1.7)	0.24(9)	17.74(98)	1.54	0.20(14)	0.2	8.72(8)	8.17(5)
MnO	0.142(1)	MDL	0.29(9)	0.31(14)	NA	0.41(2)	NA	0.13(1)	0.09(2)
Na ₂ O	3.70(5)	4.5(1.2)	MDL	0.40(4)	NA	MDL	0.2	3.99(5)	3.40(7)
K ₂ O	0.66(9)	0.14(9)	MDL	0.03(1)	NA	MDL	NA	0.68(2)	0.52(5)
P ₂ O ₅	0.264(3)	MDL	MDL	MDL	NA	MDL	NA	NA	NA
H ₂ O (EPMA) ^b	NA	NA	NA	NA	NA	NA	NA	NA	3.89(59)
H ₂ O (FTIR) ^c	NA	NA	NA	NA	NA	NA	NA	0.19(4)	3.57(29)
Total	100.01	100.87(70)	100.33(70)	100.62(62)	100	91.76(40)	95.3	99.99(24)	100.00(0)
Mg [#] /An [#] ^e	56.5(2)	75.8(7.4) ^e	79.1(4.1)	71.5(1.3)	73.7	3.88(38)	41.3	55.5(4)	55.8(2)
<i>Trace elements (ppm)</i>									
CO ₂ ^e	NA	NA	NA	NA	NA	NA	NA	591(62)	3607(417)
CO ₂ ^e	NA	NA	NA	NA	NA	NA	NA	13.2(1)	20(1)
Ni	98(1)	NA	NA	NA	NA	NA	NA	NA	NA
Cr	54(2)	NA	NA	NA	NA	NA	15204	NA	NA
Sc	23(2)	NA	NA	NA	NA	NA	NA	NA	NA
V	179(5)	NA	NA	NA	NA	NA	NA	NA	NA
Ba	274(9)	NA	NA	NA	NA	NA	NA	NA	NA
Rb	8(1)	NA	NA	NA	NA	NA	NA	NA	NA
Th	0(2)	NA	NA	NA	NA	NA	NA	NA	NA
Pb	2(2)	NA	NA	NA	NA	NA	NA	NA	NA
Sr	566(1)	NA	NA	NA	NA	NA	NA	NA	NA
Zr	114(1)	NA	NA	NA	NA	NA	NA	NA	NA
Nb	9.5(5)	NA	NA	NA	NA	NA	NA	NA	NA
La	20(10)	NA	NA	NA	NA	NA	NA	NA	NA
Ce	32(10)	NA	NA	NA	NA	NA	NA	NA	NA
Pr	3.22(3)	NA	NA	NA	NA	NA	NA	NA	NA
Nd	14.62(12)	NA	NA	NA	NA	NA	NA	NA	NA
Sm	3.97(6)	NA	NA	NA	NA	NA	NA	NA	NA
Eu	1.42(2)	NA	NA	NA	NA	NA	NA	NA	NA
Gd	4.04(6)	NA	NA	NA	NA	NA	NA	NA	NA
Tb	0.66(1)	NA	NA	NA	NA	NA	NA	NA	NA
Dy	4.12(7)	NA	NA	NA	NA	NA	NA	NA	NA
Ho	0.85(1)	NA	NA	NA	NA	NA	NA	NA	NA
Er	2.21(5)	NA	NA	NA	NA	NA	NA	NA	NA
Yb	1.88(3)	NA	NA	NA	NA	NA	NA	NA	NA
Lu	0.30(1)	NA	NA	NA	NA	NA	NA	NA	NA
Y	21(1)	NA	NA	NA	NA	NA	NA	NA	NA
Ga	18(1)	NA	NA	NA	NA	NA	NA	NA	NA
Cu	73(2)	NA	NA	NA	NA	NA	NA	NA	NA
Zn	75(2)	NA	NA	NA	NA	NA	NA	NA	NA

(1) XRF and ICP-MS analysis of NS-02-66 from Schmidt (2005); (2) mean of 8 microprobe analyses of two plagioclase phenocrysts; (3) mean of 10 microprobe analyses of two olivine phenocrysts; (4) mean of 3 microprobe analyses of one clinopyroxene groundmass microphenocryst; (5) Schmidt, 2005; (6) mean of 3 microprobe analyses of one Ti-magnetite groundmass microphenocryst; (7) Schmidt, 2005; (8) mean of 12 microprobe analyses of 10 kbar, anhydrous, super-liquidus experiment run in graphite-lined Pt capsule for 7 h; (9) composition determined by re-normalizing microprobe analyses of 10 kbar, super-liquidus experiment run in graphite-lined Pt (7.5 h) to prevent Fe-loss to 3.57 wt% H₂O, the H₂O content determined by FTIR from another 10 kbar, super-liquidus experiment run in a Au₇₅Pd₂₅ capsule (9 h) to prevent H₂O-loss. Units in parentheses represent 1σ standard deviation of least units cited, [e.g. 52.52(18) is equivalent to 52.52 ± 0.18]

NA not analyzed; MDL below the 99% minimum detection limit

^a Total Fe reported as FeO*

^b H₂O measured by microprobe using water-by-difference

^c Volatile contents of super-liquidus glass run products measured by FTIR

^d Mg # = 100*molar[MgO/(MgO+ FeO*)]

^e An # = 100*molar[CaO/(CaO+Na₂O)]

(~20 mg) was loaded into Au₇₅Pd₂₅ capsules, then weighed (with a precision of ± 0.1 mg) in order to calculate the mass of water required to yield our nominal desired H₂O contents (i.e., 5, 10, or 15 wt% H₂O). Distilled water was added to the powder using a 1.0 μ l micro-syringe (with a precision of ± 0.1 mg) and the capsule was again weighed to check that no water was lost by poor micro-syringe application or evaporation. Finally the capsule was crimped, welded shut, and weighed again to check that no water was lost upon welding. As developed further below, H₂O determinations by difference from microprobe totals at times deviated significantly from desired nominal values indicating some combination of poor precision of the micro-syringe and microbalance (± 0.1 mg), evaporation on welding, and errors associated with determining water-by-difference.

Experiments were run at 5, 10, 15, and 20 kbar and were maintained to within ~100 bars using nominal Heise gauge values with no correction applied for possible friction effects. The furnace assembly was pressurized to the target pressure at room temperature after which power was applied to heat the assembly to the target temperature. Thermal expansion generally resulted in the final pressure adjustment being a decrease in line pressure (hot piston-out). Temperatures ranged from 1000-1400°C and were maintained to within $\pm 5^\circ\text{C}$ of the set point using Eurotherm 808 temperature controllers and W-Re₅/W-Re₂₆ thermocouples relative to Omega electronic ice points (0°C). No pressure correction was applied to thermocouple e.m.f. The thermal gradient is estimated to be $\sim 10^\circ\text{C}$ over the length of most samples, as in Pickering et al. (1998), however we estimate the gradient to be $\sim 15^\circ\text{C}$ for a few runs with larger capsules. Run durations ranged from 6-24 hours and were chosen based on previous work and evidence of equilibrium conditions in run products (e.g., euhedral crystals, homogeneous phases). In general, experiments above or near the liquidus temperature were run for shorter durations while experiments much cooler than the liquidus temperature ($\geq 75^\circ\text{C}$) were run for longer durations. As our goal was to map the mineralogy onto the H₂O-undersaturated liquidus surface, most experiments were run at near-liquidus temperatures for 6-9 hours (Table 2).

Table 2 Summary of experimental run conditions and phase percentages present

P (kbar)	Run	T (°C)	Duration (h)	Gl	Plag	Aug	OI	Opx	Gt	Amph	Sp
<i>Anhydrous — graphite/Pt capsules</i>											
5	CNM-9	1225	7	96.2(8)	3.8(6)						
10	CNM-6	1275	6	98.5(8)	1.5(6)						
	CNM-3*	1300	6	100.0							
15	CNM-12	1290	6	96.4(8)	3.5(6)						
	CNM-10	1315	6	100.0							
20	CNM-14	1325	7	82.5(1.2)	2.1(1.7)	9.0(1.1)	0.0(1.9)	0.0(2.0)	6.3(1.7)		
	CNM-41	1325	24	56.6(1.6)	19.3(1.7) ^b	19.9(3.9)	0.0(3.0)	0.0(6.8)	4.2(1.3)		
	CNM-15	1350	8	94.3(1.2)		4.8(7) ^c	0.1(1.0)	0.0(1.5)	0.8(9)		
	CNM-17	1360	6	100.0							
<i>~3.5 wt% H₂O — Au₇₅Pd₂₅ capsules</i>											
5	CNM-58	1100	24	99.4(5.7)			0.6(7.5)	0.0(12.6)			
	CNM-30	1125	6	93.9(5)	6.0(3)						
	CNM-32	1150	6	98.6(5)	1.4(4)						
	CNM-23	1175	6	100.0							
10	CNM-59	1100	24	95.9(4)				4.3(2)			
	CNM-38	1125	7	100.0(2)	0.5(4)						
	CNM-28	1150	9	99.1(5)	0.8(4)						
	CNM-34	1175	6	100.0							
15	CNM-39	1140	7	77.5(1.7)	3.4(1.0)	4.6(5)			14.5(6)		
	CNM-29	1165	6	96.1(5)		0.8(4)			3.1(4)		
	CNM-37	1190	7	100.0							
20	CNM-40	1190	6	77.2(9)		2.0(7)			20.9(8)		
	CNM-31	1215	7	87.2(5)		0.5(4)			12.2(4) ^d		
	CNM-35	1240	6	90.6(5)					9.3(3) ^d		
	CNM-26	1265	6.5	100.0							
<i>~5 wt% H₂O — Au₇₅Pd₂₅ capsules</i>											
5	CNM-53	1050	10	92.6(7)		4.5(9)	0.5(2)				2.4(2)
	CNM-42	1075	8	94.6(8)		3.4(1.0)	0.0(2)				1.9(2)
	CNM-46	1100	6	100.0							
10	CNM-51	1075	7	89.8(6)		8.6(1.5)				1.7(1.5)	
	CNM-44	1100	7	96.3(6)		3.6(5)					
	CNM-48	1125	6	100.0							
15	CNM-57	1100	25	88.8(7)		11.2(6)					
	CNM-43	1125	8	90.1(8)		9.8(7)					
	CNM-56	1150	7	99.9(6)		0.1(5)					
20	CNM-54	1175	21	88.2(6)		7.9(1.0)			3.9(8)		
	CNM-45	1200	7	94.5(6)		2.7(9)			2.7(7)		
	CNM-50	1225	7	100.0							

Table 2 continued

P (kbar)	Run	T (°C)	Duration (h)	Gl	Plag	Aug	OI	Opx	Gt	Amph	Sp
<i>~10 wt% H₂O — Au₇₅Pd₂₅ capsules</i>											
5	CNM-64	1025	7	100.0(4)							0.0(2)
	CNM-60	1050	7	100.0(4)							0.0(2)
10	CNM-66	1050	8	100.0							trace
	CNM-62	1075	7	100.0							
15	CNM-65	1075	7	98.7(8)		1.3(7)					
	CNM-61	1100	7	100.0							
20	CNM-69	1100	16	98.7(8)		1.3(7)					
	CNM-68	1125	12.5	100.0							
<i>~15 wt% H₂O — Au₇₅Pd₂₅ capsules</i>											
10	CNM-75	1000	13.5	95.3(1.9)						4.0(1.9)	0.7(3)
	CNM-73	1025	12	100.0(7)							0.0(3)
15	CNM-78	1025	21	91.1(3.1)						8.9(3.4)	0.1(8)
	CNM-77^a	1050	21	97.0		1.5				1.5	
20	CNM-76^c	1050	13	94.0		1.0				5.0	
	CNM-74	1075	13.5	100.0							

Phase proportions in wt% calculated by least squares mass balance; run labels in bold print denote experiments used to construct the phase diagram in Fig. 4; numbers in parentheses next to each value represent errors in the mode estimate propagated from the 1σ errors of the analyzed phase compositions and bulk compositions; errors given in terms of least units cited [e.g., 96.2(8) represents 96.2±0.8]

^aThis experiment contained a small amount of iron droplets that were not analyzed, but they represent a negligible percentage

^bPlagioclase rim composition used in mass balance calculation

^cAugite rim composition used in mass balance calculation

^dGarnet rim composition used in mass balance calculation

^eThe method of least squares could not be confidently applied to these run products due to complications from quench crystallization and thus phase proportions without errors represent best visual estimates

Power consumption in the experiments stabilized after ~2 hours, fluctuating <1% relative thereafter. Thermocouples were inspected after each experiment and showed no signs of oxidation. These observations indicate that thermocouple drift was minimal.

Experimental oxygen fugacity was not controlled or measured, however graphite-lined Pt capsules tend to buffer the oxygen fugacity at $\leq \text{NNO}-2$ in the temperature range of 1000-1400°C and 5-20 kbar (Holloway et al. 1992; Ulmer and Luth 1991) and Au₈₀Pd₂₀ capsules, similar to the Au₇₅Pd₂₅ capsules used here, have been shown to maintain experimental oxygen fugacity within 1 log f_{O_2} unit of the initial f_{O_2} of the starting material (Hall et al. 2004). None of the experiments showed signs of reduction due to H infiltration (e.g., Brooker et al. 1998). As the redox state of arc magmatic

systems ranges from NNO-1 to NNO +3 (Ballhaus et al. 1990; Brandon and Draper 1996; Parkinson and Arculus 1999), our more reducing experimental conditions could have some impact on phase stabilities, particularly for Fe³⁺-bearing phases such as magnetite.

Experiments were quenched rapidly (~200°C/sec) by turning off the power to the furnaces. Run products with ≤~5 wt% H₂O quenched well (Fig. 2c) while those with ~10-15 wt% H₂O showed variolitic textures (radiating fibers of crystals, probably pyroxene or amphibole) due to rapid quench crystallization (Fig. 2f). Growth of quench crystals did not affect our ability to measure equilibrium crystal and glass compositions as large areas of glass between varioles were present and easily analyzed.

After quenching, furnace assemblies were carefully disassembled and the capsule position and assembly parts were measured. Run products were mounted in epoxy, cut in half, and polished to 0.25 μm for analysis. Polished halves were cut to show the gravity section of each experiment so that crystals that settled to the bottom could be detected and analyzed. The polished samples were then carbon or gold coated for SEM/EPMA or ion probe analysis.

Analytical techniques

SEM and EPMA analyses

These data were collected at the Micro Analytical Facility at the University of Oregon. Backscattered electron (BSE) images were taken on a Zeiss Ultra SEM to evaluate textures and compositional zoning. Cameca SX-50 and SX-100 electron microprobes were operated using two setups optimized for hydrous glasses and mineral phases, respectively. Glasses were analyzed using a 15 keV accelerating potential, a 10 nA beam

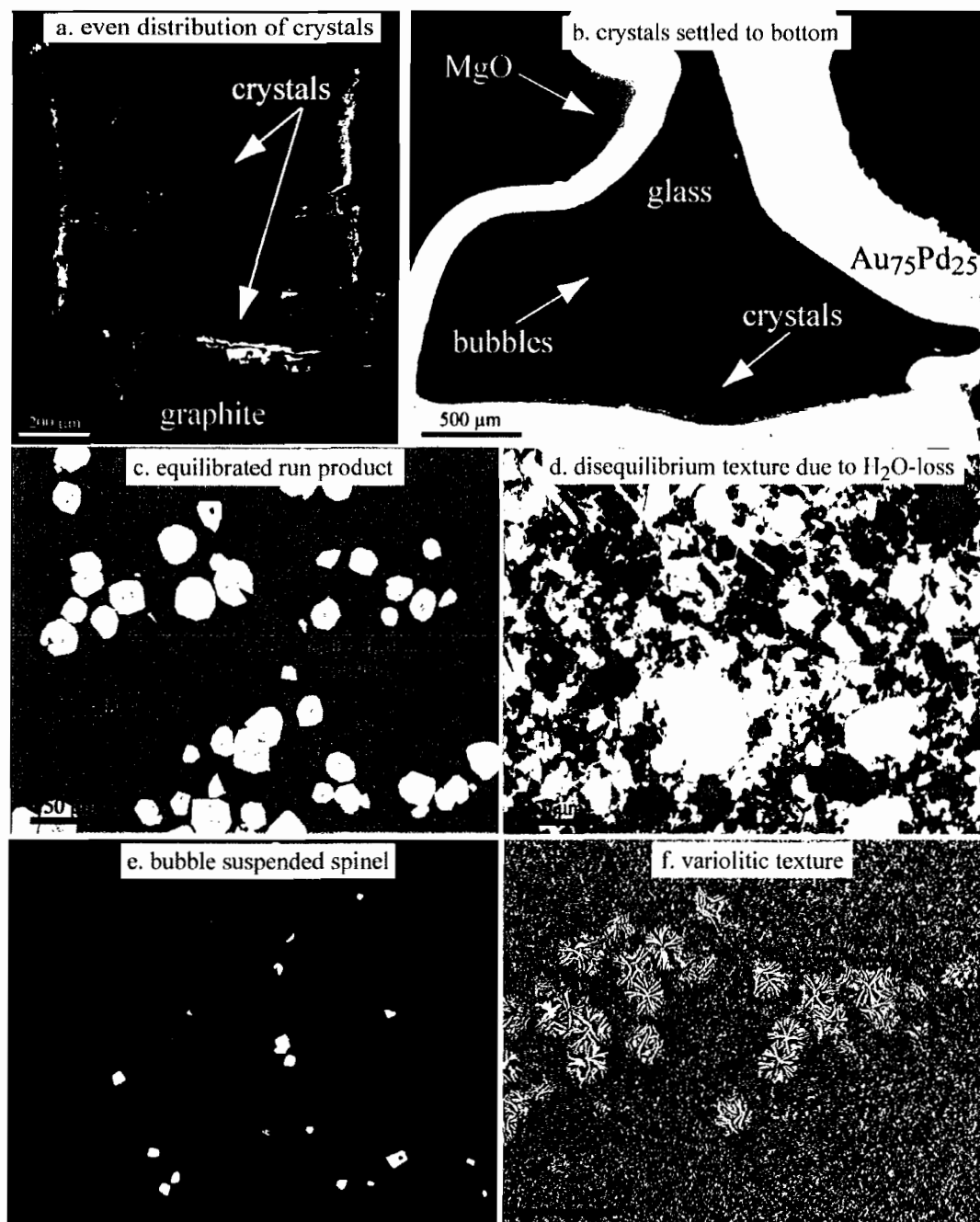


Fig. 2 Backscattered electron images of experimental run products, showing (a) even distribution of crystals in an anhydrous run product (CNM-14), (b) crystals that settled to the bottom in a hydrous run product (CNM-45, 5 wt% H₂O), (c) euhedral crystals in an equilibrated run product (CNM-35, 3.5 wt% H₂O), and (d) a highly crystalline run product with a severe disequilibrium texture due to loss of H₂O, (e) spinel crystals suspended with bubbles in a hydrous run product (CNM-64, 10 wt% H₂O), and (f) variolitic texture due to quench crystallization in a hydrous run product (CNM-61, 10 wt% H₂O)

current, and a 10 μm spot size to minimize volatilization, while crystalline phases were analyzed using a 10 keV accelerating potential, a 20 nA beam current, and a <1 μm spot size. A small interaction volume and a focused beam were required for mineral analyses because some crystals were very small (<5 μm). Natural and synthetic minerals and glasses were used as standards for the electron microprobe. To avoid loss of Na and K, these elements were counted first to collect x-ray counts with minimal beam exposure. A correction was also applied for Na- and K-loss (Nielsen and Sigurdsson 1981) using Probe for Windows software. H_2O was measured using the water-by-difference method in the Probe for Windows software, calibrated by Roman et al. (2006). This method calculates the “missing” water by iteratively adjusting the water contents and recalculating the sample matrix correction until the analysis totals 100% (Donovan and Tingle 1996).

Infrared spectroscopy

These analyses were performed using a Thermo Nicolet Nexus 670 Fourier Transform Infrared (FTIR) spectrometer interfaced with a Thermo Spectra-Tech Continuum microscope in Dr. P. Wallace’s lab at the University of Oregon. Samples were prepared by mounting half of an experimental charge onto a slide and cutting the charge into a thin slice. The slice was then doubly ground and polished into a thin (~ 30 - 200 μm) wafer with parallel sides. The thickness of each wafer was measured using a micrometer with a precision of ± 2 μm . Measurements of dissolved H_2O and carbonate (CO_3^{2-}) in experimental glasses were obtained using Beer’s law:

$$c = MA / \rho d \epsilon, \quad (1)$$

where c is the concentration (weight fraction) of the volatile species, M is the molecular weight of H_2O (18.02) or CO_2 (44.00), A is the absorbance intensity of the species of interest, ρ is the room temperature density of hydrous basaltic andesite glass

($\sim 2660 \text{ kg m}^3$), d is the thickness of the glass wafer, and ϵ is the molar absorption coefficient (Dixon and Pan 1995; Fine and Stolper 1985; Mandeville et al. 2002).

Ion Probe analyses

These analyses were performed using the Cameca IMS-3f SIMS at the Northeast Regional Ion Microprobe Facility at Woods Hole Oceanographic Institution, directed by Dr. N. Shimizu, using analytical conditions and standards outlined by Johnston and Schwab (2004). Each analysis spot consisted of five separate ion counting intervals and 1σ errors were calculated based on the variability of these intervals. The estimated 1σ uncertainties are 10% relative for La, Ce, and Ti; 15% relative for Nd, Sr, and Zr; 20% relative for Sm, Dy, Er, Yb, and Y; and 30% relative for Rb. These errors are due to the small beam diameter ($\sim 11 \mu\text{m}$), the low beam current used, and low analyzed concentrations.

Iron and water loss

Iron and water loss from experimental charges have long been known to be potential problems with experiments such as these (e.g., Freda et al. 2001; Grashoff et al. 1983; Hall et al. 2004; Johannes and Bode 1978; Kägi et al. 2005; Kawamoto and Hirose 1994; Merrill and Wyllie 1973; Truckenbrodt and Johannes 1999), so care was taken to evaluate them here. In the course of bracketing the liquidus of our starting material at several pressures with several H_2O contents, we ran quite a few experiments above the samples' liquidus. These super-liquidus glasses were ideal for evaluating Fe-loss as it could be evaluated directly by comparison of the starting material composition with microprobe analyses of these glasses, without need to account for coexisting crystalline phases. Fig. 3a shows relative Fe-loss from these super-liquidus glasses evaluated in this

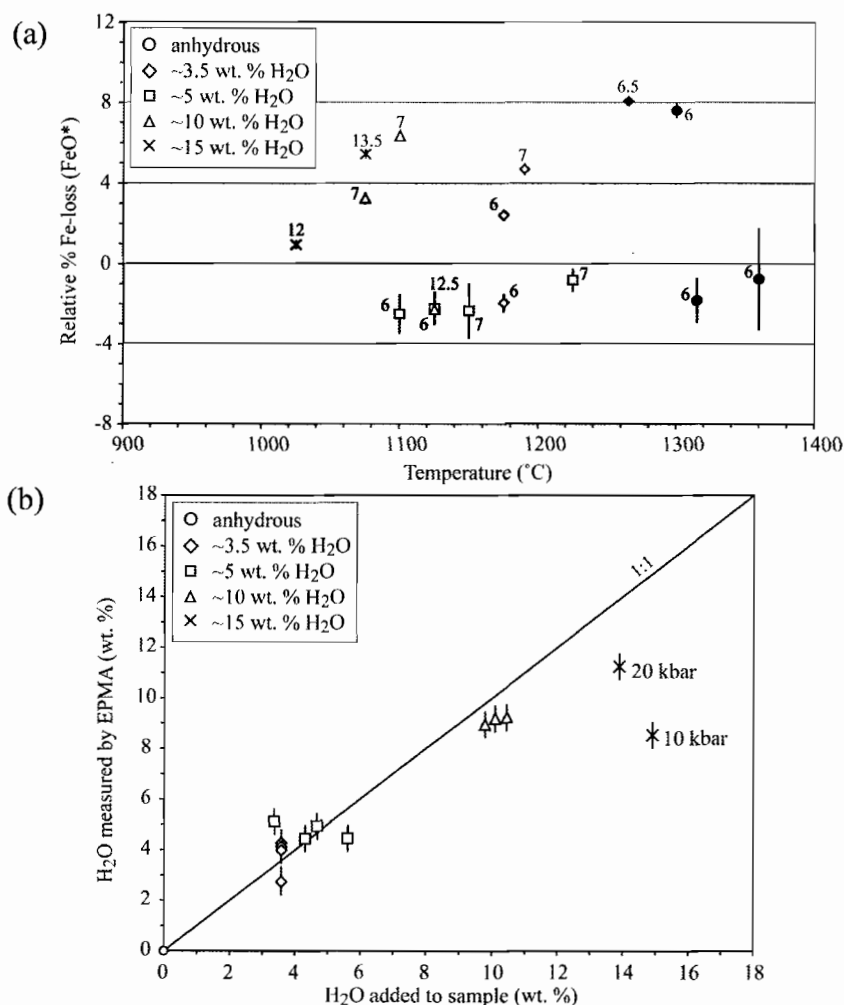


Fig. 3 Variation in Fe-loss and water contents in experimental run products (a) Super-liquidus glasses from each series of experiments show minimal Fe-loss, which is plotted as relative % FeO*-loss. *Filled symbols* represent experiments run in graphite-lined Pt capsules and *open symbols* represent experiments run in Au₇₅Pd₂₅ capsules. *Numbers* beside data represent run durations in hours. All super-liquidus glasses lost ≤ 8 relative % FeO* and most glasses lost < 4 % relative FeO* (*shaded bar*), in agreement with the findings of Hall et al. (2004). (b) Variation in water contents (water-by-difference from microprobe totals) in super-liquidus glasses (*open symbols*) used in phase diagram in Fig. 4. *Numbers* beside 15 wt% H₂O series show experimental pressure (kbar). Line represents 1:1 correlation. *Error bars* represent 1σ standard deviations

way. Loss of Fe was found to be minimal in the experiments run in both graphite lined Pt and unlined Au₇₅Pd₂₅ capsules (loss of ≤ 8 % relative FeO* for all glasses; generally < 4 % relative, shaded bar) so we felt no need to Fe-presaturate the Au₇₅Pd₂₅ capsules. The virtual absence of Fe-loss in anhydrous experiments run in graphite lined Pt capsules is

consistent with other studies (Hall et al. 2004; Kushiro and Thompson 1972). Minimal Fe-loss in hydrous experiments run in Au₇₅Pd₂₅ capsules can be attributed to the relatively oxidized starting materials (~NNO for synthetic starting materials) and the use of MgO assemblies which may result in more oxidizing conditions than other assemblies such as boron nitride (Hall et al. 2004; Kägi et al. 2005).

Bulk water contents appear to have been acceptably maintained in nearly all experiments. Three super-liquidus glasses were analyzed by FTIR to confirm their water contents yielding 0.19 wt% H₂O (vs. 0.0 nominal wt% H₂O); 3.57 wt% H₂O (vs. 3.50 wt% H₂O); and 4.93 wt% H₂O (vs. 5.0 wt% H₂O), well within acceptable bounds. Variation of water contents in super-liquidus glasses is shown in Fig. 3b. Measured H₂O contents in super-liquidus glasses are within ~1.5 wt% absolute of the H₂O added, except in the 15 wt% H₂O series in which measured H₂O contents are ~2.5 to 6 wt% low. In the 15 wt% H₂O series we interpret the 10 kbar experiment to be water-saturated while the 15 and 20 kbar experiments likely vesiculated upon quench, with some water residing in vapor bubbles rather than the glass. The other small deviations shown in Fig. 3b are likely due to errors in measuring H₂O by EPMA water-by-difference (see below), quench problems, variable bubble content of run products, and in the case of experimental series where H₂O was added as a liquid, additional errors from adding water to the capsules using a micro-syringe and evaporation before and during welding. Only two experiments appeared to have lost significant water which was easily detected, as they had much higher-than-expected crystal contents (>90% crystals) and severe disequilibrium textures (Fig. 2d). These experiments were discarded.

Attainment of equilibrium

All experiments were nominally equilibrated before quenching. Starting materials were ground to ~10 μm to increase surface area and speed reaction rates. Relict crystals of olivine (present in the original rock but not stable in the experiments) were found in only

a few experiments (CNM-14, 15, 41, 42, 53, and 58) and comprise a negligible mass (<1 wt%). Equilibrium crystals in experimental run products are euhedral and show little evidence of zoning in BSE images (Fig. 2c). Major and trace element compositions of glass and crystals are relatively homogeneous (Tables 3 and 4). The spatial distribution of crystalline phases was variable. Distributions were more homogeneous in experiments with lower water contents (Fig. 2a) while crystals tended to settle to the bottom of the charge in experiments with higher water contents (Fig. 2b) consistent with their expected lower melt viscosities. Spinel remained suspended in the melt due to small bubbles around the edges of the crystals (Fig. 2e). Additional support for preservation of H₂O and attainment of equilibrium comes from the observations that liquidus temperatures decrease with increasing H₂O contents and melt fractions vary sensibly with temperature.

Results

P-T-H₂O near-liquidus phase relations

Table 2 gives a summary of experimental run conditions and phase proportions calculated by least-squares mass balance, using the glass and mineral major element data given in Table 3. These calculations utilized SIMPLEX3 (M. Baker, personal communication), a program that implements the algorithm of Albarède and Provost (1977) and propagated analytical uncertainties to provide uncertainty estimates for the phase abundances. All oxides apart from MnO and P₂O₅ were used in the calculations. Rim compositions were used in SIMPLEX3 in the few instances where we encountered zoned crystals. This method could not be confidently applied to two run products (CNM-76 and 77) because of complications due to quench crystals in the glass and the values in Table 2 represent our best visual estimates. Major element compositions of experimental glass and mineral phases are given in Table 3. Trace element analyses (Table 4) were performed on a subset of five run products.

Table 3 Major element compositions from microprobe analyses of experimental run products

P (kbar)	Run	T (°C)	Phase	SiO ₂	Al ₂ O ₃	TiO ₂	FeO ^{*2}	MgO	CaO	MnO	Na ₂ O	K ₂ O	P ₂ O ₅	Cr ₂ O ₃	H ₂ O ^b	Total	Mg ^{#c} /An ^{#d}	
<i>Anhydrous</i>																		
5	CNM-9	1225	Glass (n=6)	53.31(53)	17.93(9)	1.17(7)	7.76(11)	5.69(6)	8.57(8)	NA	3.90 (5)	0.70(2)	NA	NA	NA	99.03(48)	56.7(4)	
			Plag (15)	50.2(1.1)	30.06(74)	0.07(4)	0.93(14)	0.19(4)	13.92(70)	MDL	3.55(45)	0.10(3)	NA	NA	NA	99.04(49)	81.2(2.7)	
10	CNM-6	1275	Glass (6)	53.60(56)	18.29(10)	1.21(7)	7.83(9)	5.62(4)	8.70(3)	NA	3.86(11)	0.68(1)	NA	NA	NA	99.81(67)	56.1(2)	
			Plag (9)	49.99(66)	30.03(42)	0.06(2)	0.86(7)	0.24(5)	14.44(20)	MDL	3.44(14)	0.09(2)	NA	NA	NA	99.19(66)	82.3(8)	
15	CNM-3	1300	Glass (6)	52.51(17)	18.47(7)	1.17(1)	7.25(9)	5.74(7)	9.14(11)	0.13(1)	4.04(7)	0.68(1)	NA	NA	NA	99.40(17)	58.5(5)	
			Fe droplets	NA	NA	NA	NA	NA	NA	NA	NA	NA	NA	NA	NA	NA	NA	NA
			Glass (6)	54.76(47)	18.08(13)	1.23(4)	8.04(6)	5.79(9)	8.62(5)	NA	3.82(8)	0.68(1)	NA	NA	NA	101.02(55)	56.2(4)	
			Plag (12)	50.23(94)	30.68(64)	0.07(4)	0.91(9)	0.21(4)	13.70(64)	MDL	3.59(39)	0.11(3)	NA	NA	NA	99.56(50)	80.8(2.4)	
20	CNM-10	1315	Glass (10)	53.38(47)	18.87(5)	1.18(7)	7.99(9)	5.77(3)	8.66(6)	0.13(6)	4.35(12)	0.70(1)	NA	NA	NA	101.04(48)	56.3(3)	
			Glass (6)	55.51(25)	18.60(4)	1.25(7)	7.69(6)	4.23(3)	7.98(6)	NA	4.44(12)	0.81(1)	NA	NA	NA	100.52(33)	49.5(1)	
20	CNM-14	1325	Augite (9)	48.50(77)	13.0(1.3)	0.64(9)	7.25(32)	12.67(75)	15.41(39)	0.19(6)	1.81(15)	MDL	NA	NA	NA	99.58(72)	75.7(7)	
			Garnet (9)	40.48(58)	23.34(5)	0.71(5)	13.58(24)	14.77(6)	7.24(10)	0.40(8)	0.04(2)	MDL	NA	NA	NA	100.59(40)	65.0(4)	
			Olivine (11)	37.77(55)	0.05(1)	MDL	19.73(35)	41.05(25)	0.26(1)	0.21(6)	0.02(1)	MDL	NA	NA	NA	99.16(61)	78.8(3)	
			Opx (12)	51.71(69)	6.20(19)	0.35(5)	11.73(31)	27.40(48)	1.72(23)	0.19(8)	0.17(4)	MDL	NA	NA	NA	99.53(64)	80.6(6)	
			Plag (9)	50.35(87)	31.15(49)	0.08(2)	0.89(8)	0.19(2)	13.93(55)	MDL	3.35(24)	0.11(3)	NA	NA	NA	100.15(90)	82.1(1.6)	
			Glass (6)	54.32(18)	18.08(17)	1.52(5)	9.12(6)	4.20(4)	7.39(3)	0.12(5)	4.40(9)	1.03(2)	NA	NA	NA	100.60(23)	45.1(2)	
			Augite (11)	49.19(45)	11.53(70)	0.74(14)	10.43(69)	13.41(66)	12.69(91)	0.25(8)	1.76(14)	MDL	NA	NA	NA	100.05(42)	69.6(1.0)	
			Garnet (8)	40.28(27)	22.51(8)	0.87(27)	16.41(43)	14.26(23)	6.11(17)	0.41(11)	0.04(2)	MDL	NA	NA	NA	100.98(17)	60.8(1.0)	
			Olivine (8)	38.38(10)	0.08(2)	MDL	23.19(36)	38.65(25)	0.24(13)	0.15(5)	MDL	MDL	NA	NA	NA	100.80(25)	74.8(4)	
			Opx (2)	51.08(4)	7.67(40)	0.28(24)	12.7(1.4)	21.1(2.1)	6.3(2.1)	0.24(10)	0.74(23)	MDL	NA	NA	NA	100.19(96)	74.8(3)	
			Plag core (9)	51.22(55)	30.82(33)	MDL	0.51(10)	0.15(4)	13.08(40)	MDL	3.78(21)	0.17(3)	NA	NA	NA	99.83(27)	79.2(1.4)	
			Plag rim (10)	58.31(37)	26.22(30)	0.11(16)	0.55(18)	0.09(2)	7.91(33)	MDL	6.68(16)	0.48(4)	NA	NA	NA	100.41(24)	56.6(1.5)	
20	CNM-15	1350	Glass (3)	53.55(4)	18.55(10)	1.30(5)	7.85(7)	5.02(2)	8.30(2)	NA	4.08(6)	0.72(0)	NA	NA	NA	99.40(28)	53.3(2)	
			Augite (9)	48.70(65)	12.57(60)	0.57(5)	6.95(44)	13.33(27)	15.55(16)	0.17(9)	1.78(7)	MDL	NA	NA	NA	99.73(88)	77.4(1.0)	
			Aug core (2)	51.11(27)	2.71(35)	0.84(6)	9.54(15)	16.25(15)	17.68(24)	0.28(4)	0.44(3)	MDL	NA	NA	NA	99.13(39)	75.2(5)	
			Aug rim (3)	48.7(1.4)	11.7(1.6)	0.59(3)	8.2(1.2)	13.54(85)	15.09(95)	0.18(5)	1.71(5)	MDL	NA	NA	NA	99.70(96)	74.8(1.6)	
			Garnet (8)	41.40(71)	23.60(17)	0.66(4)	12.52(35)	15.13(34)	6.83(8)	NA	0.12(14)	0.04(5)	NA	NA	NA	100.40(34)	68.3(5)	
			Olivine (9)	38.69(42)	0.17(34)	MDL	18.11(36)	41.79(49)	0.25(7)	NA	0.06(13)	MDL	NA	NA	NA	99.31(49)	80.4(4)	
20	CNM-17	1360	Opx (3)	51.99(58)	7.17(66)	0.29(3)	10.11(42)	27.13(75)	2.04(50)	0.14(5)	0.22(9)	MDL	NA	NA	NA	99.13(70)	82.7(1.0)	
			Glass (11)	52.88(25)	18.40(14)	1.17(6)	7.91(10)	5.72(10)	8.71(5)	0.18(6)	3.95(9)	0.67(1)	NA	NA	NA	99.50(34)	56.3(3)	
<i>~3.5 wt% H₂O</i>																		
5	CNM-58	1100	Glass (5)	51.84(16)	18.17(51)	1.31(13)	8.12(21)	4.96(14)	7.45(34)	0.14(2)	3.37(48)	0.64(5)	NA	NA	3.90(44)	99.98(2)	52.2(5)	
			Olivine (5)	39.16(26)	0.08(5)	0.07(7)	17.97(47)	42.62(31)	0.28(12)	0.25(7)	MDL	MDL	NA	NA	0.00(0)	100.46(47)	80.9(5)	
			Opx (12)	52.21(61)	5.96(1.14)	0.42(16)	11.83(94)	27.47(1.84)	1.85(81)	0.20(8)	0.18(20)	0.03(8)	NA	NA	0.00(0)	100.16(40)	80.5(1.4)	
10	CNM-30	1125	Glass (9)	51.84(36)	18.71(2)	1.13(7)	7.82(10)	5.78(4)	8.08(4)	0.13(4)	3.74(7)	0.53(2)	NA	NA	2.25(24)	100.00(0)	56.9(3)	
			Plag (9)	50.16(36)	31.45(14)	0.06(1)	0.85(12)	0.15(2)	14.56(12)	MDL	3.19(6)	0.07(1)	NA	NA	0.00(0)	100.51(38)	83.4(2)	
10	CNM-32	1150	Glass (9)	50.81(41)	19.18(7)	1.09(3)	7.10(6)	5.47(4)	8.43(4)	0.12(4)	3.71(8)	0.51(1)	NA	NA	3.57(42)	100.00(0)	57.9(3)	
			Plag (6)	49.46(49)	31.77(20)	0.06(3)	0.67(19)	0.16(3)	14.81(12)	MDL	2.91(9)	0.05(1)	NA	NA	0.00(0)	99.94(49)	85.9(5)	
10	CNM-23	1175	Glass (6)	51.71(38)	19.39(6)	1.10(6)	7.18(9)	5.31(2)	8.33(6)	0.14(4)	3.59(10)	0.50(2)	NA	NA	2.74(50)	100.00(0)	56.9(3)	

Table 3 continued

P (kbar)	Run	T (°C)	Phase	SiO ₂	Al ₂ O ₃	TiO ₂	FeO ^{a*}	MgO	CaO	MnO	Na ₂ O	K ₂ O	P ₂ O ₅	Cr ₂ O ₃	H ₂ O ^b	Total	Mg [#] /An ^{#d}	
10	CNM-59	1100	Glass (7)	49.86(15)	18.53(15)	1.21(11)	7.23(19)	4.34(5)	7.17(19)	MDL	3.62(11)	0.63(3)	NA	NA	7.19(22)	99.99(1)	51.7(7)	
			Opx (6)	50.25(23)	7.10(47)	0.45(8)	15.36(33)	25.55(27)	1.33(27)	0.25(10)	0.09(1)	MDL	NA	NA	NA	0.0(0)	100.40(43)	74.8(4)
	CNM-38	1125	Glass (9)	51.57(42)	18.74(8)	1.13(3)	7.34(15)	5.15(3)	8.17(5)	0.11(1)	3.28(9)	0.48(1)	NA	NA	4.03(33)	100.00(0)	55.6(5)	
			Plag(6)	51.84(51)	30.37(10)	MDL	0.43(21)	0.12(1)	13.14(18)	MDL	4.00(23)	0.10(3)	NA	NA	0.00(0)	100.07(68)	78.4(1.1)	
	CNM-28	1150	Glass (9)	51.22(53)	19.42(6)	1.09(6)	7.23(6)	5.43(4)	8.37(6)	MDL	3.83(9)	0.50(2)	NA	NA	2.82(54)	100.00(0)	57.2(3)	
			Plag (10)	50.92(44)	31.07(22)	0.07(2)	0.71(17)	0.13(1)	13.54(11)	MDL	3.53(42)	0.08(2)	NA	NA	0.0(0)	100.07(48)	80.9(2)	
	CNM-34	1175	Glass (9)	49.80(39)	19.16(6)	1.08(4)	7.50(9)	5.48(3)	8.50(3)	0.11(3)	3.59(10)	0.51(3)	NA	NA	4.27(35)	100.00(0)	56.6(3)	
			Glass (9)	54.00(43)	18.90(8)	1.16(2)	6.22(23)	3.51(4)	7.87(4)	MDL	3.12(37)	0.58(2)	NA	NA	4.57(39)	100.00(0)	50.2(8)	
	15	CNM-39	1140	Garnet (7)	40.25(55)	21.50(65)	1.39(19)	14.84(46)	13.94(44)	7.68(36)	0.35(8)	0.04(4)	MDL	NA	NA	0.0(0)	100.00(55)	62.6(1.4)
				Augite (11)	47.90(60)	11.65(38)	1.02(7)	7.95(39)	11.60(40)	17.99(48)	0.09(5)	1.29(7)	MDL	NA	NA	0.0(0)	99.53(40)	72.2(1.5)
Plag(6)				53.84(71)	28.30(23)	MDL	0.77(29)	0.06(1)	11.14(27)	MDL	5.29(8)	0.11(1)	NA	NA	0.0(0)	99.61(62)	70.0(7)	
Glass (9)				51.78(42)	19.32(4)	1.12(4)	6.99(9)	4.99(3)	8.48(4)	0.11(6)	4.29(9)	0.51(3)	NA	NA	2.41(45)	100.00(0)	56.0(3)	
CNM-29		1165	Garnet (4)	40.57(36)	23.30(11)	0.90(20)	12.69(9)	15.41(38)	7.41(36)	0.35(6)	0.02(1)	MDL	NA	NA	0.0(0)	100.69(37)	68.4(6)	
			Augite (5)	49.29(96)	10.95(92)	0.73(11)	7.22(28)	13.11(44)	18.26(64)	0.12(6)	1.11(3)	MDL	NA	NA	0.0(0)	100.80(39)	76.4(3)	
CNM-37		1190	Glass (9)	51.78(29)	18.88(6)	1.11(2)	7.01(18)	5.01(3)	8.22(5)	0.11(2)	3.27(11)	0.47(1)	NA	NA	4.13(31)	100.00(0)	56.0(6)	
			Glass (9)	54.70(38)	18.49(7)	1.09(2)	5.25(18)	3.10(4)	8.06(5)	MDL	4.45(9)	0.62(3)	NA	NA	4.19(40)	100.00(0)	51.3(9)	
20		CNM-40	1190	Garnet (15)	40.22(46)	21.31(66)	1.58(32)	15.82(78)	12.31(63)	8.64(38)	0.29(9)	0.14(7)	MDL	NA	NA	0.0(0)	100.33(70)	58.1(2.0)
				Augite (12)	48.82(70)	13.86(93)	0.86(26)	6.15(75)	10.05(94)	17.9(1.1)	MDL	1.92(8)	0.04(4)	NA	NA	0.0(0)	99.74(43)	74.3(3.9)
	CNM-31	1215	Glass (9)	52.44(44)	18.92(5)	1.11(3)	6.39(9)	4.02(3)	8.49(5)	MDL	4.93(10)	0.57(2)	NA	NA	3.06(40)	100.00(0)	52.9(5)	
			Garnet rim(9)	40.52(51)	22.95(18)	0.51(16)	12.53(22)	14.84(18)	8.13(13)	0.35(7)	0.05(6)	MDL	NA	NA	0.0(0)	99.91(53)	67.9(6)	
			Garnet core (9)	39.12(62)	21.83(63)	1.63(7)	15.15(70)	13.35(52)	7.66(21)	0.33(11)	0.08(3)	MDL	NA	NA	0.0(0)	99.16(73)	61.1(1.9)	
			Augite (9)	46.67(39)	13.62(52)	0.66(8)	6.51(17)	10.59(19)	18.64(12)	MDL	1.77(7)	MDL	NA	NA	0.0(0)	98.56(37)	74.4(7)	
	CNM-35	1240	Glass (9)	50.03(40)	19.10(7)	1.13(5)	6.78(8)	4.30(3)	8.59(3)	MDL	4.56(14)	0.56(3)	NA	NA	4.90(51)	100.00(0)	53.1(3)	
			Garnet rim(9)	40.29(42)	22.68(12)	0.78(9)	12.51(29)	15.15(44)	8.25(49)	0.33(6)	0.04(3)	MDL	NA	NA	0.0(0)	100.05(62)	68.3(8)	
	CNM-26	1265	Garnet core (9)	40.88(61)	23.49(12)	0.30(6)	11.42(26)	17.11(18)	6.33(11)	0.33(4)	0.03(1)	MDL	NA	NA	0.0(0)	99.91(47)	72.8(6)	
			Glass (6)	50.74(30)	19.32(4)	1.10(9)	6.76(9)	5.44(3)	8.38(6)	0.11(3)	3.63(10)	0.54(2)	NA	NA	3.98(32)	100.00(0)	58.9(2)	
5 wt% H ₂ O																		
5	CNM-53	1050	Glass (7)	51.27(21)	18.47(11)	1.16(11)	5.82(19)	4.88(1)	7.78(11)	0.14(3)	3.89(9)	0.68(3)	0.26	NA	5.57(29)	100.00(1)	59.9(8)	
			Augite (6)	45.2(1.0)	8.61(93)	1.36(37)	9.09(48)	13.06(63)	21.26(46)	0.14(10)	0.56(4)	MDL	MDL	MDL	NA	0.0(0)	99.32(23)	71.9(1.8)
			Olivine (3)	40.31(29)	0.05(2)	MDL	12.36(9)	46.7(1.0)	0.34(4)	0.21(11)	MDL	MDL	MDL	0.05(1)	NA	0.0(0)	100.1(1.2)	87.1(3)
			Spinel (7)	0.10(3)	9.71(16)	2.31(10)	70.25(90)	8.95(14)	0.14(5)	0.27(11)	MDL	MDL	MDL	0.28(42)	0.0(0)	92.06(54)	18.5(4)	
	CNM-42	1075	Glass (6)	51.83(19)	18.39(20)	1.07(12)	6.54(11)	5.22(4)	8.03(5)	0.11(4)	3.88(8)	0.68(2)	0.34(1)	NA	3.92(39)	100.00(0)	58.7(5)	
			Augite (16)	46.8(1.1)	7.83(66)	1.25(24)	8.58(56)	13.77(49)	20.52(49)	0.18(9)	0.53(9)	MDL	MDL	NA	0.0(0)	99.47(31)	74.1(1.7)	
			Olivine (7)	40.07(32)	MDL	MDL	13.7(1.2)	45.8(1.0)	0.06(14)	0.36(13)	MDL	MDL	0.04(3)	NA	0.0(0)	100.16(32)	85.6(1.4)	
			Spinel (6)	0.12(2)	9.81(18)	3.46(29)	70.54(83)	7.74(9)	0.13(6)	0.28(6)	MDL	MDL	MDL	0.73(48)	0.0(0)	92.85(96)	16.4(2)	
	CNM-46	1100	Glass (9)	50.24(16)	17.81(11)	1.12(14)	7.66(10)	5.57(4)	8.23(26)	0.13(5)	3.82(13)	0.65(2)	0.25(3)	NA	4.44(48)	99.98(4)	56.5(3)	
			Glass (7)	49.77(17)	18.59(12)	1.22(13)	7.57(16)	4.58(2)	7.26(30)	0.13(4)	3.90(11)	0.71(2)	0.28(3)	NA	5.91(29)	100.00(1)	51.9(5)	
CNM-51	1075	Augite (4)	48.23(59)	5.2(2.0)	1.59(43)	12.0(2.2)	13.61(40)	17.6(1.1)	0.27(24)	0.60(17)	MDL	0.03(2)	NA	0.0(0)	99.05(28)	67.2(4.2)		
		Amphibole (6)	39.86(43)	15.10(16)	2.49(34)	11.91(34)	13.72(26)	10.37(40)	0.11(6)	2.84(4)	0.34(2)	MDL	NA	3.25(30)	100.00(0)	67.2(8)		
		Glass (6)	50.68(29)	18.23(11)	1.09(11)	7.69(12)	5.22(4)	7.92(7)	0.16(4)	3.63(87)	0.68(3)	0.34(1)	NA	4.36(58)	100.00(0)	54.8(6)		
		Augite (13)	48.7(1.2)	6.4(1.8)	1.00(40)	9.2(1.1)	14.25(88)	19.01(75)	0.26(17)	0.65(11)	MDL	MDL	NA	0.0(0)	99.41(23)	73.4(2.6)		
CNM-48	1125	Glass (9)	50.15(24)	17.77(14)	1.17(9)	7.64(9)	5.53(4)	8.35(28)	0.17(8)	3.79(24)	0.66(2)	0.24(2)	NA	4.44(29)	99.98(3)	56.3(4)		

Table 3 continued

P (kbar)	Run	T (°C)	Phase	SiO ₂	Al ₂ O ₃	TiO ₂	FeO ^{as*}	MgO	CaO	MnO	Na ₂ O	K ₂ O	P ₂ O ₅	Cr ₂ O ₃	H ₂ O ^b	Total	Mg [#] /An [#] ^d
15	CNM-57	1100	Glass (9)	50.19(21)	18.72(19)	1.22(16)	7.52(16)	4.58(5)	7.04(15)	0.12(5)	4.35(10)	0.70(3)	0.29(1)	NA	5.20(40)	99.96(6)	52.0(6)
			Augite (7)	48.23(78)	8.3(1.1)	0.81(22)	9.16(46)	13.28(59)	18.51(37)	0.11(16)	1.02(6)	MDL	MDL	NA	0.0(0)	99.42(27)	72.1(9)
	CNM-43	1125	Glass (6)	50.85(14)	18.73(11)	1.08(5)	7.58(11)	4.75(3)	7.11(3)	0.10(7)	4.23(24)	0.72(3)	0.34(2)	NA	4.49(29)	100.00(0)	52.8(4)
			Augite (9)	48.53(98)	7.9(1.7)	0.94(23)	9.78(82)	13.4(1.0)	17.99(72)	0.24(9)	0.97(18)	MDL	MDL	NA	0.0(0)	99.84(40)	71.0(1.2)
	CNM-56	1150	Glass (9)	49.67(19)	17.62(7)	1.14(13)	7.65(22)	5.53(4)	8.33(18)	0.10(4)	3.88(8)	0.62(4)	0.25(3)	NA	5.12(18)	99.96(5)	56.3(7)
			Augite (4)	48.36(10)	8.60(16)	0.50(10)	7.82(42)	13.75(8)	18.82(25)	0.24(27)	0.95(9)	MDL	MDL	NA	0.0(0)	99.07(50)	75.8(9)
20	CNM-54	1175	Glass (9)	50.09(12)	18.18(12)	1.16(22)	7.41(17)	4.52(4)	7.46(26)	0.12(6)	4.09(16)	0.73(3)	0.28(3)	NA	5.88(28)	99.98(2)	52.1(6)
			Garnet (13)	40.36(16)	21.76(19)	0.67(36)	14.31(45)	14.82(17)	7.87(14)	0.48(8)	0.04(2)	MDL	0.05(1)	NA	0.0(0)	100.37(37)	64.9(8)
	CNM-45	1200 °C	Augite (6)	48.04(33)	10.40(40)	0.64(7)	7.99(40)	12.29(20)	18.36(18)	0.14(9)	1.59(6)	MDL	MDL	NA	0.0(0)	99.49(47)	73.3(1.2)
			Glass (6)	50.80(15)	18.14(20)	1.14(9)	7.56(9)	5.09(2)	7.91(6)	0.11(5)	4.06(9)	0.68(4)	0.35(2)	NA	4.16(31)	100.00(0)	54.5(3)
	CNM-50	1225	Garnet (8)	40.90(23)	22.32(19)	0.52(12)	13.45(42)	15.14(52)	7.73(42)	0.47(8)	0.04(3)	MDL	0.04(2)	NA	0.0(0)	100.62(32)	66.7(1.2)
			Augite (7)	48.84(47)	9.86(40)	0.60(15)	7.90(94)	13.04(25)	17.90(62)	0.12(9)	1.44(9)	MDL	0.03(4)	NA	0.0(0)	99.75(3)	74.7(2.1)
			Augite (7)	48.84(47)	9.86(40)	0.60(15)	7.90(94)	13.04(25)	17.90(62)	0.12(9)	1.44(9)	MDL	0.03(4)	NA	0.0(0)	99.75(3)	74.7(2.1)
			Glass (9)	49.86(18)	17.72(16)	1.07(14)	7.54(9)	5.65(4)	8.31(21)	0.15(3)	3.77(7)	0.64(3)	0.26(3)	NA	4.93(40)	99.95(5)	57.2(2)
			~10 wt% H ₂ O														
5	CNM-64	1025	Glass (9)	48.81(18)	17.03(20)	1.08(10)	7.34(9)	5.56(3)	8.49(18)	0.12(4)	3.70(19)	0.60(2)	0.25(2)	NA	6.98(44)	99.99(2)	57.5(3)
			Spinel (9)	0.15(8)	6.58(7)	4.01(26)	73.6(1.4)	6.77(9)	0.20(8)	0.22(5)	MDL	MDL	MDL	1.77(89)	0.0(0)	93.33(92)	14.1(4)
	CNM-60	1050	Glass (9)	48.60(20)	17.02(14)	1.14(15)	7.56(8)	5.53(3)	8.38(22)	0.13(4)	3.66(8)	0.59(2)	0.25(3)	NA	7.08(33)	99.99(3)	56.6(4)
10	CNM-66	1050	Glass (9)	48.33(28)	16.91(12)	1.00(14)	6.89(10)	5.29(5)	7.91(15)	0.13(4)	3.58(14)	0.59(3)	0.24(3)	NA	9.05(34)	99.98(3)	57.8(3)
			Spinel	NA	NA	NA	NA	NA	NA	NA	NA	NA	NA	NA	NA	NA	NA
	CNM-62	1075	Glass (9)	47.99(14)	16.82(25)	1.07(30)	6.90(20)	5.21(15)	8.29(29)	0.11(5)	3.46(23)	0.63(4)	0.24(3)	NA	9.19(55)	99.99(2)	57.4(8)
15	CNM-65	1075	Glass (9)	48.47(25)	16.86(12)	1.10(14)	6.84(15)	5.12(17)	8.02(22)	0.13(5)	3.45(14)	0.65(4)	0.24(3)	NA	9.04(32)	99.96(7)	57.2(5)
			Augite (7)	49.82(34)	5.2(1.0)	0.79(30)	8.9(2.0)	14.27(39)	19.8(1.2)	0.30(13)	0.69(10)	MDL	MDL	NA	0.0(0)	99.79(19)	74.2(4.3)
	CNM-61	1100	Glass (8)	48.23(19)	16.83(8)	1.01(11)	6.68(17)	5.12(9)	8.14(13)	0.14(5)	3.63(14)	0.66(2)	0.23(2)	NA	9.24(19)	99.97(6)	57.7(6)
20	CNM-69	1100	Glass (11)	46.55(32)	16.64(17)	0.89(12)	6.79(19)	5.60(15)	8.21(20)	0.13(6)	2.60(17)	0.52(4)	0.20(1)	NA	11.87(49)	100.00(0)	59.5(7)
			Augite (8)	49.94(64)	6.27(84)	0.57(7)	6.61(47)	14.42(44)	21.21(57)	0.11(10)	0.81(5)	MDL	MDL	0.15(5)	0.0(0)	100.14(54)	79.5(1.4)
	CNM-68	1125	Glass (12)	48.72(44)	16.59(21)	1.07(13)	7.30(17)	5.36(15)	8.13(23)	0.14(3)	2.77(20)	0.62(4)	0.25(2)	NA	8.95(52)	99.98(4)	56.7(5)
			~15 wt% H ₂ O														
10	CNM-75	1000	Glass (9)	49.98(40)	17.58(21)	1.06(9)	5.72(14)	4.49(24)	8.09(11)	0.13(4)	2.01(41)	0.75(7)	0.26(2)	NA	9.82(74)	99.94(11)	58.3(9)
			Amphibole (9)	42.49(61)	13.64(44)	1.49(21)	10.19(65)	16.11(80)	11.76(17)	0.07(8)	2.73(15)	0.41(3)	0.03(6)	NA	1.06(87)	99.99(2)	73.8(2.1)
			Spinel (8)	0.11(3)	5.93(10)	2.84(16)	77.57(86)	5.98(4)	0.16(12)	0.28(9)	MDL	MDL	MDL	MDL	0.0(0)	92.94(81)	12.1(2)
	CNM-73	1025	Glass (12)	49.55(33)	16.96(13)	1.07(5)	6.62(17)	5.52(21)	8.23(33)	0.13(4)	2.38(42)	0.67(7)	0.24(2)	NA	8.54(54)	99.98(4)	59.7(6)
			Spinel (13)	0.11(2)	5.81(13)	2.95(18)	76.8(1.1)	6.50(7)	0.12(6)	0.23(7)	MDL	MDL	MDL	0.33(15)	0.0(0)	92.90(92)	13.1(2)
15	CNM-78	1025	Glass (8)	48.71(50)	17.37(34)	0.83(6)	5.76(77)	2.97(72)	8.59(35)	0.16(4)	2.68(30)	0.51(6)	0.25(3)	NA	12.2(1.0)	100.00(0)	47.5(3.0)
			Amphibole (13)	41.77(43)	14.50(36)	1.49(13)	11.00(56)	14.52(26)	11.45(33)	0.13(7)	2.74(6)	0.50(4)	MDL	MDL	1.83(39)	99.99(1)	70.2(1.1)
			Spinel (5)	0.14(2)	6.92(13)	5.05(18)	74.06(79)	4.15(6)	0.12(12)	0.08(9)	MDL	MDL	2.65(18)	0.0(0)	93.19(85)	9.1(2)	
	CNM-77	1050	Glass (12)	48.32(42)	17.01(27)	0.88(9)	6.98(39)	5.04(44)	8.70(56)	0.10(6)	2.36(19)	0.50(4)	0.20(2)	NA	9.91(54)	100.00(0)	56.2(1.1)
			Amphibole (8)	42.4(38)	14.05(35)	1.39(22)	9.40(57)	15.92(23)	11.45(38)	0.13(11)	2.84(4)	0.48(2)	MDL	MDL	1.77(59)	99.99(2)	75.1(1.3)
			Augite (10)	51.06(67)	4.33(73)	0.46(17)	6.51(49)	15.12(54)	21.87(66)	0.17(9)	0.55(7)	MDL	MDL	MDL	0.0(0)	100.17(54)	80.6(1.4)

Table 3 continued

P (kbar)	Run	T (°C)	Phase	SiO ₂	Al ₂ O ₃	TiO ₂	FeO ^{a*}	MgO	CaO	MnO	Na ₂ O	K ₂ O	P ₂ O ₅	Cr ₂ O ₃	H ₂ O ^b	Total	Mg ^c /An ^d
20	CNM-76	1050	Glass (11)	47.67(43)	17.04(15)	0.91(12)	6.57(33)	4.45(29)	8.31(38)	0.11(4)	2.38(33)	0.50(3)	0.21(2)	NA	11.84(46)	100.00(0)	54.7(9)
			Amphibole (11)	41.66(28)	14.91(39)	1.28(17)	10.54(59)	14.70(41)	11.23(34)	MDL	2.81(9)	0.53(3)	MDL	MDL	2.19(58)	99.98(5)	71.3(1.5)
			Augite (3)	50.97(53)	4.75(35)	0.60(16)	7.79(40)	14.39(11)	21.81(41)	0.19(9)	0.72(4)	MDL	MDL	NA	0.0(0)	101.28(68)	76.7(8)
	CNM-74	1075	Glass (6)	48.56(48)	16.80(25)	1.04(12)	6.32(26)	3.97(34)	8.76(18)	0.14(4)	2.23(39)	0.55(4)	0.27(3)	NA	11.25(81)	99.96(5)	52.8(1.5)

Microprobe analyses in wt%; run labels in bold print denote experiments used to construct the phase diagram in Fig. 4; numbers in parentheses next to each analysis represent 1 σ standard deviation on average of multiple analyses; errors given in terms of least unit cited [e.g., 49.98(40) represents 49.98 \pm 0.40]

n Number of analyses, *NA* not analyzed, *MDL* below the 99% minimum detection limit

^a All Fe reported as FeO*

^b H₂O measured using water-by-difference

^c Mg# = 100*molar[MgO/(MgO+FeO*)]

^d An# = 100*molar[CaO/(CaO+Na₂O)]

Table 4 Ion microprobe analyses of select run products (ppm)

P (kbar)	Run	T	Phase	La	Ce	Nd	Sm	Dy	Er	Yb	Ti	Cr	Rb	Sr	Y	Zr
15	CNM-12	1290 °C	Glass	4.7	13.6	9.4	2.0	2.5	1.3	1.4	NA	NA	NA	NA	NA	NA
			Plag	0.7	1.2	1.4	0.7	0.7	0.6	0.5	0.5	NA	NA	NA	NA	NA
20	CNM-41	1325 °C	Glass	9.3	27.0	13.0	3.4	2.8	1.4	1.1	10050	28	24	775.6	19.8	160.3
			Augite	1.1	4.3	5.6	1.9	2.4	1.3	1.2	7013	1683	25	72.0	29.0	61.9
			Garnet	0.3	0.9	2.5	2.0	10.8	8.4	11.6	6211	308	23	9.2	158.3	161.5
			Plag	0.8	1.7	1.7	0.7	0.5	0.5	0.4	348	3	7	1046.8	3.9	1.9
5	CNM-42	1075 °C	Glass	10.0	24.8	14.0	3.9	3.7	1.9	1.6	4989	16	9	440.3	15.3	93.4
			Augite	1.0	4.0	4.1	2.3	1.9	1.1	1.1	5523	544	1	62.1	24.4	47.9
20	CNM-54	1175 °C	Glass	10.0	25.7	14.6	4.2	3.3	2.0	1.1	9761	44	15	927.8	28.0	171.6
			Garnet	0.3	1.2	4.1	4.2	20.5	20.6	18.3	4550	356	12	14.7	158.8	121.9
			Augite	1.1	2.6	6.1	2.3	2.7	1.6	1.3	5032	204	4	92.2	16.6	34.9
15	CNM-78	1025 °C	Glass	8.7	24.3	20.0	3.4	6.8	2.3	1.4	7957	24	16	811.0	34.0	149.0
			Amphibole	2.1	7.0	15.8	7.5	6.3	6.4	3.3	12974	158	7	376.7	29.9	43.1

Ion probe analyses in ppm; run labels in bold print denote experiments used to construct the phase diagram in Fig. 4; estimated 1σ uncertainties from SIMS intra-analysis statistics (see text): 10% relative: La, Ce, Ti, Cr; 15% relative: Nd, Sr, Zr; 20% relative: Sm, Dy, Er, Yb, Y; 30% relative: Rb; data generally represent averages of two to four different analysis spots on each run product

The inverse approach experiments presented here provide constraints on mineral assemblages and compositions in which North Sister basaltic andesite melt could have been saturated under different P-T-H₂O conditions, before its ascent to the surface. Only the near-liquidus experiments (>90 % melt) marked in bold in Tables 2, 3, and 4 were used for this purpose because the melts in these run products closely resemble the bulk composition of the North Sister basaltic andesite; therefore, the minerals in these run products represent permissible phases with which a liquid with the bulk composition studied here could have been in equilibrium at the conditions of the experiments. Experiments of this type do not speak to petrologic processes, however, and reveal only what crystalline phases this bulk composition would be saturated in at the experimental pressures, temperatures, and H₂O contents. Multiple interpretations of this information are possible allowing for the saturating crystalline phases to represent: (1) those crystallizing from North Sister basaltic andesite just prior to eruption, presuming it was derived from a more primitive parent; (2) those remaining in the source, presuming it to be a primary melt of a suitable protolith; or (3) those comprising a sub-volcanic cumulate pile where originally primitive mantle-derived melts stalled en route to the surface and re-equilibrated with this assemblage. Our experiments cannot distinguish between these possibilities. However, given the enigmatic, compositionally monotonous character of the North Sister lavas, our preferred interpretation is (3) as this might provide a means of buffering the melts to the observed near-constant composition.

Our near-liquidus results are summarized in Fig. 4, which shows the H₂O-undersaturated liquidus surface for our basaltic andesite starting material projected onto the P-T plane. Figure 4 is of a type first introduced by Green (1973) and utilized extensively by Wyllie (e.g., Wyllie 1979) and others, and differs fundamentally from more commonly seen P-T diagrams which show the phase relations within the melting interval, between the solidus and liquidus of a bulk composition, with a fixed H₂O content. The bulk composition is constant in such phase diagrams, but the melt composition changes continuously with changes in pressure and temperature as more and more crystallization occurs. In contrast, the liquidus surface in Fig. 4 applies to a fixed

liquid composition, equaling the bulk composition, with variable amounts of dissolved H₂O over ranges of pressure and temperature. The mineral fields shown in Fig. 4 are those that are stable at the liquidus; sub-liquidus phase relations cannot be represented.

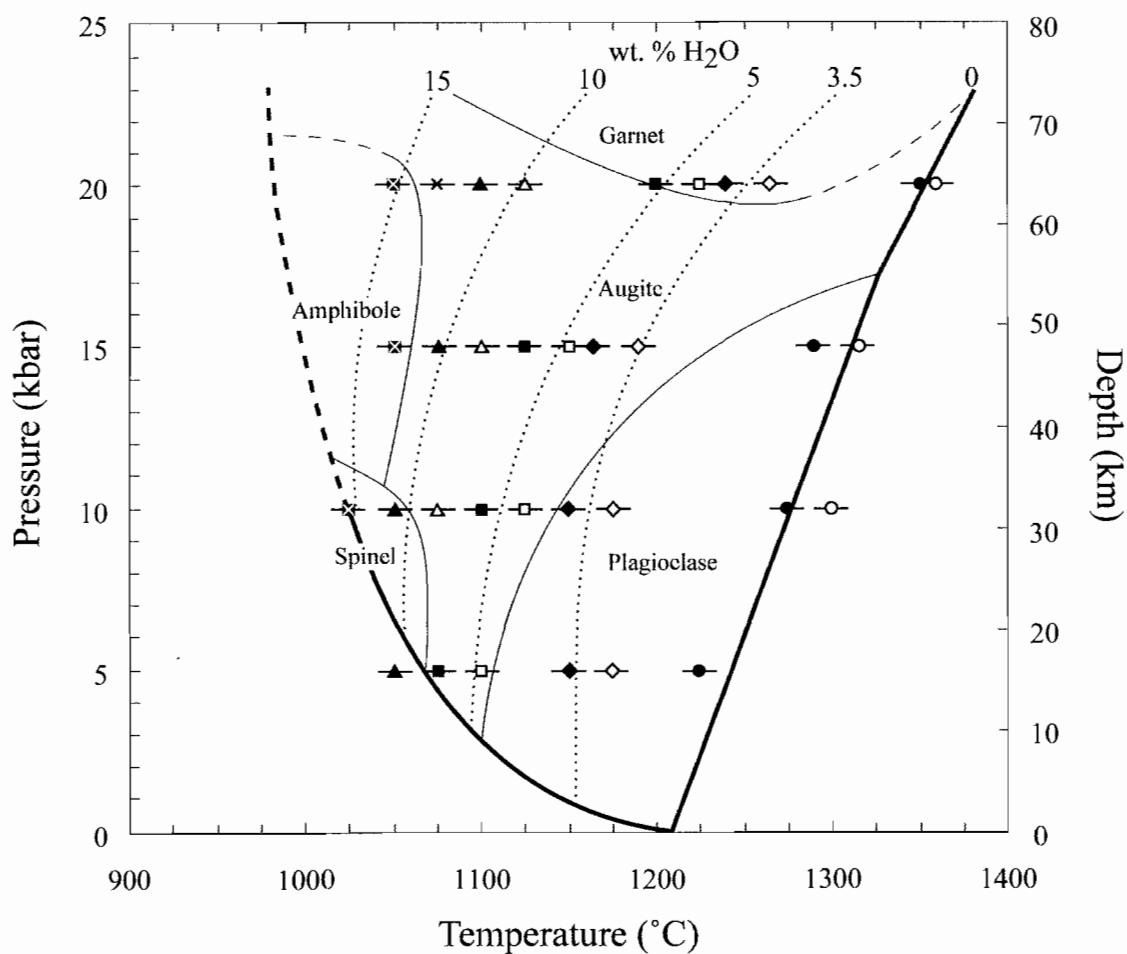


Fig. 4 Water-undersaturated liquidus surface with H₂O contours for North Sister basaltic andesite. *Open symbols* represent super-liquidus experiments and *filled symbols* represent sub-liquidus experiments. Nominally anhydrous runs are shown with *circles*, 3.5 wt. % H₂O with *diamonds*, 5 wt. % H₂O with *squares*, 10 wt. % H₂O with *triangles*, and 15 wt. % H₂O with *cross symbols*. Temperature uncertainties were estimated to be $\pm 10^\circ\text{C}$

In Fig. 4 the concave-up, partially dashed curve in bold to the left is the H₂O-saturated liquidus and the positively sloping, nearly straight, bold line to the right is the dry liquidus. Between these is the H₂O-undersaturated liquidus surface which is contoured for wt% H₂O with dotted lines. The locations of these isopleths are bracketed by our experiments (rather than with a H₂O-solubility model) with different symbols (circles, squares, etc.) corresponding to different nominal H₂O contents. The open symbols correspond to our lowest temperature super-liquidus run and the closed symbols correspond to the highest temperature sub-liquidus run. While all runs with the nominally dry starting material and those with 3.5 wt% H₂O (added as Mg(OH)₂) had exactly these water contents, each run in our 5, 10, and 15 wt% H₂O series contained slightly different H₂O contents since the H₂O in these materials was added by micro-syringe to each capsule, resulting in variability from capsule to capsule. Despite this, the H₂O contours shown in Fig. 4 comply with experiments shown within experimental and analytical error. Most experiments shown with solid symbols in Fig. 4 contain very small quantities (<4%) of only one crystalline phase. These runs enable us to map mineral phase stabilities onto the H₂O-undersaturated liquidus surface. For example, all runs shown within the field “plagioclase” contained plagioclase as the sole crystalline phase coexisting with melt with essentially the same composition as our bulk starting material. Two runs (CNM-45, -77) contain equally small quantities of two crystalline phases (e.g., 1.5 % each) even though they are near liquidus conditions. For example, CNM-45, plotting near the 5 wt% H₂O contour at 20 kbar, contains equal amounts of garnet and augite. We interpret this run to plot on the augite-garnet field boundary. Similarly, we interpret run CNM-77 to plot on the amphibole-augite field boundary at 15 kbar and ~15 wt% H₂O. Four other runs (CNM-15, -29, -42, -76) contain small but unequal quantities of two crystalline phases, and for three of these we interpret the more abundant phase to be the true liquidus phase presuming that if we had repeated these experiments at a slightly higher temperature, the small amount of the less abundant phase would have dissolved, leaving only the more abundant phase coexisting with melt. The one exception

to this is CNM-29 (Table 2; 15 kbar, 1165°C; 0.8% augite, 3.1% garnet) which we interpret to plot in the augite-only liquidus field based on the runs around it.

Under anhydrous conditions, the liquidus extends from about 1240°C at 5 kbar to 1355°C at 20 kbar with an apparent change in slope where augite replaces plagioclase as the liquidus phase. Relative to this reference the liquidus is displaced down-temperature by ~110°, ~160°, ~210°, and ~230°C respectively with 3.5, 5, 10, and 15 nominal wt% H₂O. Under anhydrous conditions, plagioclase (An₈₁) is the liquidus phase between 5 and 15 kbar but is replaced by augite at 20 kbar. With 3.5 wt% H₂O, plagioclase persists on the liquidus to just above 10 kbar, and is replaced by augite from ~12-20 kbar, and by garnet above 20 kbar. With 5 wt% H₂O, plagioclase is no longer a liquidus phase. Instead the liquidus phase is augite at 5, 10, and 15 kbar and garnet above 20 kbar. With 10 wt% H₂O, spinel is the liquidus phase at 5 kbar and is replaced by augite at 10, 15, and 20 kbar. Under the most hydrous experimental conditions, with 15 wt% added H₂O, the basaltic andesite melt has spinel, then amphibole, then augite as the liquidus phase with increasing pressure.

Phase compositions

Glass

Glass compositions are homogeneous within each run product (Table 3). Experiments used to define the H₂O-undersaturated liquidus surface contain >90% glass with major element oxide concentrations generally within ~10 relative % of the starting bulk composition. Run products in the 15 wt% series showed a variolitic texture (thin, radiating fibers of crystals, probably pyroxene or amphibole; Fig. 2f) owing to the difficulty of quenching such hydrous melts. Quench crystallization changes the composition of the glass only locally and thus we were able to obtain homogenous glass analyses in large pools far away from quench crystals in these experiments.

Vesicles

Vesicles were found in many run products, especially those with higher H₂O contents. They are generally small (5-10 μm) and homogeneously distributed, although some low pressure experiments have several large vesicles ($\sim 200 \mu\text{m}$) in addition to small vesicles. It is difficult to know whether these vesicles existed as a distinct phase in equilibrium at experimental conditions or whether they formed upon quenching. In many cases, particularly at higher pressures, water saturation is not a reasonable explanation for the existence of vesicles because the added water contents were lower than the known solubility. Thus, we infer that these vesicles were probably generated during quenching of the experiments.

Minerals

Plagioclase is anorthite-rich with compositions ranging from An_{80.8} to An_{85.9} with no strong correlation with temperature or H₂O. Crystals are generally euhedral and sometimes have thin quench “wisps” on the edge of otherwise well-formed crystals.

Augite compositions range in Mg# from 71.0 to 80.6, in wt% CaO from 15.5 to 21.9, and in wt% Al₂O₃ from 4.3 to 12.6 with no apparent correlation to pressure. But, with increasing temperature Al₂O₃ increases while CaO decreases (Fig. 5a). With increasing bulk H₂O contents the opposite is true, as the experimental temperature systematically decreases (Fig. 5b). Crystals are euhedral to subhedral, occasionally slightly zoned, and show quench “wisps” in experiments with higher H₂O contents.

Garnet contains 45-54 mol% pyrope, 25-32 mol% almandine, and 21-23 mol% grossular. Compositions range slightly in Mg# from 66.7 to 68.4 while CaO and Al₂O₃ contents remain nearly constant. Crystals are commonly euhedral, occasionally slightly zoned, and often contain small ($< 1 \mu\text{m}$) melt inclusions.

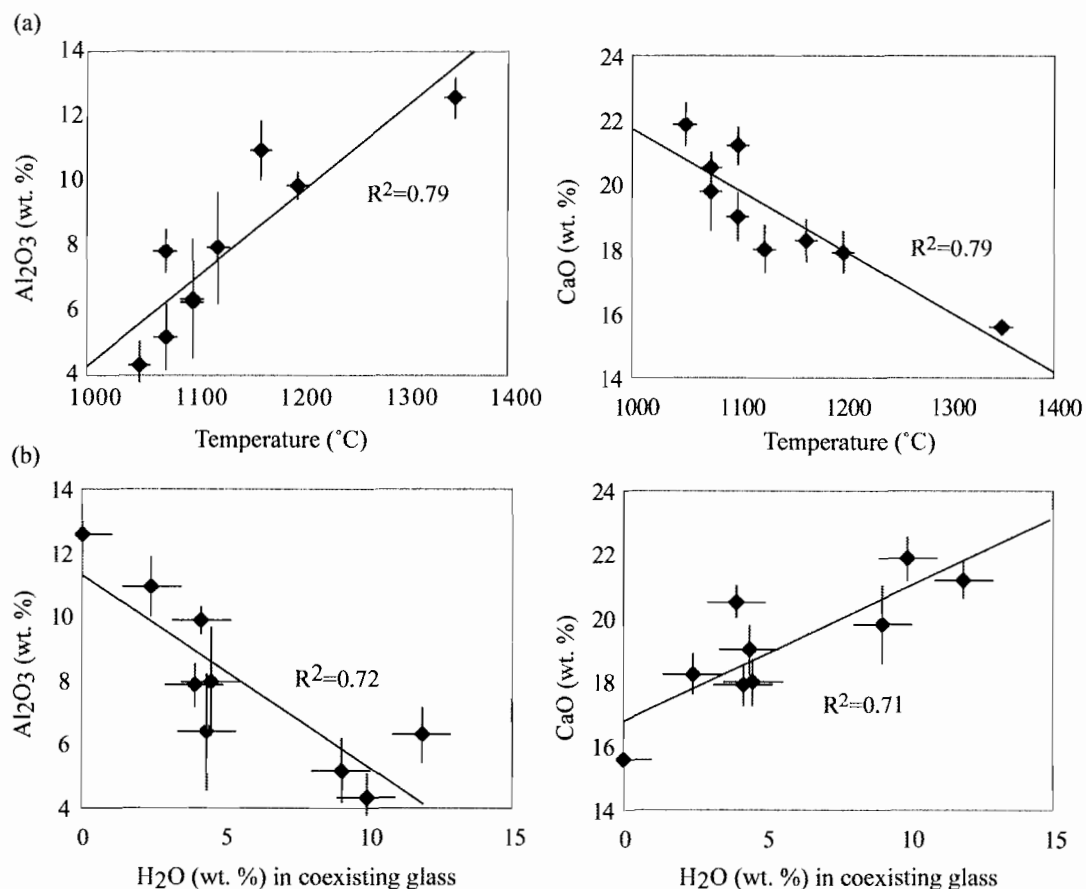


Fig. 5 Variation of near-liquidus augite compositions with (a) experimental temperature and (b) H_2O content in coexisting glass

Amphibole compositions range in Mg# from 71.3 to 75.1 while CaO contents remain nearly constant. Crystals are euhedral to subhedral and occasionally have quench “wisps”.

Spinel were found in experiments with high H_2O contents. They are largely magnetite-magnesioferrite solid solutions with minor Ti and Al components, suggesting relatively oxidizing conditions in these H_2O -rich experiments. Crystals are commonly euhedral and often are suspended in the melt by small attached bubbles (Fig. 2e).

Trace Element Distribution coefficients

Selected samples were analyzed for trace elements by ion probe (Table 4) to derive distribution coefficients, D , from these experiments. Average distribution coefficients for each mineral phase are listed in Table 5 and those for the REE are plotted in Fig. 6 where the generally smooth patterns suggest well-equilibrated run products. The obvious exception is the $D^{amph/liq}$ for Dy (plotted triangle) which deviates downward from the dashed trend extrapolated between Sm and Er; we surmise that this is an analytical artifact. Spinels were not analyzed for trace elements because with the exception of Cr, they have a negligible trace element budget. Measured distribution coefficients generally agree well with those found in other experimental studies (e.g., Drake and Weill 1975; Dunn and Sen 1994; Halliday et al. 1995; Johnston and Schwab 2004; Kelemen et al. 1993). In detail, our measured plagioclase D s agree well with literature values for light rare earth elements (LREE), Ti, Cr, and Sr, however they are slightly higher than literature values for heavy rare earth elements (HREE), Rb, Y, and Zr. Augite D s agree well with literature values for all rare earth elements (REE), Ti, Cr, Sr, Y, and Zr, while they are higher than literature values for Rb. Garnet distribution coefficients are the most uniform among the different samples analyzed. They agree well with literature values for the HREE, Ti, Cr, Y, and Zr while they are slightly higher than literature values for Rb, Sr, and the LREE. Amphibole distribution coefficients are similar to literature values for Ti, Cr, Rb, Sr, Y, and Zr while they are generally higher than literature values for the REE.

Table 5 Mineral/melt distribution coefficients determined for experimental mineral phases

Element	$D^{pl/liq}$	$D^{gt/liq}$	$D^{cpx/liq}$	$D^{amph/liq}$
La	0.13(4)	0.03(1)	0.11(3)	0.2(1)
Ce	0.08(2)	0.04(1)	0.13(4)	0.29(7)
Nd	0.14(6)	0.2(1)	0.4(2)	0.8(3)
Sm	0.3(2)	0.8(5)	0.6(3)	2(1)
Dy	0.3(2)	5(3)	0.8(4)	0.9(5) [2.5 ^a]
Er	0.4(3)	8(5)	0.8(5)	3(1)
Yb	0.4(2)	14(8)	1.1(6)	2(1)
Y	0.2(1)	6(3)	1(1)	0.9(4)
Ti	0.04(1)	0.5(1)	0.9(4)	1.6(3)
Cr	0.11(2)	9(2)	30(15)	7(1)
Rb	0.3(3)	0.9(6)	0.3(6)	0.4(3)
Sr	1.4(4)	0.02(1)	0.12(7)	0.5(1)
Zr	0.01(1)	0.8(3)	0.4(3)	0.3(1)

Units in parentheses represent 1σ standard deviation of least units cited [e.g., 0.13(4) is equivalent to 0.13 ± 0.04]

^a Apparent negative anomaly in the amphibole D for Dy is likely an analytical artifact and thus we extrapolate this value from Fig. 6

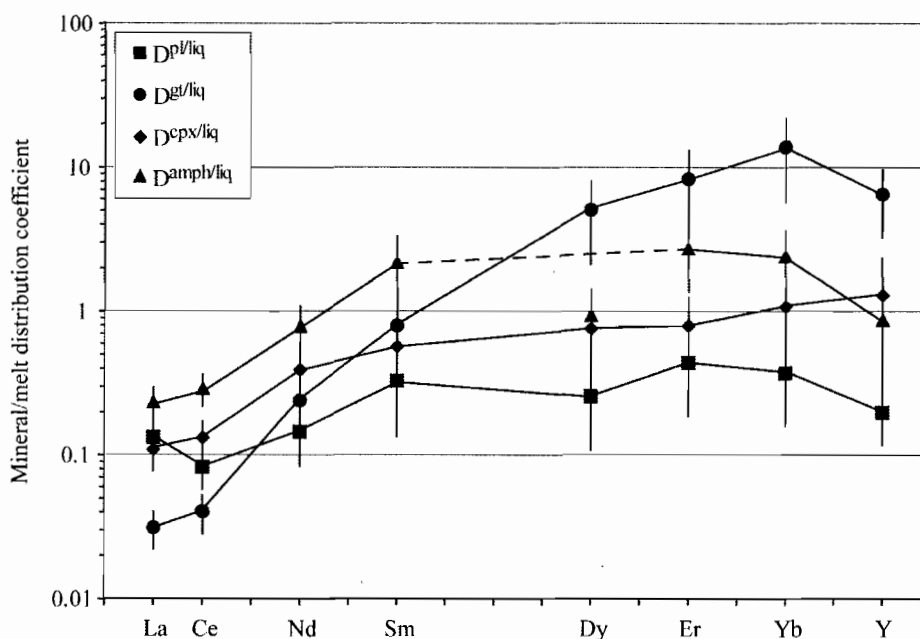


Fig. 6 Average mineral/melt distribution coefficients for REEs in plagioclase (*squares*), garnet (*circles*), augite (*diamonds*), and amphibole (*triangles*). 1σ uncertainties are shown with *vertical lines*. Low Dy value for amphibole (*filled symbol*) is likely an analytical artifact so dashed line shows extrapolation between Sm and Er

Discussion

Comparison with mineral phases in North Sister lavas

North Sister lavas contain phenocrysts or microphenocrysts of plagioclase (~15%, 0.25-1.5 mm diameter), olivine (<5%, 0.25-1.0 mm diameter), ± minor pyroxene (<1%, <0.1 mm), chromite (<1 %), and magnetite (<1 %) (Schmidt 2005). All of these minerals, except chromite, were produced in our experiments (Tables 2 and 3). Analyses of natural crystal compositions (Table 1) allow comparison with experimental crystal compositions (Table 3).

Natural plagioclase phenocrysts and microphenocrysts display a wide range in An contents (An₂₂₋₇₈; Schmidt 2005), likely due to polybaric crystallization during magma ascent, accompanied by magma degassing. The maximum An content, An₇₈, is still lower than near-liquidus plagioclase compositions from our experiments (An₈₁₋₈₆) which grew at high pressures (5-15 kbar) with up to ~3.5 wt% total H₂O. This difference supports the notion that the natural plagioclase phenocrysts are products of shallow crystallization during magma ascent and degassing as also concluded by Schmidt (2005) from geochemical modeling.

Olivine phenocrysts and microphenocrysts show a wide range in forsterite contents (Fo₅₄₋₈₄; Appendix A; Schmidt, 2005), as expected if due to crystallization during shallow magma ascent. Crystals of olivine (<1 wt%) were found in only a few experiments as mentioned earlier. These crystals are similar in composition to natural olivine phenocrysts, and have thin (<8 μm) orthopyroxene overgrowths, indicating that they are relict olivine grains that did not completely dissolve during the experiment. Relict olivine grains comprise a negligible mass and do not affect the equilibrium phases in these experiments.

Orthopyroxene microphenocrysts are a minor phase in lavas containing >54 wt% SiO₂ (Schmidt, 2005). Natural orthopyroxene compositions (Mg# ~74, wt% Al₂O₃ ~2) are distinct from those of experimental orthopyroxene (Mg# ~75-83, wt% Al₂O₃ ~6-8).

Clinopyroxene microphenocrysts found in the lava matrix contain low Al_2O_3 concentrations (~3 wt%; Schmidt 2005) while our near-liquidus augite compositions span a large range of concentrations (~4-13 wt% Al_2O_3). Experimental augite crystals with elevated Al_2O_3 contents grew at hotter and drier conditions than those with low-Al concentrations (Fig. 5). It is likely that low-Al clinopyroxene in the natural lavas also formed at lower temperatures, consistent with matrix crystallization at or near the surface during lava emplacement. However, near surface crystallization would suggest degassed conditions, as opposed to wet conditions, and low pressure phase relations are probably better suited to explain the natural clinopyroxene compositions. This is consistent with the findings of Schmidt (2005) that clinopyroxene crystallized at shallow depth.

Ti-magnetite microphenocrysts found in the lavas contain high TiO_2 (~19 wt%), low Al_2O_3 (0.7 wt%), and have Mg# ~4 (Appendix A; Schmidt, 2005). In contrast, experimental magnetite contains lower TiO_2 (~2-5 wt%), higher Al_2O_3 (~6-10 wt%), and higher Mg# (~9-19).

Potential lower-crustal mineral assemblages

As noted earlier, the inverse approach experiments presented here constrain permissible minerals and mineral compositions with which North Sister magmas could have been saturated in the deep crust prior to final ascent and eruption. However such experiments provide no information on the relative abundances of these minerals and this technique can overlook possible equilibrium minerals if there is a peritectic reaction relation involved. Despite these limitations, we can narrow down the possible crustal mineral assemblages that may have served to buffer the compositions of the compositionally monotonous basaltic andesite magmas that characterize North Sister Volcano.

In Fig. 7 we have reproduced the H_2O -undersaturated liquidus surface from Fig. 4 and have overlain the Cascades MOHO as estimated by Stanley et al. (1990) from seismic refraction and magnetotelluric data. The fields shown represent P-T- H_2O

conditions under which basaltic andesite liquid would be saturated in one phase alone, whereas the curves represent conditions of two phase saturation and the single triple point represents the unique conditions under which this composition would be triply saturated in spinel + augite + amphibole. Presuming the lower crust to consist of a polymineralic assemblage, we assign special significance to conditions of multiple saturation and note that possibilities include garnet + augite at high pressure, amphibole + augite, spinel + augite, and spinel + augite + amphibole at very low temperatures and high water contents, and an anhydrous gabbroic assemblage, plagioclase + augite, at low to moderate pressures, temperatures and H₂O-contents.

Garnet is unlikely to be involved in deep crustal processes beneath North Sister Volcano because mantle-normalized rare earth element patterns of North Sister lavas are low (~10 times primitive mantle) with shallow negative slopes (Fig. 8; Schmidt 2005), and lack the marked heavy rare earth element depletion that garnet would cause.

Amphibolite (amphibole + plagioclase) has often been invoked as a common lower crustal assemblage and has been used as an assimilant in models of deep crustal processes (Annen et al. 2006). Figures 4 and 8 show that amphibole does not become stable as a liquidus phase for our bulk composition until temperatures below ~1060°C with very high H₂O contents (~12 wt%). Moreover, amphibole and plagioclase do not coexist on our phase diagram eliminating amphibolite as a possible crustal mineral assemblage beneath North Sister (Fig. 4). This is likely due to the Cascades geotherm simply being too hot to stabilize amphibolite.

North Sister melt inclusions contain up to 3.25 wt% H₂O (Appendix A) which is not enough to stabilize amphibole or spinel (Fig. 4). In addition, lavas do not contain amphibole phenocrysts, suggesting that these magmas never experienced conditions conducive to amphibole formation. Therefore, amphibole and spinel are not likely constituents involved in deep crustal processes beneath North Sister Volcano.

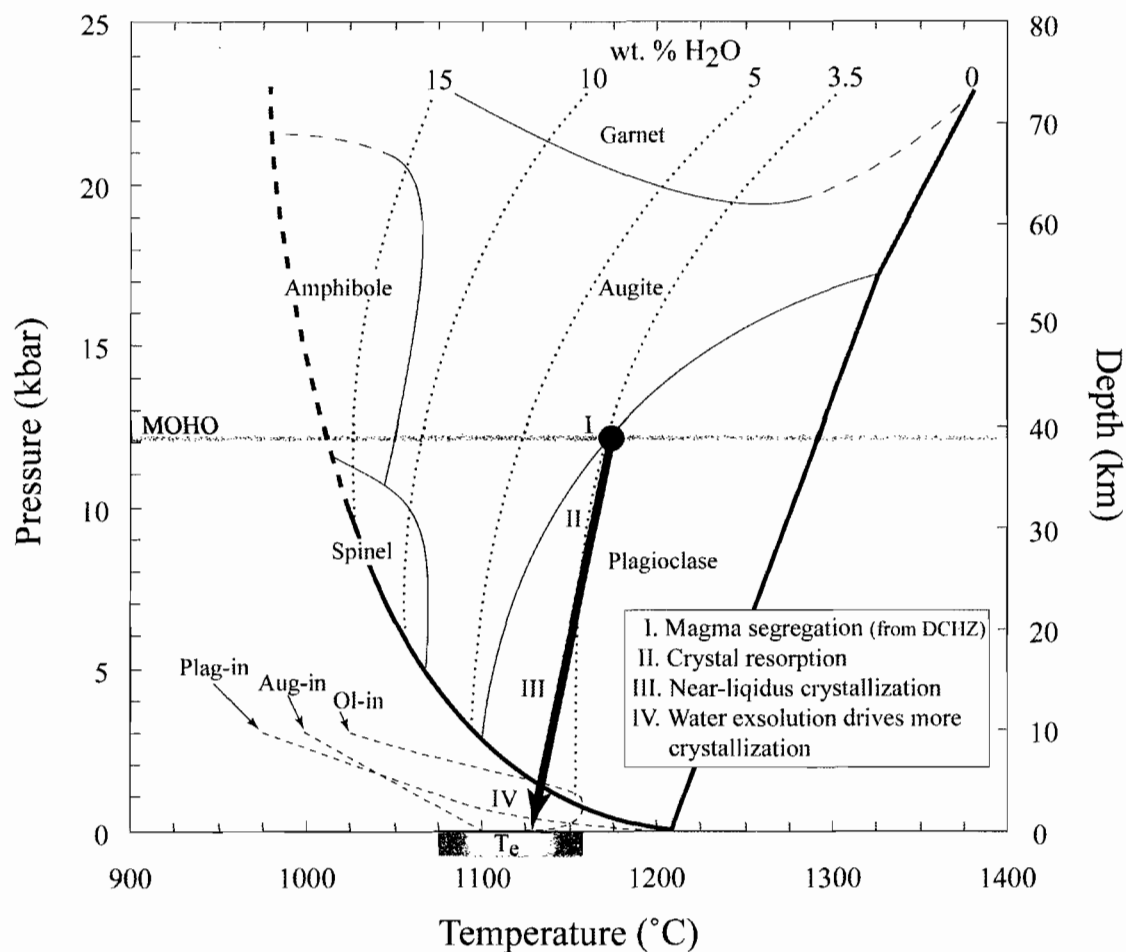


Fig. 7 Water-undersaturated liquidus surface showing possible “deep crustal hot zone” and ascent path for North Sister basaltic andesite melt with ~3.5 wt% water generated at ~12 kbar. Melt is assumed to ascend adiabatically with cooling of ~4°C/kbar (Annen et al., 2006). Cascades MOHO (*large shaded bar*) is from Stanley et al. (1990). Inferred eruption temperature (T_e ; *small shaded bar*) is from Moore and Carmichael (1998). (I) Basaltic andesite melt with 3.5 wt% H₂O segregates from deep crustal hot zone (DCHZ). Adiabatic ascent at or above the liquidus (II) superheats the melt so that any entrained crystals (cumulates or xenocrysts) are resorbed. (III) Near-liquidus crystallization occurs with further ascent until the melt crosses the H₂O-saturated liquidus at ~1 kbar (IV), at which point crystallization of low-pressure phases (*thin dashed lines*: olivine-in, plagioclase-in, and augite-in from Moore and Carmichael, 1998) is accelerated

Thus we infer that the most likely crustal lithology that North Sister magmas interacted with in the deep crust is an anhydrous gabbroic assemblage of augite + plagioclase. We further suggest that this likely occurred at about 40 km depth and

1175°C, where the augite-plagioclase field boundary, the ~3.5 wt% H₂O isopleth (the amount measured by FTIR in North Sister melt inclusions) and the MOHO (Stanley et al., 1990) all intersect, as shown on Fig. 7. Energy-constrained petrologic modeling of the generation of North Sister magmas (Schmidt, 2005) assumed a refractory lower crust, specifically one made of plagioclase-bearing mafic cumulates and our experimental data support this assumption. Furthermore, Schmidt (2005) found that high recharge rates of mantle melts into the deep crust are required to produce the persistent, monotonous basaltic andesites erupted at North Sister Volcano. These high recharge rates would provide a high heat flux into the deep crust, which has been shown to create basaltic andesite compositions in deep crustal hot zone processes (Annen et al. 2006). These models further support the involvement of a high temperature, anhydrous, mafic gabbroic assemblage in deep crustal processes beneath North Sister Volcano.

Although our inverse approach experiments cannot constrain the mode of the plagioclase + augite in the deep crustal hot zone beneath North Sister Volcano, our REE Ds pertain, at least qualitatively. Referring back to Fig. 6, we see that the REE Ds for augite define an approximately linear positive slope with increasing atomic number, from about 0.1 for La to about 1.2 for Yb and Y. This is in good agreement with Ds predicted by the model of Wood and Blundy (1997) given our melt compositions and those of our near-liquidus augites at lower H₂O contents, which are quite rich in Al₂O₃ and poor in CaO (Fig. 5), compositional characteristics that lead to higher Ds in this model. By contrast, the Ds for plagioclase are more constant, ranging from about 0.1 to 0.4, with a suggestion of slight downward curvature. We can consider two regional end member parental melts, (1) typical primitive calc-alkaline basalt (CAB) and (2) typical primitive low-K tholeiite (LKT) (e.g. Conrey et al. 1997), and ask whether equilibration of a mantle derived melt with a plagioclase- or augite-dominated lower crustal assemblage would better account for the REE patterns of North Sister basaltic andesites. Our preferred parental melt is the LKT because it has lower concentrations of REEs (except for the heavy REEs) than the North Sister lavas while the CAB has equal or higher concentrations of REEs (Fig. 8). Although LKTs are not generally thought of as a

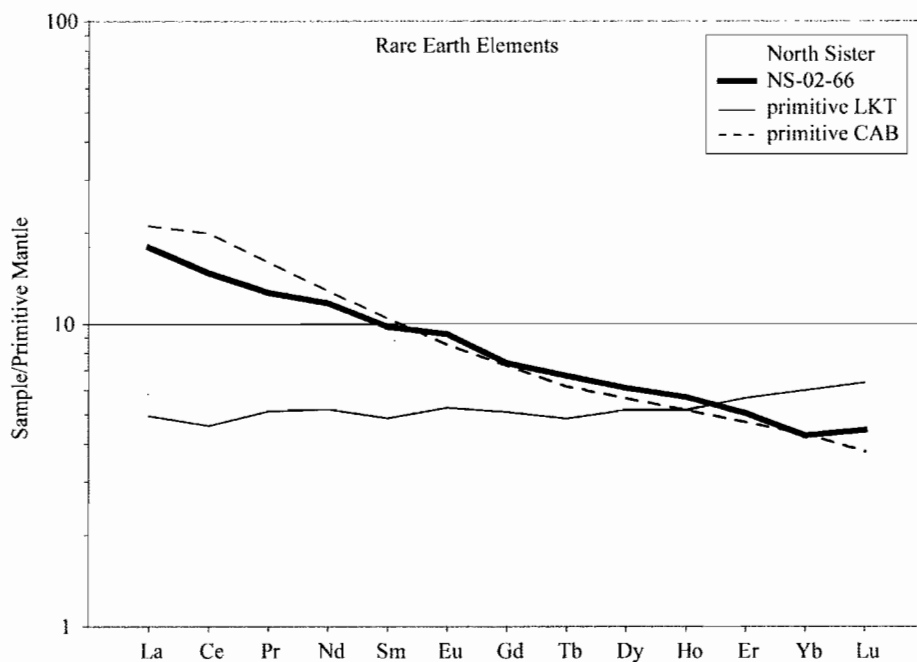


Fig. 8 Primitive mantle normalized rare earth elements (REE; McDonough and Sun, 1995) for representative North Sister lavas (*shaded area*; Schmidt, 2005), including our experimental starting material NS-02-66 (*heavy line*), regional primitive low-K tholeiite (LKT, *thin line*; Conrey et al., 1997), and regional primitive calc-alkaline basalt (CAB, *thin dashed line*; Conrey et al., 1997)

subduction-related magma type, LKTs are commonly found throughout the Central Oregon High Cascades (Bacon et al. 1997; Conrey et al. 1997; Leeman et al. 2005). As shown in Fig. 8, primitive LKTs in the region have essentially flat REE patterns at about 6X primitive mantle (PM; McDonough and Sun 1995), in contrast to North Sister basaltic andesites which have gently negatively sloping linear patterns, from about 15X PM for La to about 4X PM for Yb and Lu. Thus we require a means of rotating the original LKT into the shaded band, requiring enrichment in LREEs by about a factor of three and depletion of the HREEs by a factor of about 0.9. Clearly our D_s for augite alone, with the LREEs significantly incompatible (~ 0.1) and the HREEs slightly compatible (~ 1.2) could readily yield this rotation, whereas those for plagioclase alone could not, suggesting an augite-dominated assemblage in the deep crustal hot zone. Proceeding one step further, we note that any more than about 25 wt% plagioclase, the remainder being augite, would

yield bulk D_s for the HREEs that are no longer >1.0 and thus could not yield the HREE depletion, relative to LKT, observed on the North Sister lavas. Thus, we suggest that the buffering assemblage with which North Sister basaltic andesites equilibrated in the deep crustal hot zone was greatly dominated by augite. Beyond this, we cannot say much more as the relative masses of equilibrating melt and lower crustal solid are a matter of conjecture.

Proposed equilibration conditions and ascent path

Figure 7 shows a simplified version of our phase diagram that includes the depth of the MOHO beneath the Cascades from Stanley et al. (1990). The plagioclase-augite field boundary and the 3.5 wt% H_2O isopleth (corresponding to the H_2O contents measured in North Sister melt inclusions; Appendix A) both intersect with the MOHO at $\sim 1175^\circ C$ and ~ 12 kbar. Thus, we propose that the “deep crustal hot zone” within which North Sister basaltic andesites acquired their distinctive geochemical characteristics is at the base of gabbroic crust (~ 40 km) and that these melts had about 3.5 wt% dissolved H_2O , prior to beginning their ascent to the surface. Interestingly, the conductive Cascades geotherm of Stanley et al. (1990) also intersects with these boundaries, however more recent considerations suggest that the conductive Cascades geotherm is considerably cooler with local variability near magmatic centers (E.D. Humphreys, personal communication, 2007). Thus the high temperature of our proposed deep crustal hot zone likely represents a local thermal anomaly, not the ambient deep crustal temperature.

A hypothetical adiabatic ascent path for a North Sister basaltic andesite melt is shown with the thick, black arrow connecting likely conditions for a deep crustal hot zone with probable eruption temperatures (Fig. 7). Inferred eruption temperatures (T_e) are based on comparison of lava phenocryst assemblages and low pressure mineral-in curves from Moore and Carmichael (1998). Hypothetically, mantle derived melt stalls and equilibrates at the base of a gabbroic crust (~ 12 kbar, $1175^\circ C$) in a deep crustal hot zone,

producing North Sister basaltic andesite containing ~3.5 wt% H₂O (Fig. 7, step I). When the melt becomes buoyant enough (hydrous enough?) it segregates from the deep crustal hot zone and ascends adiabatically, cooling ~4°C/kbar (Annen et al. 2006) but remaining at or above the liquidus temperature (II). Adiabatic ascent “superheats” the melt so that any entrained crystals (e.g., cumulates or xenocrysts from the deep crustal hot zone) are resorbed. With further ascent, the melt cools below the liquidus temperature and near-liquidus crystallization of plagioclase occurs (III). When the melt crosses the H₂O-saturated liquidus at ~1 kbar (~3.5 km), crystallization of low-pressure phases such as olivine, plagioclase, ± augite (thin dashed lines; Moore and Carmichael 1998) is driven by magma degassing (IV).

This hypothetical ascent path explains a puzzling textural characteristic of the North Sister lavas. Schmidt and Grunder (2009) observed that the lavas are relatively crystal-poor (<20 % phenocrysts). This observation is at odds with the observation by Sisson and Grove (1993b) that upon ascent, hydrous magmas undergo large amounts of degassing-induced crystallization and erupt highly crystalline. Instead, an adiabatic ascent path such as the one we propose would inhibit crystallization until the melt crosses the H₂O-saturated liquidus. As the hypothetical path is drawn, abundant crystallization is only allowed for the last 3.5 km of ascent. This contrasts with an ascent path starting at higher water concentrations, for example, the three-phase saturation point (~10 kbar, 1040°C, 12 wt% H₂O). This path would cross the H₂O-saturated liquidus at much greater depths (~23 km) allowing a much greater amount of degassing induced crystallization, leading to a more crystal-rich magma.

Summary and Conclusions

Our hydrous, high pressure experiments provide P-T-H₂O and compositional constraints on possible lower crustal mineral assemblages with which North Sister magmas may have last equilibrated before eruption. These data help elucidate the deep crustal lithology

that is involved in the production and buffering of monotonous mafic arc magmas. Combining our experimental results with examples of tectonically exposed lower arc crust, geophysical constraints, trace element geochemistry, and melt inclusion volatile contents, we have determined that an anhydrous, mafic gabbroic assemblage at ~12 kbar and 1175°C is the most probable deep crustal lithology involved in deep crustal processes involving moderately hydrous (~3.5 wt% H₂O) basaltic andesite magma beneath North Sister Volcano.

Bridge

In the previous chapter I addressed the lower crustal lithology in an active arc setting and its ability to buffer hydrous mafic subduction zone magma compositions. In the next chapter, I discuss magmatic processes related to the evolution of hydrous magmas in the upper arc crust. Specifically, I describe how the exsolution of CO₂ and H₂O from vapor saturated silicic magmas controls the depth at which hydrothermal systems occur and porphyry copper deposits form.

CHAPTER III

MAGMATIC VOLATILE CONTROLS ON THE FORMATION DEPTH OF PORPHYRY COPPER ORE DEPOSITS

This chapter is in preparation to be submitted to *Geology*. This paper was co-authored with Paul J. Wallace and Mark H. Reed, who provided advising and editorial support.

INTRODUCTION

Porphyry copper deposits are large, low-grade ore deposits that are the world's primary source of Cu and Mo. They form in and around silicic plutons, porphyry dikes, and associated volcanic rocks from exsolved magmatic fluids that carry metals and sulfur from large magma volumes and concentrate them into a cupola (Fig. 1). Above the cupola, pulses of hydro-fracturing, porphyry dike injection, and fluid flow through fractures lead to host rock alteration and metal sulfide deposition (Cloos, 2001; Seedorff et al., 2005). Porphyry copper deposits are inferred to form at 1 to 5 km depth at the top of silicic plutons (Seedorff et al., 2005). Ore precipitation requires a favorable combination of magma composition, temperature, f_{O_2} , volatile content, crystallization history, emplacement depth, and volatile phase composition (e.g., Seedorff et al., 2005). In this study, we investigate the volatile controls on porphyry deposit formation.

Determining what controls the pressure at which magma exsolves a large mass of fluid is the key to understanding the depth of porphyry ore formation. H_2O , CO_2 , and Cl are the dominant magmatic volatile components, and magma may become fluid saturated either by isobaric crystallization or decompression. CO_2 has a lower solubility than H_2O in silicic melts, thus CO_2 -rich fluid saturates first. However, once the melt becomes

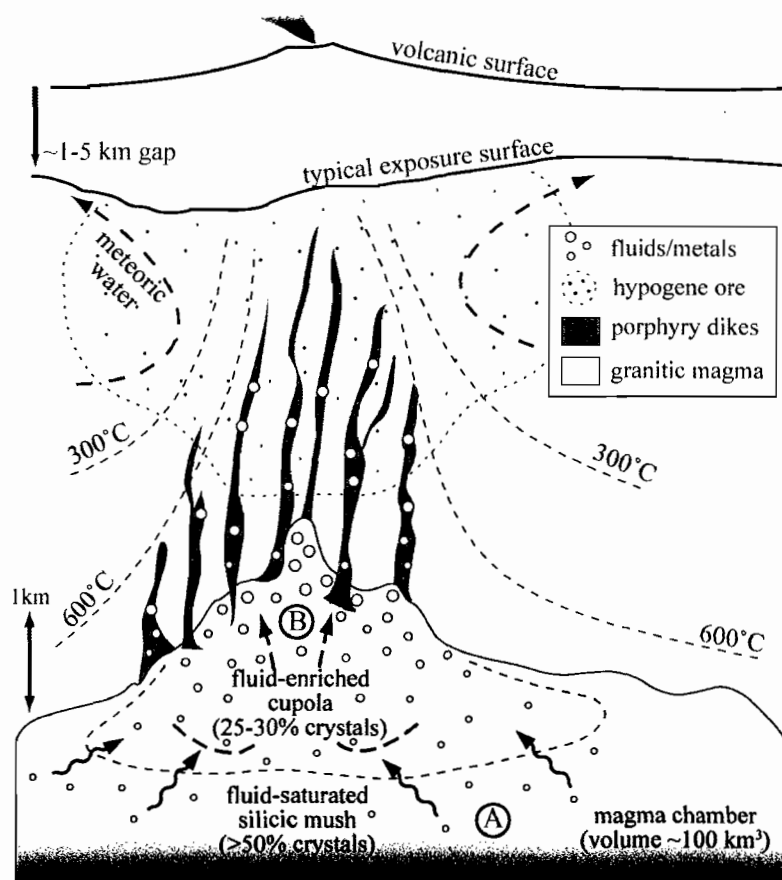


Figure 1. Schematic cross section of fluid-saturated crystallizing magma beneath a porphyry copper deposit. During isobaric fractional crystallization of fluid-saturated granodioritic mush (A), H_2O increases in the residual melt, but CO_2 is preferentially lost to the fluid phase due to its lower solubility. Exsolved fluid is initially CO_2 -rich and significant amounts of H_2O are not exsolved until CO_2 is largely degassed, after which the melt becomes saturated with nearly pure H_2O fluid and further crystallization drives exsolved fluids to more H_2O -rich compositions. Decompression driven degassing (B) results in analogous variations in H_2O and CO_2 . We consider isobaric fractional crystallization to be the main fluid saturation mechanism leading to hydrofracturing and formation of porphyry deposits and thus we consider effects of decompression to be less significant. (Modified from Seedorff et al., 2005; Shinohara et al., 1995; Dilles, 1987; and Hedenquist and Lowenstern, 1994.)

saturated with H_2O -rich fluid a large mass of fluid will exsolve. This causes abundant crystallization (Lowenstern, 2001) that leads to a positive feedback of more volatile exsolution and more crystallization (Annen et al., 2006). Once magma reaches 20-50% crystallinity it becomes a rigid crystal-supported mush (Saar et al., 2001) that cannot ascend further through the crust (Cloos, 2001). At this critical magma emplacement

depth, accumulation of a large mass of exsolved fluid within a cupola leads to overpressurization, hydrofracturing of roof rocks, and porphyry deposit formation.

Estimating H₂O and CO₂ concentrations in ore-forming magmas is difficult. Experimental phase relations and stability requirements of hydrous phases such as hornblende and biotite have commonly been used to constrain magmatic H₂O contents (Candela, 1997; Dilles, 1987). For example, stability of hornblende in a granitic magma requires ~4 wt% H₂O dissolved in the coexisting melt (Dall'Agnol et al., 1999; Klimm et al., 2003; Naney, 1983). Measurements of volatiles dissolved in melt inclusions trapped within porphyry phenocrysts or deep hydrothermal veins suggest ore-forming magma H₂O concentrations of up to 4.5 wt% (Davidson et al., 2005; Rapien et al., 2003), but such melt inclusions are difficult to study and interpret because they are commonly small, crystallized, and hydrothermally altered. In contrast, melt inclusion studies from volcanic analogs in geologic settings similar to those of porphyry deposits provide indirect estimates of ore-forming magma H₂O and CO₂ concentrations, and often yield higher magmatic H₂O contents ranging from 4 to 7 wt%, and CO₂ contents ranging from 0 to 1000 ppm (Lowenstern, 1994; Wallace, 2005).

There are few published analyses of volatile compositions of fluid inclusions representative of deep fluids trapped soon after exsolution from porphyry copper-forming magma. Existing data suggest that fluid compositions are typically >90 mol% H₂O with the remainder being dominantly CO₂ with small amounts of SO₂, H₂S, and salts (Graney and Kesler, 1995; Redmond, 2002; Rusk et al., 2008).

In this study we investigate the mass and composition of exsolved CO₂-H₂O fluid from silicic melts as a function of isobaric fractional crystallization (Fig. 1, A) and polybaric degassing (Fig. 1, B). The relationship between CO₂ and H₂O solubility along with fluid inclusion compositions allows us to determine the bulk CO₂ and H₂O concentration of the ore-forming parental magma that produced the supergiant porphyry Cu-Mo deposit at Butte, Montana. These estimates may explain the distinctively deep generation of the Butte deposit (6-9 km; Rusk et al., 2008) compared to other porphyry copper deposits (Seedorff et al., 2005). We then apply this volatile solubility model to

other porphyry deposits for which deposit depth, melt inclusion volatile contents, or fluid inclusion compositions are known to further examine the conditions of porphyry copper deposit formation.

METHODS

We modeled volatile solubility using the empirical model of Liu et al. (2005) to calculate pressures at which rhyolitic melts containing dissolved CO₂ and H₂O are saturated with CO₂-H₂O fluid. This model is calibrated for metaluminous high-silica rhyolitic melts and is appropriate for many porphyry ore-related metaluminous granitic rocks including those from Butte, Montana. We investigated temperatures between 600-800°C, which approximate the overlap between pre-eruption temperatures for rhyolitic magma (Wark et al., 2007), and temperatures estimated for associated ore-bearing hydrothermal veins (Field et al., 2005; Rusk et al., 2008; Seedorff et al., 2005; Chapter IV). Model pressures of 50-400 MPa were chosen to cover the estimated range for known porphyry deposits (Seedorff et al., 2005). We considered fluid phase compositions ranging from 20-98 mol% H₂O (80-2 mol% CO₂), which overlap with fluid inclusion compositions (70-98 mol% H₂O) common in porphyry copper deposits (Graney and Kesler, 1995; Redmond, 2002; Rusk et al., 2008).

To model variations in CO₂ and H₂O in melt and exsolved fluid during isobaric crystallization between 200 to 400 MPa, we calculated fluid/melt distribution coefficients for CO₂ and H₂O along 700°C isobars from the model of Liu et al. (2005). We assumed a constant distribution coefficient to solve the Rayleigh crystal fractionation equation for each iterative step (e.g., Maaløe, 1985). Initial modeled volatile concentrations ranged from 1800 to 1190 ppm CO₂ and 2 to 4 wt% H₂O. We modeled changes in CO₂ and H₂O in the melt and fluid during open- and closed-system polybaric degassing starting from 300 and 400 MPa using the program VolatileCalc (Newman and Lowenstern, 2002).

Estimation of the bulk porphyry magma fluid content requires knowledge of the crystallinity of the porphyry magma at the time of fluid exsolution. We measured crystallinities of porphyry dikes from Butte, Montana, Bingham, Utah, and Ann Mason,

Nevada, by scanning polished slabs and digitizing the phenocrysts (quartz, potassium feldspar, plagioclase, \pm biotite, \pm amphibole) using *Adobe Illustrator* software. Phenocryst area fractions were then determined using *ImageJ* software. Errors in crystallinity measurements ($\pm 2\%$) come from uncertainty in defining small, poorly defined groundmass phenocrysts.

VOLATILE SOLUBILITY MODEL RESULTS

During isobaric fractional crystallization of a magma at 350 MPa that is fluid-saturated with 3 wt% H₂O and 1790 ppm CO₂ (Fig. 2, path A), model results indicate that H₂O increases in the residual melt (Fig. 3a), and CO₂ preferentially partitions into the fluid phase due to its lower solubility. Exsolved fluid initially has a high CO₂/H₂O ratio, but after $\sim 60\%$ crystallization the melt becomes saturated with H₂O-rich fluid, and further crystallization drives exsolved fluids to nearly pure H₂O (Fig. 3b). When the magma begins to exsolve dominantly H₂O fluid, the mass of exsolved fluid increases greatly with each progressive step of crystallization (Fig. 3b). Fluid compositions reach >90 mol% H₂O after 85% crystallization. Decreasing the initial CO₂ concentration of the magma decreases the amount of crystallization that is required to exsolve H₂O-rich fluid. For example, by decreasing the initial CO₂ by $\sim 30\%$, the fluid composition becomes H₂O-dominated after only 45% crystallization, and the fluid reaches >90 mol% H₂O after 80% crystallization. Changing the pressure by ± 100 MPa results in negligible changes in melt compositions, and 5-15% changes in fluid compositions at any given step of crystallization, because the fluid/melt distribution coefficients do not change appreciably as adjacent isobars have similar slopes (Fig. 2).

Open- and closed-system polybaric degassing of magma (Fig. 2, path B) display similar variations in CO₂ and H₂O, such that CO₂-rich fluid exsolves first, resulting in a small mass of exsolved fluid until the magma saturates in nearly pure H₂O fluid, after which a large mass of fluid exsolves. CO₂ is nearly totally degassed after 40% decompression for an open-system, and 55% decompression for a closed-system.

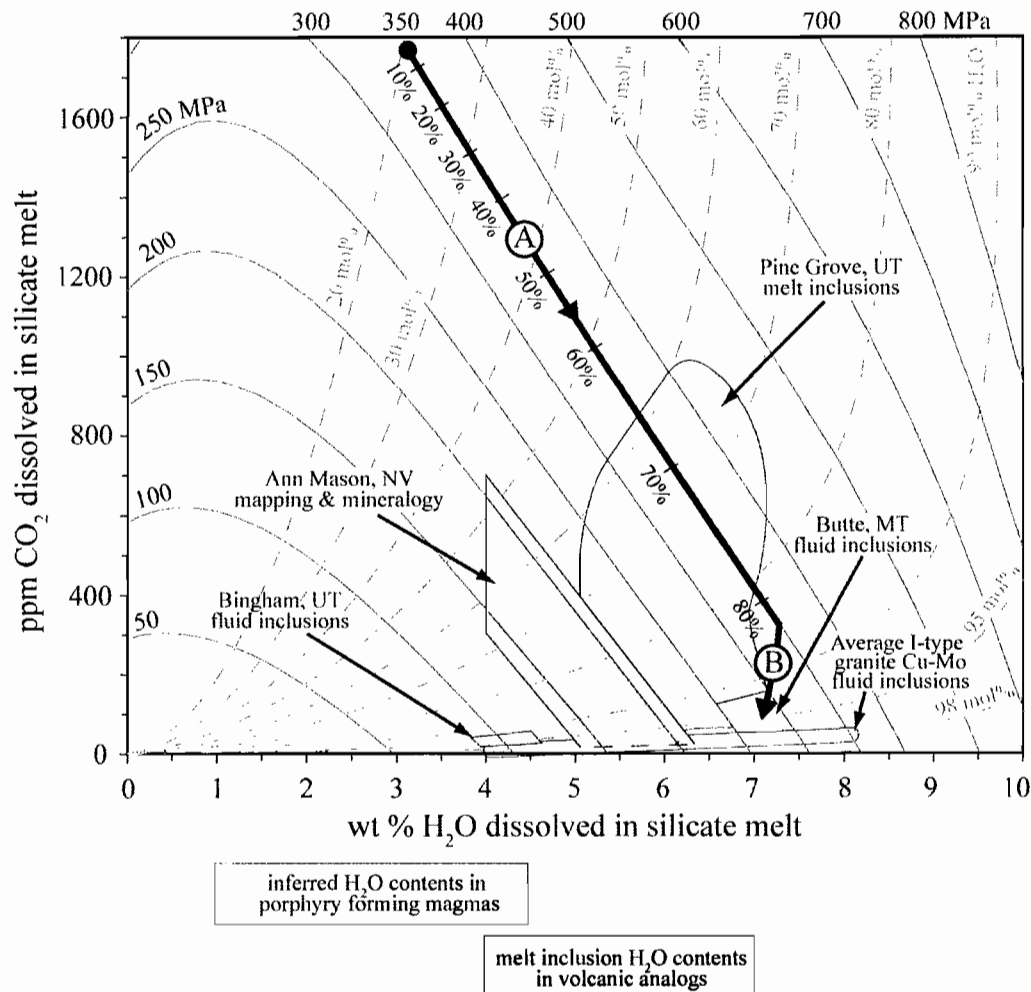


Figure 2. Modeled CO₂ and H₂O fluid saturation isobars and isopleths. Isobars from 50-800 MPa (solid lines) represent the pressure at which a CO₂- and H₂O-bearing metaluminous high silica rhyolitic melt at 700°C would be saturated with mixed H₂O-CO₂ fluid (using the solubility model of Liu et al., 2005). Isopleths of constant fluid compositions from 20-98 mol% H₂O (grey dashed lines) represent the composition of aqueous fluid in equilibrium with the fluid-saturated melt. The remaining composition of the fluid that is not H₂O is dominantly CO₂ with minor concentrations of salts, metals, and sulfur. Grey shaded fields indicate conditions for either silicate melts or aqueous fluids from porphyry deposits at Bingham, UT, Ann Mason, NV, Pine Grove, UT, and Butte, MT. Average fluid inclusion compositions from I-type granite Cu-Mo deposits are from Valley Copper, B.C., Bingham, UT, Hall, Nevada, Granisle, B.C., Bell, B.C., Questa, New Mexico, and Copper-Flat, New Mexico (see text for references). Hypothetical isobaric fractional crystallization path with increments of % crystallization (A) and open-system polybaric degassing path (B) are shown with thick black lines.

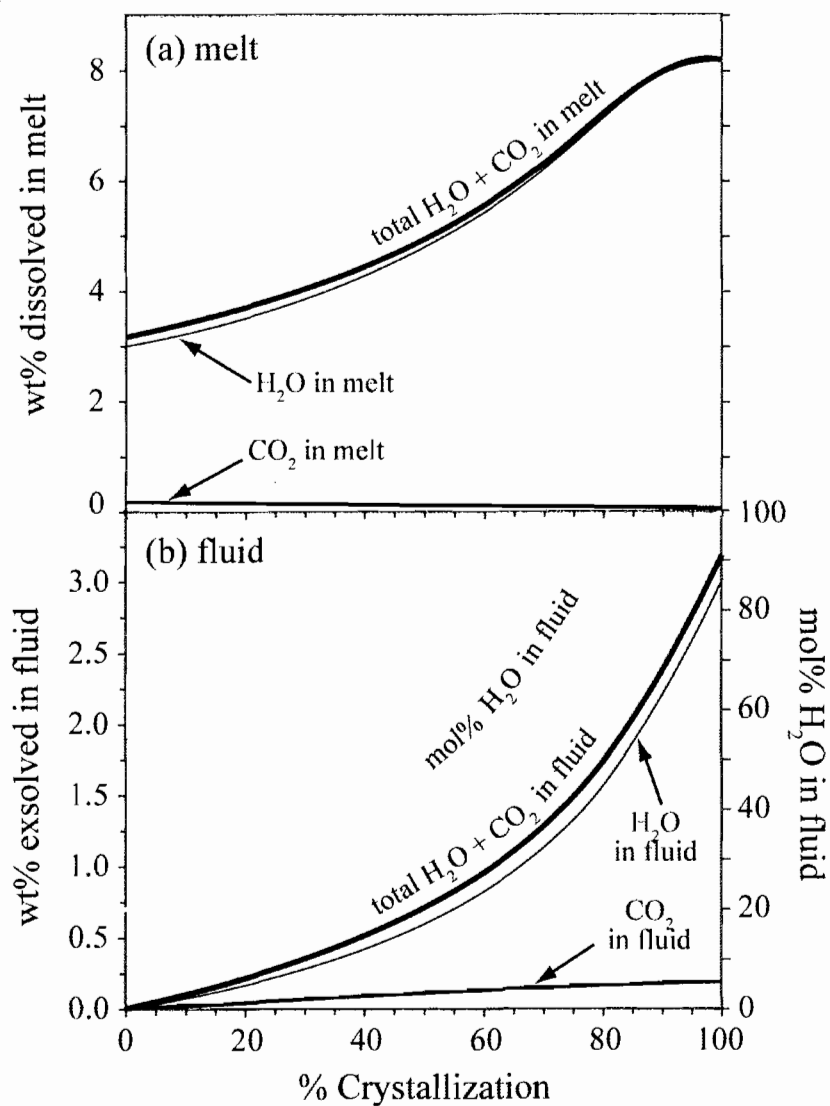


Figure 3. Variation in H_2O and CO_2 in melt and fluid during isobaric fractional crystallization at 350 MPa and 700°C . Results are shown for an initial magma that is fluid-saturated with 3 wt% H_2O and 1790 ppm CO_2 . (a) wt% H_2O , CO_2 , and total $\text{H}_2\text{O} + \text{CO}_2$ dissolved in melt (black lines), and (b) wt% H_2O , CO_2 , and total $\text{H}_2\text{O} + \text{CO}_2$ exsolved in fluid (black lines) and fluid composition in mol% H_2O (grey line).

As we discuss later, we consider polybaric degassing to play a minor role as a mechanism for magma fluid saturation leading to the formation of porphyry deposits in comparison to isobaric fractional crystallization (Fig. 1). Therefore we do not emphasize these results, but acknowledge this process as one that could further accentuate the same CO₂ and H₂O variations that result from fractional crystallization.

The CO₂ and H₂O solubility model (Fig. 2) illustrates relationships among four variables: pressure, dissolved CO₂, dissolved H₂O, and fluid composition (mol% H₂O). If pressure and fluid composition are specified, then dissolved CO₂ and H₂O in the melt can both be determined or vice versa. For example, fluid inclusions representative of early exsolved magmatic fluids from Butte, Montana (deep B35-type inclusions; Rusk et al., 2008), which were trapped in deep veins at pressures of 250-300 MPa (7-9 km depth, assuming lithostatic pressures and rock density of 2.85 g/cm³), indicate that there is a limited fluid compositional range between 92 and 97 mol% H₂O (Rusk et al., 2008). If these fluids were in equilibrium with rhyolitic magma at 700°C and 250-300 MPa, then the melt must have contained at least 60-160 ppm CO₂ and 6.5-7.5 wt% H₂O (Fig. 2). This corresponds to 40-110 ppm CO₂ and 4.9-5.6 wt% H₂O in the parent magma once we account for the 25% crystallinity that we measured in the porphyry.

Uncertainty in the model temperature does not change the solubility relations appreciably; an increase of 100°C results in a slight decrease in CO₂ and H₂O solubility in the rhyolitic melt, and a small decrease in H₂O mole fraction in the coexisting aqueous fluid. For example, an increase to 800°C in the Butte model temperature leads to a decrease of only ~0.2 wt% dissolved H₂O in the modeled melt.

Using pressure, CO₂, and H₂O data from other porphyry deposits, we can evaluate them as we did for Butte. Melt inclusions from Pine Grove, Utah, contain 60-960 ppm CO₂ and 5-7 wt% H₂O (Lowenstern et al., 1994), similar to the high H₂O concentrations inferred for the Butte melt (Fig. 2). Using the most degassed melt inclusion volatile contents and accounting for 30% crystals at Pine Grove, the bulk magma volatile concentration was 45-70 ppm CO₂ and 4.1-4.9 wt% H₂O. We have no fluid inclusion composition data for Pine Grove, but if the deep fluids were typical of average I-type

granite porphyry Cu-Mo deposits (~98 mol% H₂O based on 7 deposits; Graney and Kesler, 1995), then the deposit at Pine Grove could have formed between 4.3 and 7.1 km (150-250 MPa) once the magma degassed and crystallized enough to stall in the crust. This pressure estimate overlaps with that of Keith et al. (1986) who estimate that Pine Grove mineralization occurred between 4 and 5 km based on mapping and drill core samples.

Fluid inclusion compositions from deep veins at Bingham, Utah (Type I inclusions, Redmond, 2002; analogous to B35-type inclusions at Butte) contain ~92-96 mol% H₂O and were trapped between 2.5 and 3.5 km (90-120 MPa; Graney and Kesler, 1995; Redmond, 2002). Magma in equilibrium with these fluids must have contained <50 ppm CO₂ and at least 3.8-4.6 wt% H₂O (Fig. 2), which indicates a bulk parental magma CO₂ content of <40 ppm CO₂ and at least 3.0-3.7 wt% H₂O once we account for 20% crystallinity of the porphyry. Given that hornblende is stable in nearly all mineralized porphyry dike intrusions at Bingham (Redmond, 2002) indicating a minimum of ~4 wt% H₂O, the minimum modeled H₂O concentration seems reasonable.

Geologic reconstruction and mineral geobarometry of the porphyry deposit at Ann Mason, Nevada show that the transition from the cupola to the Cu ore body occurred between 4 to 6 km depth (140-210 MPa; Dilles, 1987). If deep fluid inclusions from Ann Mason have compositions typical of average I-type granite porphyry Cu-Mo deposits (~98 mol% H₂O; Graney and Kesler, 1995) then this model suggests melt CO₂ contents of <20 ppm and H₂O contents of at least 5.0-6.4 wt% in the melt; or after accounting for 25% crystallinity, <15 ppm CO₂ and ~3.8-4.8 wt% H₂O in the bulk parental magma. This H₂O content is close to previous estimates of 4-5 wt% H₂O based on hornblende in the dikes (Dilles, 1987).

HIGH H₂O CONTENT IN THE BUTTE PORPHYRY MAGMA

Our estimate of the parental Butte porphyry magma CO₂ and H₂O concentrations presumes that CO₂ and H₂O from the cupola and porphyry dikes were trapped in fluid inclusions in early-formed veins. This assumption is likely quite good given the spatial

gradation between the cupola, porphyry dikes and deep, early-formed hydrothermal veins (Brimhall, 1977; Dilles, 1987). Our magmatic CO₂ and H₂O estimates are the minimum concentrations required to saturate the magma. Given the enormous volume of veined and altered rock at Butte, the porphyry magma likely emanated from a fluid-enriched cupola above a large pluton of granodioritic mush (Fig. 1). The bulk porphyry magmatic H₂O content is therefore estimated to be >5-6 wt%. This is higher than previous estimates for ore-forming magma (≤ 4.5 wt% H₂O), however it is still within the typical range of estimates from volcanic analogs (4-7 wt% H₂O).

Although the absence of amphibole in the Butte porphyry dikes is consistent with <4 wt% H₂O (Naney, 1983), higher magma H₂O concentrations may exist without forming amphibole under the highly oxidizing conditions (e.g., NNO+2.5) typical of porphyry copper-forming environments (Černý et al., 2005). For example, a 700°C magma with 6 wt% H₂O at 300 MPa and NNO+2.5 would form biotite rather than hornblende (Fig. 4; Dall'Agnol et al., 1999). Further, more evolved rhyolitic compositions such as the Butte porphyry favor formation of biotite over hornblende (Klimm et al., 2003). Thus we conclude that the lack of hornblende in the Butte porphyry magma does not preclude the existence of high magmatic H₂O contents.

H₂O in granitic magma can be derived from various sources, including small amounts from formation waters in adjacent country rocks or dehydration of hydrous minerals in partially molten source rocks, and larger amounts from subduction components derived from dehydration of a subducting oceanic slab. The Late Cretaceous Boulder Batholith, which hosts the Butte porphyry deposit, intruded into regionally metamorphosed Archean metamorphic rocks of unknown thickness, layered and folded Proterozoic, Paleozoic, and Mesozoic marine sediments more than 6 km thick, Mesozoic continental sediments 1 km thick, and Upper Cretaceous calc-alkaline volcanic rocks more than 4 km thick (Vejmelek and Smithson, 1995). Thus there is potential to contribute both formation H₂O from sediments and mineral dehydration H₂O to a granitic melt ascending through the crust in this region, however it is unlikely that either of these processes would contribute a large mass of H₂O.

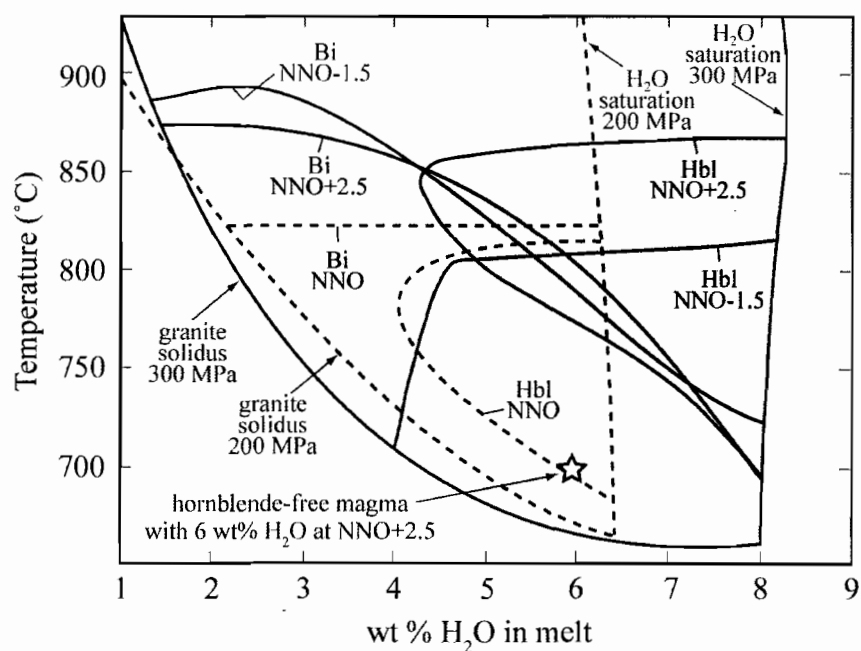


Figure 4. Experimental hornblende and biotite stability at 300 MPa (solid lines) and $f_{O_2} = \text{NNO}-1.5$ and $\text{NNO}+2.5$ (Dall'Agnol et al., 1999); and 200 MPa (dashed lines) and $f_{O_2} = \text{NNO}$ (Klimm et al., 2003). Stability of hornblende (Hbl) and biotite (Bi) at highly oxidized conditions of porphyry copper-forming environments, $\text{NNO}+2.5$, are shaded dark grey (hornblende) and light grey (biotite).

If granitic melts in this region do not derive H_2O largely from the country rock then a subduction component is required to produce such high magmatic H_2O concentrations. Humphreys et al. (2003) suggest that the flat-slab subduction geometry of the western United States during the Late Cretaceous caused slab de-watering far inland from the subduction trench leading to hydration of the base of the continental lithosphere beneath the Rocky Mountains. Low-angle subduction geometries have been suggested as favorable for porphyry deposit formation owing to potential for mantle wedge metasomatism, increased flux of sulfur and oxidized metal bearing fluids, and transpressional tectonism. This style of tectonism promotes crustal magmatism without frequent eruption so that magmatic volatiles are accumulated at depth and are transferred to the overlying hydrothermal system (Cooke et al., 2005; Richards, 2003). We speculate that the hydrated lithosphere during Late Cretaceous flat-slab subduction beneath Butte,

Montana, could account for the generation of a H₂O-rich parental magma that produced the deep porphyry Cu-Mo deposit.

CO₂ AND H₂O CONTROLS ON PORPHYRY DEPOSIT FORMATION DEPTH

Formation of porphyry copper deposits requires a large volume of exsolved fluid (~25 km³ H₂O for Butte, MT; Reed, unpublished) to initiate hydrofracturing and transport silica, sulfur, and metals. The CO₂ and H₂O solubility and crystal fractionation models we apply indicate that magma exsolves a large mass of fluid only after CO₂ fluid has largely degassed and H₂O-rich fluid begins to exsolve. Published volatile analyses of deep fluid inclusions representative of exsolved porphyry magma fluids from eight different porphyry-Cu-Mo deposits indicate that these fluids are CO₂-poor (<10 mol% CO₂; Graney and Kesler, 1995; Redmond, 2002; Rusk et al., 2008). These data support the hypothesis that ideal porphyry formation conditions occur after the parental magma has exsolved most of its CO₂. Without melt inclusion data, it is difficult to estimate the initial magma CO₂ or H₂O content, but we do know that the initial magma CO₂ content controls the depth at which magma initially becomes fluid saturated and how much crystallization or decompression must occur before exsolved fluid becomes H₂O-rich. The pressure at which CO₂-degassed magma saturates with a large mass of H₂O-rich fluid controls the depth at which porphyry copper deposits may form.

Whether porphyry-forming magma becomes fluid saturated due primarily to isobaric crystallization or polybaric decompression is debatable. However our preferred model of porphyry magma generation (Fig. 1) incorporates a large silicic magma body (~100 km³ for Butte, MT; Reed, unpublished) that is comprised of an isobarically degassing crystal mush pile (Bachmann and Bergantz, 2004) that exsolves a large mass of fluid that charges an overlying fluid-enriched granitic cupola containing ~25-30% crystals. While the cupola may convect (Shinohara and Kazahaya, 1995) allowing ~2 km of polybaric degassing (Figs. 1 and 2), we suggest that isobaric crystallization is the primary processes leading to hydrofracturing and porphyry dike injection. If this is the case, then the initial magma H₂O concentration plays a key role in determining the depth

at which CO_2 degassed magma is saturated with nearly pure H_2O fluid, and thus the depth at which silicic plutons and dikes are emplaced and where porphyry deposits may form.

Our model results show a positive correlation between deposit depth and parent magma H_2O content, and independent methods of determining magma volatile contents and deposit formation depths are consistent with the model estimates (Fig. 5). The Butte deposit has long been thought of as anomalously deep compared to other porphyry deposits. But we suggest that the parental Butte magma was on the H_2O -rich end of typical rhyolitic magmas for the reasons discussed above, and therefore it became saturated with an H_2O -rich fluid at greater depth than other porphyry deposits.

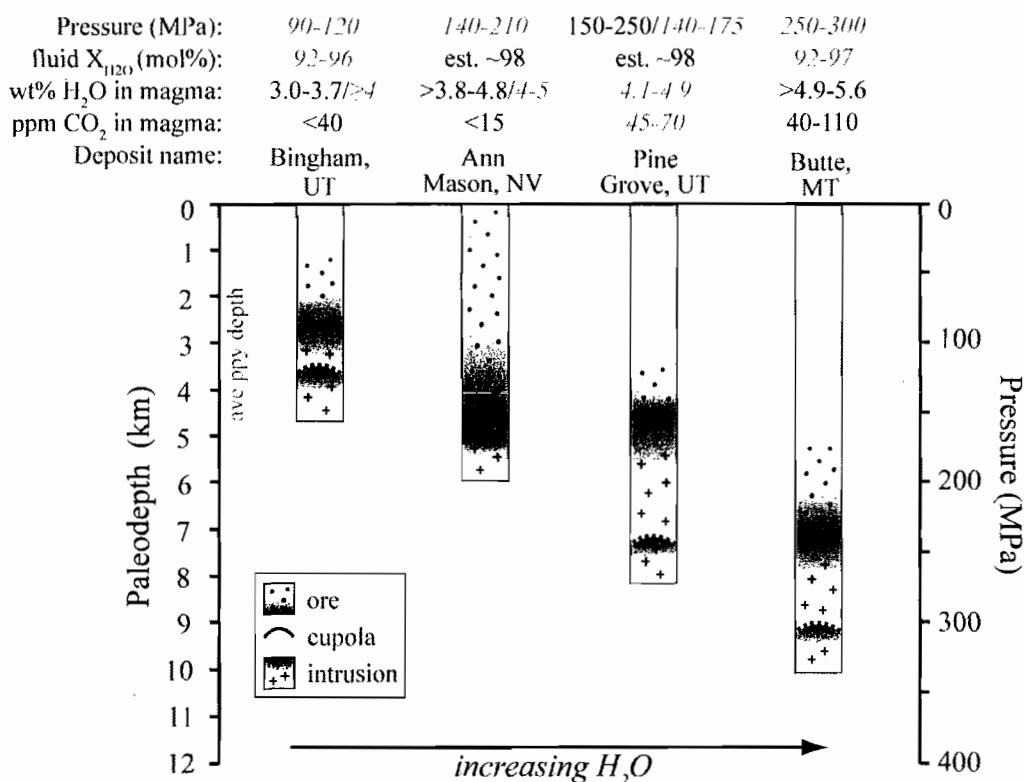


Figure 5. Schematic depth profile for porphyry deposits in this study. Formation pressures, fluid compositions, and bulk magmatic CO_2 and H_2O contents are listed above. Modeled variables are shown in black text while estimates from other studies are shown in grey italics (see text for references). Dashed cupola lines indicate estimated range of cupola depths. Shaded background indicates average inferred porphyry depth (Seedorff et al., 2005).

We consider Butte to represent the deep, H₂O-rich endmember of known porphyry deposits, however it is not extraordinarily H₂O-rich in comparison to other known rhyolitic magmas. The CO₂ and H₂O solubility and crystal fractionation models discussed here provide a simple framework for understanding the depths at which a large mass of fluid accumulates within upper crustal magma chambers. Additionally, they provide a model for understanding the depths at which hydrofracturing and porphyry formation are likely to occur and may explain why the deposit at Butte, Montana, formed at such great depth.

BRIDGE

In Chapter III, I described the controls of CO₂ and H₂O fluid saturation in granitic magma on the formation depth of porphyry style hydrothermal systems in the upper arc crust. In the following chapter, I discuss the magmatic-hydrothermal transition at porphyry copper deposits in more detail by assessing the temperature relationship between the two realms.

CHAPTER IV

THE TEMPERATURE CONNECTION BETWEEN MAGMATIC AND HYDROTHERMAL REALMS OF THE PORPHYRY-Cu-Mo DEPOSIT AT BUTTE, MONTANA

This chapter is in preparation to be submitted to the *Journal of Volcanology and Geothermal Research*. This paper was co-authored with Mark H. Reed, who provided advising, editorial support, and funding for this project.

1. Introduction

1.1. Porphyry ore deposits

It has long been recognized that the stockwork vein system of porphyry-style Cu-Mo mineralization is closely linked to a magmatic system at depth. Decades of studies of porphyry deposits from around the world reveal an intimate spatial and genetic relationship among magma chamber cupolas, porphyry dikes, mineralized breccias, zones of alteration, and mineralized stockwork veins (Burnham, 1979; Dilles, 1987; Seedorff et al., 2005; Sillitoe, 1973). A schematic cross section (Fig. 1) shows these established relationships as well as inferred isotherms for a typical porphyry deposit (Hedenquist and Lowenstern, 1994; Seedorff et al., 2005). Despite recognition of this close magmatic-hydrothermal relationship in porphyry systems, much remains unknown about the magmatic-hydrothermal connection.

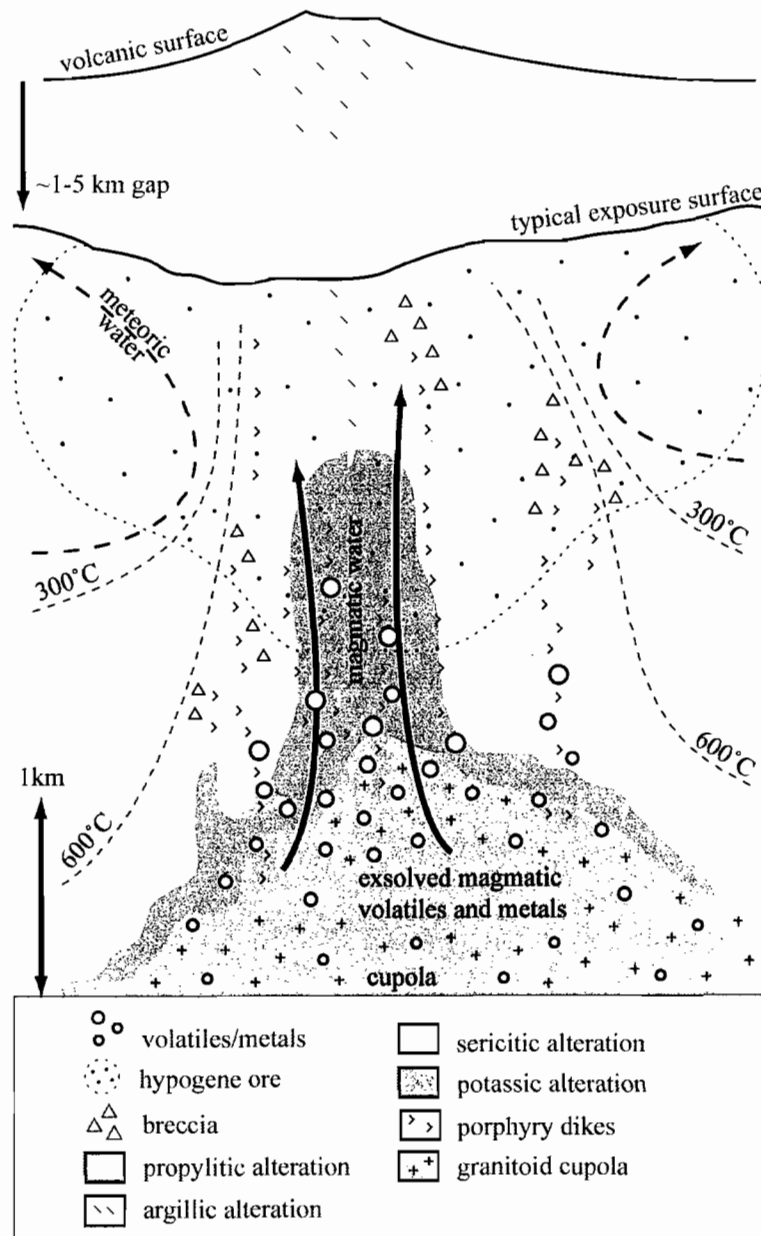


Fig. 1. Schematic cross section of a porphyry deposit showing exsolution of magmatic vapors from a cupola, porphyry dikes, magmatic and meteoric H₂O-rich fluid flow paths, breccias, hydrothermal alteration zones, ore deposition zone, and inferred isotherms (modified from Seedorff et al., 2005 and Hedenquist and Lowenstern, 1994).

Previous work on porphyry deposits has left a thermal gap between magmatic (i.e., fluid source) and hydrothermal vein formation conditions. Temperature estimates of rhyolitic porphyry magma range from 700 to 800°C and come from thermobarometry studies on dikes from the porphyry-Cu deposit at Santa Rita, New Mexico (Audétat and Pettke, 2006), granitic phase equilibrium experiments (e.g., Bogaerts et al., 2006; Dall'Agnol et al., 1999; Holtz et al., 2001; Holtz et al., 1992; Klimm et al., 2003; Naney, 1983; Tuttle and Bowen, 1958), and by analogy with other rhyolitic systems (Wark et al., 2007). By contrast, many studies of hydrothermal veins suggest vein formation temperatures between 500 and 650°C, cooler than temperature estimates for typical rhyolitic magmas (Bowman et al., 1987; Brimhall, 1977; Field et al., 2005; Redmond et al., 2004; Reed et al., 2005; Roberts, 1975; Rusk et al., 2006; Seedorff et al., 2005), with vein temperatures >650°C only recorded for deposits with dacitic porphyry compositions (Ulrich et al., 2002).

In this study we examine the thermal relationship between the magmatic and hydrothermal parts of the porphyry-Cu-Mo deposit at Butte, Montana using three independent mineral geothermometers utilizing magmatic and hydrothermal quartz (Wark and Watson, 2006), rutile (Watson et al., 2006), and biotite (Henry et al., 2005). We investigate the temperature profile of the deposit and assess the timing of vein formation relative to alteration of vein envelopes. Finally, our new temperature estimates enable reassessment of previous fluid inclusion-based geobarometry.

1.2. Geologic background of Butte, MT

The porphyry-Cu-Mo deposit at Butte has been well described in studies spanning more than 100 years (e.g., Brimhall, 1977; Meyer et al., 1968; Roberts, 1975; Rusk et al., 2008b; Sales, 1914; Weed, 1912), making it an excellent location to investigate the magmatic-hydrothermal aspects of a porphyry deposit. Ten deep drill holes, underground mine workings, and two open pits provide a comprehensive suite of samples for study. In addition, the Continental Fault has upthrown a block of the deposit by ~1,300 m in the

eastern part of the district (Meyer et al., 1968) allowing sampling very deep within the deposit.

The porphyry deposit at Butte is hosted by the 77-75 Ma Butte granite (Fig. 2; Lund et al., 2002), previously referred to as the “Butte Quartz Monzonite” (see discussion in O’Neill et al., 2002), which makes up over 75% of the exposed Boulder Batholith (Doe et al., 1968). This Cretaceous batholith intruded into Archean metamorphic basement, Proterozoic, Paleozoic, and Mesozoic marine sedimentary rocks, Mesozoic continental sedimentary rocks, and late Cretaceous calc-alkaline volcanic rocks (Klepper et al., 1971; Vejmelek and Smithson, 1995). The Butte granite is remarkably homogenous throughout the district (Doe et al., 1968; Smedes, 1973; Smedes et al., 1973) providing a uniform starting place to evaluate features of the Butte porphyry deposit itself.

Within the Boulder Batholith, quartz porphyry dikes that cut the Butte granite (Fig. 3a) are unique to the Butte mining district. Porphyry dikes are significantly younger (by ~10 Ma) than the Butte granite and represent a separate magmatic event (Lund et al., 2002). The number and duration of dike intrusions are not well constrained, nor is the source stock or cupola from which these dikes emanated, however, the deepest drill holes (2 km) intersect a porphyry-rich zone in the center of the district that may be the uppermost portion of a cupola. Regardless of their heritage, these dikes have long been thought to be genetically related to the early porphyry-style mineralization in the district based on crosscutting relationships between porphyry dikes and mineralized veins (Brimhall, 1973; Meyer et al., 1968). Among the Butte porphyries, the Steward-type dikes are a prominent set that strike approximately east-west (Fig. 3a), dip steeply to the south, and range in thickness from 3-15 m. U-Pb ages suggest that Steward-type dikes are 66 Ma (Lund et al., 2002). The northernmost quartz porphyry dike in the district, the Modoc, widens into a steeply plunging irregular plug reaching a maximum width of 300 m (Fig. 3a; Meyer et al., 1968). U-Pb ages suggest the Modoc plug is 64 Ma (Dilles et al., 2003), intruding after pre-main stage porphyry-Cu-Mo mineralization but before the main stage base metal lode mineralization. All quartz porphyries are cut by main stage veins (Meyer et al., 1968).

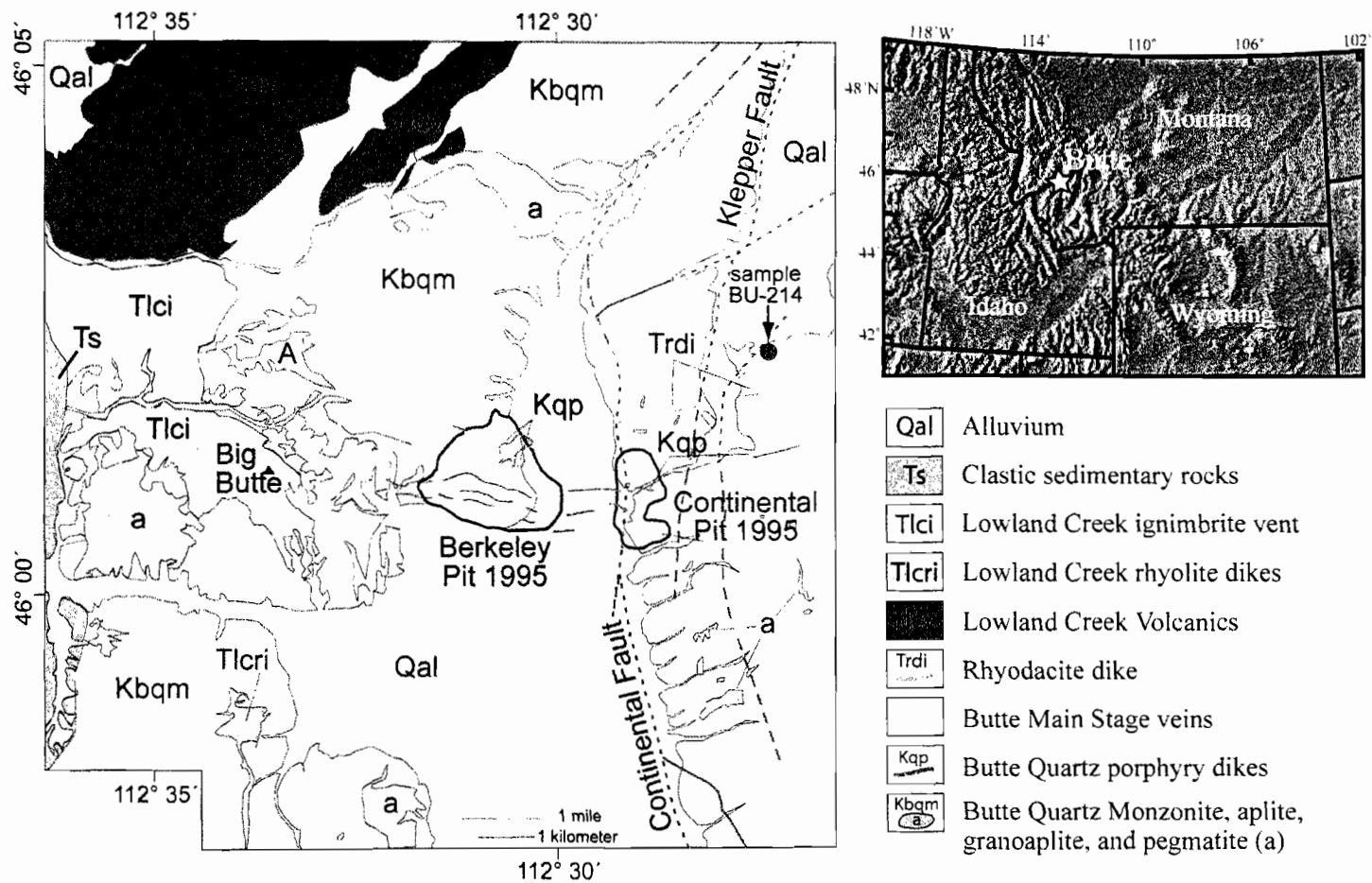
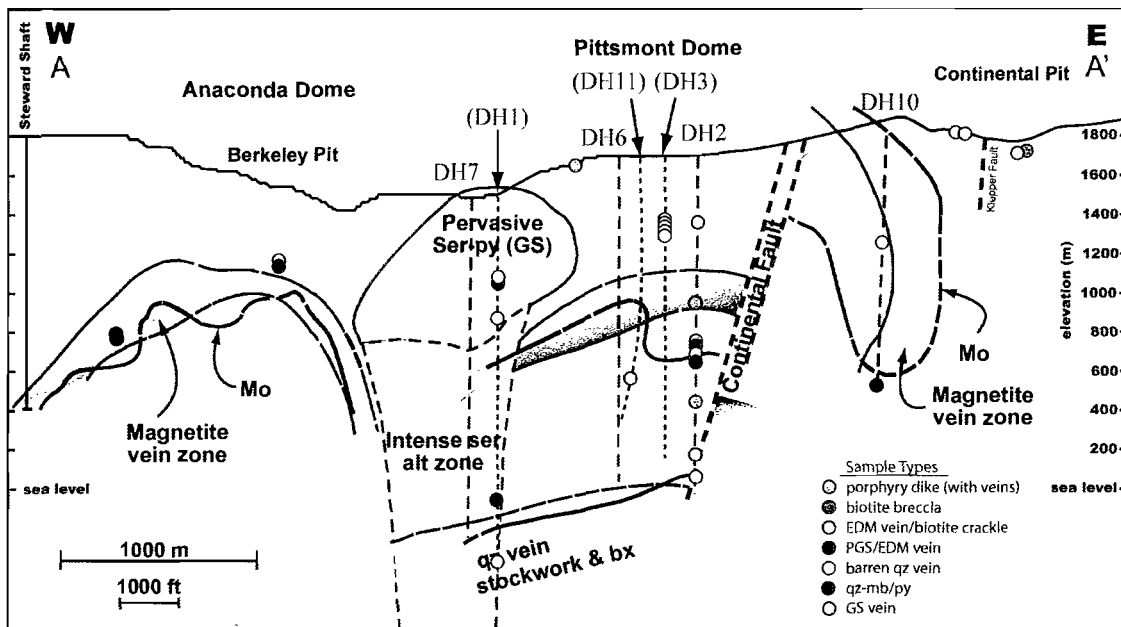
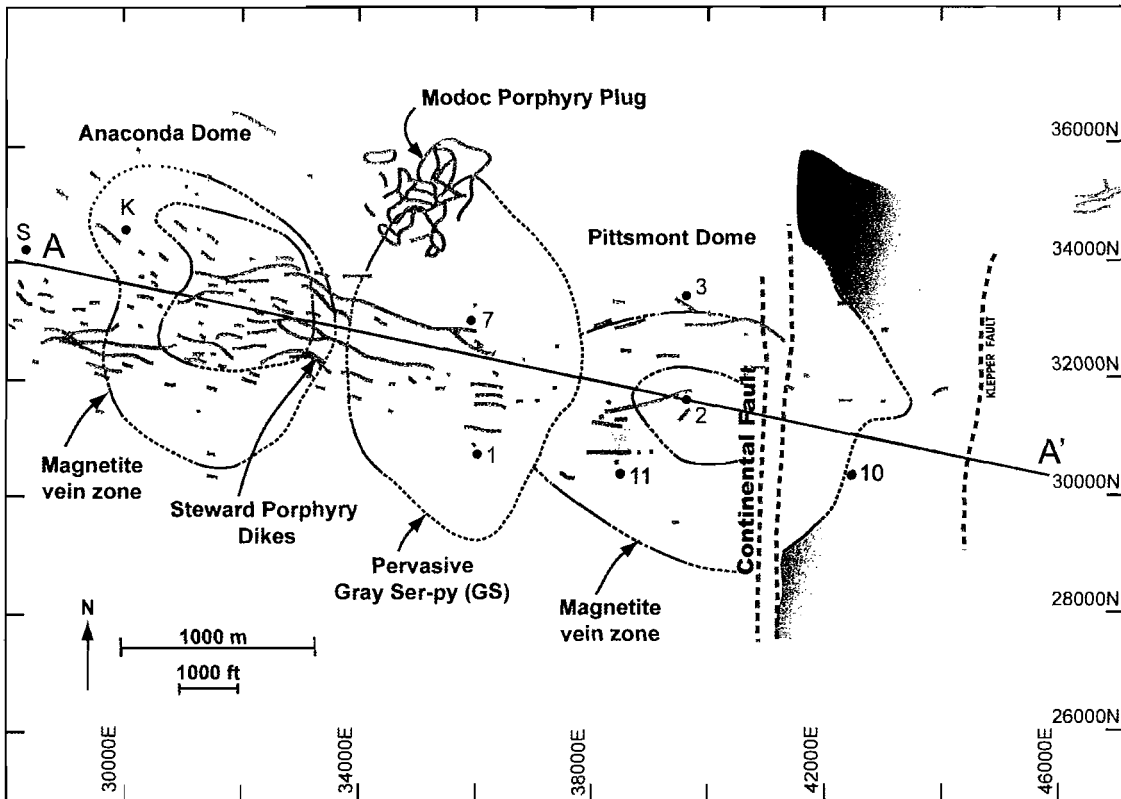


Fig. 2. Location map and regional geologic setting of the Butte district (modified from Rusk et al., 2008b). Fresh Butte granite sample, BU-214, is shown with red circle.

Fig. 3. Maps of porphyry dikes, pre-main stage mineralization, and sample locations. (a) The subsurface trace of porphyry dikes mapped at all depths is shown projected on one plane with orange lines. The subsurface position of pre-main stage mineralization centers are shown in purple for the Anaconda and Pittsmont dome copper centers. Separating the two porphyry-Cu mineral centers in the subsurface is a zone of pervasive sericitic alteration, shown in yellow. The deep drill holes (DH) sampled in this study are numbered. The locations of two mine shafts are also shown: S = Steward, K = Kelly. Cross section A-A' is shown below. (b) East-west cross section (A-A') of pre-main stage porphyry Cu-Mo mineralization at Butte. To the west is the Anaconda dome and to the east is the Pittsmont dome. These domes are defined by a zone of abundant magnetite veins (purple) and by Mo grade contours (blue lines). The Continental Fault displaces the Pittsmont dome upward by ~1,300 m (Meyer et al., 1968). Dashed lines indicate drill holes and mine shafts (those in parentheses indicate holes projected into this cross section). Colored circles show sample locations for this study.



Mineralization at Butte formed in two distinct stages during a time interval of ~4 Ma. The “pre-main stage” porphyry-Cu-Mo system likely formed between 66 and 64 Ma, overlapping with Steward-type porphyry dike emplacement (Dilles, personal communication). The large “main stage” base metal lode veins containing Cu-, Zn-, Pb-, and Ag-sulfides formed later, from 63 to 62 Ma (Snee et al., 1999; Dilles, personal communication). While the names “pre-main stage” and “main stage” suggest that these are part of a single, overlapping mineralized system, the genetic relationship between the two remains debatable and they may represent a continuum of mineralization (Rusk et al., 2008b) or they may be two genetically distinct pulses of mineralization (Lund et al., 2002). The pre-main stage porphyry-Cu-Mo system is the focus of this study.

Pre-main stage Cu and Mo mineralization lies in two zoned domes that are ~2 km in diameter (Fig. 3; Reed, 1999). These zoned domes were apparently produced by a single magmatic fluid that changed pressure, temperature, and pH conditions as it ascended (Reed et al., 2005). The shapes of the Anaconda and Pittsmont domes are defined by magnetite-bearing vein zones and Mo grade contours (Fig. 3). Between these two domes is a 1.2 km bulb shaped zone of intense pyrite-quartz veins with pervasive grey sericitic (GS) alteration that extends downward more than 2 km. All three bodies are superimposed among a porphyry dike swarm (Fig. 3a).

The contacts of the quartz porphyry dikes are sinuous with some brecciation of the Butte granite host rock. Dikes are often bound by chalcopyrite-bearing biotite breccias that stream into biotite crackle veinlets that emanate away from porphyry dikes, and constitute the earliest Cu mineralization. Both the Anaconda and Pittsmont domes have typical porphyry-style concentric, overlapping alteration zones around stockwork veins. The innermost zone in the Pittsmont dome consists of barren quartz veins with minor molybdenite and K-feldspar alteration. The Butte granite and porphyry dikes are intensely sericitized in this zone. Barren quartz veins grade upward and outward into quartz-molybdenite veins which generally do not contain alteration envelopes. Quartz-molybdenite veins cut veins of the next outward zone which consists of quartz-chalcopyrite-pyrite veins with early dark micaceous (EDM) biotite-K-feldspar-sericite

alteration envelopes (Brimhall, 1977; Meyer, 1965). EDM dominant alteration grades upward and outward into abundant quartz-chalcopyrite-magnetite veins with pale-green sericitic (PGS) sericite-K-feldspar-chlorite alteration envelopes (Reed, 1999; Reed et al., 2005). Both EDM and PGS veins are cut by barren quartz and quartz-molybdenite veins in the Anaconda and Pittsmont domes. Above the PGS zone, is a zone of sparse quartz-pyrite-chalcopyrite veins with chlorite-sericite-K-feldspar alteration envelopes (Geiger et al., 2002; Reed, 1999). Pyrite-quartz veins with grey sericitic (GS) alteration in the central bulb cut all other pre-main stage vein types throughout the district. The outermost alteration zone contains K-feldspar-sericite-chlorite-epidote propylitic alteration with sphalerite and galena (Reed, 1999; Reed et al., 2005).

1.3. Petrography of igneous and hydrothermal rocks

Butte granite

The Butte host granite contains ~65 wt% SiO₂ and is generally equigranular with isolated dikes of aplite and pegmatite scattered throughout. It contains 35-40 vol% plagioclase and roughly equal amounts of K-feldspar and quartz, totaling 40-45 vol%. The remaining 15-20 vol% is comprised of biotite, hornblende, magnetite, minor sphene, and trace amounts of ilmenite, zircon, apatite, pyroxene, tourmaline, and armalcolite (Meyer et al., 1968; Roberts, 1975). Some Butte granite that appears fresh in hand sample has been affected by widespread “early pervasive” alteration (Roberts, 1975). This slightly altered granite contains relict recrystallized biotite, secondary “shreddy” biotite replacing hornblende, K-feldspar partially converted to plagioclase, sphene converted to Fe-Ti oxides and quartz, and minor disseminated sulfides and anhydrite (Roberts, 1975).

Porphyry dikes

Quartz porphyry dikes are high-silica rhyolites with 72 wt% SiO₂ (Dilles, unpublished), however it is difficult to constrain their composition precisely due to abundant hydrothermal alteration. Dikes contain 25-30 vol% phenocrysts comprised

dominantly of euhedral K-feldspar and plagioclase, 5 vol% rounded and resorbed quartz eyes, and <3 vol% small biotite books within a fine-grained, tan groundmass of quartz and alkali feldspar (Brimhall, 1973; Meyer et al., 1968).

Biotite breccias and biotite crackles

Chalcopyrite and pyrite bearing biotite breccias bounding the margins of porphyry dikes represent the earliest recognized pre-main stage Cu mineralization (Brimhall, 1977). However, several biotite-bearing breccias from the Continental and Berkeley Pits contain fragments of quartz veins, indicating that deep vein formation began before all porphyry dikes had intruded (Rusk et al., 2008b). Biotite breccias range from centimeters to >3 m in width and contain fragments with rounded quartz eyes and euhedral alkali feldspar phenocrysts in a fine-grained groundmass of secondary biotite, alkali feldspar, chalcopyrite, pyrite, and blocky rutile.

Biotite “crackles”, or 1-2 mm veinlets, stream away from biotite breccias and porphyry dikes (Brimhall, 1977) and persist outward even into the distal propylitic alteration zone. They contain secondary quartz, alkali feldspar, biotite, anhydrite, chalcopyrite, pyrite, magnetite, and blocky rutile.

Early dark micaceous veins

Early dark micaceous (EDM) veins are 3-10 mm wide with an envelope that is generally 2 to 3 times the width of the vein. The veins contain secondary quartz, K-feldspar, anhydrite, with sparse chalcopyrite, pyrite, magnetite, and rutile (“whisker-like”, Fig. 7a, and blocky, Fig. 7b and c). Alteration envelopes contain secondary shreddy biotite, alkali feldspar, magnetite, blocky rutile, chalcopyrite, and pyrite (Brimhall, 1973; Roberts, 1975). At shallow levels the distinction between EDM, barren quartz, and quartz-molybdenite veins is clear, while at deeper levels within the quartz-rich core the distinction is vague. In shallower EDM veins the EDM envelopes are much more developed and the veins generally contain more pyrite, chalcopyrite, and magnetite than do deeper EDM veins.

Pale green sericitic veins

Overlapping some EDM veins and extending upwards and outwards from the EDM-rich zone are pale green sericitic (PGS) veins which contain magnetite, chalcopyrite, pyrite, and quartz. Alteration envelopes are dominated by K-feldspar, quartz, green sericite, chlorite, and minor calcite (Reed, 1999). PGS veins typically have wider alteration envelopes (5 cm) than other vein types and occur at shallower levels, coinciding with the zone of highest pre-main stage Cu grade.

Barren quartz and quartz-molybdenite veins

Barren quartz veins are most abundant in the core of the deposit and they grade into quartz-molybdenite veins upward and outward towards the EDM zone. Most barren quartz veins contain traces of molybdenite and many grade into quartz-molybdenite veins. Alteration envelopes are absent from most veins of these types, but some have mm-scale K-feldspar alteration envelopes. Both types cut each other at all levels of the deposit and they cut EDM and PGS veins at shallower depths. A few deeper samples are cut by EDM veins. At depth both barren quartz and quartz-molybdenite veins contain anhydrite, K-feldspar, calcite, and rutile (whisker-like and blocky) while shallower veins contain quartz, molybdenite, pyrite, and rutile.

Pyrite-quartz grey sericitic veins

Pyrite-quartz veins with grey sericitic (GS) alteration are dominant in the shallowest levels of the deposit and in the interior bulb-shaped zone of intense sericitic alteration. GS veins cut all other vein types except main stage. Veins are dominantly pyrite with lesser quartz, and envelopes contain muscovite, quartz, pyrite, rutile (whisker-like and blocky), and colorless chlorite. Original Butte granite biotite is absent in GS envelopes near pyrite-quartz veins but relict biotite is present in the outer margins of many GS envelopes.

2. Methods

We described and analyzed 33 samples of the Butte igneous and hydrothermal system. Igneous samples include fresh Butte granite and Steward-type and Modoc porphyries (Table 1, Fig. 3). Hydrothermal samples include biotite breccias from the margin of porphyry dikes, biotite crackles that stream away from biotite breccias, and pre-main stage veins including early dark micaceous, pale green sericitic, barren quartz, quartz-molybdenite, quartz-molybdenite-pyrite, and pyrite-quartz grey sericitic (Table 1, Fig. 3b). Most samples are from deep drill holes in the Pittsmont dome and the adjacent pervasive sericitic alteration zone in the center of the district at depths from 350 to 2070 m below the surface. The deepest core samples represent the quartz vein stockwork with abundant porphyry dikes that are interpreted to be from near the top of the inferred cupola. Five samples of the Pittsmont dome are from the Continental and Berkeley pits and four are from underground drill holes in the Anaconda dome at depths of 400 to 1000 m below the surface.

We characterized samples by petrographic microscope and scanning electron microscope (SEM), and then measured major and trace elements in quartz and rutile by electron microprobe. We applied three independent mineral geothermometers including Ti-in-quartz, Zr-in-rutile, and Ti-in-biotite. Finally, we performed fluid inclusion microthermometry with quartz from a subset of samples.

2.1. SEM analyses

We carried out SEM imaging at the University of Oregon using an FEI Quanta 200 FEG scanning electron microscope equipped with an Oxford Instruments cathodoluminescence (CL) detector and a Thermo EDS detector. Polished 200 μm thick sections were carbon coated (15-20 nm) and analyzed at 10 keV with a beam current of 0.5-5 nA for quartz, and 15-20 keV with a beam current of 2-8 nA for rutile and zircon. We collected more than 300 SEM-CL images of plutonic, igneous, and hydrothermal

Table 1
Sample locations and types

Location	Sample no.	Location Description	Depth below surface (m)	Elevation (m)	Host rock	Vein//alteration type
<i>West of CF</i>						
Anaconda	10772-32a	Kelly Shaft, 3400' level	1037	763.4	BG	qz-py-cp//PGS/EDM
Anaconda	10778-6	Kelly Shaft, 3400' level	1037	763.4	BG	qz-mt//PGS/EDM
Pittsmtont	11185-3771	DH 11	1150	553	BG	qz-cp//EDM cut by qz-cp-py//NA
Pittsmtont	11135-2470	DH 2	753	965	Steward ppy	py-qz//GS
Pittsmtont	11135-3481	DH 2	1061	656.9	BG	qz-py-cp//EDM
Pittsmtont	11135-3568	DH 2	1088	630.4	BG	qz-py-cp//PGS/EDM
Pittsmtont	11135-3586	DH 2	1093	624.9	BG	qz-py-cp//EDM
Pittsmtont	11135-3597	DH 2	1097	622	BG	bi crackles cut by qz-mb//NA
Pittsmtont	11135-2-4209	DH 2	1283	435	Steward ppy	qz-mb//NA cut by barren qz//NA
Pittsmtont	11135-5051	DH 2	1540	178	BG	qz-py-cp//EDM
<i>Pervasive GS zone</i>						
Central GS zone	10969-1571c	DH 1	479	1217	BG	py-qz//GS/SBr
Central GS zone	10969R-2075	DH 1	633	1063	BG	py-qz//GS
Central GS zone	10969-2101	DH 1	641	1055	BG	py//GS cut by qz-mb-py//GS
Central GS zone	10969-2665	DH 1	813	884	BG	py-qz-op//GS cut by qz-mb-py//NA
Central GS zone	10969-5699	DH 1	1738	-41	aplite	qz-mb//NA
<i>Quartz vein stockwork</i>						
Central	10969-6804	DH 1	2074	-378	aplite	qz-mb//NA cut by qz//NA
Pittsmtont	11135-5461	DH 2	1665	53	aplite	qz//NA
<i>Shallow GS</i>						
Anaconda	F2033-488	DH F2033	402	1168	BG	qz-py-cp//EDM
Anaconda	F2033-513	DH F2033	405	1165	BG	qz-mb//NA cut by qz-mb//NA
Pittsmtont	11067-1	5480 bench	0	1670	Modoc ppy	none
Pittsmtont	11148-1141	DH 3	348	1372	BG	py-qz//GS/SBr
Pittsmtont	11148-1169.4	DH 3	356	1364	BG	py-qz//GS/SBr
Pittsmtont	11148-1197	DH 3	365	1355	BG	py-qz//GS/SBr
Pittsmtont	11148-1293	DH 3	394	1326	BG	py-qz//GS/SBr
Pittsmtont	11148-1300	DH 3	396	1324	BG	py-qz//GS/SBr
Pittsmtont	11135-1150	DH 2	351	1368	BG	qz-py-cp//EDM
<i>East of CF</i>						
Pittsmtont	11172-1847	DH 10	563	1247	BG	bi crackles cut by qz//NA
Pittsmtont	11172-4247	DH 10	1295	515	BG	qz-mb//NA
Pittsmtont	BUR-03-213	6080 bench	0	1853	BG	bi crackles
Pittsmtont	BUR-03-214	6080 bench	0	1853	BG	qz-py//EDM
Pittsmtont	BU96MR-11	5680 bench	0	1731	BG	bi breccia
Pittsmtont	BUR98-13	5480 bench	0	1670	BG	bi crackles
Pittsmtont	BU-214	Road cut, 46°02'26"N 112°27'25"W	0	2072	BG	fresh

Abbreviations: CF = Continental Fault, DH = drill hole, BG = Butte granite, ppy = porphyry, qz = quartz, py = pyrite, cp = chalcopyrite, mb = molybdenite, bi = biotite, op = open, PGS = pale green sericitic, EDM = early dark micaceous, GS = grey sericitic, NA = no alteration, SBr = sericite with remnant biotite.

quartz with corresponding SEM-backscattered electron (BSE) and secondary electron (SE) images. The CL image brightness is a function of operating conditions such as carbon coat thickness, beam conditions, bias, and gain, which we kept nominally constant except for the beam current, which we had to change depending on the luminosity of the quartz. For the following discussion, relative CL brightnesses are described as CL-dark, CL-grey, and CL-bright. We identified rutile and zircon using SEM-energy dispersive spectrometry (EDS) and we collected over 100 SEM-BSE images of these minerals.

2.2. Microprobe analyses

Trace element concentrations in quartz and rutile were measured at the University of Oregon using a Cameca SX-100 electron microprobe operated using two setups optimized for Ti in quartz and Zr in rutile. Quartz was analyzed using a 15 keV accelerating potential, a 200 nA beam current, and a 20 μm spot size. Ti was measured simultaneously on two spectrometers with LPET and PET crystals while Fe, K, and Al were measured on the remaining spectrometers. The “aggregate intensity” technique (Lowers et al., in review) was applied using Probe for Windows software to improve Ti counting statistics. Ti, Fe, K, and Al were counted for 600 s on-peak and 600 s off-peak. Synthetic rutile was used as a Ti standard, synthetic magnetite was used for Fe, and natural orthoclase was used for K and Al. To reduce systematic continuum artifact errors, a matrix “blank” correction was applied to Ti data using a synthetic quartz standard as a Ti-free blank (Lowers et al., in review). Detection limits (99% confidence) achieved on spot analyses are 3 ppm for Ti, 12 ppm for Fe, 11 ppm for K, and 6 ppm for Al. We avoided analyzing quartz within 100 μm of rutile whiskers to avoid excitation of Ti atoms by Bremsstrahlung radiation (e.g., Wark and Watson, 2006), and consequent erroneously high Ti concentrations in quartz analyses contaminated by rutile were easily identified and eliminated.

Rutile was analyzed using a 15 keV accelerating potential, a 200 nA beam current and a <1 μm spot size, which was required because some crystals were very small (<5

μm). Zr was measured simultaneously using two spectrometers with LPET and PET crystals while Fe and W were measured on one spectrometer, and Nb and Ta were measured on the remaining spectrometers. As for quartz, the “aggregate intensity” technique (Lowers et al., in review) was also applied to improve Zr counting statistics. Zr, Ta, and Nb were counted for 300 s on-peak and 300 s off-peak while Fe was counted for 120 s on-peak and 120 s off-peak and W was counted for 180 s on-peak and 180 s off-peak. Synthetic zircon was used as a Zr standard, synthetic magnetite was used for Fe, and pure metals were used for W, Nb, and Ta standards. Interference corrections were required for the Zr $L\alpha$ and Ta $M\alpha$ lines. Matrix “blank” corrections were applied for both Zr and Ta data using a synthetic TiO_2 standard as a Zr-free blank (Lowers et al., in review). Calculated detection limits (99% confidence) on spot analyses are 11 ppm for Zr, 27 ppm for Fe, 130 ppm for W, 52 ppm for Nb, and 34 ppm for Ta.

We made no new analyses of biotite, but used unpublished analyses provided by Dr. A. Soule and Dr. L. Zhang who used a Cameca SX-50 electron microprobe at the University of Oregon and Oregon State University, respectively. We supplemented these analyses with additional biotite analyses from Roberts (1975).

2.3. Mineral geothermometry

Ti-in-quartz thermometry

We employed the experimentally calibrated TitaniQ geothermometer of Wark and Watson (2006) to calculate quartz precipitation temperatures. Rutile is not present in the plutonic quartz, so we assumed an activity of TiO_2 (a_{TiO_2}) of 0.6 based on activities for similar silicic magma systems determined by equilibria among coexisting FeTi oxides (Wark et al., 2007) and by an experimentally determined TiO_2 saturation model for rhyolite (Hayden and Watson, 2007). While whisker-like rutile ($\sim 20 \mu\text{m}$ long) is present in all porphyry quartz, suggesting rutile saturation ($a_{\text{TiO}_2}=1.0$), the porphyry magma was unlikely to be saturated with rutile due to its low TiO_2 content (Hayden and Watson, 2007). We therefore consider that rutile grew during subsequent hydrothermal alteration

of these samples which is supported by the abundance of fluid inclusions within porphyry quartz eyes. Hence we used $a_{\text{TiO}_2}=0.6$ for the porphyry quartz calculations as well. Rutile whiskers and blocky rutile ($<50\mu\text{m}$) occur in the biotite breccia, biotite crackles, and all hydrothermal veins and so we used $a_{\text{TiO}_2}=1.0$ for all calculations of hydrothermal quartz. Assuming an a_{TiO_2} of 1.0 gives a minimum temperature estimate and the use of an a_{TiO_2} of 0.6 increases the calculated temperature by $\sim 50^\circ\text{C}$.

Ti is known to diffuse $\sim 15\mu\text{m}$ in quartz at 600°C over a million years (Cherniak et al., 2007), which changes the original Ti concentration and thus the significance of the temperatures we calculate. By using a microprobe beam spot size of $20\mu\text{m}$, we average the diffusional alteration of Ti concentrations and thus we consider the effects of diffusion negligible.

Zr-in-rutile thermometry

We calculated hydrothermal rutile precipitation temperatures using the experimentally calibrated thermometer of Watson et al. (2006). Most analyses of rutile in veins and alteration envelopes were near the locations of analyzed quartz. Zircon grains, mostly $<20\mu\text{m}$ in size, were identified in 60% of the samples. The small grain size made it difficult to find zircon in all samples, but given that silicic rocks of this kind ubiquitously contain zircon (Watson et al., 2006) we assume that all samples contained zircon. Thus the chemical potential of ZrO_2 in the system is essentially fixed by zircon-quartz equilibrium, making this geothermometer quite robust.

Ti-in-biotite thermometry

We used the empirical Ti-in-biotite geothermometer of Henry et al. (2005) to calculate plutonic and hydrothermal biotite precipitation temperatures. Biotite compositions from Butte samples fall within the calibrated compositional, temperature, and pressure range specified for the geothermometer ($X_{\text{Mg}}=0.275-1.000$, $\text{Ti}=0.04-0.60$ apfu, $T=480-800^\circ\text{C}$, and $400-600\text{ MPa}$). We normalized biotite analyses on an

anhydrous basis with 22 oxygens to determine the Ti atoms per formula unit (apfu) (Henry et al., 2005).

2.4. Fluid inclusion microthermometry

Microthermometry of fluid inclusions was completed using a Fluid Inc.-adapted U.S. Geological Society Gas-Flow Heating/Freezing System at the University of Oregon. Thermocouples were calibrated at -56.6°, 0.0°, and 374.1°C using synthetic fluid inclusions. The precision of temperature measurements on heating cycles is $\pm 2^\circ\text{C}$. Ice-melting temperatures were observed at a heating rate of $< 1^\circ\text{C}/\text{s}$ and homogenization temperatures were observed at a heating rate of $\leq 2^\circ\text{C}/\text{s}$. Clathrates were observed in 14% of the inclusions. Hydrohalite was observed in high salinity inclusions at approximately -20°C upon heating without cycling. Salinities, CO_2 contents, and fluid densities of inclusions that formed clathrate upon cooling were estimated using the program ICE (Bakker, 1997) and the data of Duan et al. (1992a; 1992b). The same properties of inclusions that did not form clathrates upon cooling were estimated using the program BULK (Bakker, 2003) and the data of Archer (1992). Salinities of inclusions for which we could not measure homogenization temperatures were estimated using the data of (Bodnar et al., 2003), which do not account for CO_2 and thus provide maximum salinity estimates. Isochores were calculated using the program ISOC (Bakker, 2003) and the data of Anderko and Pitzer (1993a; 1993b) and Duan et al. (1995).

3. Results

3.1. Plutonic, porphyry, and hydrothermal quartz

CL textures typical of quartz in the host Butte granite, quartz phenocrysts in porphyry dikes, and hydrothermal quartz in biotite crackles and pre-main stage veins are shown in Fig. 4. CL images were used to distinguish different generations of quartz

Fig. 4. Examples of cathodoluminescent textures in quartz. Images are dominantly quartz (qz) unless marked otherwise: bi=biotite, mt=magnetite, py=pyrite, cp=chalcopyrite, kf=K-feldspar, mb=molybdenite, anh=anhydrite, gm=groundmass; en=envelope. Dashed lines indicate edge of vein. Example analysis spots are shown with calculated Ti-in-quartz temperatures in °C. (a) CL-bright plutonic quartz from Butte granite (BU-214_Q5), (b) CL-bright porphyritic quartz “eye” from Modoc porphyry dike (11067-1_Q1), (c) biotite crackle with rounded CL-dark quartz overgrown by CL-grey to CL-bright quartz (BUR-03-213_Q1), (d) deep EDM vein quartz with thin concentric CL-bright growth bands (11185-3771_Q4), (e) shallow CL-dark EDM vein quartz with euhedral growth bands (F2033-488_Q1), (f) shallow CL-dark EDM vein quartz cementing fragments of CL-bright Butte granite breccia (11135-1150_Q2), (g) CL-dark EDM quartz vein cut by CL-bright barren quartz vein (11185-3771_Q5); grains of both veins are cut and surrounded by cobwebs and spiders of CL-black quartz, and (h) deep barren quartz vein with blotchy and homogenous quartz as well as bright euhedral growth bands (10969-6804_Q2); *825°C is not considered a quartz-Ti equilibration temperature.

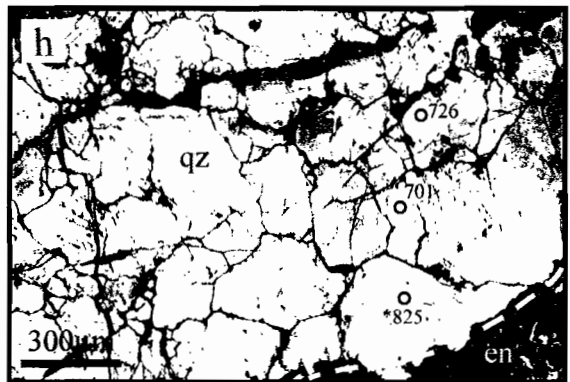
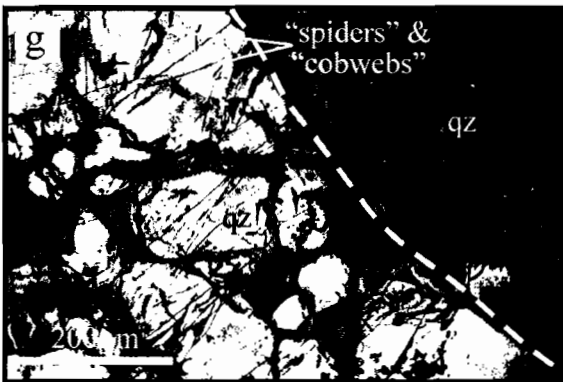
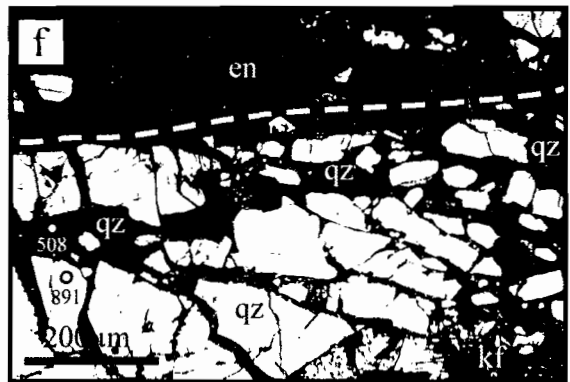
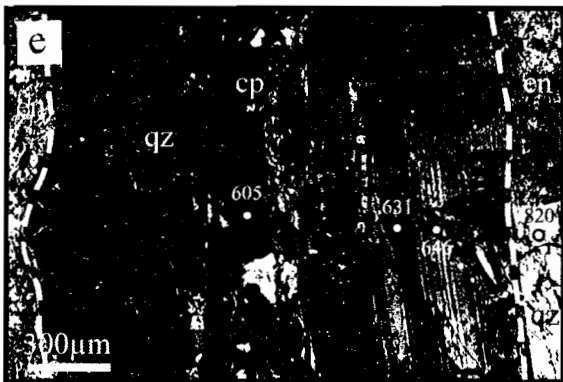
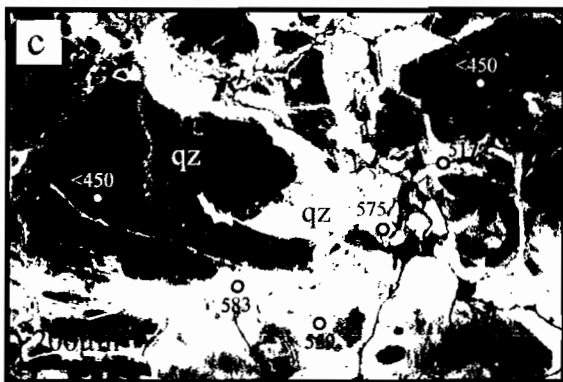
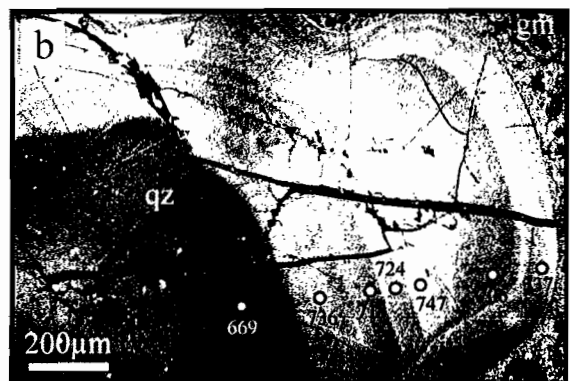
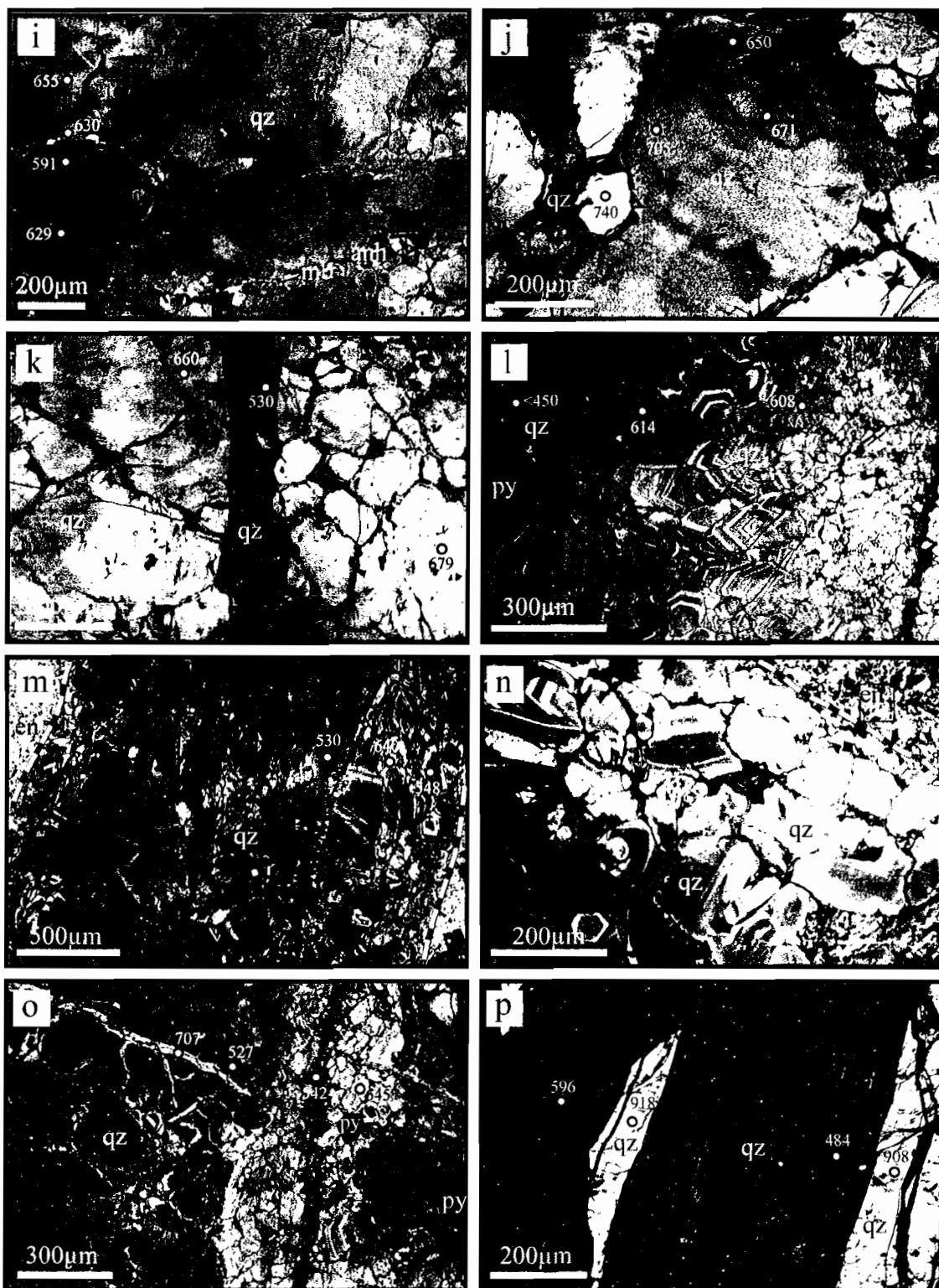


Fig. 4, continued. Examples of cathodoluminescent textures in quartz. (i) quartz-molybdenite vein with CL-grey monotonous grains (11172-4247_Q2), (j) quartz-molybdenite vein with blotchy grains, grains with different CL brightness, and CL-dark grain boundaries (10969-5699_Q2), (k) quartz-molybdenite vein cut by later stage CL-dark veinlet (11135-2-4209_Q1), (l) transitional quartz-molybdenite-pyrite vein with euhedral growth bands and monotonous grains (10969-2101_Q1), (m) pyrite-quartz GS vein with euhedral growth bands along both vein edges as well as blotchy and monotonous grains (11135-2470_Q5b), (n) euhedral growth bands along vein edge from pyrite-quartz GS vein (11135-2470_Q2b), (o) pyrite-quartz GS vein with euhedral growth bands along vein parallel and linear vein features (10969-2665_Q2), and (p) shallow pyrite quartz vein (CL-dark) with angular Butte granite quartz fragment (CL-bright) (10969R-2075_Q1).



precipitation within each sample, all of which we then analyzed for trace elements by microprobe. Consequently while our data portray the range of Ti concentrations within each sample, they do not reflect the statistical distribution of Ti concentrations. The biotite breccia sample contained small amounts of hydrothermal quartz (<50 μm grains) and therefore we did not analyze quartz from the biotite breccia.

Butte granite quartz grains are 0.5-3 mm in diameter and CL-bright. Many large grains show CL-bright cores with rounded alternating CL-grey and CL-bright concentric bands resembling growth bands in quartz phenocrysts, while small grains of interstitial quartz are relatively monotonous and CL-grey (Fig. 4a). Porphyry quartz eyes from dike samples are 0.5-7 mm in diameter and are characteristically rounded. CL images reveal CL-grey cores surrounded by ~3-15 concentric, rounded to euhedral alternating CL-grey and CL-bright bands (Fig. 4b). Most plutonic and igneous quartz grains contain secondary CL-dark features that overprint primary, relatively CL-bright textures (e.g., hydrothermal quartz-filled microcracks, grain boundaries, and star-like decrepitation traces around fluid inclusion-rich zones).

Hydrothermal quartz displays a large variety of CL brightness, textures, and cross-cutting relationships within individual samples and among sample types. Deep biotite crackles display CL-dark, rounded grains that are overgrown by CL-bright quartz with some concentric growth zones (Fig. 4c). Most deep EDM veins show CL-bright to CL-grey blotchy grains, some of which have thin (5 μm) CL-bright concentric bands (Fig. 4d). Some EDM samples, both deep and shallow, display euhedral growth bands, particularly along vein edges (Fig. 4e). Shallow, CL-grey EDM veins contain CL-bright angular pieces of broken Butte granite quartz (Fig. 4f). An example of CL-bright barren quartz cutting a CL-grey EDM vein is shown in Fig. 4g. Barren quartz and quartz-molybdenite veins exhibit CL-bright to CL-grey, blotchy and monotonous grains (Fig. 4h-k). Deep and shallow quartz of both types show euhedral growth bands along vein edges (Fig. 4h), around individual quartz grains, and along vein-parallel fractures within the vein adjacent to grains with monotonous textures. Many barren quartz and quartz-molybdenite veins contain wide (50-200 μm) CL-grey to CL-dark veinlets that cut

original brighter grains (Fig. 4k). Shallow quartz-molybdenite veins contain brecciated and slightly rounded CL-bright Butte granite quartz. The sample of a relatively shallow, transitional quartz-molybdenite-pyrite vein displays CL-bright to CL-grey blotchy and monotonous quartz interlayered with euhedral banded quartz along the vein edge and within the vein (Fig. 4l). That sample also contains rounded CL-bright Butte granite breccia fragments (not visible in Fig. 4l). Pyrite-quartz GS veins display euhedral growth bands more commonly than any other vein types however they also commonly exhibit CL-grey to CL-dark blotchy and monotonous quartz. GS veins that are somewhat deeper or farther away from the center of the pervasive sericite-pyrite alteration show euhedral growth bands that are commonly along vein edges (Fig. 4n), around individual quartz grains within the vein (Fig. 4m), and along vein-parallel or linear features within the vein (Fig. 4o). Shallow GS veins in the interior of the pervasive sericite-pyrite alteration bulb commonly display monotonous CL-grey to CL-dark quartz filling fractures with an abundance of large, angular brecciated pieces of Butte granite (Fig. 4p). Most quartz grains from nearly all vein types display CL-dark grain boundaries (Fig. 4) and some contain CL-dark “spiders” connected to networking CL-dark “cobwebs” (Fig. 4g; Rusk and Reed, 2002).

Microprobe trace element analyses of quartz (Table 2) show that concentrations of Fe, Al, and K within each sample are highly heterogeneous. Ti concentrations are less heterogeneous and correlate positively with relative CL brightness as found by others for high temperature (>500°C) quartz (e.g., Landtwing and Pettke, 2005; Mueller et al., 2003; Rusk et al., 2008a). Concentrations of Al and K show a weak positive correlation but they do not correlate with Ti or CL brightness. Fe concentrations do not correlate with CL brightness or any other trace element we measured.

Quartz-Ti equilibration temperatures calculated using the Ti-in-quartz geothermometer are shown in Table 2 and Fig. 5. High temperatures (high Ti) correlate with CL-bright zones in quartz and low temperatures (low Ti) correlate with CL-dark zones (Fig. 4). The Butte granite ranges from 720 to 925°C, overlapping porphyry quartz phenocryst temperatures, which range from 630 to 770°C. All hydrothermal vein quartz

Table 2
Microprobe analyses of trace elements in quartz and calculated Ti-in-quartz temperatures

Sample	n	Ti ppm	Fe ppm	Al ppm	K ppm	assumed $a_{\text{H}_2\text{O}}$	Ti-in-qz Temperature (°C)
GRANITE AND PORPHYRY QUARTZ, CL-bright							
<i>Fresh Butte granite quartz, CL bands</i>							
BU-214_Q5	14	108(23)	25(15)	127(69)	15(8)	0.6	821(30)
BU-214_Q9	10	111(43)	22(8)	87(21)	13(2)	0.6	831(48)
BU-214_Q10	6	58(10)	16	69(9)	13(6)	0.6	741(20)
<i>Fresh Butte granite quartz, interstitial</i>							
BU-214_Q4	3	81(5)	33(3)	146(34)	16(6)	0.6	785(7)
BU-214_quartzA	3	74(2)	22(13)	189(114)	48	0.6	713(3)
<i>Butte granite quartz in vein wall or vein breccia</i>							
11135-1150_Q1	3	73(2)	312(74)	461(612)	80(103)	0.6	771(4)
11135-1150_Q2	4	171(55)	124(107)	218(51)	47(21)	0.6	885(61)
F2033-488_Q1	2	124(26)	78(86)	315	107(71)	0.6	842(30)
F2033-513_Q1	2	63(16)	46(33)	796(522)	26(12)	0.6	751(31)
10969-2101_Q1	1	92	24	255	17	0.6	802
10969R-2075_Q1	5	176(31)	4189(9221)	197(272)	123(166)	0.6	894(30)
10969-2665_Q1	2	73(7)	62	161(54)	14(7)	0.6	771(12)
<i>Steward-type porphyritic quartz</i>							
11135-2470_Q1	10	45(13)	145(87)	265(188)	78(51)	0.6	707(31)
11135-2470_Q3	16	41(8)	21(9)	177(54)	46(53)	0.6	701(22)
11135-2-4209_Q2	4	51(8)	21(9)	317(80)	36(14)	0.6	728(17)
<i>Modoc-type porphyritic quartz</i>							
11067-1_Q1	20	48(10)	65(7)	220(41)	22(4)	0.6	718(25)
11067-1_Q3-A	18	41(10)	65(59)	187(79)	74(29)	0.6	701(25)
11067-1_Q3-B	15	40(9)	48(37)	170(26)	20(3)	0.6	699(28)
HYDROTHERMAL QUARTZ, CL-grey veins							
<i>Biotite crackles</i>							
BUR-03-213_Q1	14	14(4)	53(39)	75(14)	22(14)	1.0	556(22)
BUR-03-213_Q1-B	8	15(5)	33(10)	82(31)	23(16)	1.0	559(25)
BUR-03-213_Q2	5	29(16)	82(27)	107(40)	37(24)	1.0	607(51)
<i>EDM veins</i>							
11185-3771_Q4	6	12(4)	16(3)	79(20)	MDL	1.0	544(24)
BUR-03-214_Q1	16	9(3)	16(3)	49(29)	19(7)	1.0	533(48)
BUR-03-214_Q3	5	MDL	15(2)	54(11)	32(17)	1.0	MDL
11135-5051_Q1	8	24(6)	52(60)	54(7)	21	1.0	599(25)
11135-1150_Q1	6	10(7)	707(148)	145(20)	44(19)	1.0	521(53)
11135-1150_Q2	4	9(3)	169(61)	145(28)	31(17)	1.0	517(23)
F2033-488_Q1	12	24(12)	102(189)	1579(952)	263(204)	1.0	590(46)
<i>Barren quartz veins</i>							
11185-3771_Q3	9	53(15)	36(19)	131(58)	49(22)	1.0	674(27)
11172-1847_Q2	4	56(7)	MDL	119(10)	MDL	1.0	682(14)
11135-5461_Q1	8	63(16)	16(4)	158(31)	27(19)	1.0	692(28)
11135-5461_Q2	8	80(12)	16(3)	169(68)	36(22)	1.0	720(16)
11135-2-4209_Q3	7	24(12)	21	224(301)	11(1)	1.0	591(49)
10969-6804_Q2	5	88(55)	21	621(438)	69(117)	1.0	720(64)
10969-6804_Q3	8	65(20)	MDL	190(145)	19(9)	1.0	695(33)
<i>Quartz-molybdenite veins</i>							
10969-5699_Q1	12	36(7)	20(11)	52(18)	25(29)	1.0	636(18)
10969-5699_Q2	10	66(15)	45	105(91)	47(83)	1.0	698(26)
10969-5699_Q3	10	39(11)	15(6)	52(11)	12(2)	1.0	644(24)
10969-5699_Q4	5	69(21)	MDL	73(18)	MDL	1.0	701(38)
11172-4247_Q1	9	17(4)	72(89)	1066(1668)	24(17)	1.0	568(20)
11172-4247_Q2	8	32(6)	18(6)	146(51)	25(9)	1.0	627(18)
10969-6804_Q1	9	52(20)	33(8)	694(1022)	17(6)	1.0	668(47)
F2033-513_Q1	9	26(11)	114(153)	561(254)	70(127)	1.0	602(36)
F2033-513_Q2	9	22(8)	111(179)	869(1026)	174(316)	1.0	589(31)
11135-3597_Q1	9	24(8)	24(9)	139(48)	22(10)	1.0	595(31)
11135-3597_Q2	10	32(19)	99(195)	220(245)	59(98)	1.0	614(58)
11135-2-4209_Q1	7	41(9)	59	155(65)	15(5)	1.0	649(22)
<i>Quartz-molybdenite-pyrite veins</i>							
10969-2101_Q1	15	23(8)	115(202)	850(1261)	11(2)	1.0	590(38)

Table 2
Continued

Sample	n	Ti ppm	Fe ppm	Al ppm	K ppm	assumed $a_{\text{H}_2\text{O}}$	Ti-in-qz Temperature (°C)
<i>Pyrite-quartz veins</i>							
11135-2470_Q2b	20	16(10)	88(63)	194(142)	82(92)	1.0	551(45)
11135-2470_Q5b	10	23(9)	25(8)	112(95)	75(92)	1.0	545(132)
10969-2075_Q1	15	21(12)	69(89)	918(1062)	106(87)	1.0	584(51)
10969-2075_Q2	15	11(5)	25(10)	202(338)	56(42)	1.0	533(36)
10969-2665_Q1	8	18(13)	622(862)	1000(1436)	170(290)	1.0	565(52)
10969-2665_Q2	9	28(20)	103(62)	1161(1206)	191(215)	1.0	597(63)
HYDROTHERMAL QUARTZ, CL-dark veinlets/fracture fillings							
<i>Filling Modoc-type porphyritic quartz</i>							
11067-1_Q1_darkqz	5	7(1)	56(8)	159(69)	MDL	1.0	502(19)
<i>Filling EDM veins</i>							
11135-5051_Q1	2	MDL	27(15)	52(17)	28	1.0	MDL
<i>Filling barren quartz veins</i>							
11185-3771_Q3	4	12(3)	33(14)	268(128)	71(50)	1.0	545(17)
10969-6804_Q2	3	12(7)	12	1096(1527)	126(162)	1.0	531(56)
<i>Filling quartz-molybdenite veins</i>							
11172-4247_Q2	1	19	17	573	50	1.0	581
11135-2-4209_Q1	2	14(5)	473(31)	128(7)	14	1.0	551(30)
HYDROTHERMAL QUARTZ, CL-dark grain boundaries							
<i>Along grains in barren quartz veins</i>							
11185-3771_Q3	2	19(3)	20(4)	78(6)	MDL	1.0	579(12)
11135-5461_Q1	1	16	MDL	114	9	1.0	564
11135-5461_Q2	1	36	14	263	9	1.0	638
10969-6804_Q2	1	7	MDL	103	12	1.0	501
10969-6804_Q3	1	6	MDL	494	15	1.0	496

Data are reported as averages of multiple microprobe analyses. Samples with large standard deviations are highly heterogeneous. Number in parentheses next to each analysis represents 1σ standard deviation. Errors given in terms of least unit cited (e.g., 108(23) represents 108 ± 23).

n Number of analyses, MDL below 99% minimum detection limit

overlaps somewhat with porphyry quartz temperatures, regardless of their depth within the deposit. Biotite crackles range from 520 to 660°C. EDM veins are slightly cooler, ranging from below the detection limit (450°C) to 670°C. Barren quartz veins range from 510 to 750°C with one exceptionally high temperature of 825°C corresponding to a finely oscillatory zoned (<10 μm) area that is likely an “intrinsic” diffusion controlled boundary layer effect (D'lemos et al., 1997; Shore and Fowler, 1996) and thus is not representative of quartz-Ti equilibrium temperature (Fig. 4h). Quartz-molybdenite veins range from 520 to 740°C while the transitional quartz-molybdenite-pyrite vein ranges from 500 to 740°C. Pyrite-quartz veins range from below the detection limit (450°C) to 660°C, with one sample containing a CL-bright linear band at 707°C (Fig. 4o). All types of quartz show a large range in temperature spanning 50 to 225°C within single generations of quartz in individual samples. Many samples contain CL-dark veinlets, fracture fillings, and grain

boundaries that are difficult to assign to any previously mentioned quartz generation. Some of these features have Ti concentrations above the detection limit, and are distinguished from primary vein quartz with dashes or crosses in Fig. 5. Ti concentrations in most CL-black quartz that fills microcracks and thin grain boundaries are consistently below the detection limit, and likely reflect low Ti concentrations in main stage hydrothermal quartz, which fluid inclusions indicate formed at $\leq 400^{\circ}\text{C}$ (Rusk et al., 2008b).

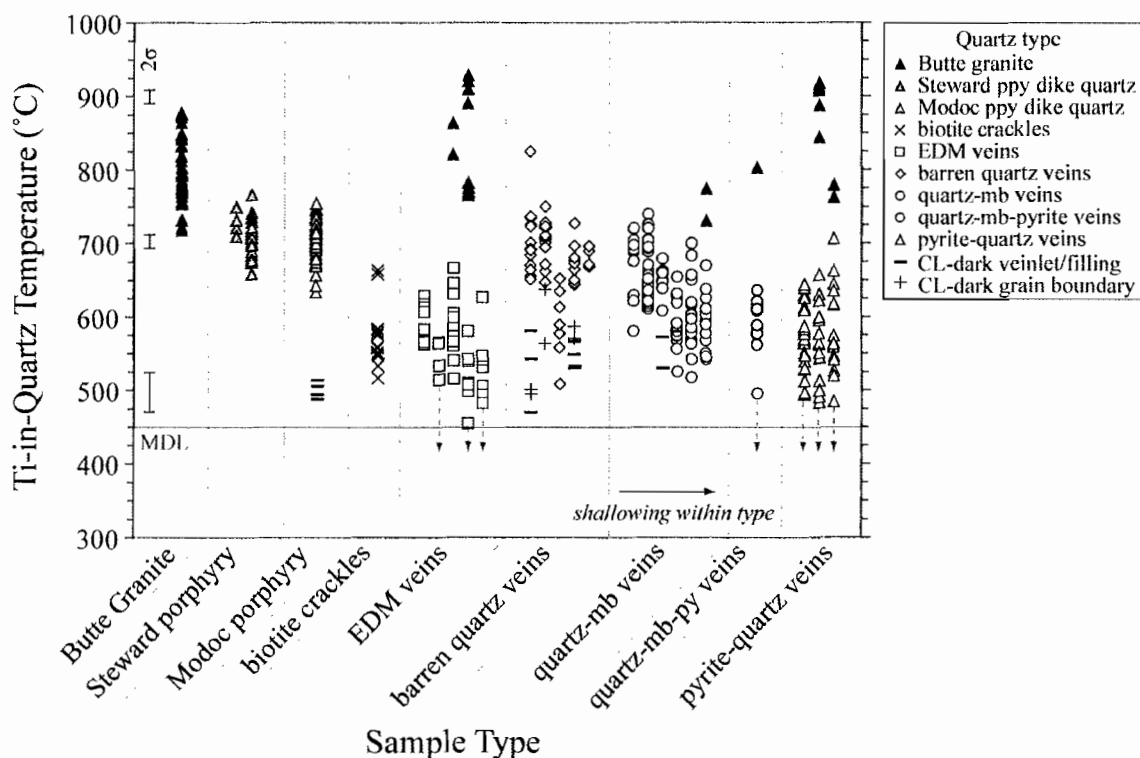


Fig. 5. Ti-in-quartz temperatures calculated for all sample types. Each column of data displays individual analyses from single samples. Within each sample type, individual samples are arranged left to right from deeper to shallower. Fragments of Butte granite quartz within hydrothermal veins are distinguished from the vein quartz, as shown with filled triangles. CL-dark veinlets and fracture fillings (dashes) and grain boundaries (crosses) are also distinguished from primary vein and porphyry quartz. 2σ temperature precision is shown with bars to the left. MDL = 99% minimum detection limit (450°C). Dashed arrows indicate samples containing quartz with Ti concentrations below the detection limit.

Analytical precision for Ti analyses and the geothermometer are shown in Fig. 6 along with estimated 2σ analytical precision from Wark and Watson (2006) for EPMA and SIMS techniques. One-sigma analytical errors on individual analyses range from 1.5% at high Ti concentrations to 10% at 16 ppm Ti. As Ti concentrations approach 0 ppm the analytical errors grow exponentially with an error of $\sim 50\%$ at the detection limit of 3 ppm Ti. Precision in the geothermometer is best at $>650^\circ\text{C}$ with a 2σ error of $\pm 10^\circ\text{C}$. At the detection limit (450°C) the temperature error is $\pm 60^\circ\text{C}$.

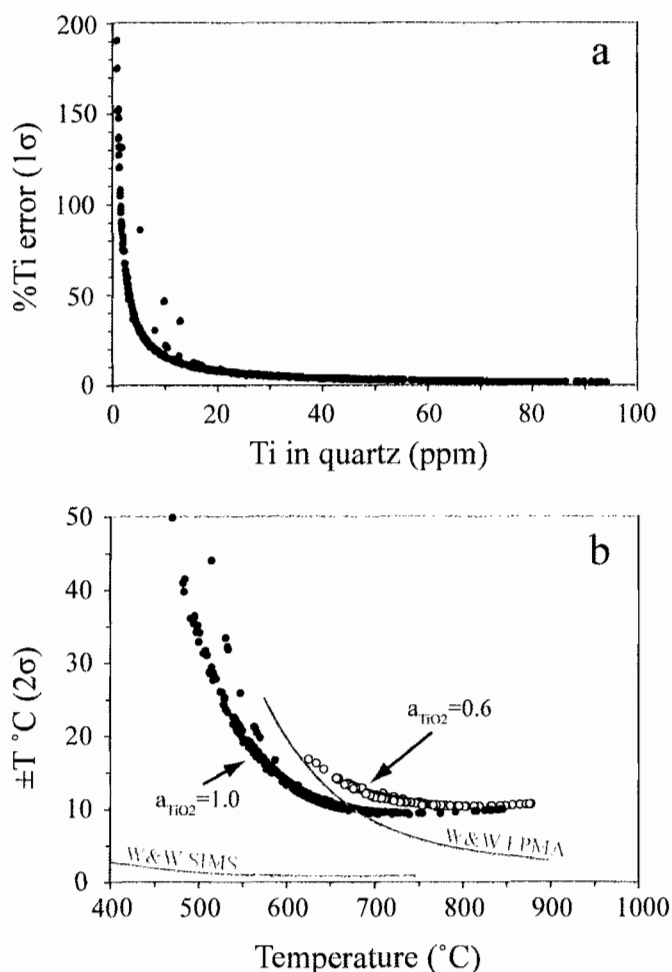


Fig. 6. Analytical error and temperature precision of quartz geothermometer. (a) Percent analytical error (1σ) for each Ti microprobe analysis using two spectrometers. (b) Absolute temperature precision (2σ) of Ti-in-quartz geothermometer for our analyses using $a_{\text{TiO}_2} = 1.0$ (black filled circles) and $a_{\text{TiO}_2} = 0.6$ (open circles). Outliers were analyzed using a beam current < 200 nA. Estimated analytical precision (2σ) from Wark and Watson (2006) for EPMA and SIMS techniques is shown by grey lines.

3.2. Hydrothermal rutile

Blocky rutile grains (Fig. 7b and c) are subhedral to anhedral and typically occur in clusters near hydrothermal biotite and pyrite within veins, and near remnant plutonic biotite in altered wall rock within 1 to 2 mm of the vein. Grains range in diameter from 5 to 50 μm and show either homogeneous BSE textures (Fig. 7b) or sector zoned textures (Fig. 7c). Both texture types are observed within single samples. Rutile was not measured in the Butte granite or the porphyry dikes since these samples do not contain primary rutile.

Rutile contains up to several wt% Fe, Nb, and W, with Zr and Ta in the 100s to 1000s ppm range, respectively, and concentrations of these elements within each sample are heterogeneous (Table 3). Energy dispersive spectroscopy (EDS) maps show bright rutile zones to be higher in W and Fe than darker rutile zones (Fig. 7c). Zr concentrations do not correlate with Fe or W and thus we conclude that the zones do not result from differing temperatures.

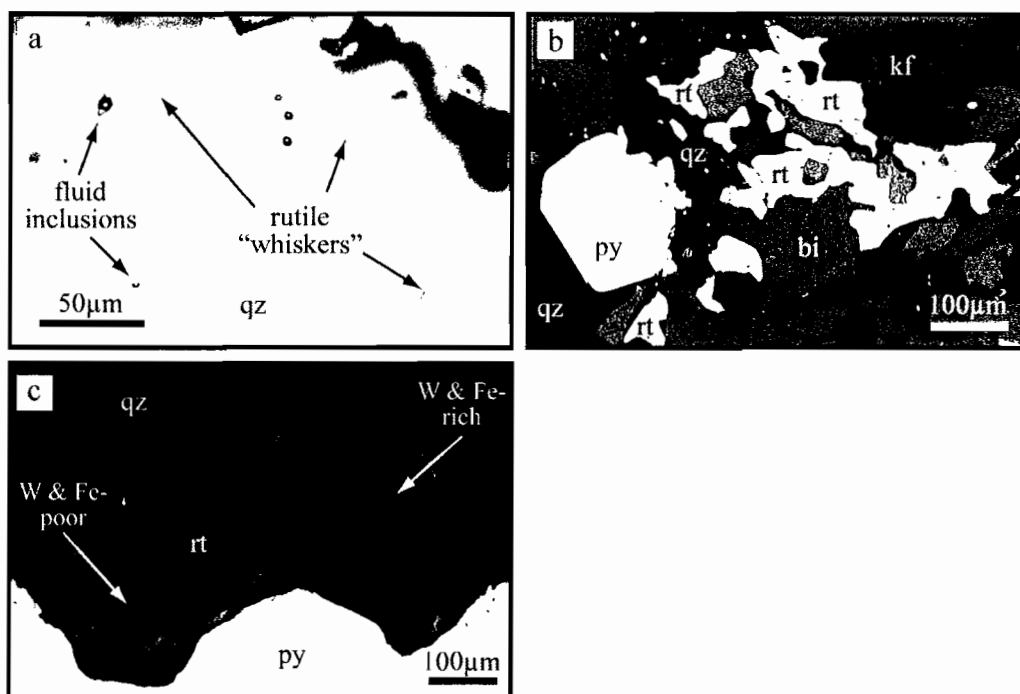


Fig. 7. Example images of hydrothermal rutile (rt). (a) Optical photomicrograph of whisker-like rutile in quartz, (b) BSE image of blocky rutile, and (c) BSE image of sector zoned rutile. Relatively bright zones are rich in W and Fe.

Table 3
Microprobe analyses of trace elements in rutile and calculated Zr-in-rutile temperatures

Sample	n	Zr ppm	Ta ppm	Fe wt%	Nb wt%	W wt%	Zr-in-rt Temperature (°C)
HYDROTHERMAL RUTILE, in vein							
<i>Biotite breccia</i>							
BU96MR_rutile	6	202(38)	977(1561)	2.4(1.8)	0.13(4)	1.2(3)	610(17)
BU96MR_rutile2	6	57(14)	245(324)	0.1(1)	0.10(8)	0.10(6)	523(17)
<i>Biotite crackles</i>							
BUR-03-213_rutile2	5	305(28)	153(83)	1.2(9)	0.14(4)	NA	643(7)
* BUR98-13_rutile4	6	504(52)	57	1.0(4)	0.13(3)	1.1(1.2)	686(9)
BUR98-13_rutile3	6	351(18)	77(18)	1.1(2)	0.21(2)	0.78(5)	655(4)
BUR98-13_rutile	6	342(95)	187(218)	1.5(1.1)	0.17(4)	0.7(4)	651(25)
<i>EDM veins</i>							
11185-3771_rutile2	14	85(50)	522(572)	0.4(2)	0.2(2)	NA	538(46)
BUR-03-214_rutile2	12	438(123)	87(22)	1.0(7)	0.27(6)	NA	672(24)
11135-5051_rutile	6	258(23)	56(11)	1.2(8)	0.18(3)	NA	630(7)
11135-5051_blockyrutile	14	242(67)	147(137)	0.9(3)	0.8(4)	NA	622(25)
11135-5051_blockyrutile2	9	336(20)	407(257)	1.2(2)	1.3(1)	NA	651(5)
* F2033-488_rutile3	8	209(185)	498(548)	1.8(8)	0.8(1.4)	2.1(1.5)	593(64)
* 11135-1150_rutile	6	25	47(18)	1.7(8)	0.05(6)	2.4(1.7)	477
<i>Barren quartz veins</i>							
11185-3771_rutile	12	63(19)	511(523)	0.45(5)	0.15(3)	NA	528(22)
11135-2-4209_rutile	5	245(26)	172(143)	1.1(2)	0.6(2)	1.7(6)	626(9)
* 11135-2-4209_rutile2	5	284(44)	211(123)	1.3(3)	1.0(3)	1.2(9)	637(13)
11135-5461_rutile5	7	434(177)	843(585)	1.1(6)	2.3(1.2)	0.31(8)	668(35)
<i>Quartz-molybdenite veins</i>							
10969-5699_rutile	10	227(19)	337(250)	0.21(7)	0.6(2)	NA	620(7)
* F2033-513_rutile4	4	35(16)	55(18)	1.6(8)	0.09(2)	3.0(1.9)	489(37)
10969-6804_rutile2	6	123(14)	369(136)	0.42(2)	0.385(8)	0.45(4)	575(8)
10969-6804_rutile3	5	368(8)	1273(637)	1.10(3)	1.88(3)	0.32(3)	659(2)
* 11135-3597_rutile2	6	148(33)	34	1.0(3)	0.06(4)	1.7(9)	587(15)
<i>Pyrite-quartz veins</i>							
* 11135-2470_blockyrutile3	11	170(51)	103(19)	0.8(3)	0.1(1)	NA	595(24)
* 11135-2470_blockyrutile2	10	228(67)	57(10)	1.0(3)	0.12(8)	NA	618(25)
10969R-2075_rutile	12	35(28)	91(36)	0.3(1)	0.11(4)	NA	481(51)
HYDROTHERMAL RUTILE, in envelope							
<i>Biotite breccia</i>							
BU96MR_rutile3	6	630(166)	742(253)	1.2(3)	0.8(2)	0.6(5)	705(23)
BU96MR_rutile4	6	213(96)	243(218)	2.5(1.5)	1.1(6)	1.4(6)	607(44)
<i>Biotite crackles</i>							
BUR-03-213_rutile	9	122(37)	40	0.34(2)	0.042(6)	NA	572(21)
BUR-03-213_rutile3	14	358(44)	91(59)	0.9(2)	0.4(1)	NA	656(11)
* BUR98-13_rutile2	6	475(173)	102(99)	1.1(2)	0.5(1)	1.2(5)	678(29)
<i>EDM veins</i>							
BUR-03-214_rutile	12	190(86)	84(75)	0.7(1)	0.5(2)	NA	596(53)
* F2033-488_rutile	10	119(42)	82(35)	1.0(8)	0.2(1)	1.5(1.7)	568(33)
* F2033-488_rutile2	9	90(38)	231(316)	1.6(8)	0.1(1)	2.7(1.7)	549(29)
11135-1150_rutile2	5	44(27)	55(22)	0.71(5)	0.10(5)	0.10(3)	501(39)
11135-1150_rutile3	6	31(13)	59(15)	0.55(4)	0.10(3)	0.013(2)	484(26)
<i>Barren quartz veins</i>							
11172-1847_rutile	12	569(90)	1224(289)	2.2(2)	3.1(4)	NA	696(17)
* 11172-1847_rutile2	14	489(232)	261(160)	1.6(6)	1.6(7)	NA	671(59)
10969-6804_rutile	5	117(24)	2371(1374)	0.5(2)	1.4(4)	0.2(1)	570(15)
11135-5461_rutile	4	47(27)	4051(4063)	0.12(2)	0.11(7)	0.08(1)	506(35)
11135-5461_rutile3	5	270(32)	267(95)	0.68(8)	1.56(3)	0.2(2)	634(9)
<i>Quartz-molybdenite veins</i>							
10969-5699_rutile2	7	59(12)	217(134)	0.07(1)	0.23(6)	NA	525(12)
* F2033-513_rutile123	9	61(35)	71(36)	0.6(5)	0.13(8)	1.2(1.8)	520(38)
* F2033-513_rutile5	5	34(5)	39	0.8(5)	0.17(6)	0.9(1.1)	493(9)
* 11135-3597_rutile	8	129(44)	52(17)	0.9(4)	0.05(4)	1.4(1.2)	575(23)
11135-3597_rutile3	3	77(4)	89(61)	0.76(5)	0.33(4)	0.5(2)	543(3)
11135-2-4209_rutile3	5	328(14)	1660(1520)	1.2(3)	1.2(1)	0.3(1)	650(4)
11172-4247_rutile	9	413(36)	141(96)	0.73(5)	0.51(9)	0.25(8)	669(8)
11172-4247_rutile2	9	330(43)	114(66)	0.68(8)	0.39(8)	0.2(1)	650(11)

Table 3
Continued

Sample	n	Zr ppm	Ta ppm	Fe wt%	Nb wt%	W wt%	Zr-in-rt Temperature (°C)
<i>Quartz-molybdenite-pyrite veins</i>							
* 10969-2101_rutile	6	102(12)	114(118)	0.12(6)	0.08(2)	0.2(1)	562(8)
* 10969-2101_rutile2	6	74(16)	80(40)	0.2(1)	0.12(4)	0.3(2)	540(14)
* 10969-2101_rutile3	7	399(374)	811(1059)	0.5(5)	0.3(1)	0.8(1.2)	626(103)
<i>Pyrite-quartz veins</i>							
11135-2470_rutile_zircon-prism-area	6	382(55)	110(43)	0.66(7)	0.58(7)	NA	662(12)
* 11135-2470_blockyrutile	8	136(41)	248	0.8(4)	0.1(2)	NA	580(20)
11135-2470_blockyrutile4	6	310(52)	220(89)	0.7(1)	0.6(2)	NA	644(14)
10969R-2075_rutile2	14	51(25)	59(34)	0.7(4)	0.17(4)	NA	512(29)
10969-2665_rutile	6	53(27)	68(17)	0.44(3)	0.12(3)	0.5(1)	515(28)
* 10969-2665_rutile2	4	43(19)	143(86)	0.9(3)	0.24(7)	1.5(7)	504(25)
10969-2665_rutile3	4	58(4)	332(503)	0.23(2)	0.055(4)	0.58(8)	526(4)
10969-2665_rutile4	3	262(103)	710(561)	0.6(3)	0.37(4)	0.8(7)	628(30)

Data are reported as averages of multiple microprobe analyses. Samples with large standard deviations are highly heterogeneous. Numbers in parentheses next to each analysis represent 1 σ standard deviation. Errors given in terms of least unit cited (e.g., 202(38) represents 202 \pm 38)

n Number of analyses, NA not analyzed

*denotes sector zoned rutile

Calculated hydrothermal rutile temperatures (Table 3, Fig. 8) overlap with those determined from Ti in quartz. Biotite breccias range from 490 to 740°C and biotite crackles range from 540 to 730°C. EDM veins range from 450 to 720°C. Barren quartz veins range from 470 to 730°C, quartz-molybdenite veins range from 430 to 680°C, and quartz-molybdenite-pyrite veins range from 510 to 740°C. Pyrite-quartz veins range from 440-680°C. As for the quartz thermometry, rutile displays a large range in temperature within single samples, spreading over 50 to 250°C.

In twelve samples we analyzed rutile grains in a vein and in the alteration envelope within 1 to 2 mm of that vein. We found that mean vein rutile temperatures are within one standard deviation of mean alteration envelope rutile temperatures for all samples, except for one biotite breccia sample in which the rutile in altered breccia fragments has a higher mean temperature than rutile in the breccia filling (Fig. 9).

Analytical precision for Zr analyses and the geothermometer are shown in Fig. 10 as well as estimated 2 σ analytical precision from Watson et al. (2006) for EPMA analyses using either one spectrometer or four spectrometers simultaneously. One sigma analytical errors on individual microprobe analyses range from 1.5% at high Zr concentrations to 10% at ~50 ppm Zr (Fig. 10a). As for Ti errors, analytical error grows exponentially as Zr concentrations approach 0 ppm with an error of ~50% at the detection

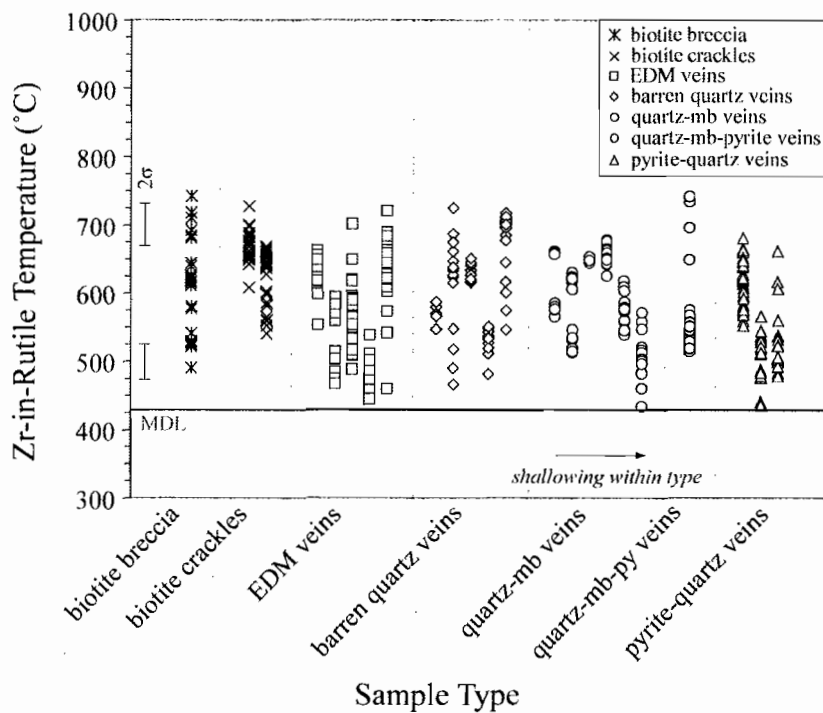


Fig. 8. Zr-in-rutile temperatures calculated for all sample types. Each column of data displays individual analyses from single samples. Within each sample type, individual samples are arranged left to right from deeper to shallower. 2σ temperature precision shown with bars at left. MDL = 99% minimum detection limit (430°C).

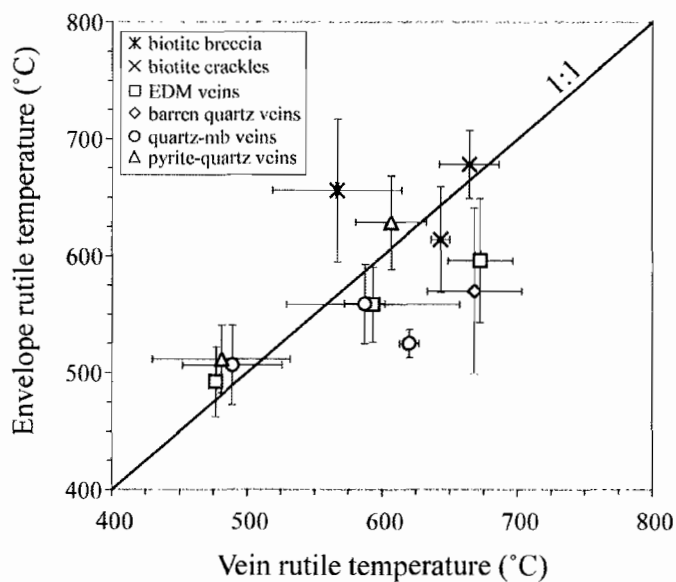


Fig. 9. Average Zr-in-rutile temperatures for rutile in veins and in adjacent alteration envelopes (within 1 to 2 mm of vein). 1σ standard deviations are shown with black bars.

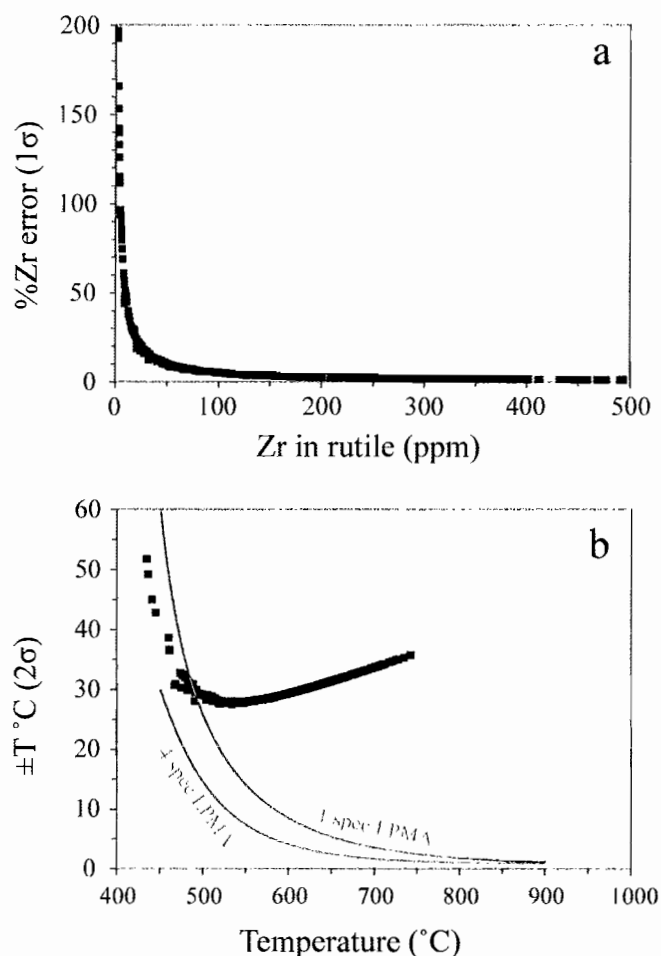


Fig. 10. Analytical error and temperature precision of rutile geothermometer. (a) Percent analytical error (1σ) for each Zr microprobe analysis using two spectrometers. (b) Absolute temperature precision (2σ) of Zr-in-rutile geothermometer for our analyses (black squares). Estimated analytical precision (2σ) from Watson et al. (2006) for EPMA analyses using either one spectrometer or four spectrometers simultaneously is shown by grey lines.

limit of 11 ppm Zr. Precision of the geothermometer is best at 530°C with a 2σ error of ± 28 °C (Fig. 10b). At high temperatures of 750°C the error is ± 35 °C and at the detection limit (430°C) the temperature error is ± 50 °C.

3.3. Plutonic and hydrothermal biotite

Primary biotite in the Butte granite is fresh outside of the Butte district, but is recrystallized (“relict”) with a changed composition within the deposit (Fig. 11a and b).

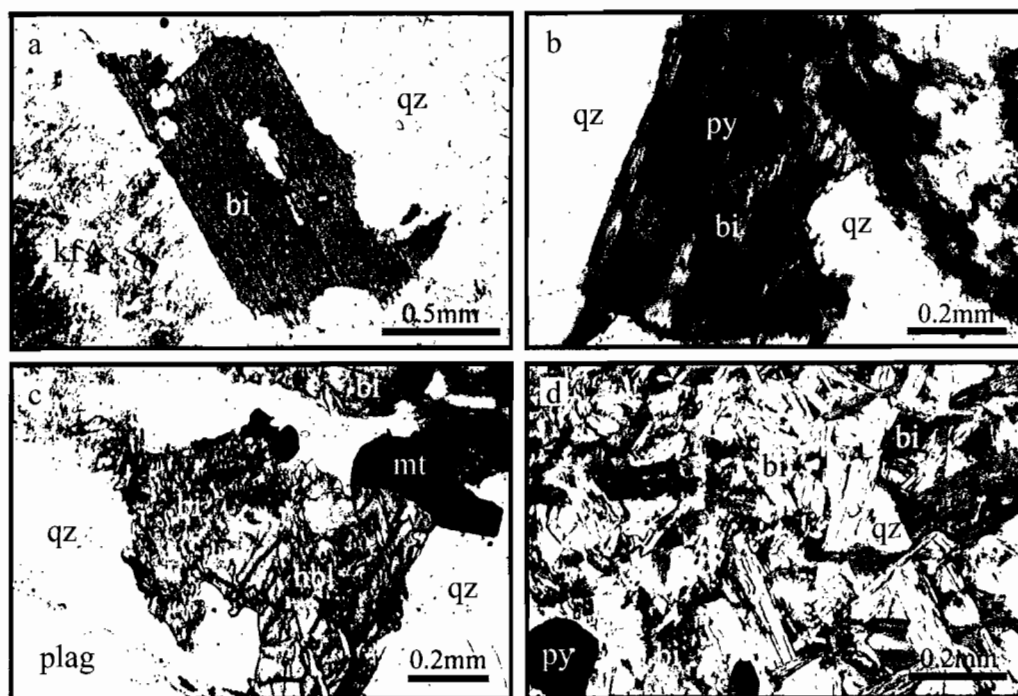


Fig. 11. Optical photomicrographs of biotite types. (a) Fresh Butte granite biotite (BU-214), (b) partially altered relict plutonic biotite (10969-2101), (c) shreddy biotite partially replacing primary hornblende (10969-555.1), and (d) shreddy EDM biotite (BUR-03-214). Abbreviations: qz = quartz, bi = biotite, kf = K-feldspar, py = pyrite, hbl = hornblende, mt = magnetite, plag = plagioclase.

Secondary, shreddy hydrothermal biotite occurs in veins and envelopes and replaces primary hornblende (Fig. 11c and d; Roberts, 1975). Microprobe analyses of biotite (Table 4) show that X_{Mg} (molar $Mg/(Mg+Fe)$) ranges from 0.5 to 0.85 and TiO_2 contents range from 0.7 to 4.8 wt%. Biotite X_{Mg} and Ti apfu (atoms/formula unit) are plotted in Fig. 12a along with isotherms from Henry et al. (2005). F contents in biotite range from 0.5 to 2.5 wt% and correlate positively with X_{Mg} (Fig. 12b).

Metasomatic alteration proceeds through chemical reactions mediated by a complex mixture of grain boundary diffusion and internal grain diffusion fed by fluid infiltration through fractures. Consequently, many reactions reach equilibrium only on the scale of centimeters or millimeters, and some never reach equilibrium. In applying the Ti-in-biotite geothermometer to natural rocks, Henry et al. (2005) state that significant

Table 4

Microprobe analyses of biotite, calculated formulas (based on 22 O), and calculated Ti-in-biotite temperatures

Type	EDM	EDM	EDM	PGS/EDM	PGS/EDM	PGS/EDM	GS/SBr	GS/SBr	GS/SBr	GS/SBr	GS/SBr	GS/SBr/chlorite
Texture	relict	shreddy	shreddy	shreddy	shreddy	shreddy	relict	relict	relict	relict	relict	relict
Sample	11135-3481	11135-3481	11135-3586	10772-32a	10778-6	11135-3568	11148-1197	11148-1141	11148-1300	11148-1293	11148-1169.4	10969-1571
n	7	9	9	4	4	7	8	9	8	7	7	6
<i>Major and minor elements (wt%)</i>												
SiO ₂	31.77(13)	31.10(84)	30.14(53)	31.00(42)	30.73(80)	30.8(2.7)	31.63(19)	31.70(31)	31.48(28)	32.05(25)	32.2(1.0)	31.60(37)
Al ₂ O ₃	25.71(25)	26.3(1.7)	26.7(1.4)	24.03(59)	24.5(1.1)	27.1(3.3)	23.26(30)	23.68(85)	22.42(54)	25.6(1.3)	26.9(1.0)	23.84(49)
TiO ₂	1.95(11)	1.59(26)	1.85(36)	1.99(29)	1.72(69)	1.58(42)	3.50(13)	3.49(21)	3.46(13)	3.34(21)	1.75(85)	3.65(22)
FeO* ^a	6.11(8)	7.9(1.8)	11.2(2.2)	13.26(45)	11.7(1.3)	10.1(1.9)	12.07(88)	11.5(2.1)	14.3(1.1)	6.7(1.4)	6.2(1.2)	9.1(1.1)
MgO	15.20(20)	13.93(74)	11.7(1.3)	11.90(58)	12.7(1.3)	12.3(1.5)	11.90(48)	12.2(1.0)	10.71(41)	13.9(1.1)	14.9(1.1)	13.40(79)
MnO	0.10(2)	MDL	MDL	0.10(4)	0.12(4)	MDL	0.26(4)	0.19(5)	0.29(5)	MDL	0.27(2)	MDL
K ₂ O	16.39(25)	16.41(27)	16.24(20)	15.99(22)	16.14(23)	16.10(57)	16.09(19)	15.82(44)	16.04(27)	16.21(23)	15.92(29)	15.58(28)
Na ₂ O	0.33(1)	0.38(19)	0.22(6)	0.23(6)	0.33(7)	0.23(4)	0.23(4)	0.22(6)	0.23(4)	0.32(7)	0.18(4)	0.31(3)
CaO	MDL	MDL	MDL	MDL	MDL	MDL	MDL	MDL	MDL	MDL	MDL	MDL
H ₂ O	NA	NA	NA	NA	NA	NA	NA	NA	NA	NA	NA	NA
F	2.42(6)	2.18(22)	1.77(30)	1.40(3)	1.97(23)	1.71(43)	0.88(8)	1.02(21)	0.92(7)	1.64(13)	1.63(50)	2.29(17)
Cl	0.03(1)	0.04(1)	0.07(2)	0.09(2)	0.08(1)	0.06(2)	0.18(4)	0.17(3)	0.19(3)	0.14(3)	0.05(2)	0.15(2)
Total	100	100	100	100	100	100	100	100	100	100	100	100
<i>Formula per 22 O + 4(OH,F,Cl)</i>												
Si	4.643	4.577	4.489	4.645	4.605	4.547	4.696	4.688	4.731	4.655	4.645	4.674
^{iv} Al	3.357	3.423	3.511	3.355	3.395	3.453	3.304	3.312	3.269	3.345	3.355	3.326
Sum iv	8	8	8	8	8	8	8	8	8	8	8	8
Ti	0.215	0.176	0.208	0.224	0.193	0.175	0.391	0.389	0.391	0.365	0.190	0.406
^{vi} Al	1.066	1.142	1.170	0.885	0.933	1.248	0.762	0.810	0.698	1.036	1.216	0.826
Fe	0.747	0.978	1.402	1.661	1.471	1.240	1.499	1.427	1.792	0.813	0.745	1.127
Mg	3.311	3.055	2.588	2.658	2.828	2.703	2.633	2.681	2.400	3.012	3.199	2.956
Mn	0.012	0	0	0.012	0.015	0	0.032	0.024	0.037	0	0.033	0
Sum vi	5.350	5.351	5.368	5.441	5.441	5.365	5.317	5.331	5.318	5.226	5.382	5.314
K	3.056	3.080	3.086	3.057	3.086	3.028	3.047	2.985	3.074	3.004	2.928	2.940
Na	0.093	0.109	0.063	0.068	0.094	0.067	0.065	0.063	0.067	0.091	0.050	0.088
Ca	0	0	0	0	0	0	0	0	0	0	0	0
Sum xii	3.149	3.189	3.149	3.124	3.181	3.095	3.112	3.049	3.142	3.096	2.979	3.029
Sum cations	16.499	16.541	16.517	16.565	16.621	16.460	16.430	16.380	16.459	16.322	16.361	16.343
X _{Mg} ^b	0.82(1)	0.76(5)	0.65(7)	0.62(2)	0.66(5)	0.68(6)	0.64(3)	0.65(6)	0.57(3)	0.79(4)	0.81(4)	0.72(3)
Temperature °C	n/a	661(20)	641(22)	642(21)	617(74)	620(46)	n/a	n/a	n/a	n/a	n/a	n/a

Numbers in parentheses next to each analysis represent 1 σ standard deviation on average of multiple analyses. Errors given in terms of least unit cited (e.g., 31.77(13) represents 31.77 \pm 0.13). n Number of analyses, NA not analyzed, MDL below the 99% minimum detection limit, n/a not applicable

^a All Fe reported as FeO*, ^b X_{Mg} = molar[Mg/(Mg+ Fe)]

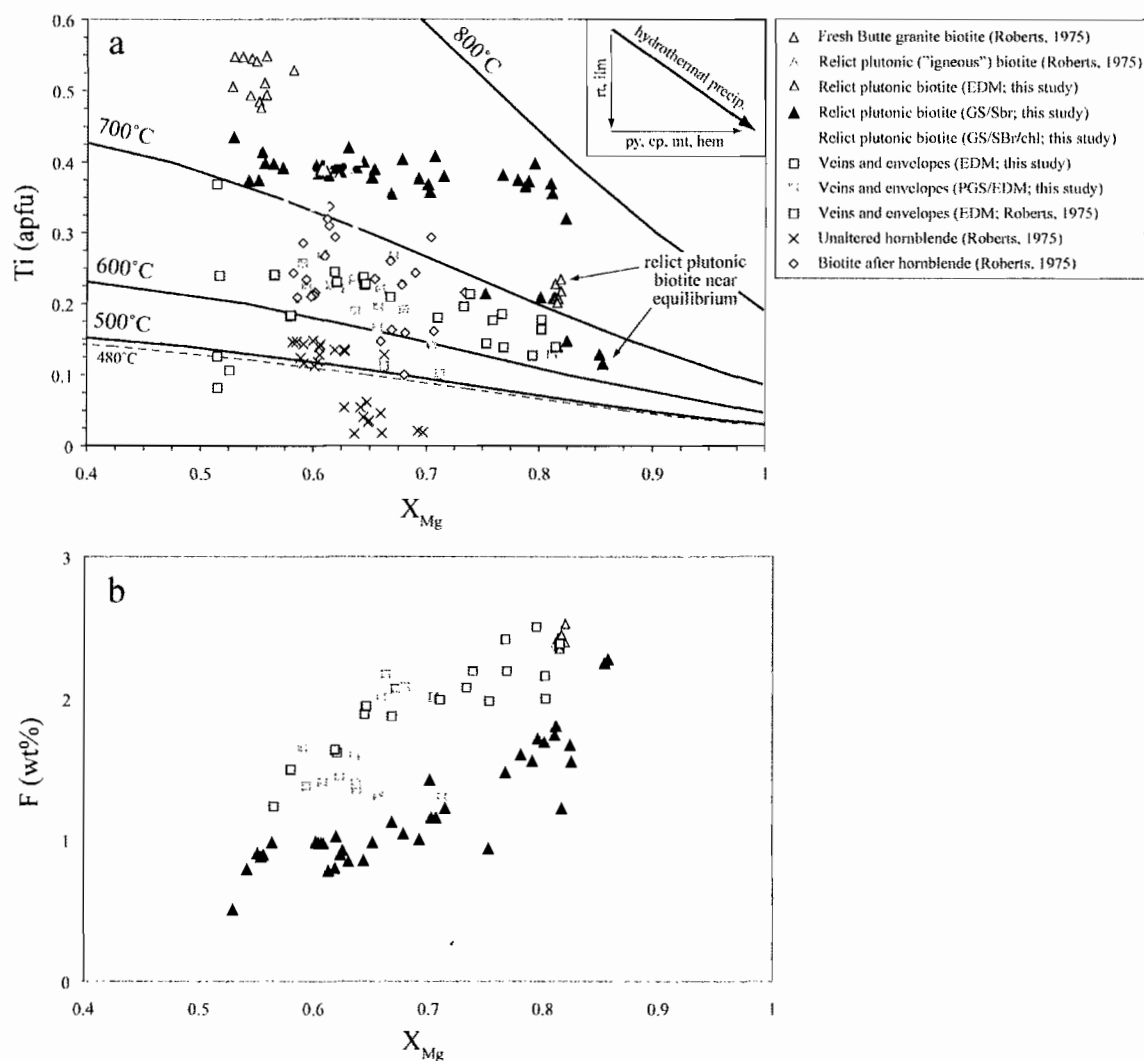


Fig. 12. Plutonic and hydrothermal biotite compositions. (a) Biotite Ti concentration (apfu=atoms/formula unit) vs. Mg biotite mole fraction (X_{Mg} = molar Mg/(Mg+Fe)) from this study (filled symbols) and Roberts (1975; open symbols) with isotherms from the thermometer of Henry et al. (2005). EPMA data provided by Dr. A. Soule and Dr. Lihua Zhang are given in Table 4, but those from Roberts (1975) are not. Calibrated temperature range for thermometer is 480-800°C. Precision of the biotite geothermometer is estimated to be $\pm 24^\circ\text{C}$ in the range of 480-700°C and $\pm 12^\circ\text{C}$ in the range of 700-800°C. Granite hornblende compositions are shown for comparison, but the geothermometer does not apply (compositions calculated based on 23 O). Hydrothermal precipitation of Fe- and Ti-bearing minerals (e.g., rt = rutile, ilm = ilmenite, py = pyrite, cp = chalcopyrite, mt = magnetite, hem = hematite) tends to drive biotite compositions to lower Ti concentrations and higher X_{Mg} as shown in inset. (b) F content in biotite increases with increasing X_{Mg} .

disagreements between biotite temperatures and other estimates may indicate alteration, disequilibrium, local equilibrium, or reequilibration of the biotite following peak temperature conditions. Application of this thermometer to rocks from porphyry systems requires evaluation of whether chemical equilibrium was ever attained or preserved. We evaluate equilibrium for each type of biotite below and report biotite temperatures we consider representative of crystallization conditions.

All biotites are within the compositional calibration range of the geothermometer of Henry et al. (2005). Biotite from five samples of fresh Butte granite (Roberts, 1975) has a pristine texture and uniform chemical composition (Fig. 12a, Table 4). The Butte granite contains ubiquitous accessory ilmenite as lamellae within or adjacent to magnetite grains that buffers the chemical potential of TiO_2 . Thus we interpret temperatures from these biotites (740-760°C) to reflect equilibrium crystallization during granite cooling. Early EDM and PGS/EDM veins with newly crystallized shreddy hydrothermal biotite (this study; Roberts, 1975) contain ubiquitous rutile which acts as a TiO_2 buffer, and biotite temperatures ranging from 520 to 700°C appear to represent crystallization of hydrothermal biotite (Fig. 12a, Table 4). The wide spread in X_{Mg} of EDM and PGS/EDM biotite is likely due to (1) variable Fe availability in the hydrothermal fluid due to local equilibrium and variable precipitation of magnetite, pyrite, and chalcopyrite within the adjacent vein and envelope (Fig. 12a, inset), and (2) incorporation of increasing amounts of F (Fig. 12b; Grew et al., 2006).

Hydrothermal recrystallization of plutonic biotite was rarely complete (Roberts, 1975) and most such relict biotite appears to have been out of chemical equilibrium. The indicated temperatures, between 680 and 740°C (Fig. 12a), are not representative of the hydrothermal event, but rather show an incomplete compositional transition between primary granite biotite (740-760°C) and EDM-type biotite that precipitated newly from early hydrothermal fluids (520 to 700°C).

Relict plutonic biotite adjacent to GS alteration envelopes was rarely completely recrystallized and appears to be out of chemical equilibrium as well, even though rutile exists in these veins. Temperatures indicated by the isotherms range from 700 to 790°C

(Fig. 12a) and are significantly hotter than previous estimates for this type of late alteration (400-550°C; Rusk et al., 2008b), and it is unlikely that the temperatures are representative of GS alteration conditions. These relict biotite compositions spread to higher X_{Mg} than do those of relict biotite adjacent to EDM alteration, which is likely the effect of Fe removal from biotite into pyrite that formed in adjacent intense sericitic alteration.

Hydrothermal biotite replacing primary hornblende is compositionally variable even within a single pseudomorphic hornblende grain (Roberts, 1975). Such biotite cannot be at chemical equilibrium and probably inherited much of its compositional heterogeneity from the original hornblende (Fig. 12a), which occurs as two discrete compositions (actinolite and hornblende) together in single grains that likely exsolved at subsolidus conditions (Roberts, 1975), and concurrent precipitation of varying amounts of Fe-Ti-oxides and Fe-sulfides. Thus, as in the case with relict plutonic biotite, the suggested temperatures of 500-715°C are not indicative of hydrothermal alteration conditions.

Two relict plutonic biotite samples fall within somewhat reasonable isotherms and may indicate approach to equilibrium (Fig. 12a). For example, six analyses from one GS sample (11148-1169.4) range from 650 to 710°C, and one indicates 770°C. It is possible that this sample records an approach to equilibrium of this particular biotite with GS fluids, perhaps due to a high fluid/biotite ratio.

In summary, all relict biotites appear to be out of chemical equilibrium and we do not consider them further. Fresh plutonic biotite and newly crystallized shreddy EDM and PGS/EDM biotite are likely in equilibrium and we discuss their implied temperatures further in the next section.

Errors arising from application of this geothermometer are due to uncertainties in the analyses and in the precision of the empirical fit reported by Henry et al. (2005). Precision of the geothermometer is estimated to be $\pm 24^\circ\text{C}$ in the range of 480 to 700°C and $\pm 12^\circ\text{C}$ in the range of 700 to 800°C (Henry et al., 2005).

3.4. Fluid inclusion thermobarometry

We measured 80 fluid inclusions in quartz from six samples spanning different depths and sample types to ascertain whether our samples contain fluid inclusions representative of the fluids characterized extensively by Rusk et al. (2008). We focused on measuring fluid inclusions in quartz that we analyzed by SEM and EPMA. Fluid inclusion homogenization temperatures, ice and clathrate melting temperatures, and inclusion types (based on the room temperature vapor bubble volume %: B35, B60, B15H, and B20; Rusk et al., 2008b) are shown in Table 5. Also shown are calculated bulk mole fractions of H₂O and CO₂, salinities (wt% NaCl equiv.), and densities (ρ).

B35 inclusions contain bubbles with approximately 35 vol% vapor at room temperature, and homogenize to liquid between 290 and 380°C, with a mean of 339°C (Fig. 13). Inclusions within single samples homogenize within 10 to 80°C of each other. Clathrate in B35 inclusions melts between 4 and 13°C while ice melts between -6 and 0°C, corresponding to salinities in the range of 1 to 5 wt% NaCl equivalent. Salinities range from 1 to 8 wt% NaCl equivalent for CO₂-bearing B35 inclusions for which we did not observe clathrate. The average density of B35 inclusions is 0.78 g/cm³. B35 inclusions contain 3 to 10 mol% CO₂, with a mean of 6 mol% (Table 5).

B60 inclusions have room temperature bubbles with approximately 60 vol% vapor. Those that homogenize to liquid were preferentially measured because those that homogenize to vapor were difficult to observe. B60 inclusions homogenize to liquid between 290 and 370°C, with a mean of 341°C (Fig. 13). Within single samples, B60 inclusions homogenize within 10 to 90°C of each other. Clathrate was observed in one B60 inclusion, melting at 8°C. In this same inclusion, ice melts at -4°C, corresponding to a salinity of 3 wt% NaCl equivalent. Ice in non-clathrate-bearing B60 inclusions melts between -5 and 0°C. Salinities for B60 inclusions for which we did not observe clathrate range from 0 to 7 wt% NaCl equivalent. The average density of B60 inclusions is 0.71 g/cm³. B60 inclusions contain 3 to 10 mol% CO₂, with a mean of 7 mol% (Table 5).

Table 5
Fluid inclusion homogenization temperatures, melting temperatures, and calculated compositions and densities

Sample	B type	T _h (°C)	T _{m(ice)} (°C)	T _{m(clath)} (°C)	X _{H2O}	X _{CO2}	wt% NaCl equiv.	ρ (g/cm ³)
<i>Butte granite quartz</i>								
BU_214_Q1-7	20	301.4	-6.9		0.90	0.04	9.7	0.96
BU_214_Q1-3	20	304.6	-8.3		0.89	0.03	11.3	0.97
BU_214_Q1-5	20	308.3	-6.2		0.91	0.04	8.8	0.95
BU_214_Q1-4	20		-6.5			0.00	9.9	-
BU_214_Q1-1	35	313.8	-4.9	11.9	0.89	0.10	1.0	1.03
BU_214_Q1-2	35		-6.7	12.4	0.91	0.08	1.9	1.04
BU_214_Q1-6	15H	278.4	-8.2		0.89	0.03	11.2	0.97
<i>Early dark micaceous vein</i>								
11185-3771_Q4-3	20	272.9	-5.0		0.92	0.04	7.3	0.94
11185-3771_Q4-2	35	313.4	-3.3		0.92	0.05	4.9	0.84
11185-3771_Q4-5	15H	190.1	-2.2		0.95	0.03	3.5	1.00
11185-3771_Q4-6	15H	230.4	-2.7		0.91	0.03	4.2	0.96
11185-3771_Q4-1	15H	313.8	-5.4		0.91	0.04	7.8	0.95
11185-3771_Q4-4	15H		-3.4			0.00	5.6	-
Bur_03_214_Q2-2	20	332.3	-5.9		0.91	0.04	8.5	0.95
Bur_03_214_Q2-1	20		-3.2			0.00	5.3	-
Bur_03_214_Q2-3	35	340.5	-4.5		0.91	0.05	6.5	0.85
Bur_03_214_Q2-4	35		-5.0			0.00	7.9	-
Bur_03_214_Q4-4	35	342.4	-3.6		0.89	0.07	5.0	0.71
Bur_03_214_Q4-2	35	346.2	-3.3		0.90	0.06	4.7	0.75
Bur_03_214_Q4-3	35		-1.7			0.00	2.9	-
Bur_03_214_Q4-1	60	354.1	-4.2		0.90	0.06	5.9	0.76
Bur_03_214_Q7-3	20	327.5	-4.2		0.92	0.04	6.3	0.93
Bur_03_214_Q7-6	20	341.4					-	-
Bur_03_214_Q7-4	35	354.6	-4.2		0.91	0.05	6.1	0.85
Bur_03_214_Q7-7	35	358.7					-	-
Bur_03_214_Q7-1	60	330.0	-4.3		0.90	0.06	6.1	0.80
Bur_03_214_Q7-5	60	349.7					-	-
Bur_03_214_Q7-2	60	351.4	-4.2		0.90	0.06	5.9	0.76
<i>Barren quartz vein</i>								
11185-3771_Q2a-5	20	207.2	-0.9		0.96	0.03	1.5	0.98
11185-3771_Q2a-6	20	262.1	-3.3		0.93	0.04	5.0	0.93
11185-3771_Q2a-7	20	268.3	-5.5		0.91	0.04	8.0	0.95
11185-3771_Q2a-4	35	281.5	-2.5	8.4	0.92	0.05	3.6	0.80
11185-3771_Q2a-8	15H	314.8	-3.9		0.92	0.04	5.8	0.89
11172-1847_Q3a-3	35	317.6	-4.9	5.0	0.93	0.04	4.1	0.71
11172-1847_Q3a-2	35	324.4	-4.8	3.1	0.94	0.03	4.5	0.70
11172-1847_Q3a-4	35	334	-3.3	8.8	0.91	0.07	2.9	0.72
11172-1847_Q3a-6	35	335.0	-3.4	4.2	0.94	0.04	4.4	0.71
11172-1847_Q3a-1	35	341.8	-5.0	7.1	0.93	0.05	3.6	0.70
11172-1847_Q3a-5	60	348.2	-5.7		0.82	0.13	6.7	0.55
11172-1847_Q3b-6	20	337.1	-5.1		0.91	0.04	7.4	0.90
11172-1847_Q3b-8	20	337.9	-4.0		0.92	0.04	5.9	0.89
11172-1847_Q3b-9	35	332.5	-4.3	7.5	0.92	0.05	3.5	0.70
11172-1847_Q3b-4	35	344.2	-3.9	6.2	0.93	0.05	3.9	0.69
11172-1847_Q3b-1	35		-4.9			0.00	7.7	-
11172-1847_Q3b-7	60	347.6	-3.8	7.8	0.90	0.09	2.1	0.47
11172-1847_Q3b-2	60		-4.5			0.00	7.1	-
11172-1847_Q3b-3	60		-3.4			0.00	5.6	-
<i>Quartz-molybdenite vein</i>								
10969-5699_Q3-3	20	251.8	-1.8		0.94	0.04	2.8	0.87
10969-5699_Q3-6	35	339.8	-0.4		0.93	0.07	0.6	0.73
10969-5699_Q3-8	35	339.9	-0.7		0.93	0.07	1.1	0.73
10969-5699_Q3-1	35	344.3	-1.8		0.92	0.07	2.7	0.74
10969-5699_Q3-2	35	352.6	-2.5		0.91	0.07	3.6	0.75

Table 5
Continued

Sample	B type	T _h (°C)	T _{n(ice)} (°C)	T _{m(clath)} (°C)	X _{H2O}	X _{CO2}	wt% NaCl equiv.	ρ (g/cm ³)
10969-5699_Q4-7	20	311.8	-1.4		0.94	0.05	2.2	0.86
10969-5699_Q4-6	20	325.7	-15.2		0.84	0.04	17.5	0.96
10969-5699_Q4-5	35	365.8	-3.2		0.90	0.07	4.5	0.71
10969-5699_Q4-2	35	366.1	-1.8		0.92	0.07	2.7	0.74
10969-5699_Q4-3	35	375.7	-1.6		0.93	0.05	2.5	0.82
10969-5699_Q4-4	15H	153.2	-2.7		0.92	0.06	4.0	0.79
<i>Pyrite-quartz vein</i>								
11135-2470_Q2b-3	20	292.4	-1.6		0.94	0.04	2.5	0.87
11135-2470_Q2b-4	20	356.9	-2.5		0.94	0.04	3.9	0.92
11135-2470_Q2b-1	35	375.2	-2.4		0.91	0.06	3.5	0.75
11135-2470_Q4-6	20	215.1	-1.1		0.95	0.04	1.8	0.90
11135-2470_Q4-7	20	274.6	-3.7		0.93	0.04	5.6	0.93
11135-2470_Q4-1	20	277.0	-3.5		0.93	0.04	5.3	0.93
11135-2470_Q4-5	20	286.5	-2.4		0.94	0.04	3.7	0.92
11135-2470_Q4-4	20	297.5	-2.2		0.93	0.05	3.3	0.83
11135-2470_Q4-2	20	299.4	-2.2		0.94	0.04	3.4	0.91
11135-2470_Q4-3	20		-1.1					
11135-2470_Q5-4	20	156.8	-1.8		0.95	0.03	2.9	0.95
11135-2470_Q5-3	20	246.6	-1.3		0.95	0.04	2.1	0.90
11135-2470_Q5-2	20	351.4	-1.0		0.96	0.03	1.6	0.98
11135-2470_Q5-1	15H	359.4	-1.9		0.92	0.06	2.8	0.78
<i>Porphyry quartz in GS alteration envelope</i>								
11135-2470_Q3-3	20	268.8	-1.7		0.94	0.04	2.7	0.91
11135-2470_Q3-5	20	274.4	-1.3		0.95	0.04	2.1	0.90
11135-2470_Q3-6	20	275.1	-1.1		0.94	0.05	1.7	0.82
11135-2470_Q3-4	20	282.3	-1.3		0.95	0.04	2.1	0.90
11135-2470_Q3-7	20		0.0					
11135-2470_Q3-1	35	304.6	-2.3		0.94	0.04	3.6	0.92
11135-2470_Q3-2	60	284.4	-2.0		0.93	0.05	3.0	0.83
11135-2470_Q3-8	60	364.3	0.0		0.95	0.05	0.0	0.81

X_{CO2} in italics are assumed values used in salinity calculations.

B20 inclusions contain a bubble with approximately 20 vol% vapor at room temperature, and homogenize to liquid over a large temperature range between 200 and 360°C, with a mean of 288°C (Fig. 13). Inclusions within single samples homogenize over a large range from 10 to 150°C of each other. Ice melts between -15 and -1°C corresponding to salinities of 2 to 18 wt% NaCl equivalent. The average density of B20 inclusions is 0.91 g/cm³. B20 inclusions contain 3 to 5 mol% CO₂.

B15H inclusions have room temperature bubbles with approximately 15 vol% vapor and contain halite daughter crystals. They homogenize by halite dissolution between 150 and 370°C, with a mean of 255°C (Fig. 13). No clathrate was observed and

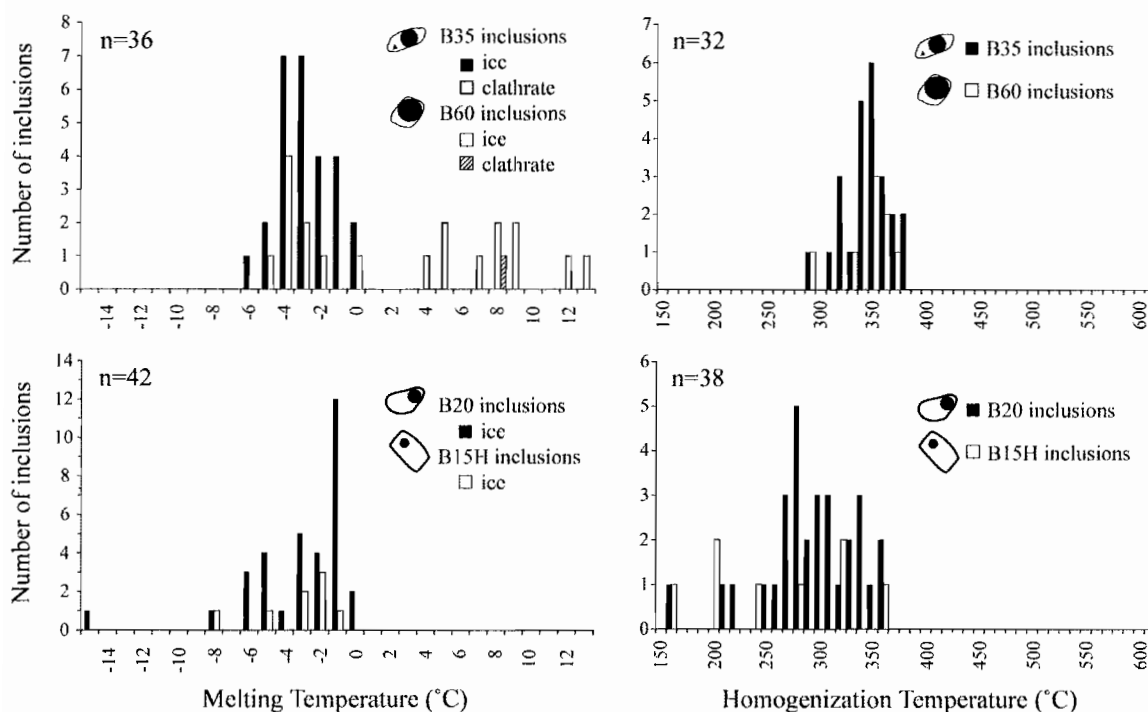


Fig. 13. Histograms showing fluid inclusion melting temperatures of ice and clathrate and homogenization temperatures in B35, B60, B20, and B15H inclusions from this study. n = number of fluid inclusions. Schematic shaded fields show temperature ranges from Rusk et al. (2008b).

ice melts between -8 and -2°C . Salinities range from 3 to 12 wt% NaCl equivalent. B85 inclusions were observed in samples containing B15H inclusions, however they were not measured as homogenization to vapor is difficult to observe. The average density of B35 inclusions is 0.92 g/cm^3 . B15H inclusions contain 3 to 6 mol% CO_2 .

Fluid inclusion homogenization temperatures for a given fluid inclusion type spread over $\sim 100^{\circ}$ to 210°C , similar to temperature spreads we found above for single generations of quartz and rutile within a given sample. Homogenization and melting temperatures from our sample suite fall within the range of those characterized by Rusk et al. (2008b) as shown in grey shaded fields in Fig. 13. Salinities and densities we calculate also overlap the ranges reported by Rusk et al. (2008b).

4. Discussion

4.1. *The magmatic-hydrothermal temperature connection*

There is broad agreement that porphyry-Cu deposits form directly from fluids exsolved from magma (e.g., Seedorff et al., 2005). Therefore, some early fluids must have been at magmatic temperatures, which could extend as low as ~650°C near the 300 MPa water-saturated granite solidus (Holtz et al., 2001), and would commonly be as high as ~750°C at the high H₂O contents (>5-6 wt%) and the 25% crystallinity we observe in the porphyries (Chapter III). Given a magmatic origin of the fluids, we expect that early-formed veins might reflect temperatures in the range of 650 to 750°C. A comparison of our findings from the three independent geothermometers (Fig. 14) establishes a temperature overlap at 650 to 750°C between the parental porphyry magma and hydrothermal veins at Butte. In addition, our data show a very substantial overlap of temperatures for all vein types. We discuss these temperature ranges below.

Temperatures of quartz formation from the Butte granite span a large range (720-925°C) that likely captures temperatures experienced throughout solidification of the granite (Fig. 14). The highest temperatures are from quartz with CL-bright porphyry-like growth bands (Fig. 4a), probably reflecting early crystallization when the granite still had a moderate melt fraction. The lowest temperatures are from CL-grey interstitial quartz representing late stages of quartz growth. Butte granite biotite temperatures (740-760°C) are much more restricted than those of quartz. Ti, Mg, and Fe are apparently highly mobile in biotite (Fig. 12a; Henry et al., 2005) and thus we interpret these restricted biotite temperatures to represent late solid-state recrystallization conditions at the end of the granite cooling history, overlapping with late stage interstitial quartz temperatures.

Temperatures from quartz phenocrysts in porphyry dikes overlap with those from the Butte granite by ~60°C but extend to much cooler temperatures, which is consistent with the more silicic composition and elevated H₂O content of the dikes (Chapter III). Phenocryst temperatures are somewhat cooler than estimates from geothermometry

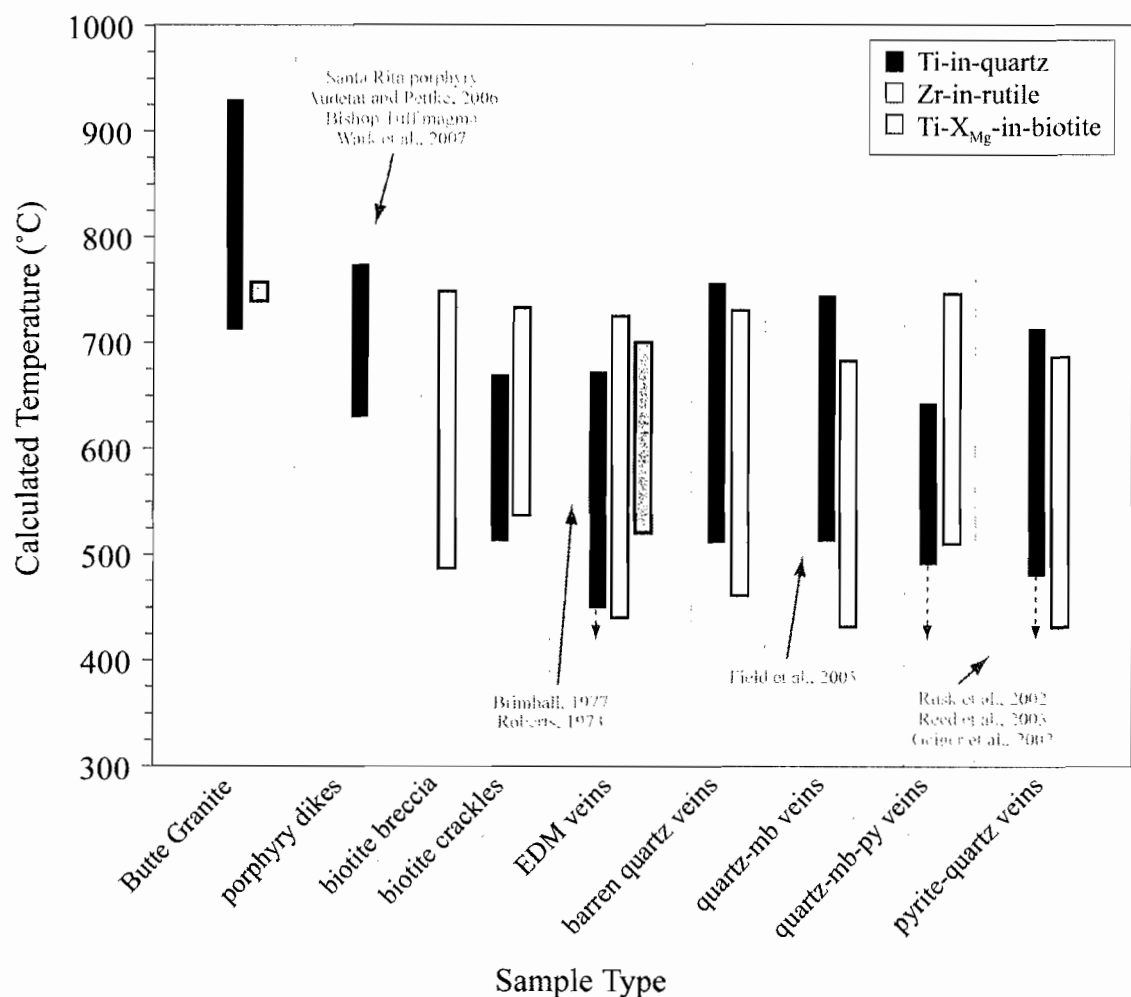


Fig. 14. Composite graph of temperatures calculated from Ti-in-quartz (black bars), Zr-in-rutile (white bars), and Ti-in-biotite (grey bars). Previous temperature estimates are shown in light grey shaded fields: Santa Rita rhyodacite porphyry dikes (magnetite-ilmenite and zircon saturation thermometry, Audétat and Pettko, 2006), Bishop Tuff rhyolitic magma (Ti-in-quartz geothermometry, Wark et al., 2007), EDM veins (K and Na partitioning between K-feldspar and muscovite in EDM vein envelopes, Brimhall, 1977; composition of coexisting ilmenite and hematite in EDM alteration envelopes, Roberts, 1973), quartz-mb veins (sulfur isotope geothermometry on adjacent molybdenite and anhydrite grains, Field et al., 2005), and pyrite-quartz veins (quartz solubility and SEM-CL observations, Rusk et al., 2002; thermodynamic fluid modeling of GS alteration envelopes from Reed, 2005 and Geiger et al., 2002). Dashed arrows indicate samples types with Ti concentrations below the detection limit.

of the Santa Rita rhyodacite porphyry dikes (730-760°C; Audétat and Pettke, 2006) and the analogous Bishop Tuff rhyolite (720-810°C; Wark et al., 2007). The spread in phenocryst temperature (630-770°C) reflects differences in Ti concentrations in alternating CL-bright and CL-grey growth bands that formed as the phenocryst grew during cooling of the parental magma at depth. As is common in rhyolites, the quartz phenocryst eyes at Butte have been resorbed and thus there is no rim from which to estimate the final dike injection temperature.

Biotite breccia and biotite crackle temperatures from quartz and rutile encompass a similar range of 490 to 740°C, which overlaps with porphyry dike temperatures by ~125°C as expected since they emanate directly from porphyry dikes. The highest temperatures recorded in these samples (~740°C) may provide a good estimate of magmatic dike injection temperatures. We hypothesize that the lower temperatures in biotite breccias and crackles are a result of variable cooling of magmatic fluids upon contact with cooler wall rock as the fluids hydrofractured through the Butte granite.

Maximum temperatures from EDM veins (725°C) are slightly lower than biotite breccias and biotite crackles, and they extend to cooler temperatures of ~450°C. We identified EDM quartz in CL images with concentrations lower than the Ti detection limit, thus temperatures likely extend to even cooler than 450°C. Temperatures of EDM shreddy biotite span a narrower range (520-700°C) and agree well with previous estimates based on K and Na partitioning in K-feldspar and muscovite (Brimhall, 1977) and on coexisting ilmenite and hematite pairs (Roberts, 1973). Rutile from paired analyses of EDM veins and envelopes has the same temperature to within one standard deviation in all but one sample (Fig. 9). These data indicate that EDM veins and envelopes formed over a large temperature range, perhaps due to variable cooling of fluids as for biotite breccias and crackles. The splotchy and mottled CL patterns (and Ti concentrations) in EDM quartz (Fig. 4d-e) may reflect this large temperature gradient. EDM veins likely formed by combined temperature drop and pressure drop, as indicated by fluid inclusions (Rusk et al., 2008b).

Barren quartz veins are most abundant in the deep core of the deposit, yielding upward to quartz-molybdenite veins, and cutting EDM veins. Most barren quartz and quartz-molybdenite veins have no alteration envelope and are hypothesized to have precipitated dominantly by a lithostatic to hydrostatic pressure drop (Rusk and Reed, 2002; Rusk et al., 2008b) as fluids traverse an up-and-out pathway along newly forming hydrofractures. Both vein types have similar quartz and rutile formation temperatures between 430 and 750°C. Two samples contain slightly higher temperature rutile within the vein than in the adjacent wall rock while other samples have similar temperatures (Fig. 9). The highest temperatures (~750°C) are similar to those in biotite breccias and biotite crackles and may reflect magmatic temperatures as the fluid emerged from the porphyry. The spread to cooler temperatures may represent a large temperature gradient within fluids expelled from a uniformly hot (~750°C) magmatic source that then cooled unevenly upon injection into cooler host rock. The splotchy and mottled CL patterns (and Ti concentrations) in quartz from these samples (Fig. 4g-k) may reflect this large temperature gradient as for EDM veins. B35 fluid inclusions which dominate in deep quartz-rich veins, record a spread of homogenization temperatures of 100 to 210°C (Fig. 13), that may reflect in part the temperature gradient. Our quartz and rutile temperature estimates for quartz-molybdenite veins (Fig. 14) overlap with previous estimates from molybdenum and anhydrite sulfur isotope geothermometry (Field et al., 2005) and expand the range upward by ~100°C and downward by ~50°C.

Pyrite-quartz veins with grey sericite (GS) alteration are prominent in the center of the district largely above the other vein zones and cut all other vein types. Quartz and rutile temperatures range from 440 to 710°C. We have identified quartz that has Ti concentrations below the detection limit so we expect quartz to extend to temperatures cooler than 450°C. Maximum quartz and rutile temperatures in the veins are slightly cooler than all other vein types (~700°C), yet they still consistently overlap with other high temperature vein and porphyry dike temperatures. Until this study, we have had no geothermometry to constrain GS temperature, and have assumed lower temperatures than for EDM because the GS veins form late, lack K-silicate alteration, and formed at

hydrostatic pressure, as indicated by the dominance of B60 fluid inclusions in these veins (Rusk et al., 2008b). The large spread in quartz and rutile temperatures in GS veins mimics the large spread in B60 fluid inclusion homogenization temperatures (Fig. 13, 80-160°C; Rusk et al., 2008b), which may reflect a large fluid temperature gradient as for the other types of veins. The common alternating CL-bright and -dark quartz bands (Fig. 4m-o) may indicate more organized euhedral growth from thermally mixed fluids, analogous to the blotchy textures noted in previous samples.

Some quartz-molybdenite veins grade into quartz-molybdenite-pyrite veins at shallow levels. Quartz and rutile temperatures for this type of vein are intermediate between the quartz-molybdenite veins and pyrite-quartz veins, show a large spread in temperature (500-740°C), and a variety of CL textures, similar to other quartz-molybdenite and GS samples.

Our data show a continuum in temperature between the magmatic and hydrothermal realms in the Butte system and demonstrate that the two realms overlap substantially. The parental porphyry magma is cool relative to volcanic rhyolitic magmas, which is reasonable given that it is particularly H₂O-rich (Chapter III). The temperatures of hydrothermal breccias and veins are higher than previously recognized, however these data support decades of research on porphyry deposits that show an intimate genetic connection between porphyries and mineralized stockwork veins. These data also show that hydrothermal veins generally form within the same temperature range as their alteration envelopes, indicating a small time gap between the two.

4.2. Porphyry deposit thermal profile

Starting with the early Butte maps by Meyer et al. (1967) where the shape of the distribution of Butte quartz-molybdenite veins was described as “the moly dome”, the distribution of Butte alteration zones mapped as metasomatic isograds describe domical shapes around the mineralization centers (e.g., Fig. 3). Although the dome forms are

accurate as isograds, our new data suggest that they do not portray the temperature distribution at any given time; i.e., we should not regard the isograds as isotherms.

CL textures and corresponding temperatures in vein quartz indicate that the large temperature spreads within each sample are ubiquitous and hold significant clues to the complex process of porphyry deposit formation. We interpret the highest temperatures from early, deep hydrothermal veins (750°C) to approximate the magmatic temperature at the time of dike injection and fluid release. These same veins have minimum temperatures (~500°C) that are above the detection limit for our geothermometry methods. Because a hydrothermal vein would not cool below the ambient host rock temperature, we interpret these minimum hydrothermal temperatures to be upper limits for the host rock temperature at the time of vein formation. The large temperature spread within veins between these two thermal limits may record variable cooling of hot (750°C) fluids upon contact with cooler (~500°C) wall rock as hydrofracturing supplied hydrothermal fluids to the crust.

In separate thermal models of hot fluid injection into hydrofractures within cooler rock (Chapter V) we find that for a fluid-rock temperature difference of 200°C, the time necessary for the fluid to cool to near the rock temperature ranges from minutes to hours. Quartz precipitating over this time frame in a single vein would form at temperatures spanning nearly 200°C. Considering that single hydrofracturing fluid injections likely extend at least two km vertically as indicated by biotite crackles that reach >2 km from the deep fluid source and quartz-molybdenite veins that extend over 2 km, it seems reasonable that hot magmatic fluids may reach shallow portions of the system without extensive cooling on relatively short time scales.

Many “anomalous” cross-cutting relationships (Seedorff et al., 2005) in our sample suite indicate that vein formation temperatures fluctuate up to 130°C within a single cm³ parcel of rock. For example, Fig. 4g shows a CL-grey EDM vein with a mean temperature of 544°C that is cut by a CL-bright barren quartz vein with a mean temperature of 674°C. This observation suggests that the temperatures we find in this study represent discrete cycles of transitory high temperature dike intrusions,

hydrofracturing, and vein formation which overprints the cooler background host rock thermal gradient that may be domical about the magmatic-hydrothermal center. Indeed as Roberts (1975) pointed out, fresh Butte granite between stockwork veins that reach upwards of 750°C shows no trace of re-melting and thus was unlikely to have been pervasively heated to 750°C.

In summary, we speculate that a dome-shaped host rock thermal gradient about the magmatic-hydrothermal center did exist, but did not reach the high temperatures recorded in hydrothermal veins. Instead, minimum vein temperatures ($\leq 500^\circ\text{C}$) more likely represent this background thermal state and the higher temperatures we record in this study are in fact transitory thermal spikes that grow with episodes of dike and fluid injection and cool relatively quickly, to the background host rock thermal state.

4.3. Reevaluation of fluid inclusion thermobarometry: Butte goes from deep to deeper?

Butte has been identified as an unusually deep porphyry deposit compared to most, which are inferred to form at 1-5 km depth (Seedorff et al., 2005). Indirect evidence for Butte's depth comes from detailed regional mapping, which shows that the carapace of cogenetic late Cretaceous Elkhorn Mountains Volcanics is missing over the Butte granite indicating deep erosion in the Butte district (Tilling, 1973). Dilles et al. (1999) applied the Al-in-hornblende geobarometer to samples from the Butte granite and estimated that it crystallized at $\sim 9.5 (\pm 2)$ km depth near the Continental Pit and $\sim 7.5 (\pm 2)$ km near the Berkeley Pit, consistent with >1 km of normal displacement along the Continental Fault (Fig. 2). Because the Butte granite was emplaced ≥ 10 Ma before porphyry mineralization at Butte (Lund et al., 2002), these estimates do not provide direct porphyry mineralization depths.

The only direct estimates of porphyry mineralization depths come from fluid inclusion thermobarometry. Roberts (1975) estimated that early vein formation at Butte occurred at ~ 6 km (~ 200 MPa) based on combined mineralogical and fluid inclusion studies. Rusk et al. (2008b) assumed fluid inclusion entrapment temperatures of

550-650°C for deep early dark micaceous, barren quartz, and quartz-molybdenite veins, to make the necessary isochoric adjustments to determine pressures of vein formation. These temperatures were based on estimates from EDM alteration envelope assemblages (Brimhall, 1977; Roberts, 1973) and sulfur isotope thermometry (Field et al., 2005), and indicate formation pressures of 170 to 270 MPa, with the majority of inclusions indicating between 200 and 250 MPa. Assuming lithostatic pressures and a rock density of 2.85 g/cm³, this corresponds to mineralization depths of 6-9 km (Rusk et al., 2008b).

Our results from the three independent geothermometers suggest that the range of formation temperatures for hydrothermal veins reaches hotter temperatures than previously recognized, and thus a reevaluation of pressure estimates is warranted. Hydrothermal phase relations depicted in Fig. 15 show inferred formation conditions of hydrothermal veins from Butte. The heavy black line represents the liquid+vapor saturation curve for a hydrothermal fluid containing 4 wt% NaCl and 5 mol% CO₂. Thin black lines show isochors (g/cm³) for the same fluid. Light grey shaded fields show fluid entrapment pressure-temperature estimates from Rusk et al. (2008b). Our study extends the upper limit of formation temperatures for EDM, barren quartz, quartz-molybdenite, and pyrite quartz (GS) veins as shown with dark grey shaded fields and fine dashed arrows. For a temperature of 750°C, fluid inclusions indicate formation pressures extending from 270 to 370 MPa (Fig. 15). Under lithostatic pressures with a rock density of 2.85 g/cm³, this higher pressure range corresponds to 8-11 km depth. Although these new thermobarometric interpretations imply that Butte may have formed at even greater depths, 8-11 km is within the range of estimates from Al in hornblende geobarometry (Dilles et al., 1999). Discussion of the unusually great depths of formation of the Butte deposit is discussed in Chapter III.

To examine how these results fit into the magmatic realm, we have overlaid magmatic phase relations onto the pressure-temperature diagram in Fig. 15. The experimentally determined haplogranite water-saturated solidus curve (heavy grey line) and liquidus curves (Holtz et al., 2001) for given amounts of H₂O in the bulk magma (thin grey lines) are shown along with dashed grey lines indicating approximate

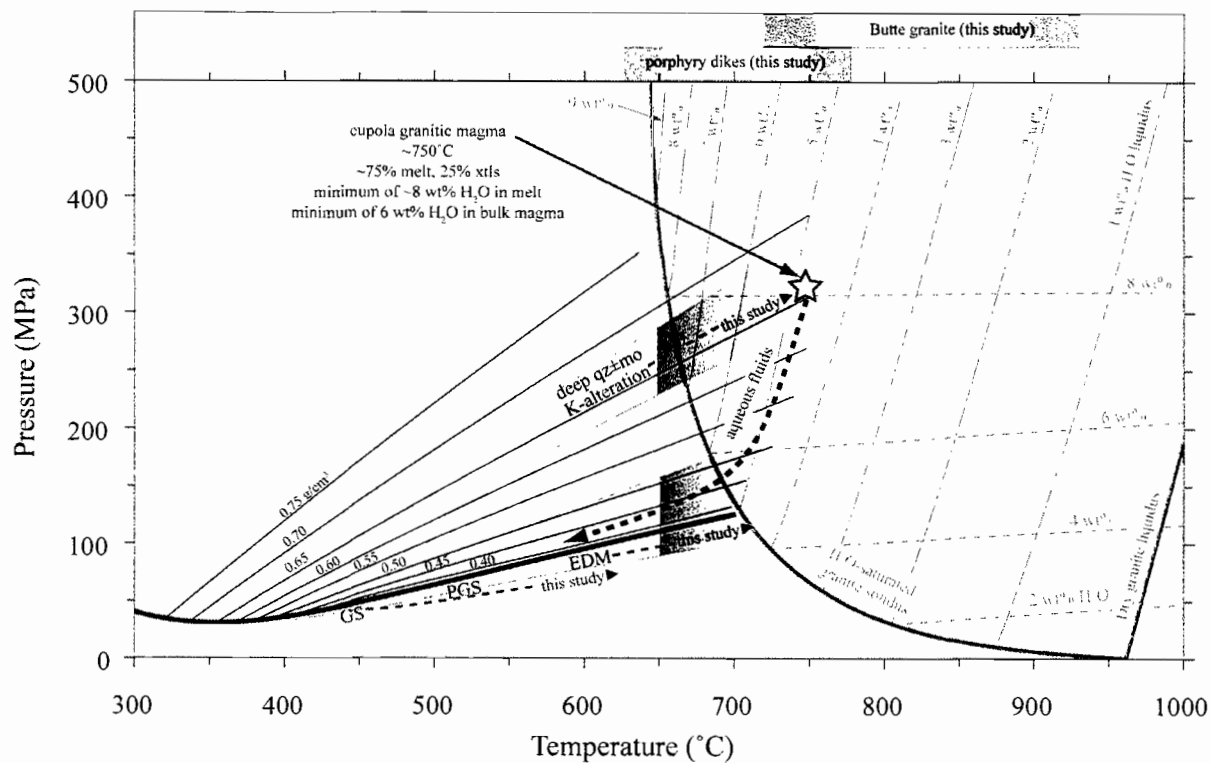


Fig. 15. Pressure-temperature diagram for hydrothermal and magmatic components. Liquid + vapor saturation curve for a fluid containing 4 wt% NaCl and 5 mol% CO₂ is shown with a heavy black line. Isochores (g/cm³) for the same fluids are shown with thin black lines (Rusk et al., 2008b). Fluid entrapment P-T estimates from Rusk et al. (2008b) are shown with light grey shaded fields. This study extends the upper limit of temperatures for EDM veins, barren quartz veins, quartz-mb veins, and pyrite-quartz (GS) veins as shown with dark grey shaded fields and dashed arrows. The haplogranite water-saturated solidus curve (heavy grey line) and liquidus curves (thin grey lines) for given amounts of H₂O are shown from Holtz et al. (2001). Approximate H₂O-saturation curves for given amounts of H₂O are shown with thin dashed grey lines (modified from Holtz and Johannes, 1994). Temperature range for porphyry dikes and Butte host granite are shown at the top with dark shaded fields. Star shows approximate P-T conditions of magmatic and hydrothermal overlap where intrusion of H₂O-saturated porphyry dikes (~8 wt% H₂O in melt, or ~6 wt% H₂O in bulk magma with 25% crystals; Chapter III) can release aqueous fluids that are trapped in nearby deep, barren quartz (±mb) veins along appropriate isochors (this study; Rusk et al., 2008b). Decompression and cooling of these same fluids leads to EDM, PGS, and GS vein formation as described by Reed (1999).

H₂O-saturation curves for given amounts of H₂O in the melt (Holtz and Johannes, 1994). The temperature range for porphyry dikes and the Butte host granite from this study are shown at the top of the P-T diagram with dark shaded fields. Superposition of magmatic-hydrothermal phase relations demonstrates that the H₂O-saturated Butte porphyritic magma with ~25% phenocrysts and ~6 wt% H₂O (Chapter III) at ~750°C would be above its solidus and could reasonably release aqueous magmatic fluids into the overlying crust to form porphyry style mineralization under conditions indicated by Butte fluid inclusions.

5. Conclusions

Our results demonstrate the thermal connection between the magmatic and hydrothermal realms of the porphyry-Cu-Mo deposit at Butte, Montana. The two realms overlap at 650 to 750°C, supporting the long held interpretation that mineralizing fluids emanate directly from porphyry magma. Maximum temperatures from early, deep hydrothermal veins (750°C) approximate magmatic temperatures at the time of dike injection and fluid release and minimum temperatures (~500°C) provide an upper limit for the host rock temperature at the time of vein formation. Hydrothermal veins generally form within the same temperature range as their alteration envelopes, indicating a small time gap between the two. We suggest that the temperatures we find in this study represent discrete cycles of transitory high temperature dike intrusions, hydrofracturing, and vein formation which overprints the cooler background host rock thermal gradient. Our results suggest that the range of formation temperatures for hydrothermal veins reaches hotter temperatures than previously recognized. In light of this discovery, we have re-examined fluid inclusion barometry and found that the porphyry deposit at Butte could have formed at 8-11 km depth, slightly deeper than previously thought.

6. Bridge

In Chapter IV, I described the temperature overlap between the magmatic and hydrothermal realms of a porphyry copper deposit. In Chapter V, I evaluate the timescales for porphyry deposit formation and cooling, and I discuss the episodic nature of these magmatic-hydrothermal systems.

CHAPTER V

TIMESCALES OF PORPHYRY-Cu DEPOSIT FORMATION: INSIGHTS FROM SEM-CATHODOLUMINESCENCE AND TITANIUM DIFFUSION IN QUARTZ

This chapter is in preparation to be submitted to *Economic Geology*. This paper was co-authored with Mark H. Reed, who provided advising, editorial support, and funding for this project.

Introduction

Porphyry copper deposits around the world show clear evidence that they form where fluid over pressurization in a magmatic cupola produces pulses of hydrofracturing, porphyry dike injection, brecciation, and stockwork veining (Burnham, 1979; Cline and Bodnar, 1991; Dilles, 1987; Seedorff et al., 2005; Titley and Beane, 1981). Metal and sulfur-rich aqueous fluids permeate the fractured rock causing host-rock alteration and depositing quartz and disseminated Cu and Mo sulfides in stockwork veins and breccias. Decades of study of porphyry deposits have advanced our knowledge of magmatic and tectonic controls on porphyry mineralization, hydrothermal alteration zones, mineralization patterns, and hydrothermal fluid evolution (e.g., Candela and Piccoli, 2005; Cloos, 2001; Cooke et al., 2005; Dilles and Einaudi, 1992; Guillou-Frottier and Burov, 2003; Landtwinning et al., 2005; Richards, 2003; Rusk et al., 2008b; Seedorff et al., 2005; Tosdal and Richards, 2001), yet much remains to be understood about the timescales of porphyry-Cu processes. Our goal is to examine the fundamental question of timing and duration of porphyry dike magmatism and hydrothermal vein formation in the porphyry-Cu-Mo deposit at Butte, Montana (Fig. 1).

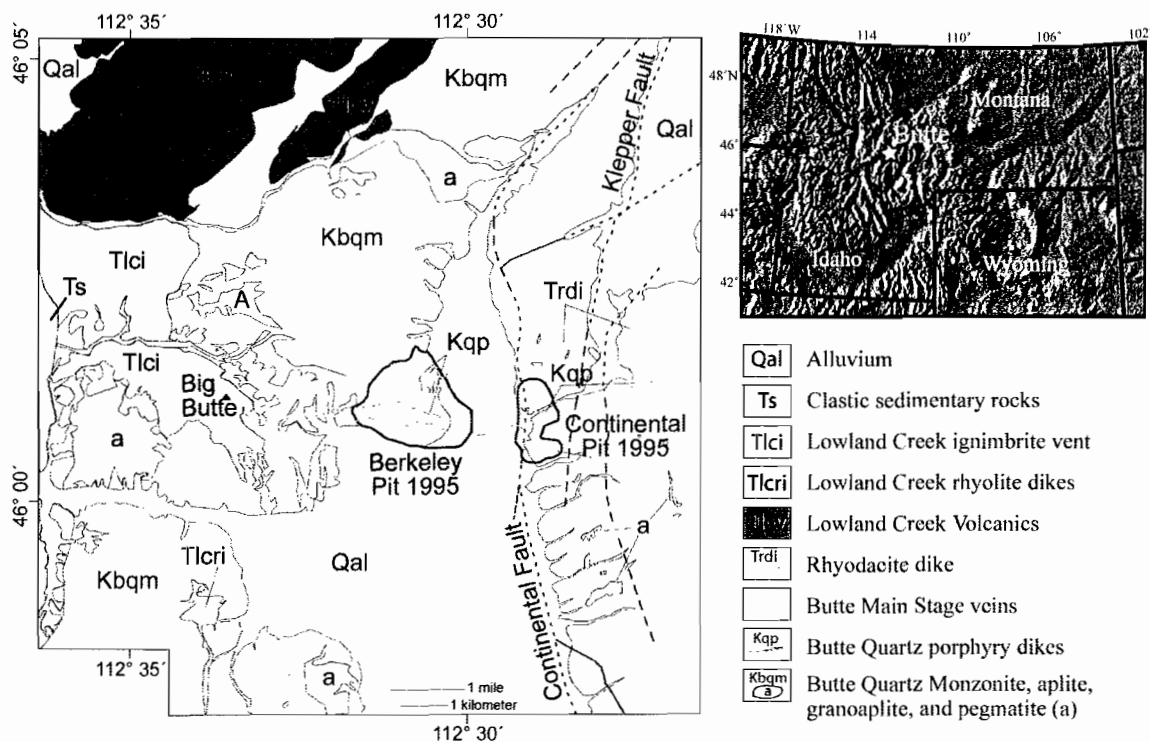


FIG. 1. Location map and regional geologic setting of the Butte district (modified from Rusk et al., 2008b).

Several studies have provided absolute age constraints for the porphyry deposit at Butte. U-Pb zircon ages suggest that the Butte porphyries date to 65.7 (± 0.9) Ma (Lund et al., 2002). Porphyry-style “pre-main stage” mineralization occurred in two pulses, each lasting 1 Ma. The first pulse produced the Pittsmond dome from 66.4 to 65.8 (± 0.2) Ma while the second pulse produced the Anaconda dome from 64.5 to 63.9 Ma (Fig. 2; Dilles, personal communication). Cross-cutting relationships, U-Pb monazite ages, and Ar-Ar ages show that pre-main stage porphyry mineralization was followed by another porphyry injection at 64 (± 1) Ma (Dilles et al., 2003), after which “main stage” base metal lodes formed from 63.0 to 61.5 (± 0.2) Ma (Snee et al., 1999; Dilles, personal communication). U-Pb zircon dates show that all of these magmatic and hydrothermal generations were cut by post-mineralization rhyolite dikes between 62.7 (± 1.5) (Lund et al., 2005) and 60.4 (± 0.3) Ma (Dilles et al., 2003).

These absolute age constraints reveal that the deeper portions of the deposit formed after the shallower portions, but it is not yet clear how long individual dike injections and stockwork veins took to form during each 1 Ma time window. A widely accepted idea for porphyry-Cu formation is that fractured crust overlying the magma source “stews” in hot, magmatic fluids for several Ma during which multiple generations of cross-cutting hydrothermal veins form. Contrasting with this notion, modeling of reactive transport in sericitic alteration envelopes (1-2 cm), which are common in pre-main stage pyrite-quartz stockwork veins, suggests that alteration envelopes could have formed in <100 yr (Geiger et al., 2002). If this is true for alteration along other stockwork vein types as well, a model of short lived, episodic fluid injections which span several Ma may be a more accurate explanation of porphyry-Cu deposit generation.

In this study, we investigate the formation and cooling timescales of quartz from porphyry dike intrusions and a variety of pre-main stage veins from Butte. Scanning electron microscope-cathodoluminescence (SEM-CL) images reveal detailed quartz growth histories and microprobe trace element analyses verify that Ti is the primary CL-activator in high temperature magmatic and hydrothermal quartz from Butte. By calibrating relative CL brightness to corresponding Ti concentrations, we use brightness gradients as a proxy for Ti gradients within our samples. We model the diffusion of Ti between distinct quartz generations in order to determine the timescales of quartz precipitation and cooling for magmatic and hydrothermal quartz throughout the porphyry deposit. To create a temporal reference point to compare to chemical diffusion timescales, we model heat conduction thermal profiles for a rhyolitic dike, quartz vein, and hydrothermal fluid injection.

Geologic setting and sample suite

Magmatic and hydrothermal quartz from pre-main stage porphyry-Cu-Mo mineralization at Butte, Montana were selected from porphyry dikes and stockwork veins at various depths (Table 1, Fig. 2). The Butte porphyry deposit is centered on an east-west striking swarm of early Paleocene rhyolitic dikes (Fig. 1) that intruded the late

Table 1. Sample Locations, Descriptions, and Modeled SEM-CL Boundary Types

Location	Sample no.	Location	Elevation (m)	Sample type	Host/vein/alteration	Modeled SEM-cathodoluminescence boundary types					
						(1) Phenocryst growth zones	(2) Euhedral vein zones	(3) CL-grey veinlets	(4) Intragranular variations	(5) Cemented breccia	(6) Microfractures + grain boundaries
<i>West of CF</i>											
Pittsmt	11185-3771	DH 11	553	vein	BG/qz-cp//EDM cut by qz-cp-py//NA	-	-	x	x	-	x
Pittsmt	11135-2470	DH 2	965	ppy/vein	ppy/py-qz//GS	x	x	-	-	-	-
Pittsmt	11135-2-4209	DH 2	435	ppy/vein	ppy/qz-mb//NA cut by barren qz//NA	x	-	x	x	-	-
<i>Pervasive GS Zone</i>											
Central GS zone	10969R-2075	DH 1	1063	vein	BG/py-qz//GS	-	-	-	-	x	-
Central GS zone	10969-2101	DH 1	1055	vein	BG/py//GS cut by qz-mb-py//GS	-	x	-	-	-	-
Central GS zone	10969-2665	DH 1	884	vein	BG/py-qz-op//GS cut by qz-mb-py//NA	-	-	-	-	x	-
Central GS zone	10969-5699	DH 1	-41	vein	aplite/qz-mb//NA	-	-	-	x	-	x
<i>Qz Vein Stockwork</i>											
Central	10969-6804	DH 1	-378	vein	aplite/qz-mb//NA cut by qz//NA	-	x	x	-	-	x
Pittsmt	11135-5461	DH 2	53	vein	aplite/qz//NA	-	-	x	-	-	x
<i>Shallow GS</i>											
Anaconda	F2033-488	DH F2033	1165	vein	BG/qz-py-cp//EDM	-	x	-	-	x	-
Anaconda	F2033-513	DH F2033	1165	vein	BG/qz-mb//NA cut by qz-mb//NA	-	x	-	-	x	-
Pittsmt	11067-1	5480 bench	1670	ppy	none	x	-	-	-	-	x
Pittsmt	11135-1150	DH 2	1368	vein	BG/qz-py-cp//EDM	-	-	-	-	x	-
<i>East of CF</i>											
Pittsmt	11172-1847	DH 10	1247	vein	BG/bi crackles cut by qz//NA	-	-	-	-	-	x
Pittsmt	BUR-03-214	6080 bench	1853	vein	BG/qz-py//EDM	-	-	-	-	-	x

Abbreviations: CF = Continental Fault, DH = drill hole, BG = Butte granite, ppy = porphyry dike, qz = quartz, py = pyrite, cp = chalcopyrite, mb = molybdenite, bi = biotite, op = open, EDM = early dark micaceous, GS = grey sericitic, NA = no alteration.

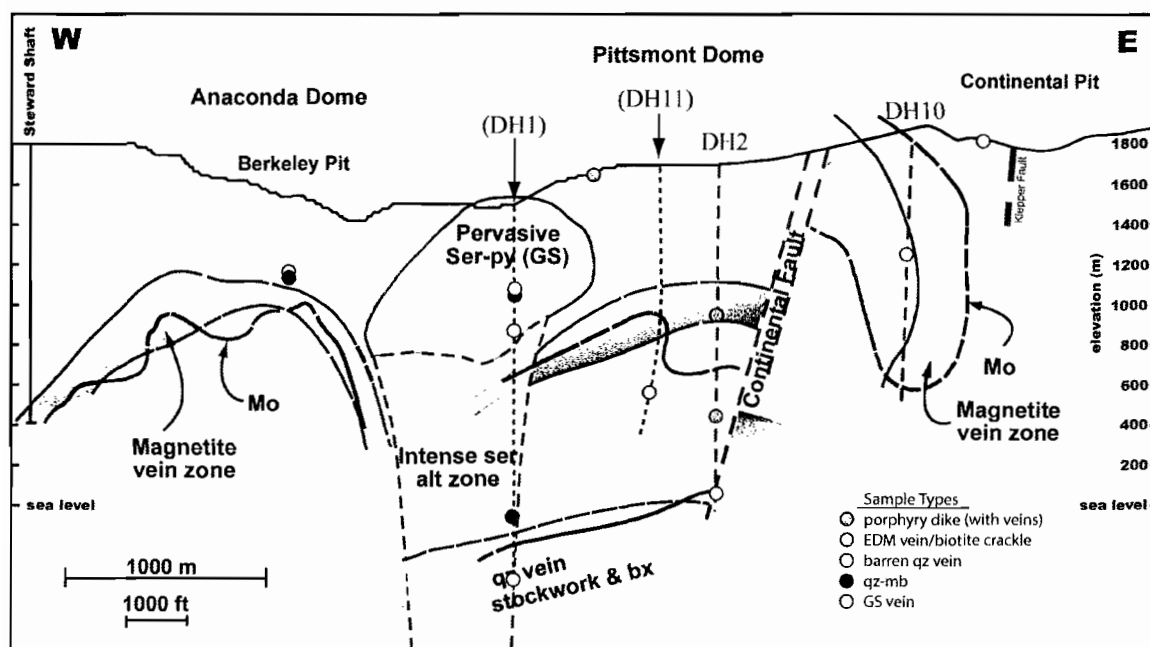


FIG. 2. East-west cross section of pre-main stage porphyry-Cu-Mo mineralization at Butte. To the west is the Anaconda dome and to the east is the Pittsmond dome. These domes are defined by a zone of abundant magnetite veins (purple) and by Mo grade contours (blue lines). The Continental Fault displaces the Pittsmond dome upward by ~1,300 m. Dashed lines indicate drill holes (DH) and mine shafts (those in parentheses indicate drill holes projected into this section). Colored circles represent sample locations for this study.

Cretaceous Butte granite (Meyer et al., 1968). Two major domes of Cu and Mo mineralization, the Pittsmond dome and the Anaconda dome, are separated by a bulb shaped zone of pervasive grey sericitic alteration (Reed, 1999). Our samples encompass a variety of mineralization types from both domes and the central zone of intense sericitic alteration. Porphyry dike samples are typically hydrothermally altered and cut by stockwork veins. Stockwork vein samples include barren quartz veins and quartz-molybdenite veins without alteration envelopes, quartz-chalcopyrite-pyrite veins with early dark micaceous (EDM) biotite-K-feldspar-sericite alteration envelopes, and pyrite-quartz veins with grey sericitic (GS) alteration envelopes, as explored in Chapter IV and by Rusk et al. (2008b). Our SEM-CL and microprobe analyses of 15 samples focused

primarily on characterizing quartz growth bands and cross-cutting generations of quartz veins with differing Ti concentrations that were used in Ti diffusion modeling with the aim of providing constraints on the timing and duration of hydrofracturing, porphyry dike injections, and vein formation.

Methods

SEM-cathodoluminescence

We acquired SEM images at the University of Oregon using an FEI Quanta 200 FEG scanning electron microscope equipped with an Oxford Instruments cathodoluminescence detector. Doubly polished 200 μm thick sections were carbon coated (15-20 nm) and analyzed at 10 keV with a beam current of 0.5-5 nA, depending on the luminosity of the quartz. We collected more than 300 SEM-CL images of igneous and hydrothermal quartz with corresponding SEM-backscattered electron (BSE) and secondary electron (SE) images. CL emissions from Ti in quartz are characteristically blue (Götze et al., 2001; van den Kerkhof et al., 2001), so we recorded grey-scale SEM-CL images captured using a blue filter to obtain the clearest SEM-CL images that incorporated Ti emissions, minimized microprobe beam damage spots, surface contamination, and bright streaks from highly fluorescent minerals (e.g., apatite) that otherwise over-saturate the signal.

Microprobe trace element traverses and mapping

Trace element concentrations in quartz were measured using a Cameca SX-100 electron microprobe at the University of Oregon operated using one setup optimized for non-destructive, high sensitivity spot analyses and another optimized for trace element mapping. Both setups were chosen to minimize sample damage to preserve the samples for additional analyses. We chose to measure Ti, Fe, K, and Al because these have been identified as CL-active in quartz (Landtwing and Pettke, 2005; Müller et al., 2003a), and their concentrations are known from previous work to be unique within particular

generations of magmatic and hydrothermal quartz from Butte (Rusk et al., 2008a; Rusk et al., 2006).

Spot analyses of quartz were acquired using a 15 keV accelerating potential, a 200 nA beam current, and a 20 μm spot size. Ti was measured simultaneously on two spectrometers while Fe, K, and Al were measured on the remaining spectrometers. The “aggregate intensity” technique (Lowers et al., in review) was applied using Probe for Windows software to improve Ti counting statistics. Ti, Fe, K, and Al were counted for 600 s on-peak and 600 s off-peak. Synthetic rutile was used as a Ti standard, synthetic magnetite was used for Fe, and natural orthoclase was used for K and Al. To reduce systematic continuum artifact errors, a matrix “blank” correction was applied to the Ti data using a synthetic quartz standard as a Ti-free blank (Lowers et al., in review). Detection limits (99% confidence) achieved on spot analyses are 3 ppm for Ti, 12 ppm for Fe, 11 ppm for K, and 6 ppm for Al. We avoided analyzing quartz within 100 μm of rutile whiskers to avoid excitation of Ti atoms by Bremsstrahlung radiation (e.g., Wark and Watson, 2006), and consequent erroneously high Ti concentrations in quartz analyses contaminated by rutile were easily identified and eliminated, as were those contaminated by other minerals such as sericite, magnetite, or K-feldspar.

High sensitivity, low resolution trace element mapping of one sample was carried out using a spectrometer setup similar to the spot analyses, however counting times for Ti, Fe, K, and Al were reduced to 300 s on-peak and 300 s off-peak to reduce analysis time resulting in a small loss of sensitivity. Despite this, mapping consumed ~70 hours of instrument time. Detection limits (99% confidence) achieved on these maps are 7 ppm for Ti, 19 ppm for Fe, 13 ppm for K, and 9 ppm for Al, only slightly higher than for spot analyses. Maps were created by acquiring 20 μm spot analyses within a 120x680 μm rectangle that we interpolated with a kriging technique using *Golden Software Surfer 8.0*.

SEM-CL brightness as a proxy for Ti concentration in quartz

The apparent CL image brightness is a function of operating conditions, such as carbon coat thickness, beam conditions, bias, and gain (Götze et al., 2001; Marshall,

1988). We kept these instrument variables nominally constant except for the beam current, which we had to change depending on the luminosity of the quartz. For the following discussion, relative CL brightnesses are described as CL-dark, CL-grey, and CL-bright.

Our analyses of trace element concentrations in relation to CL brightness described below show that brightness correlates positively with Ti concentration, but is independent of other trace elements. This correlation enabled us to calibrate a subset of SEM-CL images with microprobe data so that the relative CL brightness could be attributed to known concentrations of Ti in quartz. Quantification of relative CL brightness profiles within each image was accomplished using the program *ImageJ*. Raw relative brightness profiles were smoothed using a 9 pixel averaged sliding bin. CL profiles were then calibrated for Ti using microprobe spot analysis profiles. Once we rigorously established this technique for several samples, we were able to calibrate additional CL profiles using relatively few microprobe analyses. This technique allowed us to take advantage of the high spatial resolution of CL images, which record detailed sample history, and minimize the need for costly microprobe trace element analyses.

Ti diffusion in quartz and time scales

Different generations of magmatic and hydrothermal quartz visible in CL have distinct Ti concentrations and gradients, allowing for modeling Ti diffusion in quartz of different generations. Diffusion is modeled as simple one dimensional, concentration-independent diffusion in a semi-infinite medium (Carslaw and Jaeger, 1947) using the equation:

$$C(x,t) = \frac{c_{\min} + (c_{\max} - c_{\min})}{2} * \operatorname{erfc}\left(\frac{x}{2\sqrt{Dt}}\right), \quad (1)$$

where C is the concentration of Ti in quartz along a gradient between two distinct quartz generations with different Ti concentrations, x is the distance from the center of the gradient to the edge of the gradient, t is the time for diffusion, c_{\min} and c_{\max} are the minimum and maximum Ti concentrations, and D is the diffusivity of Ti in quartz.

Diffusivity is a function of temperature and has been experimentally calibrated by Cherniak et al. (2007). The diffusivities used in this study are summarized in Table 2. An example of model results is shown in Fig. 3 along with a time series of schematic diagrams depicting the change in CL gradients associated with Ti diffusion.

Several assumptions must be made to model the diffusion of Ti in quartz as illustrated in Fig. 3. First, we assume that Ti is the sole CL activator and thus differences in CL brightness are directly proportional to differences in the concentration of Ti in quartz. Second, we assume that all modeled CL boundaries were initially sharp and became diffuse over time at high temperature. Third, we assume diffusion took place at a constant temperature. Formation temperatures for all generations of quartz in this study were determined in Chapter IV using the Ti-in-quartz geothermometer of Wark and Watson (2006). We model diffusion at the maximum estimated temperature that any given quartz boundary may have experienced. For example, for a quartz phenocryst with

Table 2. Temperatures and Ti Diffusivities Used in Modeling

Model T(°C)	Diffusivity, D ($\mu\text{m}^2/\text{s}$)
<i>experimentally determined, parallel to c-axis:</i>	
735	6.08×10^{-10}
725	4.97×10^{-10}
700	2.99×10^{-10}
675	1.80×10^{-10}
650	1.09×10^{-10}
<i>extrapolated from experiments, parallel to c-axis:</i>	
600	3.94×10^{-11}
590	3.22×10^{-11}
565	1.94×10^{-11}
560	1.75×10^{-11}
550	1.43×10^{-11}
530	9.55×10^{-12}
520	7.80×10^{-12}
500	5.20×10^{-12}
480	3.47×10^{-12}
470	2.83×10^{-12}

Diffusivities from the experiments of Cherniak et al. (2007).

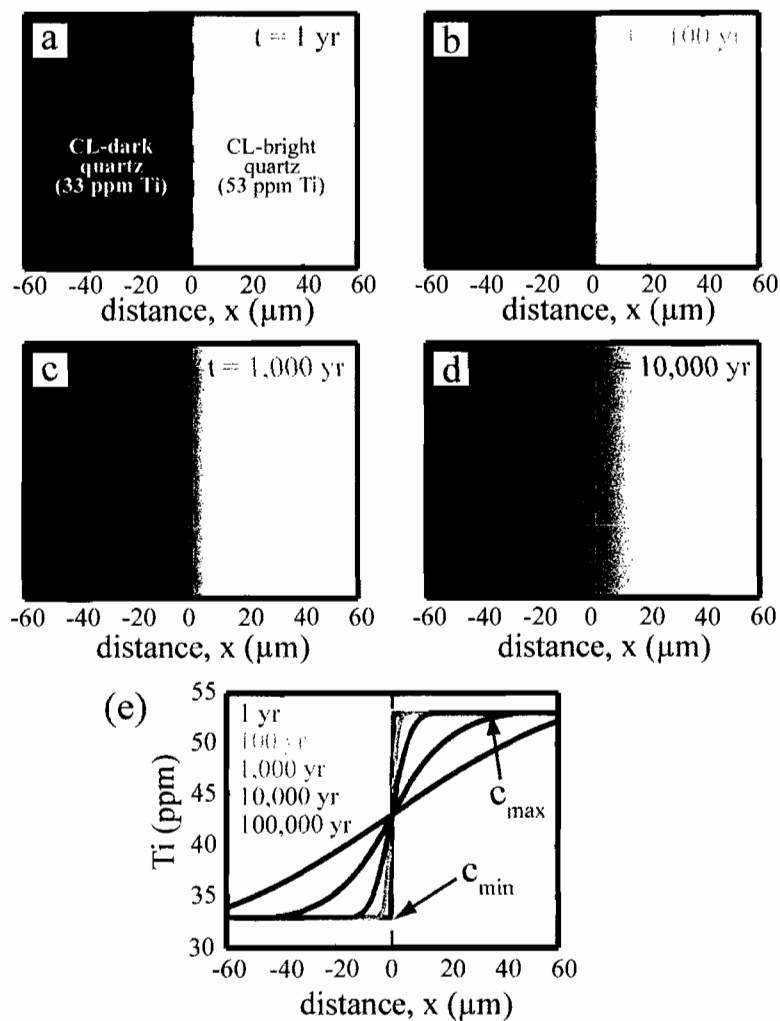


FIG. 3. Schematic diagram of cathodoluminescent brightness changes caused by diffusion of Ti in quartz at 600°C . (a) Initially, CL-bright quartz (53 ppm Ti) is cross-cut by CL-dark quartz (33 ppm Ti) and a sharp Ti gradient of 20 ppm exists. Over time (t , years) Ti diffuses smearing out the boundary between the two generations of quartz (b,c,d). Dashed line indicates original sharp boundary. (e) One dimensional model showing Ti concentration, C , as a function of x , the distance from the center of the gradient to c_{max} or c_{min} , and t , the time for diffusion in years.

a relatively Ti-poor, CL-grey core formed at 675°C that was overgrown by Ti-rich, CL-bright quartz at 720°C (Fig. 4a), we assume the core-rim boundary experienced the hotter temperature, and thus we model the core-rim boundary at the temperature of the later quartz generation, 720°C. Alternatively, for a CL-bright, Ti-rich hydrothermal quartz vein formed at 660°C that was cut by a CL-grey, Ti-poor 530°C quartz veinlet (Fig. 4c), we assume the first quartz had cooled to 530°C and we model diffusion at 530°C. Lastly, we do not take into account directly the fact that the quartz continues to cool below its formation temperature, during which time Ti can diffuse until $\leq 400^\circ\text{C}$, where diffusion of Ti is so slow that Ti gradients are essentially “frozen in”, but we do examine the implications of this process. We defined 400°C as the effective closure temperature because below this temperature, there is no significant Ti diffusion on the million year timescale of porphyry formation we are interested in. For example, at 400°C, an initially sharp Ti gradient will diffuse $\sim 20 \mu\text{m}$ in 1 Ma, potentially producing boundaries we model, but below 400°C, boundaries on this length scale would take several tens of Ma to form because diffusion is so slow. By using maximum temperatures, we calculate minimum timescales, representing the time from when the boundary between the two quartz generations formed until the quartz cooled below 400°C. The minimum diffusion times provide a starting point for exploring the likely actual timescales of porphyry magma residence, veining, and cooling.

Heat conduction profiles

We modeled the conduction of heat from injections of magma and hydrothermal fluids into cooler granite host rock to obtain a simple estimate for timescales of cooling. Heat conduction was modeled as simple one dimensional, linear flow of heat in a semi-infinite medium (Carslaw and Jaeger, 1947). For simplicity, we ignored effects from magma and fluid flow rates, latent heat of crystallization, and viscosity (e.g., Delaney and Pollard, 1982; Rubin, 1995). We used two different models, one to simulate a single thermal event, and one to simulate continuous thermal input. The first model simulates

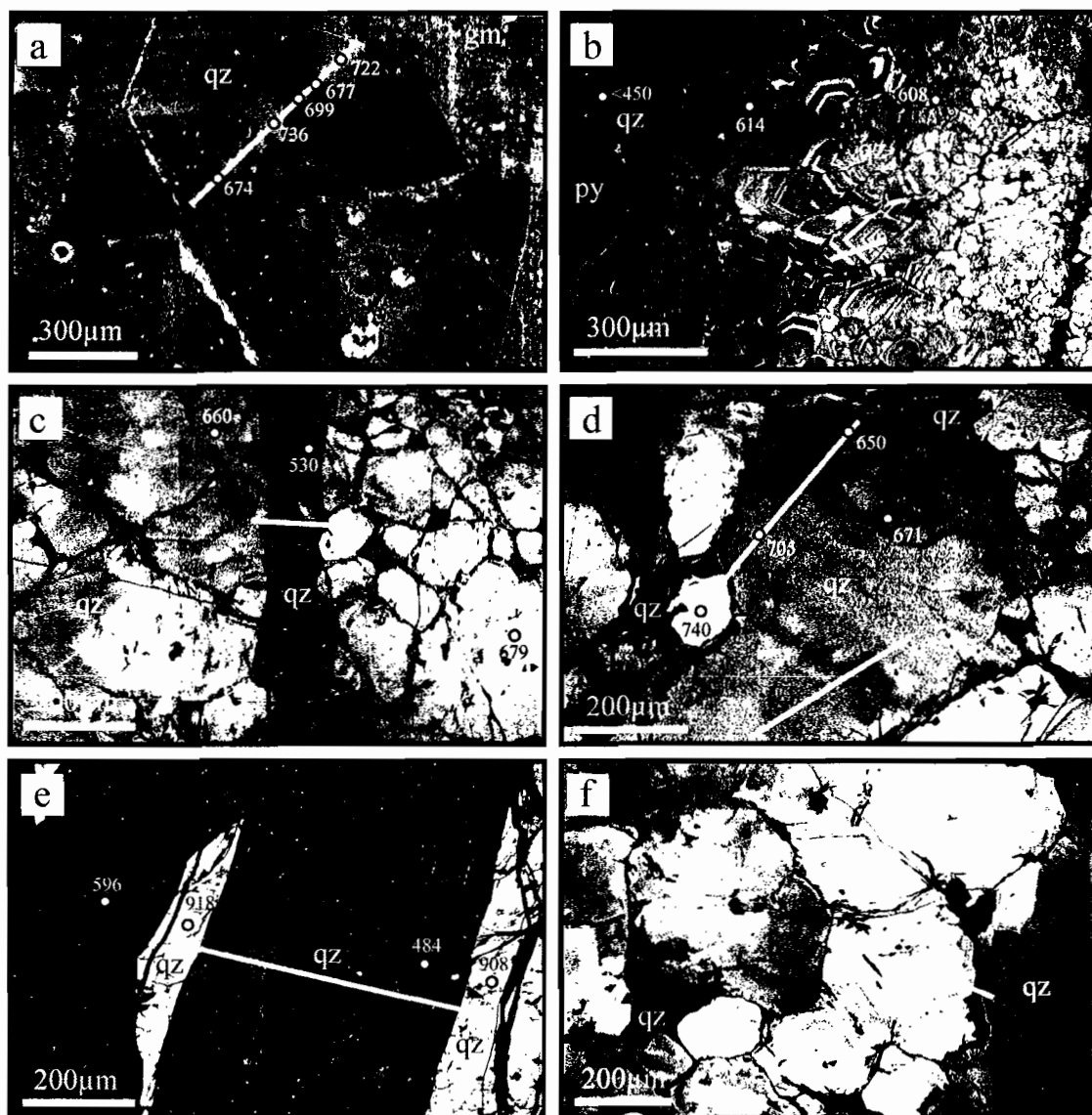


FIG. 4. Examples of cathodoluminescent textures in quartz. Images are dominantly quartz (qz) unless marked otherwise: py=pyrite, gm=groundmass. Example analysis spots are shown with calculated Ti-in-quartz temperatures in °C (Chapter IV). Bars show examples of traverses across different quartz generations for which we modeled diffusion of Ti. (a) Porphyry quartz “eye” from porphyry dike with alternating CL-bright/CL-grey growth zones and CL-dark hydrothermal quartz filling microfractures (11135-2470_Q3), (b) quartz-molybdenite-pyrite vein with euhedral growth zones (10969-2101_Q1), (c) CL-bright quartz-molybdenite vein cross-cut by CL-grey veinlet (11135-2-4209_Q1), (d) quartz-molybdenite vein with intergranular zones of differing CL brightness (10969-5699_Q2), (e) shallow pyrite quartz vein (CL-dark) with angular Butte granite quartz fragment (CL-bright) (10969R-2075_Q1), and (f) barren quartz vein showing CL-black grain boundaries (11172-1847_Q3).

the conduction of heat from a single dike injection, or a single quartz vein forming event, into a fracture in cooler granite host rock using the equation:

$$T(x, t) = \left(\frac{T_{\max} - \Delta T}{2} \right) * \left(\operatorname{erf} \left(\frac{(x + x_i)}{2\sqrt{\kappa t}} \right) - \operatorname{erf} \left(\frac{(x - x_i)}{2\sqrt{\kappa t}} \right) \right), \quad (2)$$

where T is the temperature in rock along a gradient between a hot dike or vein and cool host rock, x is the distance from the center of the gradient to the edge of the gradient, x_i is the half width of the fracture, t is the time for conduction, T_{\max} is the dike or vein temperature, ΔT is the temperature difference between the dike or vein and the host rock, and κ is the thermal diffusivity in granite ($6 \times 10^5 \mu\text{m}^2/\text{s}$; Rubin, 1995). Results from this model are dependent on the initial fracture thickness because this establishes the total thermal mass that is conserved as heat flows into the host rock.

The second model simulates the conduction of heat during the gradual formation of a quartz vein by continuous input of fluids into a fracture of inconsequential width in cooler granite host rock using the equation:

$$T(x, t) = T_g \operatorname{erf} \left(\frac{|x|}{2\sqrt{\kappa t}} \right) + T_f \operatorname{erfc} \left(\frac{|x|}{2\sqrt{\kappa t}} \right), \quad (3)$$

where T is the temperature in rock along a gradient from the edge of the fracture into the wall rock, x is the distance from the edge of the fracture to the edge of the gradient, t is the time for conduction, T_f is the temperature of the fluid, T_g is the temperature of the host rock, and κ is the thermal diffusivity of granite. The fracture width does not affect model results because the fluid continually supplies heat along the fracture edge regardless of fracture width.

Results

Quartz generations in SEM-CL

We investigated 15 samples including three porphyries, and more than a dozen stockwork veins (Table 1, Fig. 2) for their SEM-CL characteristics to identify different generations of magmatic and hydrothermal quartz precipitation. SEM-CL reveals six

major quartz boundary types including (1) alternating CL-grey to CL-bright porphyry phenocryst growth zones (Fig. 4a), (2) alternating CL-bright/dark euhedral growth zones in veins (Fig. 4b), (3) CL-grey veinlets or grain boundaries that appear to cut CL-bright vein quartz grains (Fig. 4c), (4) intragranular variations within grains of primary vein quartz (Fig. 4d), (5) brecciated CL-bright host rock quartz cemented by CL-dark hydrothermal quartz (Fig. 4e), and (6) narrow (5-20 μm) microfractures and grain boundaries in vein quartz filled with CL-black quartz (Fig. 4f).

Correlation of trace elements with SEM-CL brightness

Trace element concentration profiles and spot analyses were acquired for all samples and incorporate different generations of magmatic and hydrothermal quartz. We compared trace element profiles to relative CL brightness to determine whether trace element concentrations correlate with quartz generations of distinct brightness (Fig. 5). Ti concentrations range from below the detection limit of 3 ppm to as high as 50 ppm, Al ranges from 50 to 1600 ppm, Fe ranges from 20 to 700 ppm, and K ranges from below the detection limit of 11 ppm to 260 ppm. Concentrations of Al, Fe, and K do not correlate with CL brightness. Some Al and K concentrations parallel each other, likely owing to their coupled substitution for Si. Low concentrations of Ti correlate with CL-dark to -grey quartz while higher Ti concentrations correlate with CL-bright quartz. For example, the CL-grey core of the porphyry quartz phenocryst (Fig. 5a) is Ti-poor as are the CL-dark hydrothermal veinlets (Fig. 5b), while CL-bright growth bands in the quartz phenocryst and CL-bright hydrothermal vein quartz are relatively Ti-rich. Detailed quantitative CL brightness profiles mimic Ti traverses (Fig 5, bottom graphs), further demonstrating their positive correlation.

While the correlation between Ti concentration and CL brightness is clear for the samples shown in Fig. 5, this was less apparent for many other samples owing to complications with image quality caused by CL-bright scratches and CL-dark cracks, and contamination of data by inclusions of rutile, sericite, and K-feldspar. To examine these

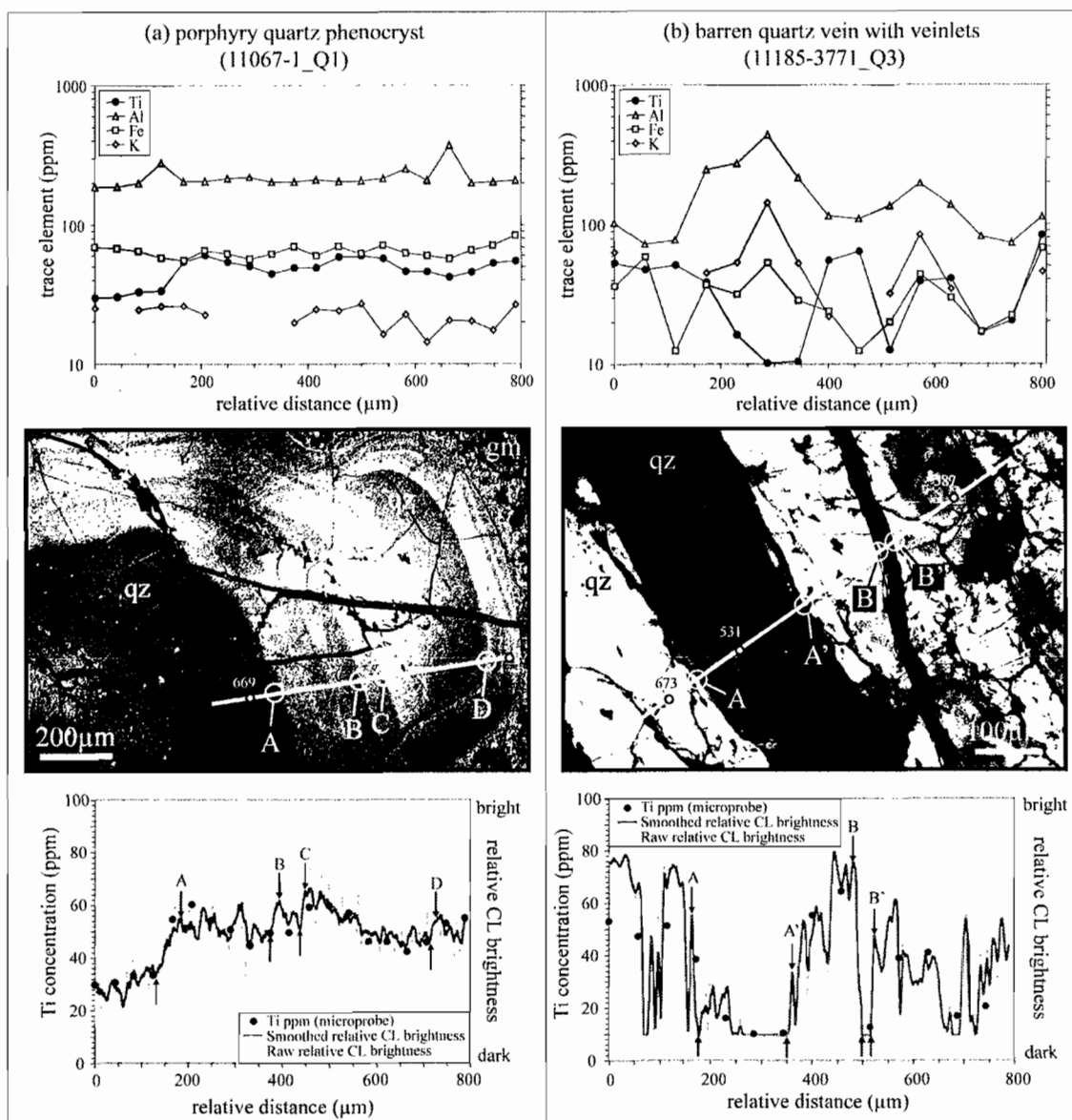


FIG. 5. Examples of microprobe trace element traverses, corresponding SEM-CL images, and SEM-CL brightness calibration. Trace element traverses are shown above corresponding CL images for (a) porphyry quartz phenocryst with a CL-dark core (11067-1_Q1) and (b) CL-bright barren quartz vein with cross-cutting CL-dark veinlets (11185-3771_Q3). Missing data points are analyses that are below the 99% detection limit. Bars in SEM-CL images indicate microprobe traverse locations and letters (A, B, C, D) denote boundaries chosen for modeling. Example spot analyses are shown with calculated Ti-in-quartz temperatures in °C (Chapter IV). Relative CL brightness profiles calibrated for Ti concentrations are shown in the bottom graphs.

effects over a larger area we acquired a high sensitivity trace element map over a 120x680 μm swath for a cross-cutting hydrothermal vein (Fig. 6).

High concentrations of trace elements in Fig. 6 are shown in red, yellow, and green while low concentrations appear in violet and cool pink colors. Dark purple colors are below the detection limit (pink). The Ti map shows good correspondence between Ti concentration and CL brightness within the 20 μm map resolution. Three spots of unusually high Ti concentrations correspond to tiny rutile inclusions (<1x20 μm rutile “whiskers”) within the quartz. A slight mismatch between the edges of CL features and Ti map concentrations can be attributed to re-polishing the sample between SEM-CL imaging and microprobe mapping, which likely moved boundaries by several μm . Maps of Al, Fe, and K show that the concentrations of these elements do not correspond to CL features. However, patterns on the Al and K maps approximately match each other, supporting the hypothesis that they participate in coupled substitution of Si. The map of Fe concentration shows that Fe does not correlate with Ti, Al, or K in quartz. Spots of high concentrations of Al, K, and Fe are likely tiny mineral inclusions of sericite, K-feldspar, or Fe-oxides.

Modeling of Ti diffusion in quartz

By modeling the diffusion of Ti in quartz we can constrain the timescales over which initially sharp CL boundaries between quartz generations become diffuse. CL boundaries were selected from the calibrated, smoothed CL brightness profiles, ensuring that boundaries were representative of a meaningful transition between quartz generations rather than image noise (e.g. scratches, cracks). Examples of modeling results for four different CL boundaries from each sample are shown for a porphyry quartz phenocryst (Fig. 7a; A, B, C, and D) and a CL-bright hydrothermal barren quartz vein which is cut by CL-dark veinlets (Fig 7b; A, A', B, and B'). CL boundaries, shown with thick grey lines, are modeled by iteratively solving equation (1) until the modeled Ti gradient most closely matches that defined by the CL image brightness profile. Model results are shown

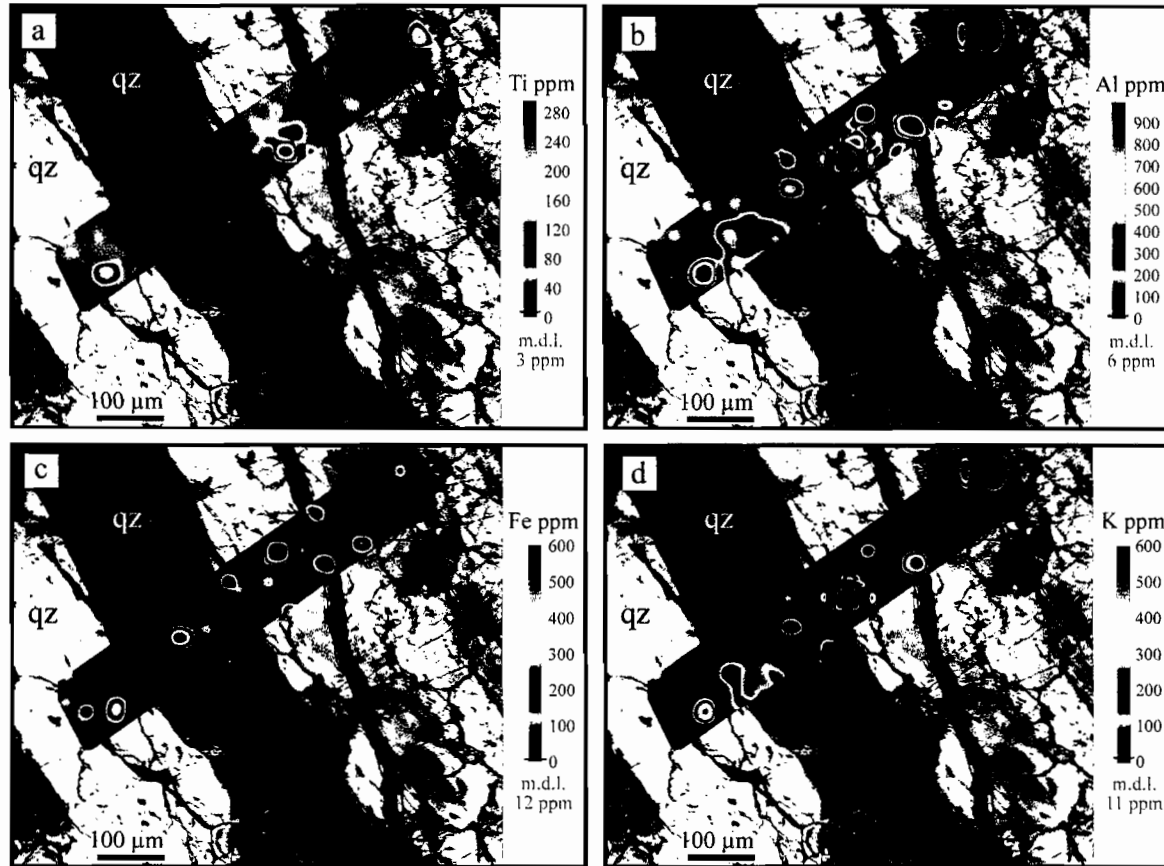
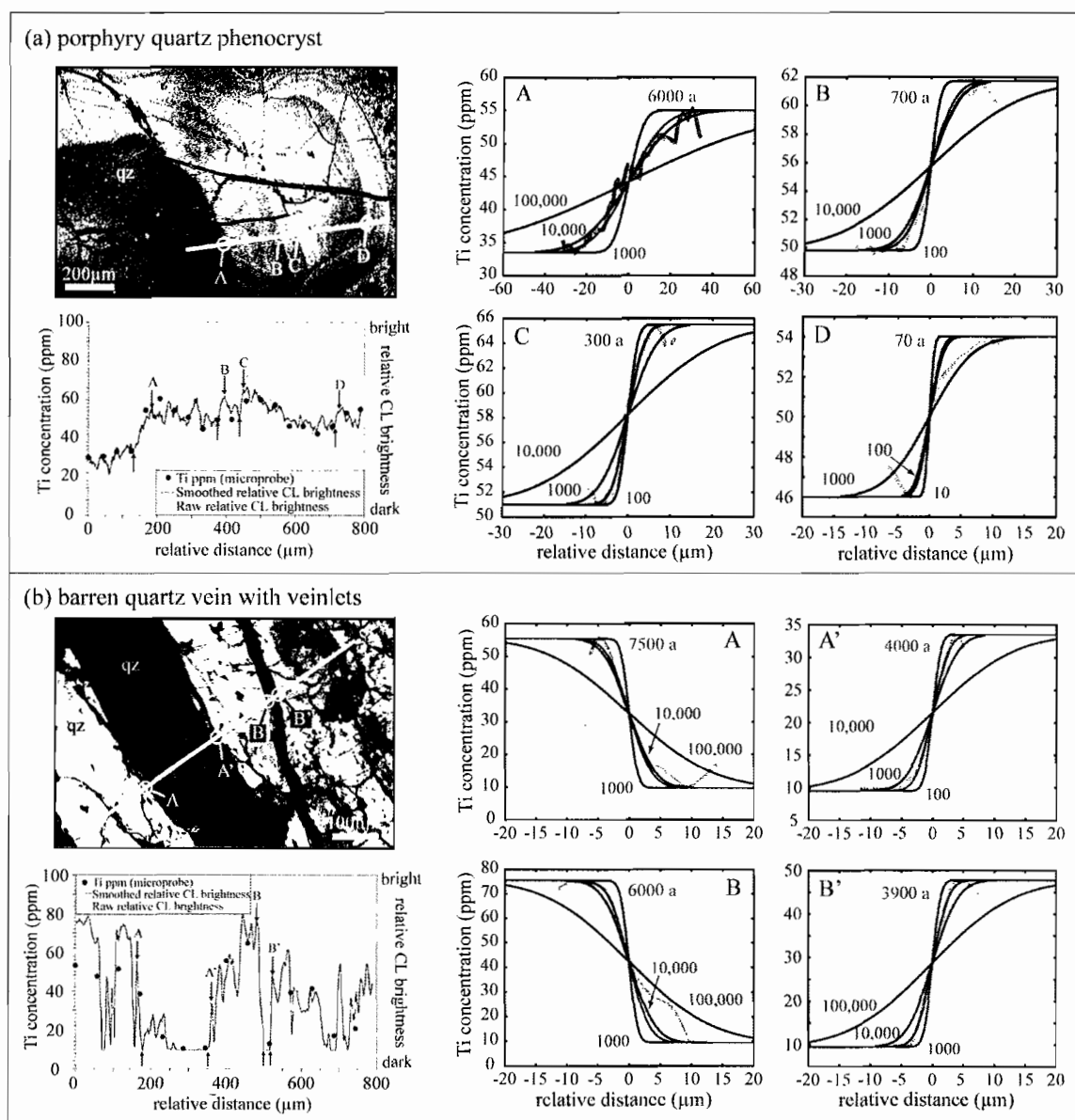


FIG. 6. High sensitivity microprobe trace element maps in CL-bright barren quartz vein that is cut by CL-dark veinlets (11185-3771_Q3). Map created by interpolating 20 μm spot analyses within a 120x680 μm rectangle. High concentrations of trace elements are shown in red, yellow, and green while low concentrations appear in blue, violet, and cool pink colors. Dark purple areas are below the detection limit (pink). (a) Ti concentration in quartz correlates positively with CL brightness. Three spots of high Ti concentrations surround rutile inclusions. (b) Al concentrations, (c) Fe concentrations, and (d) K concentrations do not correlate with CL brightness. Al and K show a moderate correlation due to coupled substitution for Si. Spots of high concentrations of Al, K, and Fe are likely tiny mineral inclusions of sericite, K-feldspar, or Fe-oxides.



with black lines and corresponding timescales of diffusion are reported in yr. Red lines represent best fit models for each boundary, judged by eye.

Timescales for diffusion of Ti between growth rim boundaries in the porphyry quartz phenocryst (Fig 7a) range from as long as 6000 yr to as short as 70 yr, decreasing from core to rim. This decreasing progression in timescales is expected since the phenocryst core spent more time at elevated temperatures than did successive phenocryst rims, allowing more Ti diffusion along the rim boundary. The core boundary provides an estimate of 6000 yr for porphyry magma residence, and the outer rim boundary provides an estimate of 70 yr for the time from phenocryst rim growth to porphyry dike injection and cooling below 400°C. Not all boundaries visible in the CL image were modeled because many had Ti concentration differences that were too small to confidently distinguish from background image noise.

Diffusion modeling of the hydrothermal quartz veinlets (Fig 7b) results in timescales ranging from 3900-7500 yr, representing the time from when the CL-dark veinlets cut the CL-bright vein until the time when the veins cooled below 400°C. Boundaries from both sides of the same veinlets show 2100-3500 yr discrepancies in timescales that are attributed to the complexity of CL features near the boundary of the veinlets that affect the shape of CL brightness profiles.

A potential drawback to our procedures for quantifying timescales is that we may bias the results towards shorter timescales corresponding to features that are easier to identify and model. For example, we cannot characterize timescales for CL features that may have existed but diffused to the point that they are now indistinguishable in CL images. However, this problem is likely unimportant because features that appear to be primary (e.g. crystal growth zones, cross-cutting veins) are preserved and easily identified in these samples and we think it unlikely that there would be an entire generation of older features that diffused away. Although there are considerable complications with this technique, these timescales represent the first attempt at approximating timescales of deposit-wide processes leading to porphyry-Cu deposit formation.

We modeled 83 different CL boundaries spanning all six quartz boundary types within these 15 samples. A summary of model timescale results are shown in Fig. 8 as a function of assumed model temperature. “Isodiffusion lines” represent lines of equal Ti gradient steepness, or equivalently, CL boundary sharpness, that we compute by calculating best fit models to a particular CL boundary at different temperatures.

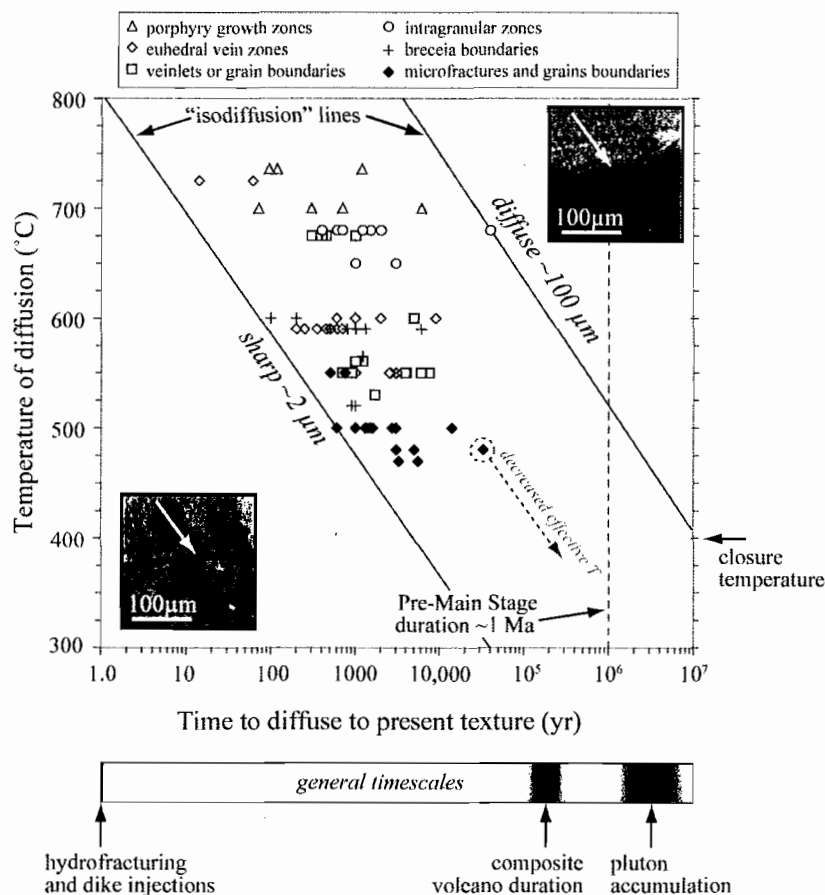


FIG. 8. Summary of modeled timescales as a function of assumed model temperature. “Isodiffusion” lines represent lines of equal Ti gradient steepness, or CL boundary sharpness, and are computed by calculating best fit models to a particular CL boundary at different temperatures. The sharpest boundary we modeled displays modified Ti concentrations over $\sim 2 \mu\text{m}$ while the most diffuse boundary displays modification over $\sim 100 \mu\text{m}$. Grey dashed arrow shows how a 100°C decrease in effective model temperature moves a modeled boundary along its isotexture line to nearly an order of magnitude longer calculated timescale. Duration of pre-main stage porphyry formation at Butte is estimated to be $\sim 1 \text{ Ma}$ by radiogenic isotopes (Dilles et al., 2003; Lund et al., 2005; Lund et al., 2002). General timescales of magmatic and hydrothermal processes are shown with shaded bars. Timescales for the formation of 2 km long hydrofractures and silicic dikes are on the order of minutes to hours, respectively (assuming a hydrofracturing rate of $\sim 1 \text{ m/s}$ (Bons, 2001) and a dike injection rate of $\sim 0.015 \text{ m/s}$ (Rutherford and Gardner, 2000)). Duration of average composite volcanoes ranges from 100 to 250 ka (Davidson and De Silva, 2000) and plutons accumulate over 1 to 10 Ma (Glazner et al., 2004).

Boundaries with steep Ti gradients plot towards the “sharp” isodiffusion line corresponding to shorter timescales for a given diffusion temperature, while boundaries with more shallow Ti gradients plot towards the “diffuse” isodiffusion line, corresponding to longer timescales. The sharpest boundary we modeled displays modified Ti concentrations over $\sim 2 \mu\text{m}$ while the most diffuse boundary displays modification over $\sim 100 \mu\text{m}$. Euhedral quartz growth zones, breccia boundaries, and CL-dark microfractures and grain boundaries have sharper boundaries while phenocryst growth zones, veinlets, and intragranular zones show both sharp and more diffuse boundaries. Diffusion timescales for porphyry quartz phenocryst formation and cooling range from 70-6000 yr, while those for hydrothermal vein formation, refilling, and cooling range from 14-40,000 yr. While there is a considerable spread of modeled timescales of diffusion, results are generally several orders of magnitude shorter than the estimated 1 Ma duration (Dilles, personal communication) of pulses of pre-main stage porphyry mineralization.

Modeling of heat conduction for dikes and veins

Timescales for the conduction of heat away from dike injections and veins (Fig. 9) provide a reference point to compare Ti diffusion timescales and an estimate of how long the dikes and veins might stay hot enough to allow Ti diffusion. Modeling of a single 5 m dike injection at 750°C into granite host rock that is 400°C (Chapter IV) illustrates that porphyry dikes would cool to 400°C on timescales of 10s to 100 yr (Fig. 9a). Formation of a 1 cm quartz vein at 600°C in a single episode would cool on timescales of minutes to hours (Fig. 9b). Modeling a single episode of vein formation may be appropriate for quartz veins without alteration envelopes that are apparently formed by episodic pressure release, while modeling vein formation with continuous fluid flow may be more appropriate for quartz veins with cm scale alteration envelopes that apparently form by both pressure drop and temperature drop (Rusk and Reed, 2002; Rusk et al., 2008b). Precipitation of a 1 cm quartz vein by gradual crystallization from

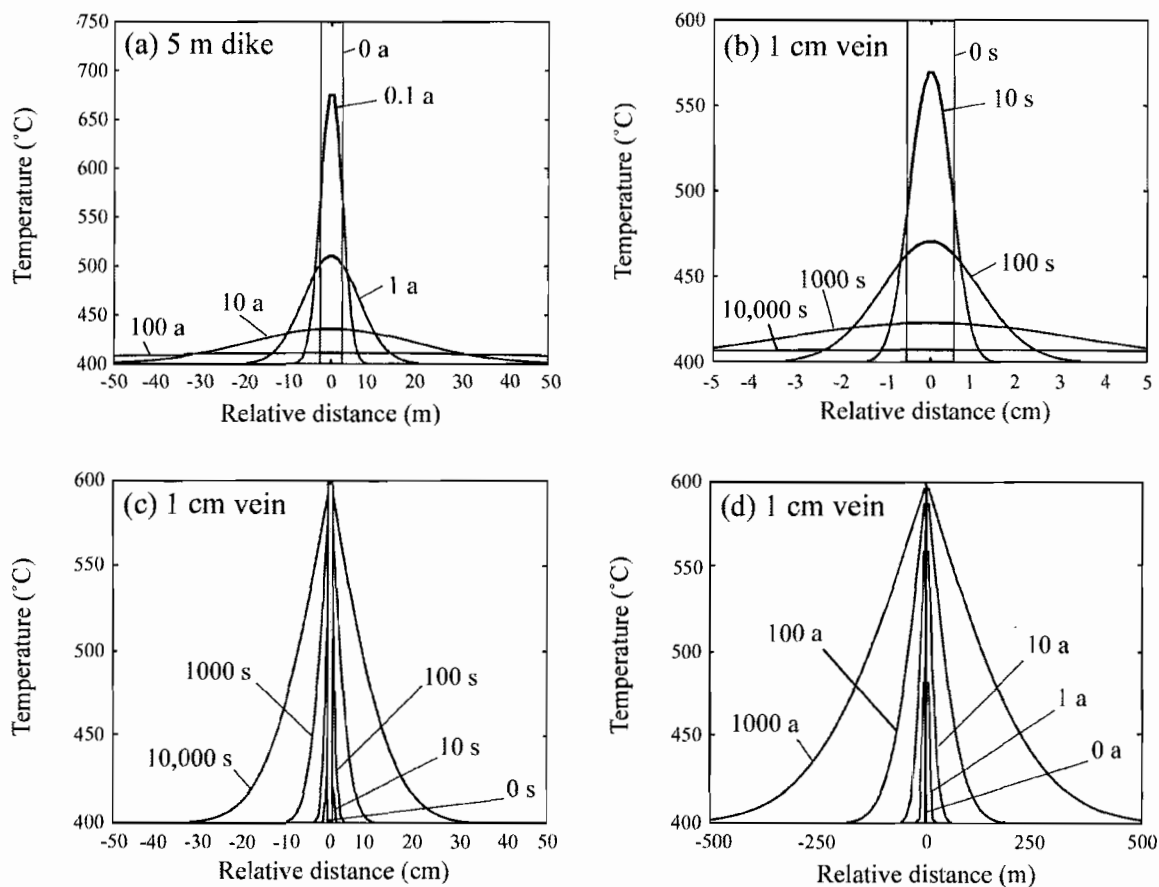


FIG. 9. Model results for conduction of heat from injections of magma or hydrothermal fluids into 400°C granite. Model uses thermal diffusivity for granite, $\kappa = 6 \times 10^5 \mu\text{m}^2/\text{s}$. The first two temperature profiles illustrate the conduction of heat from a single thermal event and the last two profiles show the conduction of heat with continuous thermal input. (a) Single injection of 5 m rhyolitic dike at 750°C cools to 510°C in 1 a and cools to near host rock temperature in 100 a. Over 100 a, the dike heats >100 m of wall rock to ~410°C. (b) Formation of 1 cm quartz vein in single episode at 600°C cools to 470°C in 100 s and cools to near host rock temperature in 10,000 s (~2.8 hours). Over 10,000 s the vein heats >10 cm of wall rock to ~410°C. (c) Gradual precipitation of 1 cm quartz vein by continuous input of 600°C fluids over the same timescales as (b) heats ~40 cm of wall rock to 470°C in 10,000 s (~2.8 hours). (d) Gradual precipitation of 1 cm quartz vein with by continuous input of 600°C fluids over much longer timescales of many years. Over 1000 a, the fluid heats ~400 cm of wall rock to 470°C. Note the different scales on the models.

continuous input of fluids at 600°C over similarly short timescales of minutes to hours heats more wall rock than the previous case. For example, after 10,000 s (2.8 hr) of fluid flow, wall rock is heated to 500°C at ~10 cm away from the fracture (Fig. 9c). Formation of a 1 cm quartz vein by continuous fluid input over longer timescales of 10s to 1000 yr heats an even larger amount of wall rock. After 1000 yr of fluid flow, the wall rock is heated to 500°C ~200 m away from the fracture (Fig. 9d). The long timescales in Fig. 9d may not be realistic because given the stockwork nature of veins, if each vein heated up a large volume of rock, the host rock could potentially increase in temperature by 100s of °C, but there is no evidence for pervasive heating of wall rock to temperatures above the granite solidus (~700°C) at Butte (Roberts, 1975).

Discussion

Ti as the primary SEM-CL activator in magmatic and hydrothermal quartz

The relationship between trace element concentrations and SEM-CL brightness in quartz is currently a topic of great interest (e.g., Götze et al., 2001; Landtwing and Pettke, 2005; Mueller et al., 2003; Penniston-Doreland, 2001; Rusk et al., 2008a; Rusk et al., 2006; van-den-Kerkhof et al., 2001; Watt et al., 1997). The positive correlation between Ti concentration and CL brightness in high temperature magmatic and hydrothermal quartz that we describe in this study (Fig. 5) agrees with previous studies of high temperature (>500°C) hydrothermal quartz veins (Rusk et al., 2008a; Rusk et al., 2006). Although Al, K, and Fe do not appear to correlate with CL brightness in our sample suite, there are several other trace elements in addition to Ti that we did not measure which could contribute to CL brightness, for example Li, Na, Cr, Mn, Pb, Eu (Götze et al., 2001; Müller et al., 2003b; van-den-Kerkhof et al., 2001). However, the striking correlation between Ti concentrations and CL brightness in both microprobe traverses (Fig. 5) and the map (Fig. 6) strongly suggests that Ti is the primary CL activator. This correlation, along with the recent Ti-in-quartz geothermometer (Wark and Watson, 2006) and calibrated diffusivity of Ti in quartz (Cherniak et al., 2007) makes the modeling

technique we present a potentially powerful tool for future studies of high temperature quartz forming processes.

Timescales of porphyry deposit formation and cooling

We interpret the modeled Ti diffusion timescales as the total time from quartz boundary formation to the time when temperatures dropped below 400°C, the effective closure temperature. This time frame does not necessarily imply constant high temperature exposure; it could also represent a summation of heating events. For example, the time could incorporate Ti diffusion during the initial high temperature just after boundary formation as well as Ti diffusion during reheating events due to subsequent magma or hydrothermal fluid injections nearby. Our technique cannot distinguish between these possibilities, thus we discuss the timescales as the total time juxtaposed generations of quartz spent at elevated temperature.

Interpretation of the diffusion data depends on temperature assumptions in our simple model and an evaluation of time-integrated cooling by considering its effect on timescales of diffusion. The Ti diffusion boundaries are defined by their Ti gradient steepness, or CL sharpness, regardless of temperature, so each boundary is confined to its own isodiffusion line—the line of equal Ti gradient steepness or CL sharpness that passes through a modeled point, parallel to the “sharp” and “diffuse” isodiffusion lines shown in Fig. 8. The cooling of any diffusion boundary has the effect of sliding any given point down its isodiffusion line toward lower effective model temperatures and longer timescales, as shown in Fig. 8 by the grey dashed arrow. For example, if the actual dominant diffusion temperature was 100°C cooler than the temperature where a given point is plotted in Fig. 8, calculated timescales would be nearly an order of magnitude longer.

Single hydrofracturing fluid injections likely extend at least two km vertically at Butte, as indicated by biotite crackles that reach >2 km from the deep fluid source, and would take approximately 30 minutes to propagate, assuming a rate of ~1 m/s (Bons, 2001). Porphyry dikes extend at least two km vertically and dike injections would take

approximately 1 to 2 days, assuming an injection rate for rhyolite of ~ 0.015 m/s (Rutherford and Gardner, 2000). Fragments in biotite breccias along the contact of porphyry dikes are matrix supported, indicating rapid quenching. Considering that rhyolite dikes would likely take ~ 10 s of years to cool once emplaced (Fig. 9a), the timescales we find for the formation and cooling of porphyry quartz phenocryst rims, ~ 70 yr (Fig. 8), seems reasonable. Wark et al. (2007) investigated Ti-concentration profiles for quartz phenocryst rims from the Bishop Tuff and found that phenocryst rims formed within 100 yr of the 0.76 Ma eruption that produced the Bishop Tuff, similar to the timescales we calculate here.

Estimates for fluid flow rates and flow duration during vein formation are not well known, and estimates of timescales for vein cooling from thermal models vary widely, from seconds to 100s of years (Fig. 9b-d) depending on assumptions about fluid flow duration. At any given temperature, we find widely varying timescales for diffusion between adjacent hydrothermal quartz generations (Fig. 8), perhaps indicating a wide spectrum of fluid flow duration. Modeling of reactive transport in sericitic alteration envelopes (Geiger et al., 2002) suggests that such cm scale envelopes could form in <100 yr at 400°C . For envelope-bearing veins, 600°C fluids could heat the surrounding rock up to 500°C several 10s of m away from the fracture (Fig. 9d), which could insulate the vein allowing prolonged diffusion of Ti until the whole mass of rock cooled below 400°C . However, the most diffuse boundaries (30-100 μm wide) correspond to higher temperature ($>650^\circ\text{C}$) quartz only (Fig. 8), suggesting that the high temperatures needed to allow such diffusion are not long lasting, and that timescales needed to produce the same scale of diffusion at lower temperatures ($\sim 500^\circ\text{C}$) are not achieved before the rock cools below 400°C . The abundance of relatively sharp CL boundaries (Fig. 8) indicates that in many cases vein quartz cooled relatively quickly, in 10s to 10,000s of years, otherwise all boundaries we observe in the quartz veins would be extremely diffuse, regardless of the temperature estimate.

In summary, we conclude that individual porphyry dikes and hydrothermal veins may reasonably cool on timescales of 10s to 10,000s of years, which is significantly

shorter than the 1 Ma time span of porphyry deposit formation indicated by radiogenic isotopes (Dilles, personal communication). Our Ti diffusion results show that porphyry copper deposits likely form by short-lived magmatic and hydrothermal injections, each creating its own thermal spike, that repeat over a span of ~1 Ma to form a porphyry deposit such as Butte. This conceptual model agrees with thermometry studies in Chapter IV that suggest porphyry phenocryst and hydrothermal vein temperatures represent discrete cycles of transitory high temperature dike intrusions (630-770°C), hydrofracturing, and vein formation (450-750°C) which overprints the cooler background host rock thermal gradient ($\leq 500^\circ\text{C}$).

Conclusions

Our results contribute to the growing evidence that Ti is a consistent CL-activator in high temperature magmatic and hydrothermal quartz. We use this correlation to calibrate SEM-CL images with Ti concentrations, enabling us to model the timescales for diffusion of Ti between distinct generations of magmatic and hydrothermal quartz. The timescale of porphyry magma residence is on the order of 1000s of years while dike injection and cooling occurs in 10s of years. Vein formation timescales range from ~10s to 10,000s of years. These times are considerably shorter than the overall time frame for porphyry copper deposit formation, which leads us to conclude that porphyry copper deposits form by short-lived episodic dike injection, hydrofracturing, and vein formation with discrete thermal spikes that repeat over a span of about one Ma.

Bridge

In Chapter V, I assessed the timescales for the formation and cooling of porphyry copper deposits and discussed the episodic nature of porphyry systems. In the next chapter, I evaluate specific physical mechanisms for hydrothermal vein growth from magmatic fluids in a porphyry copper deposit, and I discuss crustal and fluid characteristics that promote such vein formation in these dynamic magmatic-hydrothermal systems.

CHAPTER VI

SEAMLESS EPITAXIAL GROWTH OF HYDROTHERMAL QUARTZ VEINS: AN EBSD, SEM-CL, AND CHEMICAL DIFFUSION STUDY

This chapter is in preparation to be submitted to *American Mineralogist*. This paper was co-authored with Mark H. Reed, who provided advising, funding, and editorial help.

INTRODUCTION

Quartz veins are ubiquitous in a wide range of hydrothermal, sedimentary, and metamorphic environments. Although much is known about the pressure and temperature conditions of quartz vein formation, details of how quartz crystals nucleate and grow are not well understood. The pressure, temperature, and chemical conditions under which quartz veins form is improving from studies of fluid inclusions, scanning electron microscope-cathodoluminescence (SEM-CL), trace element analyses, geothermometry, and studies of silica solubility (e.g., Fournier, 1999; Hilgers and Urai, 2002; Landtwing and Pettke, 2005; Okamoto et al., 2008; Penniston-Doreland, 2001; Rusk et al., 2008a; Rusk and Reed, 2002; Rusk et al., 2008b; Seedorff et al., 2005). The electron backscatter diffraction (EBSD) technique we apply in this study, which is still relatively new in geologic studies (Prior et al., 1999), has revealed new insights into quartz growth and quartz cement formation. For example, migration of boundaries observed in metamorphic quartz is governed by several growth mechanisms involving single atoms that are randomly or preferentially attached or detached depending on crystal lattice kinks, twin boundaries, or strain fields caused by lattice defects and incorporation of trace elements (Piazolo et al., 2005). Growth of quartz cement in sandstones appears to be strongly

affected by the crystallographic orientation and surface area of detrital quartz grains (Heddad et al., 2006), and epitaxial quartz “bridges” have been observed in quartz cement-filled fractures in sandstones (Reed and Gale, 2008). Quartz grains in the fracture walls of these veins have been shown to control much of the orientation of the quartz cement, and quartz with the c-axis at a high angle to the fracture wall tends to dominate quartz bridges (Reed and Gale, 2008).

Precipitation of vein quartz may occur, for example, by isothermal fluid decompression from lithostatic loads to near hydrostatic pressures or by adiabatic cooling of fluids (Rusk and Reed, 2002). Nucleation of quartz crystals may occur along the fracture wall leading to growth of crystals toward the center of the vein (Okamoto and Tsuchiya, 2008) or within the aqueous fluid leading to growth of crystals suspended within the fluid (Okamoto and Tsuchiya, in press). Quartz dissolution is known to take place during vein formation as a result of fluid mixing or cooling resulting in retrograde quartz dissolution (Rusk and Reed, 2002).

Quartz veins that are visible only by SEM-CL in otherwise monotonous quartz (e.g., Fig. 1a and 2b) require consideration of an additional process by which these veins may form. For example, diffusion of CL-activating trace elements (e.g., Ti, Li) out of pre-existing quartz into a hydrothermal fluid flowing through a microfracture could change the observed CL properties of the affected quartz resulting in a chemically and CL-distinct “vein” with no need for new quartz precipitation.

Here we combine EBSD, SEM-CL, and chemical diffusion modeling to investigate distinct generations of quartz veins from the porphyry-Cu-Mo deposit in Butte, Montana with the goal of identifying the process by which quartz grains nucleate and grow within these hydrothermal veins. While there are several vein types (Brimhall, 1977; Reed, 1999) and vein textures recognized at Butte (Rusk and Reed, 2002), our study focuses on narrow (20-200 μm) veins that occur as bands of CL-dark quartz cutting multiple grains of CL-bright quartz (Fig. 1a and 2b). These CL-dark bands have been inferred to indicate mechanical breaking, dilation, and infilling of quartz to form veins

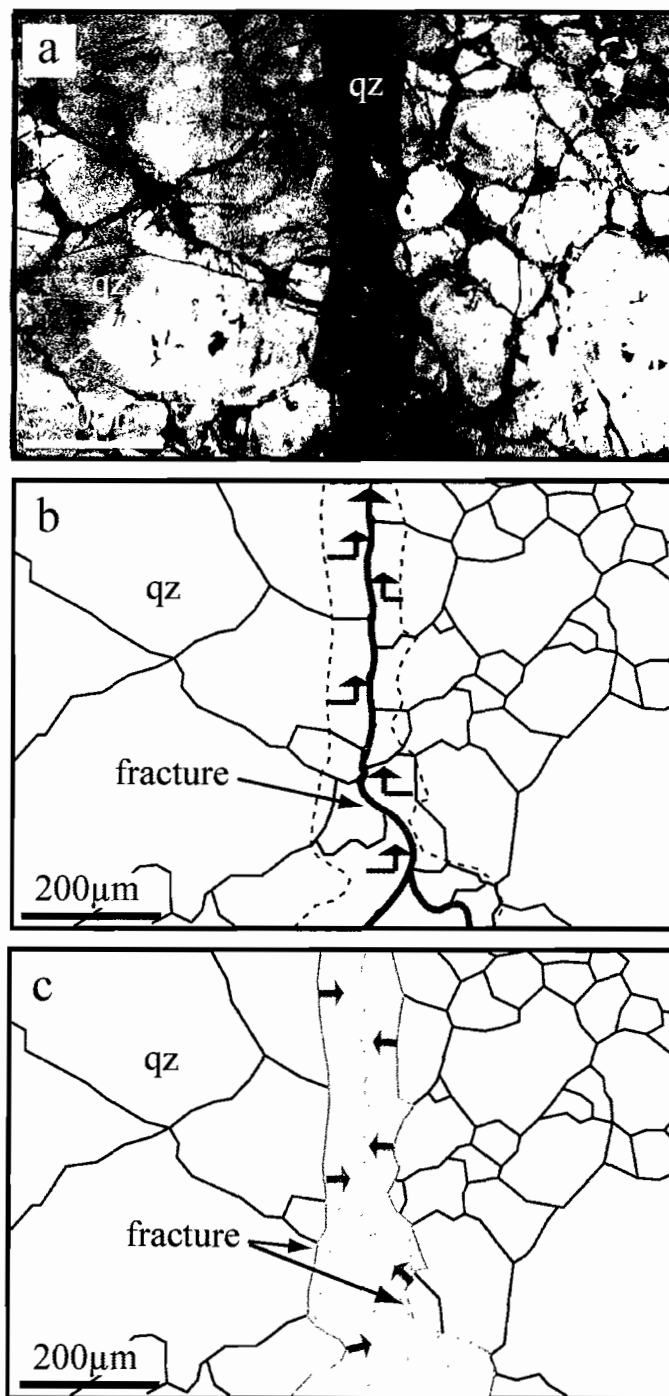


Figure 1. Vein formation possibilities. **(a)** Scanning electron microscope cathodoluminescence (SEM-CL) image of Ti-rich, CL-bright quartz vein crystals cut by Ti-poor, CL-dark quartz vein (sample 11135-2-4209_Q1). Schematic diagrams show two processes by which a CL-dark quartz band could form: **(b)** diffusion of Ti out of pre-existing quartz into hydrothermal fluid flowing through a fracture, or **(c)** epitaxial growth of quartz along a dilated fracture wall.

(Rusk and Reed, 2002). However this interpretation has not been tested and our aim here is to distinguish this possibility from the diffusion mechanism alluded to above.

Combined EBSD and SEM-CL observations in this study lead us to consider two endmember scenarios for vein formation: (1) the cutting “vein” is not a true vein, but is a zone bordering a microfracture formed by diffusion of CL-activating trace elements, in this case Ti, out of pre-existing quartz and away into a hydrothermal fluid (Fig. 1b), or (2) the vein formed by epitaxial growth of quartz into a fracture with an original width at least as wide as the CL-dark band (Fig. 1c). Formation of CL-dark bands by diffusion requires no new quartz growth within the fracture implying that hydrothermal fluids are quartz saturated. Since Ti has been shown to be the primary CL activator in high temperature hydrothermal quartz veins at Butte (Chapter V; Rusk et al., 2008a; Rusk et al., 2006), we model Ti diffusion in quartz to investigate this potential vein-forming process. In contrast, epitaxial formation of CL-dark bands requires nucleation and growth of new quartz to fill open fractures, requiring quartz super-saturation in the hydrothermal fluid. Quartz infilling of a dilated fracture produces a “true” vein whereas Ti leaching along a fracture forms a CL-dark band, but not a “vein” in the normal sense.

GEOLOGIC SETTING

Mineralization at Butte, Montana is hosted by the late Cretaceous Boulder batholith, and formed in two events during an interval of 3 Ma (Brimhall, 1977; Dilles et al., 2003; Lund et al., 2002; Snee et al., 1999). The “pre-main stage” porphyry-Cu-Mo system formed first, as a result of magmatic fluids released from a deep cupola and an east-west striking swarm of early Paleocene rhyolitic porphyry dikes. Early pre-main stage mineralization consists of disseminated chalcopyrite and molybdenite in stockwork veins (1-20 mm) with potassic alteration. Later, shallower pyrite-dominated mineralization occurred as stockwork veins with sericitic alteration. Pre-main stage mineralization at Butte exists in two domes, each containing zoned alteration patterns typical of porphyry-Cu style mineralization (Reed, 1999). The second mineralizing event at Butte consists of lower temperature, “main stage” base metal lodes containing Cu-,

Zn-, Pb-, and Ag-sulfides. Main stage mineralization is accompanied by sericitic and argillic alteration that overprints much of the early pre-main stage mineralization (Meyer et al., 1968). In this study, we focus on stockwork veins from the pre-main stage porphyry-Cu-Mo system.

METHODS

We analyzed 20 samples containing pre-main stage barren quartz, quartz-molybdenite, early dark micaceous, and pyrite-quartz veins using BSE and SEM-CL to investigate different generations of hydrothermal quartz within veins. More than 300 SEM images were collected at the University of Oregon using a FEI Quanta 200 FEG scanning electron microscope equipped with an Oxford Instruments cathodoluminescence detector. Polished 200 μm thick sections were carbon coated (15-20 nm) and examined at 10 keV with a beam current of 0.5-5 nA, depending on the luminosity of the quartz.

We chose a subset of four samples to acquire EBSD maps of quartz veins where CL textures were already characterized in order to compare quartz crystal orientations, grain boundaries, and crystal lattice misorientations to CL textures. These maps were acquired using the same SEM equipped with an Oxford Instruments HKL Technology EBSD detector. Samples were specially polished using colloidal silica and were analyzed using a 70° pre-tilted sample holder using a 20 keV acceleration voltage, a 70 nA beam current, and a 15 mm working distance. EBSD patterns were auto-indexed using HKL Channel 5 software. The edges of 7 Kikuchi bands were detected automatically and compared with calculated quartz patterns originating from 75 reflectors. EBSD patterns that could not be indexed (~5-10%) were generally in areas with other phases (e.g., feldspar, muscovite), scratches, or surface cracks. We used a step width of 3-4 μm and crystallographic orientations have a precision of $<0.5^\circ$ for each step. Raw orientation maps were processed to remove erroneous data and to optimize the reconstruction of quartz vein microstructures. Points that could not be indexed were assumed to have the most common neighboring orientation. Grain boundaries were defined by consecutive

steps with $\geq 10^\circ$ misorientations and subgrain boundaries were defined by 2-10° misorientations.

We modeled Ti diffusion in quartz to investigate the anticipated effect on CL textures and the possibility of quartz “vein” formation by diffusion. Diffusion was modeled as simple one dimensional, concentration-independent diffusion in a semi-infinite medium (Carslaw and Jaeger, 1947). We used two different models to simulate quartz growth. The first model simulates diffusion of Ti from preexisting quartz into a Ti-poor fluid of constant concentration that flows through a fracture of inconsequential width using the equation:

$$C(x,t) = c_q \operatorname{erf}\left(\frac{|x|}{2\sqrt{Dt}}\right) + c_f \operatorname{erfc}\left(\frac{|x|}{2\sqrt{Dt}}\right), \quad (1)$$

where C is the concentration of Ti in quartz along a gradient from the edge of the fracture into the wall rock, x is the distance from the edge of the fracture to the edge of the gradient, t is the time for diffusion, c_f is the concentration of Ti in the fluid, c_q is the concentration of Ti in the quartz, and D is the diffusivity of Ti in quartz. The fracture width does not affect model results because the fluid continually removes Ti from the quartz regardless of fracture width.

The second model simulates the diffusion of Ti after the growth of a single generation of Ti-poor quartz in a fracture using the equation:

$$C(x,t) = \left(\frac{c_{\max} - \Delta c}{2}\right) * \left(\operatorname{erf}\left(\frac{(x+x_i)}{2\sqrt{Dt}}\right) - \operatorname{erf}\left(\frac{(x-x_i)}{2\sqrt{Dt}}\right)\right), \quad (2)$$

where C is the concentration of Ti in quartz along a gradient between two chemically and CL distinct quartz generations, x is the distance from the center of the gradient to the edge of the gradient, x_i is the half width of the fracture, t is the time for diffusion, c_{\max} is the maximum Ti concentration in the quartz, Δc is the difference between the initial maximum and minimum Ti concentrations in the quartz, and D is the diffusivity of Ti in quartz. Results from this model are dependent on the initial fracture thickness because this establishes the total deficiency of Ti that will be conserved as Ti diffuses.

QUARTZ VEIN TEXTURES AND CRYSTALLOGRAPHY

Edges of many CL-dark bands are relatively sharp and linear, though they display asymmetrical and irregular edges in places, especially where CL-dark bands splay along quartz grain boundaries. Bands are generally monotonous in CL and do not display organized patterns seen in other varieties of quartz at Butte (e.g., euhedral growth bands, concentric banding) with the exception of very thin ($<5 \mu\text{m}$) CL-black quartz filled grain boundaries and microfractures, which are ubiquitous throughout pre-main stage Butte veins, and are likely products of late main stage fluid percolation and quartz precipitation.

Quartz crystal lattice orientations, grain boundaries, and subgrain boundaries determined by electron backscattered diffraction (EBSD) for representative CL-dark quartz veins are shown in Fig. 2c along with corresponding SEM-BSE and -CL images (Figs. 2a and b). The EBSD map shows crystallographic orientation of quartz grains using the Inverse Pole Figure (IPF) coloring scheme that depicts grains with c-axes (0001) perpendicular to the map plane shaded in red, and grains with sub-perpendicular c-axes shaded in progressively cooler colors (blue or green depending on the orientation of the non-prismatic axes, 0120 and 0210). Quartz grain boundaries are defined by thin black lines that represent crystal lattice misorientations of $\geq 10^\circ$. Subgrain boundaries with $2\text{-}10^\circ$ misorientation are shown with thin light blue lines, and grain boundaries with non-quartz phases (shaded grey) are shown with thin red lines. The crystallographic orientation map (Fig. 2c) shows that this particular sample area is dominated by a single large quartz grain with many $2\text{-}10^\circ$ subgrain boundaries. Gradational color changes between subgrain boundaries indicate gradual crystal lattice rotation ($<2^\circ$ between neighboring steps) indicative of lattice strain. Dauphiné twins, which are twins with a 180° (or apparent 60°) rotation about the c-axis, are denoted with thin dark blue grain boundaries and are abundant in these quartz veins. Comparison of crystallographic orientations and grain boundaries with CL-dark veins (thick black lines in Fig. 2c) reveals that there is no obvious crystallographic trace along the edge of CL-dark veins. In fact, crystal orientations, grain boundaries, and twin domains are continuous across the CL-dark veins, indicating epitaxial growth of the vein-filling quartz.

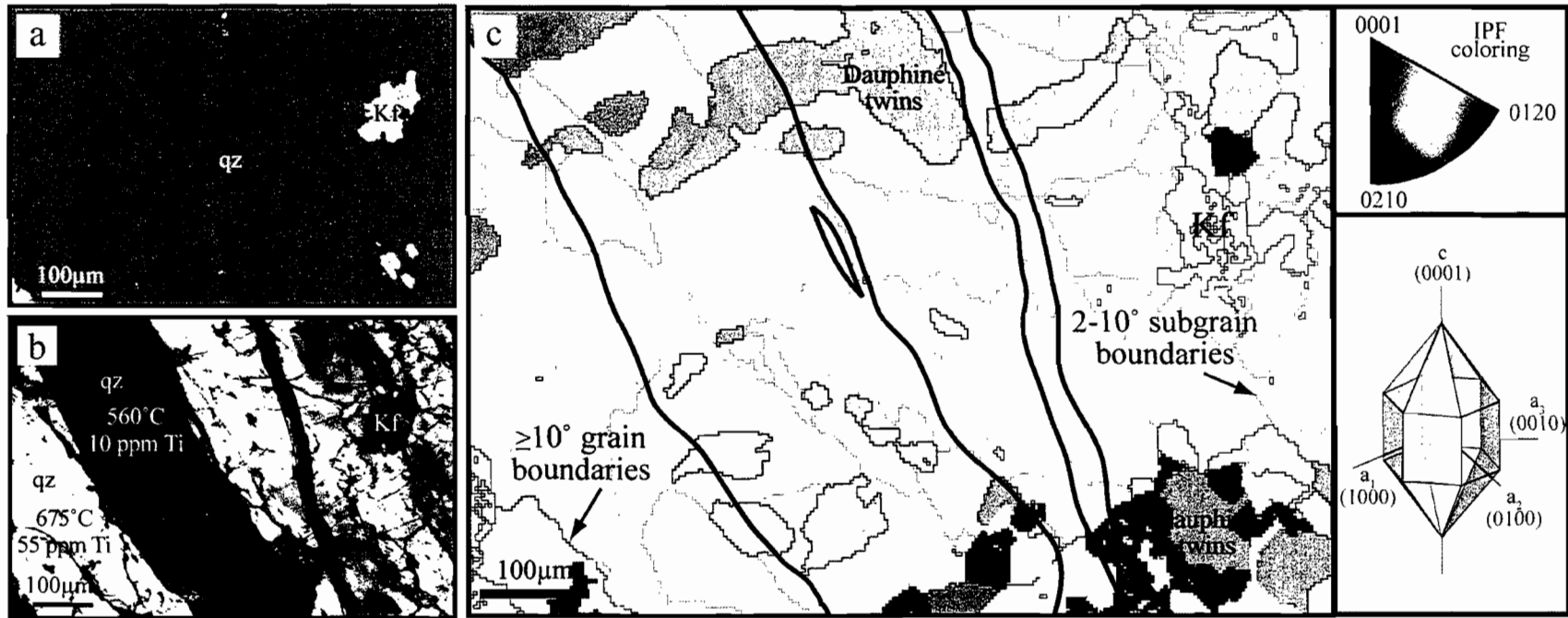


Figure 2. Crystallography of cross-cutting quartz veins. (a) Backscattered electron (BSE), (b) scanning electron microscope cathodoluminescence (SEM-CL), and (c) electron backscattered diffraction (EBSD) images of same area in barren quartz vein (sample 11185-3771_Q3). SEM-CL images show CL-bright quartz vein which is cut by CL-dark quartz veins. EBSD image shows crystallographic orientation map of quartz grains using Inverse Pole Figure (IPF) coloring which displays quartz with c-axes (0001) perpendicular to the the map shaded red, and quartz with sub-perpendicular c-axes shaded in progressively cooler colors (blue or green depending on the orientation of the non-prismatic axes, 0120 and 0210). Thin black lines indicate quartz grain boundaries defined by $\geq 10^\circ$ misorientation, thin light blue lines indicate subgrain boundaries with $2\text{-}10^\circ$ misorientation, thin dark blue lines indicate 180° (apparent 60°) Dauphiné twin boundaries, and thin red lines indicate grain boundaries with minerals other than quartz. Thick black lines indicate edges of CL-dark cross-cutting veins which show no distinct crystallographic orientation relative to the primary vein. Sample area is dominated by one large grain which shows many $2\text{-}10^\circ$ subgrain boundaries (light blue lines), and gradational colors within the grain indicating gradual crystal lattice rotation due to lattice strain. Somewhat linear $2\text{-}10^\circ$ misorientations (light blue lines) visible within the thick CL-dark vein may be a cryptic trace of the seam along which the vein sealed.

MODELED SEM-CL TEXTURES FROM Ti DIFFUSION IN QUARTZ

Diffusion of trace elements within quartz undoubtedly occurs upon cooling of hydrothermal quartz and Ti will diffuse until the temperature drops below the effective closure temperature of $\sim 400^{\circ}\text{C}$ (Chapter V). Estimates of the cooling history at Butte suggest that individual veins in the porphyry system cooled to $<400^{\circ}\text{C}$ on timescales of $\sim 10\text{s}$ to $10,000\text{s}$ of years (Chapter V), and hence diffusion of Ti could have occurred during that time. We model three different scenarios of Ti diffusion in quartz over a variety of timescales to explore the possibility that quartz vein formation may have occurred by diffusion (Fig. 1b) versus epitaxial quartz growth (Fig. 1c). Model inputs were chosen to simulate the formation of the wide and narrow CL-dark quartz bands shown in Fig. 2b. CL-bright quartz contains 55 ppm Ti, corresponding to quartz precipitation at 675°C , while CL-dark quartz contains 10 ppm Ti, corresponding to formation at 560°C (Chapter IV). Assuming that the first quartz vein had cooled to the temperature of the second, cross-cutting vein, we modeled diffusion at 560°C , where the Ti diffusion coefficient, D , is $1.75 \times 10^{-11} \mu\text{m}^2/\text{s}$ (Cherniak et al., 2007). Results from three diffusion scenarios are shown in Fig. 3 along with a time series of schematic diagrams depicting the change in CL brightness caused by Ti diffusion. The first scenario (Fig. 3a) uses equation (1) to model the formation of a thin ($20 \mu\text{m}$) fracture in which no quartz precipitates, but rather Ti diffuses from Ti-rich, CL-bright quartz into a Ti-poor fluid of constant concentration that flows continuously through the fracture until the vein finally seals with Ti-poor, CL-dark quartz after 1 Ma. The second scenario (Fig. 3b) uses equation (2) to model a narrow ($20 \mu\text{m}$) fracture in which Ti-poor, CL-dark quartz precipitated at time $t=0$ a, after which Ti diffuses from the Ti-rich, CL-bright quartz towards the CL-dark vein over 1 Ma. The third scenario (Fig. 3c) uses equation (2) to model the formation of a wide fracture ($180 \mu\text{m}$) under the same conditions as the narrow fracture in the previous scenario.

In the first scenario, CL boundaries begin to grow but all are somewhat diffuse (Fig. 3a). Initial CL boundaries in the second (Fig. 3b) and third (Fig. 3c) scenarios start out sharp and become increasingly diffuse with time. In these instances, CL boundaries

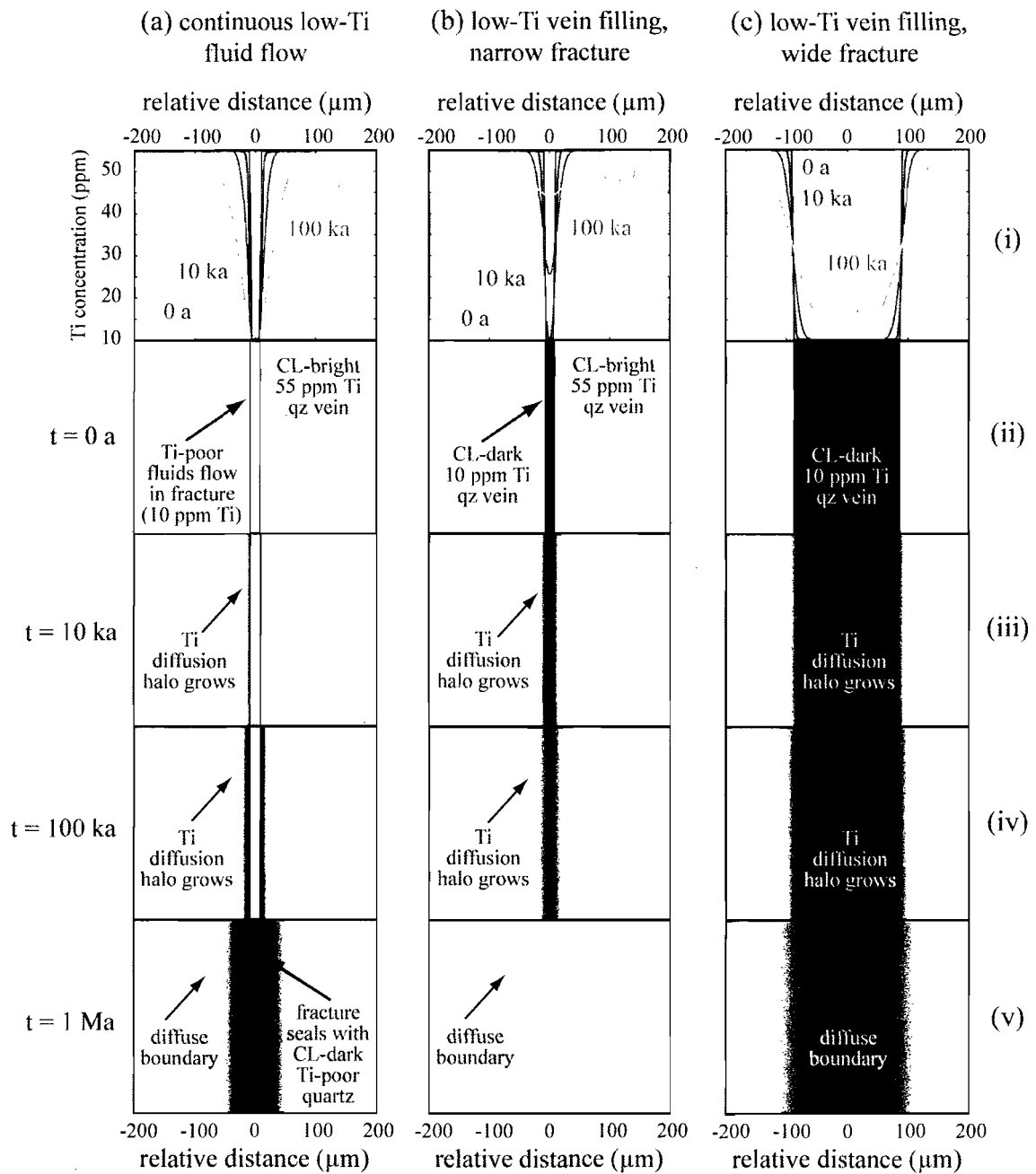


Figure 3. Model results for diffusion of Ti in quartz due to (a) continuous flow of a Ti-poor (10 ppm) aqueous fluid of constant concentration through a fracture of inconsequential width in preexisting Ti-rich (55 ppm) quartz, (b) growth of Ti-poor (10 ppm) quartz in a narrow ($20 \mu\text{m}$) fracture cutting earlier, Ti-rich (55 ppm) quartz, and (c) growth of Ti-poor (10 ppm) quartz in a wide ($180 \mu\text{m}$) fracture cutting earlier, Ti-rich (55 ppm) quartz. Frame (i) shows model results in terms of Ti concentration gradients, while frames (ii)-(v) show schematic diagrams of changes in SEM-CL brightness due to diffusion of Ti in quartz at 560°C (diffusivity, $D=1.75 \times 10^{-11} \mu\text{m}^2/\text{s}$).

change little from $t=0$ a to $t=1000$ a, but they become noticeably diffuse at $t>10,000$ a. Eventually diffusion with continuous fluid flow (Fig. 3a-v) results in formation of CL features similar to those of the wide quartz filled fracture (Fig. 3c-iv) by the time the vein reaches a width of $200\ \mu\text{m}$. In contrast, the scenario with the narrow quartz filled fracture becomes extremely diffuse by the time it has reached a width of $200\ \mu\text{m}$ (Fig. 3b-v). The sharp boundaries observed in narrow and wide CL-dark veins (Fig 2b) most closely resemble model results in frames b(ii) and c(ii), respectively, in which no diffusion has yet been allowed to occur (i.e., $t=0$ a).

DISCUSSION AND IMPLICATIONS

Modeling diffusion of Ti in quartz shows that formation of a vein on the order of $20\text{-}200\ \mu\text{m}$ wide primarily by diffusion would result in a vein with highly diffuse CL boundaries, regardless of fracture width or duration of fluid flow. The vein would also require relatively long timescales for diffusion ($100\ \text{ka}\text{-}1\ \text{Ma}$), which may not be realistic given that thermal cooling operates much more quickly than chemical diffusion, and vein quartz is likely to cool below 400°C on a shorter timescale than $100\ \text{ka}$ to $1\ \text{Ma}$ (Chapter V). In contrast, the CL-dark bands we observe do not have diffuse boundaries, but are instead relatively sharp, displaying diffuse boundaries only $0\text{-}10\ \mu\text{m}$ in width (Fig. 1a, 2b). We therefore conclude that epitaxial quartz infilling of fractures must be the dominant process by which the CL-dark veins from Butte form.

The EBSD crystallographic orientation map (Fig. 3c) shows that nucleation and growth of new CL-dark quartz along the previous fracture wall must have been remarkably seamless ($<2^\circ$ misorientation). Cryptic, roughly linear, low angle misorientations ($2\text{-}10^\circ$) near the center of the vein (light blue lines) may record a crystallographic expression of the “seam” where the vein sealed.

Growth of quartz into an open fracture at the depth inferred for the Butte deposit ($6\text{-}9\ \text{km}$; Rusk et al., 2008b) requires brittle failure of the $400\text{-}500^\circ\text{C}$ granite host rock (Chapter IV) and substantial overpressure of fluids that are super-saturated with quartz. Furthermore, cooling of these veins must occur on timescales $<1000\text{s}$ of years to preserve

the sharp boundaries of the CL-dark veins (Fig. 3b-ii and 3c-ii; Chapter V). This is consistent with observations of relatively sharp SEM-CL boundaries as well as and EBSD crystallographic observations, and still allows for small degrees of diffusion of boundaries that must occur since veins are unlikely to cool instantaneously.

In summary, SEM-CL and EBSD analyses of CL-dark hydrothermal quartz veins from the pre-main stage porphyry-Cu-Mo deposit in Butte, Montana reveal that quartz crystallographic orientations and grain boundaries are continuous across narrow (20-200 μm) CL-dark bands. This observation, combined with simple modeling of Ti diffusion in quartz indicates that remarkably seamless epitaxial nucleation and growth of quartz inward from the fracture wall is the primary process by which these veins form. The only crystallographic trace of the preexisting fracture is a cryptic trace of crystal misorientation along the seam where the vein closed. CL-dark veins of this type are likely to be found in quartz veins that grow by hydrofracturing in other geologic settings, and the distinction between epitaxial quartz growth and diffusion of CL-activating trace elements out of pre-existing quartz may prove useful in interpreting complex SEM-CL textures found in quartz veins from hydrothermal, sedimentary, and metamorphic environments.

CHAPTER VII

CONCLUSIONS

In this dissertation I explored several important aspects of magma generation, magma degassing, and the development of magmatic-hydrothermal systems in continental arc crust. This final chapter summarizes the results and implications of my research.

In Chapter II, I investigated magma generation processes in the deep crust beneath a subduction-related stratovolcano in the Oregon Cascades by conducting high pressure, water-undersaturated experiments. I mapped the mineralogy onto the H₂O-undersaturated liquidus surface of basaltic andesite from North Sister Volcano to constrain the crystalline assemblage with which, and P-T-H₂O conditions at which, the melt last equilibrated before erupting. Combining these high pressure experimental results with examples of tectonically exposed lower arc crust, geophysical constraints, trace element geochemistry, and melt inclusion volatile contents, I concluded that an anhydrous, augite-rich gabbro at ~12 kbar and ~1175°C is the most probable lithology with which North Sister basaltic andesite with ~3.5 wt.% H₂O last equilibrated before erupting. I speculated that reaction between this gabbro and primitive mantle-derived precursor melts buffered the compositions of magmas erupted from this volcano resulting in their remarkably limited compositional range. This work has provided experimental data to inform geochemical and geophysical models of deep crustal magma processes.

I then examined magmatic and hydrothermal processes for systems in which magma never erupts to the planet's surface, but instead solidifies within the upper crust. In Chapter III, I modeled CO₂ and H₂O variations during formation of granitic ore-forming porphyry magma by fluid-saturated fractional crystallization at 200 to 400 MPa and by polybaric degassing. Initial exsolved fluid has a high CO₂/H₂O ratio since CO₂ has a lower solubility than H₂O, but after ~60% crystallization the fluid becomes

dominantly H₂O. When the magma begins to exsolve nearly pure H₂O, the mass of exsolved fluid increases greatly with progressive crystallization increments, which I hypothesized creates ideal conditions for hydrofracturing and porphyry deposit formation. I used the CO₂ and H₂O solubility model and fluid inclusion compositions to estimate the original CO₂ and H₂O content of the parental ore-forming magma that produced the porphyry Cu-Mo deposit at Butte, Montana. I inferred that the ore-forming magma contained 40-110 ppm CO₂ and >5-6 wt% H₂O which may explain the distinctively deep generation of the Butte deposit. Finally, I applied the model to other porphyry copper deposits and found that to a first approximation, the parental magma H₂O concentration dictates the pressure, and therefore depth, at which these deposits are emplaced.

Building on my study of volatile exsolution during magma crystallization, I then investigated the nature of the transition from magmatic to hydrothermal systems by focusing on the development of porphyry copper deposits. Understanding the relationship between magmatic and hydrothermal realms of porphyry-Cu deposits is essential to unraveling their complex evolution. In Chapter IV, I applied three independent mineral geothermometers to estimate the formation temperatures of magmatic and hydrothermal quartz, rutile, and biotite to establish the thermal relationship between the parental porphyritic magma and hydrothermal veins in the porphyry-Cu-Mo deposit at Butte, Montana. Magmatic temperatures of porphyry dikes range from 630 to 770°C while hydrothermal stockwork veins overlap substantially with magmatic temperatures, ranging from <430 to 750°C. I estimated that final dike injection temperature, and hence the initial magmatic-hydrothermal fluid temperature was ~750°C, while ambient host rock temperatures were ≤500°C. Large temperature ranges spanning 50 to 250°C in every hydrothermal sample indicate variable cooling of hot magmatic aqueous fluids upon contact with cooler wall rock during vein growth. Mineral precipitation temperatures within veins are the same as those in adjacent envelopes, indicating approximately contemporaneous formation of veins and envelopes. Magmatic and hydrothermal samples show no systematic relationship between temperature and depth within the deposit. My

new temperatures, combined with previous fluid inclusion data indicate that the porphyry deposit at Butte may have formed 1 to 2 km deeper than previously recognized.

To further my investigation of the magmatic-hydrothermal transition, I examined the timescales of magmatic and hydrothermal processes responsible for the formation of porphyry copper deposits in Chapter V. Porphyry dikes and hydrothermal veins from the porphyry-Cu-Mo deposit at Butte, Montana contain multiple generations of quartz that are distinct in SEM-cathodoluminescence (SEM-CL) images. A comparison of microprobe trace element profiles and maps to SEM-CL images shows that the concentration of Ti in quartz correlates positively with CL brightness but Al, K, and Fe do not. After calibrating CL brightness in relation to Ti concentration, I used the brightness gradient between different quartz generations as a proxy for Ti gradients that I modeled to determine timescales of quartz formation and cooling. Model results indicate that timescales of porphyry magma residence are ~1000s of years and timescales from porphyry quartz phenocryst rim formation to porphyry dike injection and cooling are ~10s of years. Timescales for the formation and cooling of various generations of hydrothermal vein quartz range from 10s to 10,000s of years. These timescales are considerably shorter than the 1 Ma overall timeframe for porphyry formation determined from isotopic studies at Butte, Montana. Simple heat conduction model profiles provide a temporal reference point to compare chemical diffusion timescales, and I found that they support short dike and vein formation timescales. I interpreted these relatively short timescales to indicate short-lived episodes of hydrofracturing, dike injection, and vein formation, each with discrete thermal pulses, which repeat over the 1 Ma lifetime of the deposit.

From these deposit-scale studies of magmatic and hydrothermal processes, I narrowed the scope of my research, and I investigated the physical processes by which hydrothermal veins form from magmatic-derived H₂O-rich fluids in Chapter VI. Much is known about the pressure, temperature, and chemical conditions of hydrothermal quartz vein deposition, however the specific physical processes by which quartz veins nucleate and grow are still speculative. Scanning electron microscope-cathodoluminescence

(SEM-CL) combined with electron backscatter diffraction (EBSD) mapping of veins from the porphyry-Cu-Mo deposit at Butte, Montana, reveals that many cross-cutting quartz veins defined by CL-dark bands show no unique crystallographic orientation relative to the CL-bright vein they cut. This observation suggests two possibilities for vein formation: (1) the cutting “vein” is not a vein at all, but is a zone bordering a fracture where fluid leached out a CL-activating trace element by diffusion, or (2) the vein formed by epitaxial growth of quartz into a fracture at least the width of the vein. I modeled the diffusion of Ti in quartz and determined that diffusion is not a possible formation process for the veins in this study. Thus I concluded that veins form by remarkably seamless epitaxial growth, leaving only a cryptic crystallographic trace along the seam where the vein closed. Epitaxial growth into an open fracture at considerable depth requires brittle failure of host rock and an overpressure of quartz super-saturated fluids.

These studies of the transition between magmatic and hydrothermal systems have provided a new picture of the formation of porphyry copper deposits. They illustrate that the transition between magmatic and hydrothermal realms is more continuous than previously recognized, and that porphyry deposits apparently form by discrete episodes of dike and fluid injections into the crust followed by rapid vein formation and cooling.

In summary, my dissertation addresses aspects of deep crustal magma generation, shallow crustal magma degassing, and the development of magmatic-hydrothermal systems. This work illustrates that H₂O-rich volatiles play an important role in the generation of mafic subduction zone magmas in the lower crust, and that the exsolution of such volatiles from silicic magmas determines the depth at which hydrothermal systems develop in the upper crust. Further, this work illuminates the complexities of the magmatic-hydrothermal transition in porphyry copper deposits, and demonstrates the episodic nature of these ore-forming systems. Finally, this work exemplifies how utilizing multidisciplinary approaches is essential to unraveling the complex nature of magmatic and hydrothermal systems in the continental arc crust.

APPENDIX

MELT INCLUSION ANALYSES FROM NORTH SISTER VOLCANO, OREGON

I analyzed olivine-hosted melt inclusions that were sampled from four different scoria units at North Sister Volcano including NSba1, NSba2, NSba3, and NSba4. Loose olivine crystals from each of the four units were separated, cleaned in HBF₄, and examined in immersion oil (refractive index 1.678). Olivine crystals are euhedral or resorbed and contain sparse melt inclusions that are usually small (<20 μm) but some large (100-200 μm) inclusions are also present. Melt inclusions identified as suitable (fully enclosed by host crystal, bubble-poor, lacking daughter crystals) were found primarily in the NSba2 unit which is glassier than the other scoria units. Melt inclusions were prepared as doubly polished wafers and were analyzed for H₂O and CO₂ by Fourier Transform Infrared Spectroscopy (FTIR) at the University of Oregon. Melt inclusion major elements, S, and Cl were analyzed with a Cameca SX100 electron microprobe at the University of Oregon using a 15 keV accelerating voltage, 20 nA beam current, and 5 μm beam diameter. Host olivine crystals were analyzed for major elements using a 10 keV accelerating voltage, 20 nA beam current, and a beam diameter of <1 μm . A combination of glass and mineral standards was used.

Melt inclusion compositions were corrected for post-entrapment crystallization of olivine (Sobolev and Chaussidon, 1996) and diffusive loss of Fe (Danyushevsky et al., 2002) following the methods of Johnson et al. (2008). Corrected melt inclusion major element and volatile concentrations and host olivine compositions from North Sister Volcano, Oregon, are given in the following table.

Melt inclusion analyses from North Sister Volcano, Oregon

Unit	NSba2	NSba2	NSba2	NSba2	NSba2	NSba2	NSba2	NSba2	NSba2	NSba2
Inclusion	X1	CM-ab	X5	X6	X7	X8	X10	X11	X12-B	X12-A
Host olivine form	euhedral	NA	resorbed	euhedral	euhedral	euhedral	euhedral	euhedral	resorbed	resorbed
SiO ₂	53.22	52.43	56.35	54.01	53.67	52.65	52.31	53.18	57.89	51.65
Al ₂ O ₃	19.49	18.90	16.62	17.60	18.77	19.28	19.50	18.86	15.11	20.21
TiO ₂	0.98	0.92	1.32	0.99	0.91	0.85	1.18	1.21	1.76	1.19
FeO* ^a	7.77	8.44	8.46	9.13	7.92	8.26	7.74	8.61	8.49 ⁺	8.67
MgO	4.84	5.30	4.11	4.40	5.18	4.85	5.16	4.56	4.22	4.31
CaO	9.01	9.26	7.29	8.49	8.93	9.37	8.74	8.02	6.46	8.72
MnO	0.14	0.07	0.10	0.17	0.09	0.13	0.14	0.17	0.14	0.15
Na ₂ O	3.68	3.93	4.52	4.29	3.78	3.85	4.45	4.38	4.57	4.20
K ₂ O	0.69	0.60	0.98	0.72	0.59	0.59	0.57	0.79	1.01	0.63
P ₂ O ₅	0.19	0.15	0.25	0.20	0.16	0.15	0.23	0.22	0.35	0.25
H ₂ O	0.9	1.0	1.1	1.1	3.2	0.9	0.0	1.3	1.1	1.1
CO ₂ ppm	MDL	MDL	MDL	MDL	405	MDL	MDL	MDL	MDL	MDL
S ppm	764	859	384	767	846	794	838	703	188	918
Cl ppm	653	675	699	660	676	714	905	882	1057	969
Total ^b	99.57	99.55	98.02	99.56	100.51	98.93	98.98	100.03	97.62	99.48
Olivine (Fo%)	82.0	82.1	78.3	77.9	82.8	81.1	83.0	79.5	78.5	78.4
%PEC ^c	2.7	3.1	0.0	2.5	1.2	3.1	3.0	2.6	2.2	2.4

Melt inclusion analyses from North Sister Volcano, Oregon, continued

Unit	NSba2	NSba2	NSba2	NSba2	NSba2	NSba2	NSba2	NSba2	NSba2	NSba2
Inclusion	X13-B	X13-C	X14-C	X14-D	X14-F	X16	X19	X21	X25	X27
Host olivine form	resorbed	resorbed	resorbed	resorbed	resorbed	resorbed	NA	resorbed	resorbed	NA
SiO ₂	53.81	53.83	58.45	53.61	57.61	52.87	54.17	52.14	55.09	54.52
Al ₂ O ₃	17.83	17.09	14.87	17.58	14.85	19.36	17.55	20.23	18.40	18.25
TiO ₂	1.18	1.26	1.63	1.21	1.74	1.40	1.17	1.25	1.41	1.20
FeO* ^a	8.57	8.84	8.75 ⁺	9.83	9.28	7.79 ⁺	8.64	7.90	7.79 ⁺	9.61
MgO	4.93	5.06	3.89	4.35	4.19	4.60	5.09	4.41	4.67	3.72
CaO	8.64	8.95	6.69	8.51	6.92	8.46	8.24	8.84	7.21	7.08
MnO	0.10	0.11	0.11	0.10	0.15	0.12	0.13	0.13	0.09	0.15
Na ₂ O	4.09	3.99	4.40	3.99	4.06	4.54	4.13	4.20	4.13	4.49
K ₂ O	0.60	0.58	0.91	0.61	0.90	0.63	0.62	0.69	0.85	0.69
P ₂ O ₅	0.23	0.28	0.30	0.22	0.29	0.23	0.26	0.22	0.36	0.31
H ₂ O	1.0	1.1	0.4	0.2	0.2	0.1	1.5	0.6	2.2	2.3
CO ₂ ppm	MDL	MDL	MDL	MDL	MDL	MDL	MDL	MDL	MDL	MDL
S ppm	782	796	78	714	11	1786	837	792	475	670
Cl ppm	1048	955	1013	949	897	1045	957	971	473	742
Total ^b	99.45	99.04	99.75	99.68	99.93	99.83	100.60	100.12	99.78	97.46
Olivine (Fo%)	80.7	80.7	76.2	76.2	76.3	80.8	80.8	80.5	81.6	73.6
%PEC ^c	4.4	3.6	4.5	4.5	6.5	6.1	6.6	0.5	1.1	4.3

^a All Fe reported as FeO*; ^b Total = sum of all oxides plus S and Cl in original (uncorrected) microprobe analyses; ^c %PEC = wt% post-entrapment crystallization of olivine. All melt inclusion data were corrected for post-entrapment crystallization (%PEC) of olivine (Sobolev and Chaussidon, 1996) and diffusive loss of Fe (Danyushevsky et al., 2002). ⁺ Denotes melt inclusions for which Fe was added. Major element oxides reported are normalized to 100% on a volatile-free basis. MDL denotes CO₂ values below the detection limit (50 ppm). The average standard deviation based on multiple analyses (3-6 points) is as follows: SiO₂ (0.28), Al₂O₃ (0.20), TiO₂ (0.12), FeO* (0.27), MgO (0.19), CaO (0.20), MnO (0.19), Na₂O (0.20), K₂O (0.04), P₂O₅ (0.02), S (60), Cl (50). NA = host olivine forms that were not apparent.

REFERENCES

CHAPTER I

- Annen C, Blundy JD, Sparks RS (2006) The genesis of intermediate and silicic magmas in deep crustal hot zones. *Journal of Petrology* 47(3):505-539
- Cloos M (2001) Bubbling magma chambers, cupolas, and porphyry copper deposits. *International Geology Review* 43(4):285-311
- Hildreth W, Moorbath S (1988) Crustal contributions to arc magmatism in the Andes of Central Chile. *Contributions to Mineralogy and Petrology* 98:455-489
- Kushiro I (1972) Effect of water on the composition of magmas formed at high pressures. *Journal of Petrology* 13(2):311-334
- Seedorff E, Dilles JH, John M, Proffett J, Einaudi MT, Surcher L, Stavast WJA, Johnson DA, Barton MD (2005) Porphyry Deposits: Characteristics and Origin of Hypogene Features. *Economic Geology 100th Anniversary Volume*:251-298
- Wyllie PJ (1979) Magmas and volatile components. *American Mineralogist* 64:469-500

CHAPTER II

- Albarède F, Provost A (1977) Petrological and geochemical mass-balance equations: an algorithm for least-square fitting and general error analysis. *Computers and Geosciences* 3:309-326
- Annen C, Blundy JD, Sparks RS (2006) The genesis of intermediate and silicic magmas in deep crustal hot zones. *Journal of Petrology* 47(3):505-539
- Arculus RJ, Wills KJ (1980) The petrology of plutonic blocks and inclusions from the Lesser Antilles island arc. *Journal of Petrology* 21(4):743-799
- Bacon CR, Bruggman PE, Christiansen RL, Clynne MA, Donnelly-Nolan JM, Hildreth W (1997) Primitive magmas at five Cascade volcanic fields: melts from hot, heterogeneous sub-arc mantle. *The Canadian Mineralogist* 35:397-423
- Bacon CR, Nathenson M (1996) Geothermal resources in the Crater Lake area, Oregon. In: *Open-File Report 96-663*, vol. U.S. Geological Survey,

- Baker DR, Eggler DH (1983) Fractionation paths of Atka (Aleutians) high-alumina basalts: constraints from phase relations. *Journal of Volcanology and Geothermal Research* 18:387-404
- Baker MB, Grove TL, Price R (1994) Primitive basalts and andesites from the Mt. Shasta region, N. California: products of varying melt fraction and water content. *Contributions to Mineralogy and Petrology* 118:111-129
- Baker MB, Stolper EM (1994) Determining the composition of high-pressure mantle melts using diamond aggregates. *Geochimica et Cosmochimica Acta* 58(13):2811-2827
- Ballhaus C, Berry RF, Green DH (1990) Oxygen fugacity controls in the Earth's upper mantle. *Nature* 348:437-440
- Bartels KS, Kinzler RJ, Grove TL (1991) High pressure phase relations of primitive high-alumina basalts from Medicine Lake volcano, northern California. *Contributions to Mineralogy and Petrology* 108:253-270
- Berly TJ, Hermann J, Arculus RJ, Lapiere H (2006) Supra-subduction zone pyroxenites from San Jorge and Santa Isabel (Soloman Islands). *Journal of Petrology* 47(8):1531-1555
- Blackwell DD, Steele JL, Frohne MK, Murphey CF, Priest GR, Black GL (1990) Heat flow in the Oregon Cascade Range and its correlation with regional gravity, curie point depths, and geology. *Journal of Geophysical Research* 95(B12):19475-19493
- Brandon AD, Draper DS (1996) Constraints on the origin of the oxidation state of mantle overlying subduction zones: An example from Simcoe, Washington, USA. *Geochimica et Cosmochimica Acta* 60(10):1739-1749
- Brooker R, Holloway JR, Hervig R (1998) Reduction in piston-cylinder experiments: The detection of carbon infiltration into platinum capsules. *American Mineralogist* 83:985-994
- Brophy JG, Dreher ST (2000) The origin of composition gaps at South Sister Volcano, central Oregon: implications for fractional crystallization processes beneath active calc-alkaline volcanoes. *Journal of Volcanology and Geothermal Research* 102:287-307
- Cervantes P, Wallace P (2003) Magma degassing and basaltic eruption styles: a case study of ~2000 year BP Xitle volcano in central Mexico. *Journal of Volcanology and Geothermal Research* 120:249-270

- Claeson DT, Meurer WP (2004) Fractional crystallization of hydrous basaltic "arc-type" magmas and the formation of amphibole-bearing gabbroic cumulates. *Contributions to Mineralogy and Petrology* 147:288-304
- Conrad WK, Kay RW (1984) Ultramafic and mafic inclusions from Adak Island: crystallization history, and implications for the nature of primary magmas and crustal evolution in the Aleutian Arc. *Journal of Petrology* 25(1):88-125
- Conrey RM, Hooper PR, Larson PB, Chesley J, Ruiz J (2001) Trace element and isotopic evidence for two types of crustal melting beneath a High Cascade volcanic center, Mt. Jefferson, Oregon. *Contributions to Mineralogy and Petrology* 141:710-732
- Conrey RM, Sherrod DR, Hooper PR, Swanson DA (1997) Diverse primitive magmas in the Cascade Arc, northern Oregon and southern Washington. *The Canadian Mineralogist* 35:367-396
- Couch RW, Riddihough RP (1989) The crustal structure of the western continental margin of North America. In: Pakiser LC, Mooney WD (eds) *Geophysical framework of the continental United States*, vol 172. Geological Society of America, Boulder, CO, pp 103-128
- Crawford AJ, Falloon TJ, Eggins S (1987) The origin of island arc high-alumina basalts. *Contributions to Mineralogy and Petrology* 97:417-430
- Danyushevsky LV, Sokolov S, Falloon TJ (2002) Melt inclusions in olivine phenocrysts: using diffusive re-equilibration to determine the cooling history of a crystal, with implications for the origin of olivine-phyric volcanic rocks. *Journal of Petrology* 43:1651-1671
- DeBari SM, Sleep NH (1991) High-Mg, low-Al bulk composition of the Talkeetna island arc, Alaska: implications for primary magmas and the nature of arc crust. *Geological Society of America Bulletin* 103:37-47
- Dixon JE, Pan V (1995) Determination of molar absorptivity of dissolved carbonate in basaltic glass. *American Mineralogist* 80:1339-1342
- Donovan JJ, Tingle TN (1996) An improved mean atomic number correction for quantitative microanalysis. *Journal of Microscopy* 2:1-7
- Drake MJ, Weill DF (1975) Partition of Sr, Ba, Ca, Y, Eu²⁺, Eu³⁺, and other REE between plagioclase feldspar and magmatic liquid: an experimental study. *Geochimica et Cosmochimica Acta* 39:689-712

- Dunn T, Sen C (1994) Mineral/matrix partition coefficients for orthopyroxene, plagioclase, and olivine in basaltic to andesitic systems: A combined analytical and experimental study. *Geochimica et Cosmochimica Acta* 58:717-733
- Fine G, Stolper E (1985) The speciation of carbon dioxide in sodium aluminosilicate glasses. *Contributions to Mineralogy and Petrology* 91:105-121
- Freda C, Baker DR, Ottolini L (2001) Reduction of water loss from gold-palladium capsules during piston-cylinder experiments by use of pyrophyllite powder. *American Mineralogist* 86:234-237
- Gaetani GA, Grove TL (1998) The influence of water on melting of mantle peridotite. *Contributions to Mineralogy and Petrology* 131:323-346
- Gaetani GA, Grove TL (2003) Experimental constraints on melt generation in the mantle wedge. In: Eiler J (ed) *Inside the Subduction Factory*, vol. American Geophysical Union, pp 107-133
- Grashoff GJ, Pilkington CE, Conti CW (1983) The purification of hydrogen. *Platinum Metals Review* 27:157-169
- Green DH (1973) Conditions of melting of basanite magma from garnet peridotite. *Earth and Planetary Science Letters* 17:456-565
- Greene AR, DeBari SM, Kelemen PB, Blusztajn J, Clift PD (2006) A detailed geochemical study of island arc crust: the Talkeetna Arc Section, South-Central Alaska. *Journal of Petrology* 47(6):1051-1093
- Grove TL, Chatterjee N, Parman SW, Médard E (2006) The influence of H₂O on mantle wedge melting. *Earth and Planetary Science Letters* 249:74-89
- Grove TL, Elkins-Tanton LT, Parman SW, Chatterjee N, Müntener O, Gaetani GA (2003) Fractional crystallization and mantle-melting controls on calc-alkaline differentiation trends. *Contributions to Mineralogy and Petrology* 145:515-533
- Grove TL, Parman SW, Bowring SA, Price RC, Baker MB (2002) The role of an H₂O-rich fluid component in the generation of primitive basaltic andesites and andesites from the Mt. Shasta region, N. California. *Contributions to Mineralogy and Petrology* 142:375-396
- Hall LJ, Brodie J, Wood BJ, Carroll MR (2004) Iron and water losses from hydrous basalts contained in Au₈₀Pd₂₀ capsules at high pressure and temperature. *Mineralogical Magazine* 68(1):75-81

- Halliday AN, Lee D, Tommasini S, Davies GR, Paslick CR, Fitton JG, James DE (1995) Incompatible trace elements in OIB and MORB and source enrichment in the sub-oceanic mantle. *Earth and Planetary Science Letters* 133:379-395
- Hildreth W, Moorbath S (1988) Crustal contributions to arc magmatism in the Andes of Central Chile. *Contributions to Mineralogy and Petrology* 98:455-489
- Hirose K, Kawamoto T (1995) Hydrous partial melting of lherzolite at 1 GPa: the effect of H₂O on the genesis of basaltic magmas. *Earth and Planetary Science Letters* 133:463-473
- Hirose K, Kushiro I (1993) Partial melting of dry peridotites at high pressures: determination of compositions of melts segregated from peridotites using aggregates of diamond. *Earth and Planetary Science Letters* 114:477-489
- Holloway JR, Pan V, Gudmundsson G (1992) High-pressure fluid-absent melting experiments in the presence of graphite: oxygen fugacity, ferric/ferrous ratio and dissolved CO₂. *European Journal of Mineralogy* 4:105-114
- Johannes W, Bode B (1978) Loss of iron to the pt-container in melting experiments with basalts and a method to reduce it. *Contributions to Mineralogy and Petrology* 67:221-225
- Johnson ER, Wallace PJ, Cashman KV, Granados HD, and Kent AJR (2008) Magmatic volatile contents and degassing-induced crystallization at Volcán Jorullo, Mexico: Implications for melt evolution and the plumbing systems of monogenetic volcanoes. *Earth and Planetary Science Letters* 269:477-486
- Johnson ER, Wallace PJ, Granados HD (2005) Magmatic volatile variations along a trench-perpendicular transect in the Central Trans-Mexican Volcanic Belt. *Eos Trans. AGU* 86(52):Fall Meet. Suppl., Abstract V41A-1423
- Johnston AD, Schwab BE (2004) Constraints on clinopyroxene/melt partitioning of REE, Rb, Sr, Ti, Cr, Zr, and Nb during mantle melting: first insights from direct peridotite melting experiments at 1.0 GPa. *Geochimica et Cosmochimica Acta* 68(23):4949-4962
- Kägi R, Müntener O, Ulmer P, Ottolini L (2005) Piston-cylinder experiments on H₂O undersaturated Fe-bearing systems: An experimental setup approaching f_{O2} conditions of natural calc-alkaline magmas. *American Mineralogist* 90:708-717
- Kawamoto T, Hirose K (1994) Au-Pd sample containers for melting experiments on iron and water bearing systems. *European Journal of Mineralogy* 6:381-385

- Kay SM, Kay RW, Citron GP (1982) Tectonic controls on tholeiitic and calc-alkaline magmatism in the Aleutian arc. *Journal of Geophysical Research* 87(B5):4051-4072
- Kelemen PB, Rilling JL, Parmentier EM, Mehl L, Hacker BR (2003) Thermal Structure due to Solid-State Flow in the Mantle Wedge Beneath Arcs. *Inside the Subduction Factory Geophysical Monograph* 138:293-331
- Kelemen PB, Shimizu N, Dunn T (1993) Relative depletion of niobium in some arc magmas and the continental crust: partitioning of K, Nb, La and Ce during melt/rock reaction in the upper mantle. *Earth and Planetary Science Letters* 120:111-134
- Kushiro I, Thompson RN (1972) Origin of Some Abyssal Tholeiites from the Mid-Atlantic Ridge. *Year Book - Carnegie Institution of Washington* 71:403-406
- Langmuir CH, Klein EM, Plank T (1992) Petrological systematics of mid-ocean ridge basalts: constraints on melt generation beneath ocean ridges. In: *Mantle flow and melt generation at mid-ocean ridges*, Geophysical Monograph 71, vol. American Geophysical Union,
- Leeman WP, Lewis JF, Evarts RC, Conrey RM, Streck MJ (2005) Petrologic constraints on the thermal structure of the Cascades arc. *Journal of Volcanology and Geothermal Research* 140:67-105
- Mandeville CW, Webster JD, Rutherford MJ, Taylor BE, Timbal A, Faure K (2002) Determination of molar absorptivities for infrared absorption bands of H₂O in andesitic glasses. *American Mineralogist* 87:813-821
- McDonough WF, Sun SS (1995) Composition of the Earth. *Chemical Geology* 120:223-253
- Merrill RB, Wyllie PJ (1973) Absorption of iron by platinum capsules in high pressure rock melting experiments. *American Mineralogist* 58:16-20
- Moore G, Carmichael ISE (1998) The hydrous phase equilibria (to 3 kbar) of an andesite and basaltic andesite from western Mexico: constraints on water content and conditions of phenocryst growth. *Contributions to Mineralogy and Petrology* 130:304-319
- Müntener O, Kelemen PB, Grove TL (2001) The role of H₂O during crystallization of primitive arc magmas under uppermost mantle conditions and genesis of igneous pyroxenites: an experimental study. *Contributions to Mineralogy and Petrology* 141:643-658
- Nielsen CH, Sigurdsson H (1981) Quantitative methods for electron microprobe analysis of sodium in natural and synthetic glasses. *American Mineralogist* 66:547-552

- Parkinson IJ, Arculus RJ (1999) The redox state of subduction zones: insights from arc-peridotites. *Chemical Geology* 160:409-423
- Parsons T, Wells RE, Fisher MA (1999) Three-dimensional velocity structure of Siletzia and other accreted terranes in the Cascadia forearc of Washington. *Journal of Geophysical Research* 104(B8):18015-18039
- Pickering-Witter J, Johnston AD (2000) The effects of variable bulk composition on the melting systematics of fertile peridotitic assemblages. *Contributions to Mineralogy and Petrology* 140:190-211
- Pickering JM, Schwab BE, Johnston AD (1998) Off-center hot spots: Double thermocouple determination of the thermal gradient in a 1.27 cm (1/2 in.) CaF₂ piston-cylinder furnace assembly. *American Mineralogist* 83:228-235
- Roman DC, Cashman KV, Gardner CA, Wallace PJ, Donovan JJ (2006) Storage and interaction of compositionally heterogeneous magmas from the 1986 eruption of Augustine Volcano, Alaska. *Bulletin of Volcanology* 68:240-254
- Schmidt ME (2005) Deep crustal and mantle inputs to North Sister Volcano, Oregon High Cascade Range. In: Department of Geosciences, vol. Oregon State University, Corvallis, p 197
- Schmidt ME, Grunder AL (2009) The evolution of North Sister: A volcano shaped by extension and ice in the central Oregon Cascade Arc. *Geological Society of America Bulletin* 121(5-6):643-662
- Schwab BE, Johnston AD (2001) Melting systematics of modally variable, compositionally intermediate peridotites and the effects of mineral fertility. *Journal of Petrology* 42(10):1789-1811
- Scott WE, Iverson, R.M., Schilling, S.P., Fisher, B.J. (2001) Volcano hazards in the Three Sisters region, Oregon. In: Open-File Report 99-437, vol. U.S. Geological Survey,
- Sherrod DR, Mastin LG, Scott WE, Schilling SP (1997) Volcano hazards at Newberry Volcano, Oregon. In: Open-File Report 97-0513, vol. U.S. Geological Survey,
- Sisson TW, Grove TL (1993a) Experimental investigations of the role of H₂O in calc-alkaline differentiation and subduction zone magmatism. *Contributions to Mineralogy and Petrology* 113:143-166
- Sisson TW, Grove TL (1993b) Temperatures and H₂O contents of low-MgO high-alumina basalts. *Contributions to Mineralogy and Petrology* 113:167-184
- Sisson TW, Layne GD (1993) H₂O in basalt and basaltic andesite glass inclusions from four subduction-related volcanoes. *Earth and Planetary Science Letters* 117:619-635

- Sneeringer MA, Watson B (1985) Milk cartons and ash cans: two unconventional welding techniques. *American Mineralogist* 70:200-201
- Sobelev AV, Chaussidon M (1996) H₂O concentrations in primary melts from supra-subduction zones and mid-ocean ridges; implications for H₂O storage and recycling in the mantle. *Earth and Planetary Science Letters* 137(1-4):45-55
- Stanley WD, Mooney WD, Fuis GS (1990) Deep crustal structure of the Cascade Range and surrounding regions from seismic refraction and magnetotelluric data. *Journal of Geophysical Research* 95:19419-19438
- Tatsumi Y, Eggins S (1995) *Subduction Zone Magmatism*, vol. Blackwell Science, Inc., Ann Arbor, MI, pp 1-211
- Trehu AM, Asudeh I, Brocher TM, Luetgert JH, Mooney WD, Nabelek JL, Nakamura Y (1994) Crustal architecture of the Cascadia Forearc. *Science* 266:237-243
- Truckenbrodt J, Johannes W (1999) H₂O loss during piston-cylinder experiments. *American Mineralogist* 84:1333-1335
- Ulmer P, Luth RW (1991) The graphite-COH fluid equilibrium in P, T, f_{O2} space: An experimental determination to 30 kbar and 1600 degrees C. *Contributions to Mineralogy and Petrology* 106:265-272
- Wilson DS (1988) Tectonic history of the Juan de Fuca Ridge over the last 40 million years. *Journal of Geophysical Research* 93(B10):11,863-811,876
- Wood BJ, Blundy JD (1997) A predictive model for rare earth element partitioning between clinopyroxene and anhydrous silicate melt. *Contributions to Mineralogy and Petrology* 129:166-181
- Wright TL, Pierson TC (1992) Living with volcanoes. In: U.S. Geological Survey Circular, vol. U.S. Geological Survey,
- Wyllie PJ (1979) Magmas and volatile components. *American Mineralogist* 64:469-500

CHAPTER III

- Annen, C., Blundy, J.D., and Sparks, R.S., 2006, The genesis of intermediate and silicic magmas in deep crustal hot zones: *Journal of Petrology*, v. 47, p. 505-539.
- Bachmann, O., and Bergantz, G.W., 2004, On the origin of crystal-poor rhyolites: extracted from batholithic crystal mushes: *Journal of Petrology*, v. 45, p. 1565-1582.

- Brimhall, G.H., 1977, Early fracture-controlled disseminated mineralization at Butte, Montana: *Economic Geology*, v. 72, p. 37-59.
- Candela, P.A., 1997, A review of shallow, ore-related granites: textures, volatiles, and ore metals: *Journal of Petrology*, v. 38, p. 1619-1633.
- Černý, P., Blevin, P.L., Cuney, M., and London, D., 2005, Granite-related ore deposits: *Economic Geology*, v. 100, p. 337-370.
- Cloos, M., 2001, Bubbling magma chambers, cupolas, and porphyry copper deposits: *International Geology Review*, v. 43, p. 285-311.
- Cooke, D.R., Hollings, P., and Walshe, J.L., 2005, Giant porphyry deposits: characteristics, distribution, and tectonic controls: *Economic Geology*, v. 100, p. 801-818.
- Dall'Agnol, R., Scaillet, B., and Pichavant, M., 1999, An Experimental Study of a Lower Proterozoic A-type Granite from the Eastern Amazon Craton, Brazil: *Journal of Petrology*, v. 40, p. 1673-1698.
- Davidson, P., Kamenetsky, V., Cooke, D.R., and Frikken, P., 2005, Magmatic Precursors of Hydrothermal Fluids at the Río Blanco Cu-Mo Deposit, Chile: Links to Silicate Magmas and Metal Transport: *Economic Geology*, v. 100, p. 963-978.
- Dilles, J.H., 1987, Petrology of the Yerington Batholith, Nevada: Evidence for Evolution of Porphyry Copper Ore Fluids: *Economic Geology*, v. 82, p. 1750-1789.
- Field, C.W., Zhang, L., Dilles, J.H., Rye, R.O., and Reed, M.H., 2005, Sulfur and oxygen isotopic record in sulfate and sulfide minerals of early, deep, pre-Main Stage porphyry Cu-Mo and late Main Stage base-metal mineral deposits, Butte district, Montana: *Chemical Geology*, v. 215, p. 61-93.
- Graney, J.R., and Kesler, S.E., 1995, Gas composition of inclusion fluid in ore deposits: is there a relation to magmas? *in* Thompson, J.F.H., ed., *Magmas, fluids and ore deposits*, Volume Short Course 23: Victoria, B.C., Mineralogical Association of Canada, p. 221-244.
- Humphreys, E., Hessler, E., Dueker, K., Farmer, G.L., Erslev, E., and Atwater, T., 2003, How Laramide-Age Hydration of North American Lithosphere by the Farallon Slab Controlled Subsequent Activity in the Western United States: *International Geology Review*, v. 45, p. 575-595.

- Keith, J.D., Shanks, W.C., III, Archibald, D.A., and Farrar, E., 1986, Volcanic and Intrusive History of the Pine Grove Porphyry Molybdenum System, Southwestern Utah: *Economic Geology*, v. 81, p. 553-577.
- Klimm, K., Holtz, F., Johannes, W., and King, P.L., 2003, Fractionation of metaluminous A-type granites: an experimental study of the Wangrah Suite, Lachlan Fold Belt, Australia: *Precambrian Research*, v. 124, p. 327-341.
- Liu, Y., Zhang, Y., and Behrens, H., 2005, Solubility of H₂O in rhyolitic melts at low pressures and a new empirical model for mixed H₂O-CO₂ solubility in rhyolitic melts: *Journal of Volcanology and Geothermal Research*, v. 143, p. 219-235.
- Lowenstern, J.B., 1994, Dissolved volatile concentrations in an ore-forming magma: *Geology*, v. 22, p. 893-896.
- , 2001, Carbon dioxide in magmas and implications for hydrothermal systems: *Mineralium Deposita*, v. 36, p. 490-502.
- Lowenstern, J.B., Bacon, C.R., and Calk, L.C., 1994, Major-Element, Trace-Element, and Volatile-Concentrations in Silicate Melt Inclusions from the Tuff of Pine Grove, Wah Wah Mountains, Utah: U.S. Geological Survey Open-file Report 94-242, p. 1-20.
- Maaløe, S., 1985, *Fractional Crystallization, Principles of Igneous Petrology*: Berlin, Springer-Verlag, p. 182-229.
- Naney, M.T., 1983, Phase equilibria of rock-forming ferromagnesian silicates in granitic systems: *American Journal of Science*, v. 283, p. 993-1033.
- Newman, S., and Lowenstern, J.B., 2002, VolatileCalc: a silicate melt-H₂O-CO₂ solution model written in Visual Basic for excel: *Computers & Geosciences*, v. 28, p. 597-604.
- Rapien, M.H., Bodnar, R.J., Simmons, S.F., Szabo, C.S., Wood, C.P., and Sutton, S.R., 2003, Melt inclusion study of the embryonic porphyry copper system at White Island, New Zealand: *Society of Economic Geologists Special Publication*, v. 10, p. 41-59.
- Redmond, P.B., 2002, Magmatic-hydrothermal fluids and copper-gold ore formation at Bingham Canyon, Utah [PhD thesis], Stanford University.
- Richards, J.P., 2003, Tectono-magmatic precursors for porphyry Cu-(Mo-Au) deposit formation: *Economic Geology*, v. 98, p. 1515-1533.

- Rusk, B.G., Reed, M.H., and Dilles, J.H., 2008, Fluid inclusion evidence for magmatic-hydrothermal fluid evolution in the porphyry copper-molybdenum deposit at Butte, Montana: *Economic Geology*, v. 103, p. 307-334.
- Saar, M.O., Manga, M., Cashman, K.V., and Fremouw, S., 2001, Numerical models of the onset of yield strength in crystal-melt suspensions: *Earth and Planetary Science Letters*, v. 187, p. 367-379.
- Seedorff, E., Dilles, J.H., John M. Proffett, J., Einaudi, M.T., Surcher, L., Stavast, W.J.A., Johnson, D.A., and Barton, M.D., 2005, *Porphyry Deposits: Characteristics and Origin of Hypogene Features: Economic Geology*, v. 100th Anniversary Volume, p. 251-298.
- Shinohara, H., and Kazahaya, K., 1995, Degassing processes related to magma-chamber crystallization, *in* Thompson, J.F.H., ed., *Magmas, fluids, and ore deposits: Victoria, British Columbia, Mineralogical Association of Canada Short Course Series*, p. 47-70.
- Vejmelek, L., and Smithson, S.B., 1995, Seismic reflection profiling in the Boulder Batholith, Montana: *Geology*, v. 23, p. 811-814.
- Wallace, P.J., 2005, Volatiles in subduction zone magmas: concentrations and fluxes based on melt inclusion and volcanic gas data: *Journal of Volcanology and Geothermal Research*, v. 140, p. 217-240.
- Wark, D.A., Hildreth, W., Spear, F.S., Cherniak, D.J., and Watson, E.B., 2007, Pre-eruption recharge of the Bishop magma system: *Geology* v. 35, p. 235.

CHAPTER IV

- Anderko, A. and Pitzer, K.S., 1993a. Equation of state representation of phase equilibria and volumetric properties of the system NaCl-H₂O above 573 K *Geochimica et Cosmochimica Acta*, 57: 1657-1680.
- Anderko, A. and Pitzer, K.S., 1993b. Phase equilibria and volumetric properties of the systems KCl-H₂O and NaCl-KCl-H₂O above 573 K: equation of state representation. *Geochimica et Cosmochimica Acta*, 57: 4885-4897.
- Archer, D.G., 1992. Thermodynamic properties of the NaCl+H₂O system: II. Thermodynamic properties of NaCl(aq), NaCl•2H₂O(cr), and phase equilibria. *Journal of Physical Chemistry, Ref. Data* 28: 1-17.

- Audétat, A. and Pettke, T., 2006. Evolution of a porphyry-Cu mineralized magma system at Santa Rita, New Mexico (USA). *Journal of Petrology*, 47(10): 2021-2046.
- Bakker, R.J., 1997. Clathrates: Computer programs to calculate fluid inclusion V-X properties using clathrate melting temperatures. *Computers & Geosciences*, 23(1): 1-18.
- Bakker, R.J., 2003. Package FLUIDS 1. Computer programs for analysis of fluid inclusion data and for modeling bulk fluid properties. *Chemical Geology*, 194: 3-23.
- Bodnar, R.J., Samison, I., Anderson, A. and Marshall, D., 2003. Introduction to Aqueous-Electrolyte Fluid Inclusions, *Fluid Inclusions: Analysis and Interpretation*. Mineral. Assoc. Canada, Short Course 32, pp. 81-99.
- Bogaerts, M., Scaillet, B. and Auwera, J.V., 2006. Phase equilibria of the Lyngdal Granodiorite (Norway): Implications for the origin of metaluminous ferroan granitoids. *Journal of Petrology*, 47(12): 2405-2431.
- Bowman, J.R., Parry, W.T., Kropp, W.P. and Krueger, S.A., 1987. Chemical and isotopic evolution of hydrothermal solutions at Bingham, Utah. *Economic Geology*, 82: 395-428.
- Brimhall, G.H., 1977. Early fracture-controlled disseminated mineralization at Butte, Montana. *Economic Geology*, 72: 37-59.
- Brimhall, G.J., 1973. Mineralogy, texture, and chemistry of early wall rock alteration in the deep underground mines and continental area, Butte District, Montana, Butte Field Meeting of Society of Economic Geologists, pp. H1-H5.
- Burnham, C.W., 1979. Magmas and hydrothermal fluids. In: H.L. Barnes (Editor), *Geochemistry of hydrothermal ore deposits*, 2nd ed. John Wiley, New York, pp. 71-136.
- Cherniak, D.J., Watson, E.B. and Wark, D.A., 2007. Ti diffusion in quartz. *Chemical Geology*, 236: 65-74.
- D'lemos, R.S., Kearsley, A.T., Pembroke, J.W., Watt, G.R. and Wright, P., 1997. Complex quartz growth histories in granite revealed by scanning cathodoluminescence techniques. *Geological Magazine*, 134(4): 549-552.
- Dall'Agnol, R., Scaillet, B. and Pichavant, M., 1999. An Experimental Study of a Lower Proterozoic A-type Granite from the Eastern Amazon Craton, Brazil. *Journal of Petrology*, 40(11): 1673-1698.

- Dilles, J.H., 1987. Petrology of the Yerington Batholith, Nevada: Evidence for Evolution of Porphyry Copper Ore Fluids. *Economic Geology*, 82: 1750-1789.
- Dilles, J.H., Martin, M.W., Stein, H. and Rusk, B., 2003. Re-Os and U-Pb ages for the Butte copper district, Montana; a short- or long-lived hydrothermal system? *Geological Society of America-Abstract with Programs*, 35(6): 400.
- Dilles, J.H., Reed, M.H., Roberts, S., Zhang, L. and Houston, R., 1999. Early magmatic-hydrothermal features related to porphyry copper mineralization at Butte, Montana. *Geological Society of America-Abstract with Programs*, 31(7): 380-381.
- Doe, B.R., Tilling, R.I., Hedge, C.E. and Klepper, M.R., 1968. Lead and Strontium Isotope Studies of the Boulder Batholith, Southerwestern Montana. *Economic Geology*, 63: 884-906.
- Duan, Z., Møller, N. and Weare, J.H., 1992a. An equation of state for the CH₂-CO₂-H₂O system: I. Pure systems from 0 to 1000°C and 0 to 8000 bar. *Geochimica et Cosmochimica Acta*, 56(7): 2605-2617.
- Duan, Z., Møller, N. and Weare, J.H., 1992b. An equation of state for the CH₂-CO₂-H₂O system: II. Mixtures from 50 to 1000°C and 0 to 1000 bar *Geochimica et Cosmochimica Acta*, 56(7): 2619-2631.
- Duan, Z., Møller, N. and Weare, J.H., 1995. Equation of state for the NaCl-H₂O-CO₂ system: prediction of phase equilibria and volumetric properties. *Geochimica et Cosmochimica Acta*, 59: 2869-2882.
- Field, C.W., Zhang, L., Dilles, J.H., Rye, R.O. and Reed, M.H., 2005. Sulfur and oxygen isotopic record in sulfate and sulfide minerals of early, deep, pre-Main Stage porphyry Cu-Mo and late Main Stage base-metal mineral deposits, Butte district, Montana. *Chemical Geology*, 215: 61-93.
- Geiger, S., Haggerty, R., Dilles, J., Reed, M. and Matthai, S., 2002. New insights from reactive transport modeling; the formation of sericitic vein envelopes during early hydrothermal alteration at Butte, Montana. *Geofluids*, 2: 185-201.
- Grew, E.S. et al., 2006. Beryllium and other trace elements in paragneisses and anatectic veins of the ultrahigh-temperature Napier Complex, Enderby Land, East Antarctica: the role of sapphirine. *Journal of Petrology*, 47(5): 859-882.
- Hayden, L.A. and Watson, E.B., 2007. Rutile saturation in hydrous siliceous melts and its bearing on Ti-thermometry of quartz and zircon. *Earth and Planetary Science Letters*, 258: 561-568.

- Hedenquist, J.W. and Lowenstern, J.B., 1994. The role of magmas in the formation of hydrothermal ore deposits. *Nature*, 370: 519-527.
- Henry, D.J., Guidotti, C.V. and Thomson, J.A., 2005. The Ti-saturation surface for low-to-medium pressure metapelitic biotites: Implications for geothermometry and Ti-substitution mechanisms. *American Mineralogist*, 90: 316-328.
- Holtz, F., Becker, A., Freise, M. and Johannes, W., 2001. The water-undersaturated and dry Qz-Ab-Or system revisited. Experimental results at very low water activities and geological implications. *Contributions to Mineralogy and Petrology*, 141: 347-357.
- Holtz, F. and Johannes, W., 1994. Maximum and minimum water contents of granitic melts: implications for chemical and physical properties of ascending magmas. *Lithos*, 23: 149-159.
- Holtz, F., Pichavant, M., Barbey, P. and Johannes, W., 1992. Effects of H₂O on liquidus phase relations in the haplogranite system at 2 and 5 kbar. *American Mineralogist*, 77: 1223-1241.
- Klepper, M.R., Robinson, G.D. and Smedes, H.W., 1971. On the nature of the Boulder Batholith of Montana. *Geological Society of America Bulletin*, 82: 1563-1580.
- Klimm, K., Holtz, F., Johannes, W. and King, P.L., 2003. Fractionation of metaluminous A-type granites: an experimental study of the Wangrah Suite, Lachlan Fold Belt, Australia. *Precambrian Research*, 124: 327-341.
- Landtwing, M.R. and Pettke, T., 2005. Relationships between SEM-cathodoluminescence response and trace-element compositions of hydrothermal vein quartz. *American Mineralogist*, 90: 122-131.
- Lowers, H.A., Donovan, J.J. and Rusk, B.G., in review. Improved electron probe microanalysis of trace elements. *American Mineralogist*.
- Lund, K. et al., 2002. SHRIMP U-Pb and ⁴⁰Ar/³⁹Ar age constraints of relating plutonism and mineralization in the Boulder Batholith region, Montana. *Economic Geology*, 97: 241-267.
- Meyer, C., 1965. An early potassic type of wall rock alteration at Butte, Montana. *American Mineralogist*, 50: 1717-1722.
- Meyer, C. and Hemley, J.J., 1967. Wall rock alteration. In: H.L. Barnes (Editor), *Geochemistry of hydrothermal ore deposits*. Rinehart and Winston, Inc., New York, pp. 166-232.

- Meyer, C., Shea, E.P. and Charles C. Goddard, J., 1968. Ore Deposits at Butte, Montana, Ore Deposits of the U.S., pp. 1373-1415.
- Mueller, A., Wiedenbeck, M., van den Kerkhof, A.M., Kronz, A. and Simon, K., 2003. Trace elements in quartz; a combined electron microprobe, secondary ion mass spectrometry, laser-ablation ICP-MS, and cathodoluminescence study. *European Journal of Mineralogy*, 15: 747-763.
- Naney, M.T., 1983. Phase equilibria of rock-forming ferromagnesian silicates in granitic systems. *American Journal of Science*, 283: 993-1033.
- O'Neill, J.M. et al., 2002. Integrated investigation of environmental effects of historical mining in the Basin and Boulder mining districts, Boulder River watershed, Jefferson County, Montana. In: D.A. Nimick, S.E. Church and S.E. Finger (Editors), *Geologic Framework*. U.S. Geological Survey Professional Paper.
- Redmond, P.B., Einaudi, M.T., Inan, E.E., Landtwing, M.R. and Heinrich, C.A., 2004. Copper deposition by fluid cooling in intrusion-centered systems; new insights from the Bingham porphyry ore deposit, Utah. *Geology*, 32: 217-220.
- Reed, M.H., 1999. Zoning of metals and early potassic and sericitic hydrothermal alteration in the Butte, Montana, porphyry Cu-Mo deposit. *Geological Society of America Abstracts with Programs*, 31(&): A381.
- Reed, M.H., Rusk, B., Palandri, J. and Dilles, J.H., 2005. The Butte hydrothermal system: One magmatic fluid yielded all vein types. *Geological Society of America Abstracts with Programs*, 37(7): A315.
- Roberts, S.A., 1973. Pervasive early alteration in the Butte district, Montana. In: R.N. Miller (Editor), *Society of Economic Geologists, Butte field meeting Guidebook*, The Anaconda Company, pp. HH1-HH8.
- Roberts, S.A., 1975. Early hydrothermal alteration and mineralization in the Butte district, Montana. Ph.D. dissertation Thesis, Harvard University, 157 pp.
- Rusk, B., Lowers, H.A. and Reed, M.H., 2008a. Trace elements in hydrothermal quartz: Relationships to cathodoluminescent textures and insights into vein formation. *Geology*, 36(7): 547-550.
- Rusk, B. and Reed, M., 2002. Scanning electron microscope-cathodoluminescence analysis of quartz reveals complex growth histories in veins from the Butte porphyry copper deposit, Montana. *Geology*, 30: 727-730.

- Rusk, B.G., Reed, M.H. and Dilles, J.H., 2008b. Fluid inclusion evidence for magmatic-hydrothermal fluid evolution in the porphyry copper-molybdenum deposit at Butte, Montana. *Economic Geology*, 103: 307-334.
- Rusk, B.G., Reed, M.H., Dilles, J.H. and Kent, A.J.R., 2006. Intensity of quartz cathodoluminescence and trace-element content in quartz from the porphyry copper deposit at Butte, Montana. *American Mineralogist*, 91: 1300-1312.
- Sales, R.H., 1914. Ore deposits at Butte, Montana. *American Institute of Mining and Metallurgical Engineers, Transactions*, 46: 4-106.
- Seedorff, E. et al., 2005. Porphyry Deposits: Characteristics and Origin of Hypogene Features. *Economic Geology, 100th Anniversary Volume*: 251-298.
- Shore, M. and Fowler, A.D., 1996. Oscillatory zoning in minerals: a common phenomenon. *Canadian Mineralogist*, 34: 1111-1126.
- Sillitoe, R.H., 1973. The tops and bottoms of porphyry copper deposits. *Economic Geology*, 68: 799-815.
- Smedes, H.W., 1973. Regional geologic setting of the Boulder Batholith, Montana, Butte Field Meeting of Society of Economic Geologists, pp. A1-A6.
- Smedes, H.W., Klepper, M.R. and Tilling, R.I., 1973. The Boulder Batholith, Montana (Field Trip), Butte Field Meeting of Society of Economic Geologists, pp. E1-E16.
- Snee, L. et al., 1999. Thermal history of the Butte porphyry system, Montana. *Geological Society of America-Abstract with Programs*, 31: 380.
- Tilling, R., 1973. The Boulder Batholith, Montana: Product of two contemporaneous but chemically and isotopically distinct magma series, Butte Field Meeting of Society of Economic Geologists, pp. C1-C5.
- Tuttle, O.F. and Bowen, N.L., 1958. Origin of granite in the light of experimental studies in the system $\text{NaAlSi}_3\text{O}_8\text{-KAlSi}_3\text{O}_8\text{-SiO}_2\text{-H}_2\text{O}$. *Geological Society of America Mem.*, 74: 145.
- Ulrich, T., Günther, D. and Heinrich, C.A., 2002. The evolution of a porphyry Cu-Au deposit, based on LA-ICP-MS analysis of fluid inclusions: Bajo de la Alumbrera, Argentina. *Economic Geology*, 97: 1889-1920.
- Vejmelek, L. and Smithson, S.B., 1995. Seismic reflection profiling in the Boulder Batholith, Montana. *Geology*, 23: 811-814.

- Wark, D.A., Hildreth, W., Spear, F.S., Cherniak, D.J. and Watson, E.B., 2007. Pre-eruption recharge of the Bishop magma system. *Geology* 35: 235.
- Wark, D.A. and Watson, E.B., 2006. TitaniQ; a titanium-in-quartz geothermometer. *Contributions to Mineralogy and Petrology*, 152: 743-754.
- Watson, E.B., Wark, D.A. and Thomas, J.B., 2006. Crystallization thermometers for zircon and rutile. *Contributions to Mineralogy and Petrology*, 151: 413-433.
- Weed, W.H., 1912. *Geology and ore deposits of the Butte district, Montana*. U.S. Geological Survey Professional Paper, 74: 262.

CHAPTER V

- Bons, P. D., 2001, The formation of large quartz veins by rapid ascent of fluids in mobile hydrofractures: *Tectonophysics*, v. 336, p. 1-17.
- Burnham, C. W., 1979, Magmas and hydrothermal fluids, *in* Barnes, H. L., ed., *Geochemistry of hydrothermal ore deposits*, 2nd ed.: New York, John Wiley, p. 71-136.
- Candela, P. A., and Piccoli, P. M., 2005, Magmatic processes in the development of porphyry-type ore systems: *Society of Economic Geologists*, v. *Economic Geology 100th Anniversary Volume*, p. 25-37.
- Carslaw, H. S., and Jaeger, J. C., 1947, *Linear flow of heat: the infinite and semi-infinite solid*, *Conduction of Heat in Solids*: London, Oxford University Press, p. 383.
- Cherniak, D. J., Watson, E. B., and Wark, D. A., 2007, Ti diffusion in quartz: *Chemical Geology*, v. 236, p. 65-74.
- Cline, J. S., and Bodnar, R. J., 1991, Can economic porphyry copper mineralization be generated by a typical calc-alkaline melt?: *Journal of Geophysical Research*, v. 96, p. 8113-8126.
- Cloos, M., 2001, Bubbling magma chambers, cupolas, and porphyry copper deposits: *International Geology Review*, v. 43, p. 285-311.
- Cooke, D. R., Hollings, P., and Walshe, J. L., 2005, Giant porphyry deposits: characteristics, distribution, and tectonic controls: *Economic Geology*, v. 100, p. 801-818.

- Delaney, P. T., and Pollard, D. D., 1982, Solidification of basaltic magma during flow in a dike: *American Journal of Science*, v. 282, p. 856-885.
- Dilles, J. H., 1987, Petrology of the Yerington Batholith, Nevada: Evidence for Evolution of Porphyry Copper Ore Fluids: *Economic Geology*, v. 82, p. 1750-1789.
- Dilles, J. H., and Einaudi, M. T., 1992, Wall-Rock Alteration and Hydrothermal Flow Paths About the Ann-Mason Porphyry Copper Deposit, Nevada- A 6 km Vertical Reconstruction: *Economic Geology*, v. 87, p. 1963-2001.
- Dilles, J. H., Martin, M. W., Stein, H., and Rusk, B., 2003, Re-Os and U-Pb ages for the Butte copper district, Montana; a short- or long-lived hydrothermal system?: *Geological Society of America-Abstract with Programs*, v. 35, p. 400.
- Geiger, S., Haggerty, R., Dilles, J., Reed, M., and Matthai, S., 2002, New insights from reactive transport modeling; the formation of sericitic vein envelopes during early hydrothermal alteration at Butte, Montana: *Geofluids*, v. 2, p. 185-201.
- Götze, J., Plötze, M., and Habermann, D., 2001, Origin, spectral characteristics and practical applications of the cathodoluminescence (CL) of quartz - a review: *Mineralogy and Petrology*, v. 71, p. 225-250.
- Guillou-Frottier, L., and Burov, E., 2003, The development and fracturing of plutonic apices: implications for porphyry ore deposits: *Earth and Planetary Science Letters*, v. 214, p. 341-356.
- Landtwing, M. R., and Pettke, T., 2005, Relationships between SEM-cathodoluminescence response and trace-element compositions of hydrothermal vein quartz: *American Mineralogist*, v. 90, p. 122-131.
- Landtwing, M. R., Pettke, T., Halter, W. E., Heinrich, C. A., Redmond, P. B., Einaudi, M. T., and Kunze, K., 2005, Copper deposition during quartz dissolution by cooling magmatic-hydrothermal fluids: the Bingham porphyry: *Earth and Planetary Science Letters*, v. 235, p. 229-243.
- Lowers, H. A., Donovan, J. J., and Rusk, B. G., in review, Improved electron probe microanalysis of trace elements: *American Mineralogist*.
- Lund, K., Aleinikoff, J. N., and Kunk, M. J., 2005, Geochronologic evidence of multiple overlapping, fracture-controlled magmatic and hydrothermal pulses in the Butte District; genetic implications for Ag and Cu veins and porphyry Mo: *Geological Society of America-Abstract with Programs*, v. 37, p. 314.

- Lund, K., Aleinikoff, J. N., Kunk, M. J., Unruh, D. M., Zeihen, G. D., Hodges, W. C., Du Bray, E. A., and O'Neill, J. M., 2002, SHRIMP U-Pb and $^{40}\text{Ar}/^{39}\text{Ar}$ age constraints of relating plutonism and mineralization in the Boulder Batholith region, Montana: *Economic Geology*, v. 97, p. 241-267.
- Marshall, D. J., 1988, *Cathodoluminescence of Geological Materials*: Boston, Massachusetts, Unwin Hyman Ltd, 146 p.
- Meyer, C., Shea, E. P., and Charles C. Goddard, J., 1968, Ore Deposits at Butte, Montana, *Ore Deposits of the U.S.*, Chap. 65, p. 1373-1415.
- Mueller, A., Wiedenbeck, M., van den Kerkhof, A. M., Kronz, A., and Simon, K., 2003, Trace elements in quartz; a combined electron microprobe, secondary ion mass spectrometry, laser-ablation ICP-MS, and cathodoluminescence study: *European Journal of Mineralogy*, v. 15, p. 747-763.
- Müller, A., René, M., Behr, H. J., and Kronz, A., 2003a, Trace elements and cathodoluminescence of igneous quartz in topaz granites from the Hub Stock (Slavkovský Les Mts., Czech Republic): *Mineralogy and Petrology*, v. 79, p. 167-191.
- Müller, A., Wiedenbeck, M., van-den-Kerkhof, A. M., Kronz, A., and Simon, K., 2003b, Trace elements in quartz- a combined electron microprobe, secondary ion mass spectrometry, laser-ablation ICP-MS, and cathodoluminescence study: *European Journal of Mineralogy*, v. 15, p. 747-763.
- Penniston-Doreland, S. C., 2001, Illumination of vein quartz textures in a porphyry copper ore deposit using scanned cathodoluminescence: Grasberg Igneous Complex, Irian Jaya, Indonesia: *American Mineralogist*, v. 86, p. 652-666.
- Reed, M. H., 1999, Zoning of metals and early potassic and sericitic hydrothermal alteration in the Butte, Montana, porphyry Cu-Mo deposit: *Geological Society of America Abstracts with Programs*, v. 31, p. A381.
- Richards, J. P., 2003, Tectono-magmatic precursors for porphyry Cu-(Mo-Au) deposit formation: *Economic Geology*, v. 98, p. 1515-1533.
- Roberts, S. A., 1975, Early hydrothermal alteration and mineralization in the Butte district, Montana: Ph.D. dissertation thesis, Harvard University, 157 p.
- Rubin, A. M., 1995, Getting granite dikes out of the source region: *Journal of Geophysical Research*, v. 100, p. 5911-5929.

- Rusk, B., Lowers, H. A., and Reed, M. H., 2008a, Trace elements in hydrothermal quartz: Relationships to cathodoluminescent textures and insights into vein formation: *Geology*, v. 36, p. 547-550.
- Rusk, B., and Reed, M., 2002, Scanning electron microscope-cathodoluminescence analysis of quartz reveals complex growth histories in veins from the Butte porphyry copper deposit, Montana: *Geology*, v. 30, p. 727-730.
- Rusk, B. G., Reed, M. H., and Dilles, J. H., 2008b, Fluid inclusion evidence for magmatic-hydrothermal fluid evolution in the porphyry copper-molybdenum deposit at Butte, Montana: *Economic Geology*, v. 103, p. 307-334.
- Rusk, B. G., Reed, M. H., Dilles, J. H., and Kent, A. J. R., 2006, Intensity of quartz cathodoluminescence and trace-element content in quartz from the porphyry copper deposit at Butte, Montana: *American Mineralogist*, v. 91, p. 1300-1312.
- Rutherford, M. J., and Gardner, J. E., 2000, Rates of Magma Ascent, *in* Sigurdsson, H., ed., *Encyclopedia of Volcanoes*, Academic Press, p. 207-217.
- Seedorff, E., Dilles, J. H., John M. Proffett, J., Einaudi, M. T., Surcher, L., Stavast, W. J. A., Johnson, D. A., and Barton, M. D., 2005, Porphyry Deposits: Characteristics and Origin of Hypogene Features: *Economic Geology*, v. 100th Anniversary Volume, p. 251-298.
- Snee, L., Miggins, D., Geissman, J., Reed, M., Dilles, J., and Zhang, L., 1999, Thermal history of the Butte porphyry system, Montana: *Geological Society of America-Abstract with Programs*, v. 31, p. 380.
- Titley, S. R., and Beane, R. E., 1981, Porphyry Copper Deposits: *Economic Geology*, v. 75th Anniversary Volume, p. 214-269.
- Tosdal, R. M., and Richards, J. P., 2001, Magmatic and structural controls on the development of porphyry Cu \pm Mo \pm Au deposits, *Reviews in Economic Geology*, 14, p. 157-181.
- van-den-Kerkhof, A. M., Kronz, A., and Simon, K., 2001, Trace element redistribution in metamorphic quartz and fluid inclusion modification: observations by cathodoluminescence: XVI ECROFI European Current Research On Fluid Inclusions, Abstracts, v. 7, p. 447-450.
- van den Kerkhof, A. M., Kronz, A., and Simon, K., 2001, Trace element redistribution in metamorphic quartz and fluid inclusion modification: observations by cathodoluminescence: XVI ECROFI European Current Research On Fluid Inclusions, Abstracts, v. 7, p. 447-450.

- Wark, D. A., Hildreth, W., Spear, F. S., Cherniak, D. J., and Watson, E. B., 2007, Pre-eruption recharge of the Bishop magma system: *Geology* v. 35, p. 235.
- Wark, D. A., and Watson, E. B., 2006, TitaniQ; a titanium-in-quartz geothermometer: *Contributions to Mineralogy and Petrology*, v. 152, p. 743-754.
- Watt, G. R., Wright, P., Galloway, S., and McLean, C., 1997, Cathodoluminescence and trace element zoning in quartz phenocrysts and xenocrysts: *Geochimica et Cosmochimica Acta*, v. 61, p. 4337-4348.

CHAPTER VI

- Brimhall, G.H. (1977) Early fracture-controlled disseminated mineralization at Butte, Montana. *Economic Geology*, 72, 37-59.
- Carslaw, H.S., and Jaeger, J.C. (1947) Linear flow of heat: the infinite and semi-infinite solid. *Conduction of Heat in Solids*, p. 383. Oxford University Press, London.
- Cherniak, D.J., Watson, E.B., and Wark, D.A. (2007) Ti diffusion in quartz. *Chemical Geology*, 236, 65-74.
- Dilles, J.H., Martin, M.W., Stein, H., and Rusk, B. (2003) Re-Os and U-Pb ages for the Butte copper district, Montana; a short- or long-lived hydrothermal system? *Geological Society of America-Abstract with Programs*, 35(6), 400.
- Fournier, R.O. (1999) Hydrothermal processes related to movement of fluid from plastic to brittle rock in the magmatic-epithermal environment. *Economic Geology*, 94(8), 1193-1212.
- Heddad, S.C., Worden, R.H., Prior, D.J., and Smalley, P.C. (2006) Quartz Cement in the Fontainebleau Sandstone, Paris Basin, France: Crystallography and Implications for Mechanisms of Cement Growth *Journal of Sedimentary Research*, 76, 244-256.
- Hilgers, C., and Urai, J.L. (2002) Experimental study of syntaxial vein growth during lateral fluid flow in transmitted light: first results. *Journal of Structural Geology*, 24, 1029-1043.
- Landtwing, M.R., and Pettke, T. (2005) Relationships between SEM-cathodoluminescence response and trace-element compositions of hydrothermal vein quartz. *American Mineralogist*, 90, 122-131.
- Lund, K., Aleinikoff, J.N., Kunk, M.J., Unruh, D.M., Zeihen, G.D., Hodges, W.C., Du Bray, E.A., and O'Neill, J.M. (2002) SHRIMP U-Pb and ⁴⁰Ar/³⁹Ar age constraints

of relating plutonism and mineralization in the Boulder Batholith region, Montana. *Economic Geology*, 97, 241-267.

Meyer, C., Shea, E.P., and Charles C. Goddard, J. (1968) Ore Deposits at Butte, Montana. *Ore Deposits of the U.S.*, Chap. 65, p. 1373-1415.

Okamoto, A., Kikuchi, T., and Tsuchiya, N. (2008) Mineral distribution within polyminerale veins in the Sanbagawa belt, Japan: Implications for mass transfer during vein formation. *Contributions to Mineralogy and Petrology*, 156, 323-336.

Okamoto, A., and Tsuchiya, N. (2008) Kinetics and textural development of quartz veins. *Geochimica et Cosmochimica Acta*, 72(12), A703.

-. (in press) Velocity of vertical fluid ascent within mineral veins. *Geology*.

Penniston-Doreland, S.C. (2001) Illumination of vein quartz textures in a porphyry copper ore deposit using scanned cathodoluminescence: Grasberg Igneous Complex, Irian Jaya, Indonesia. *American Mineralogist*, 86, 652-666.

Piazolo, S., Prior, D.J., and Holness, M.D. (2005) The use of combined cathodoluminescence and EBSD analysis: a case study investigating grain boundary migration mechanisms in quartz. *Journal of Microscopy*, 217(2), 152-161.

Prior, D.J., Boyle, A.P., Brenker, F., Cheadle, M.C., Day, A., Lopez, G., Peruzzi, L., Potts, G., Reddy, S., Spiess, R., Timms, N.E., Trimby, P., Wheeler, J., and Zetterstrom, L. (1999) The application of electron backscatter diffraction and orientation contrast imaging in the SEM to textural problems in rocks. *American Mineralogist*, 84, 1741-1759.

Reed, M.H. (1999) Zoning of metals and early potassic and sericitic hydrothermal alteration in the Butte, Montana, porphyry Cu-Mo deposit. *Geological Society of America Abstracts with Programs*, 31(&), A381.

Reed, R.M., and Gale, J.F.W. (2008) Integrating electron backscatter diffraction and SEM-based cathodoluminescence into studies of crack-seal texture and crystal growth in quartz-lined sandstone macrofractures. *Microbeam Analysis Society EBSD Workshop Program and Abstracts*.

Rusk, B., Lowers, H.A., and Reed, M.H. (2008a) Trace elements in hydrothermal quartz: Relationships to cathodoluminescent textures and insights into vein formation. *Geology*, 36(7), 547-550.

- Rusk, B., and Reed, M. (2002) Scanning electron microscope-cathodoluminescence analysis of quartz reveals complex growth histories in veins from the Butte porphyry copper deposit, Montana. *Geology*, 30, 727-730.
- Rusk, B.G., Reed, M.H., and Dilles, J.H. (2008b) Fluid inclusion evidence for magmatic-hydrothermal fluid evolution in the porphyry copper-molybdenum deposit at Butte, Montana. *Economic Geology*, 103, 307-334.
- Rusk, B.G., Reed, M.H., Dilles, J.H., and Kent, A.J.R. (2006) Intensity of quartz cathodoluminescence and trace-element content in quartz from the porphyry copper deposit at Butte, Montana. *American Mineralogist*, 91, 1300-1312.
- Seedorff, E., Dilles, J.H., John M. Proffett, J., Einaudi, M.T., Surcher, L., Stavast, W.J.A., Johnson, D.A., and Barton, M.D. (2005) Porphyry Deposits: Characteristics and Origin of Hypogene Features. *Economic Geology*, 100th Anniversary Volume, 251-298.
- Snee, L., Miggins, D., Geissman, J., Reed, M., Dilles, J., and Zhang, L. (1999) Thermal history of the Butte porphyry system, Montana. *Geological Society of America-Abstract with Programs*, 31, 380.